Cosmic lensing of galaxies and the cosmic microwave background beyond the linear regime

Vanessa Martina Böhm

München 2017

Cosmic lensing of galaxies and the cosmic microwave background beyond the linear regime

Vanessa Martina Böhm

Dissertation
an der Fakultät für Physik
der Ludwig–Maximilians–Universität
München

vorgelegt von
Vanessa Martina Böhm
aus Heidelberg

München, den 13.06.2017

Erstgutachter: PD Dr. Torsten Enßlin
Zweitgutachter: Prof. Dr. Jochen Weller
Tag der mündlichen Prüfung: 26.07.2017

Contents

List of Figures

List of Tables

Zusammenfassung

Die großskalige Massenverteilung im beobachtbaren Universum lenkt, ganz ähnlich einer Linse, das Licht weit entfernter Objekte ab. Dieser Gravitationslinseneffekt ist zwar schwach, kann aber, dank äußerst präziser Messtechniken, nicht nur nachgewiesen, sondern sogar zur Bestimmung kosmologischer Parameter oder zur Überprüfung physikalischer Modelle verwendet werden. Dazu ist, neben sehr genauen Messinstrumenten, auch eine möglichst exakte theoretische Modellierung des Effekts notwendig. In dieser Doktorarbeit stellen wir drei Arbeiten zu alternativen oder verbesserten Analysemethoden des schwachen Gravitationslinseneffekts vor.

Messungen der gelinsten Anisotropien im kosmischen Mikrowellenhintergund ermöglichen eine Rekonstruktion des Linsenpotentials. Dieses misst die integrierte Massenverteilung vom Beobachter bis zu einer Distanz, die einer Zeit 380 000 Jahre nach dem Urknall entspricht. In der ersten Arbeit stellen wir einen Maximum A Posteriori (MAP) Schätzer für dieses Linsenpotential vor. Diese Rekonstruktionsmethode stellt eine Verbesserung gegenüber dem Standardschätzers dar, welcher lediglich auf einer Näherung des MAP Schätzers beruht und zusätzliche Korrekturen benötigt.

In der zweiten Arbeit wenden wir uns dem Standardschätzer für die spektrale Leistungsdichte desselben Linsenpotentials zu, für den wir einen neuen Korrekturterm identifizieren und abschätzen. Diese neue Korrektur wird erforderlich, da der Standardschätzer auf der Annahme eines normal verteilten Linsenpotentials beruht, dieses jedoch, aufgrund nicht-linearer Strukturbildung nicht exakt Gauß-verteilt ist. Unseren Abschätzungen zufolge sollte diese neue, nicht-lineare Korrektur bereits in aktuellen Experimenten berücksichtigt werden.

Mit den Auswirkungen nicht-linearer Strukturbildung auf Linsenrekonstruktionen beschäftigen wir uns auch in der letzten Arbeit, allerdings im Kontext des Gravitationslinseneffekts auf die gemessene Form von Galaxien. Nicht-lineare Korrekturen sind dort besonders relevant, da nicht-lineare Skalen in der Massenverteilung signifikant zu dem gemessenen Linseneffekt beitragen. Aus dieser Motivation heraus, haben wir einen neuen MAP Schätzer zur dreidimensionalen Massenrekonstruktion aus der Messung gelinster Galaxien entwickelt. Dieser unterscheidet sich von vorhandenen Rekonstruktionsmethoden vor allem dadurch, dass er statt einer Gaußschen Massenverteilung, a priori eine lognormale Massenverteilung annimmt. Letztere beinhaltet Informationen über die Schiefe der Verteilung und erzwingt postive Dichten in der Rekonstruktion. Wir belegen die Überlegenheit der lognormalen über die normale a priori Verteilung durch Tests an simulierten Daten.

Abstract

The large-scale mass distribution in the observable universe deflects the light of distant objects, similarly to a lens. This gravitational lensing effect is weak but can nevertheless be detected and – thanks to technologically advanced measurement techniques – even be used for determining cosmological parameters or testing physical models. Apart from extremely precise measuring instruments, this requires an accurate theoretical modeling of the effect. In this thesis, we present three works on alternative or improved analysis techniques for weak gravitational lensing measurements.

After a general introduction to cosmology and weak gravitational lensing, we dedicate the first two chapters to the study of weak lensing of the cosmic microwave background (CMB). Measurements of this background radiation allow to extract an estimate of the CMB lensing potential, a measure of the integrated mass distribution from today's observer to a distance corresponding to only $380\,000$ years after the Big Bang. We present a maximum a posteriori (MAP) estimator for this lensing potential which is an improvement over the quadratic estimator that has been used for all lensing measurements to date. The quadratic estimator is only an approximation to the MAP estimator and requires additional corrections and post-processing.

In the next chapter we turn to the standard estimator for the CMB lensing potential power spectrum for which we identify and compute a new significant bias term. This correction becomes necessary since the standard estimator is based on the assumption of a normally distributed lensing potential which ceases to be valid in the presence of non-linear structure formation. According to our estimates, this new non-linear bias should be relevant already for current experiments.

The influence of non-linear structure formation on lensing reconstructions is also addressed in the last chapter where we turn to the analysis of weak lensing of galaxy images. Corrections to the Gaussian model are particularly relevant in this case since non-linear scales in the matter distribution contribute significantly to the observed image distortions. Motivated by this observation, we have developed and tested a new MAP estimator that reconstructs the 3D density distribution from measured galaxy shapes. This method is different to existing methods in particular since it employs a lognormal prior on the density distribution instead of a Gaussian one. The latter contains information about the strict positiveness of the field as well as its asymmetric distribution. We prove the superiority of the lognormal prior over the Gaussian one in a series of tests on simulated data.

Notations and Conventions

Throughout this thesis, we use non-unitary Fourier conventions

$$\mathcal{F}[f(\mathbf{x})] = \tilde{f}(\mathbf{k}) = \int d\mathbf{x}\, f(\mathbf{x}) e^{-i\mathbf{k}\mathbf{x}}, \qquad \mathcal{F}^{-1}[\tilde{f}(\mathbf{k})] = f(\mathbf{x}) = \int \frac{d\mathbf{k}}{(2\pi)^n}\, \tilde{f}(\mathbf{k}) e^{i\mathbf{k}\mathbf{x}} \qquad (1)$$

and express correlations in harmonic space in terms of power spectra, bispectra and trispectra defined by

$$\langle A(\mathbf{k})B(\mathbf{k}')\rangle = (2\pi)^n \delta_{\mathrm{D}}(\mathbf{k}+\mathbf{k}') P_{AB}(|\mathbf{k}|)$$
$$\langle A(\mathbf{k})B(\mathbf{k}')C(\mathbf{k}'')\rangle = (2\pi)^n \delta_{\mathrm{D}}(\mathbf{k}+\mathbf{k}'+\mathbf{k}'') B_{ABC}(\mathbf{k},\mathbf{k}',\mathbf{k}'')$$
$$\langle A(\mathbf{k})B(\mathbf{k}')C(\mathbf{k}'')D(\mathbf{k}''')\rangle_c = (2\pi)^n \delta_{\mathrm{D}}(\mathbf{k}+\mathbf{k}'+\mathbf{k}''+\mathbf{k}''') \mathcal{T}_{ABCD}(\mathbf{k},\mathbf{k}',\mathbf{k}'',\mathbf{k}'''), \qquad (2)$$

where n denotes the spatial dimension. Vectors are indicated by bold print, their absolute values in italics, e.g. $|\mathbf{k}| = k$. In 2D the Fourier conjugate to the configuration space position is often denoted $\mathbf{l}$ instead of $\mathbf{k}$. This is because describing quantities on the sphere that have small angular extent allows to replace the spherical harmonic transform to good approximation by a Fourier transform. In this limit (referred to as flat-sky approximation) the scales of the Fourier modes correspond to the ℓ-index of the spherical harmonics $Y_{\ell m}(\boldsymbol{\theta})$ (see e.g. [95]).

Since the topics covered in this thesis require to work in many different coordinate systems, we can not avoid using similar notations for different coordinate variables in different chapters. Within individual chapters and within a certain context the meaning of the coordinate variables stays fixed. In Table 1 we summarize the notations used for different coordinates in the context of CMB lensing (Chapter 2 and 3), weak galaxy lensing (Chapter 4) and in the introduction (Chapter 1). Table 2 summarizes the symbols used to denote the most important physical fields in this thesis.

The probability distribution of a quantity x is denoted $P(x)$, other fixed variables on which it might depend are separated from the argument by a vertical line, e.g. $P(x|y)$. Following this convention we write a (multivariate) Gaussian distribution with mean m and covariance C as $\mathcal{G}(x|m,C)$ or $\mathcal{G}(x|C)$ for zero mean.

We further use a generalized sum convention where repeated indices and coordinates, if they do not appear on both sides of the equation, are either integrated over (if they are continuous) or summed over (if they are discrete), e.g.,

$$s(\mathbf{x}) = s_{\mathbf{x}} = R_{\mathbf{x}\mathbf{y}}s_{\mathbf{y}} \equiv \int d\mathbf{y}\, R(\mathbf{x},\mathbf{y})s(\mathbf{y}). \qquad (3)$$

context	variable	meaning
CMB lensing	$\mathbf{x}, \mathbf{y}, \mathbf{z}$, also primed	2D angular direction on the sky
galaxy lensing	$\boldsymbol{\theta}$	2D angular direction on the sky
introduction	$\boldsymbol{\theta}$	2D angular direction on the sky
galaxy lensing	$\mathbf{x}, \mathbf{y}, \mathbf{z}$	3D comoving coordinates
galaxy lensing	$\mathbf{x}', \mathbf{y}', \mathbf{z}'$ [short for $(\mathbf{x}', \tau)$ etc.]	3D comoving coordinates on light-cone
galaxy lensing	τ	conformal time

Table 1:   Summary of different coordinates used in this thesis together with their respective vector notation.

field/ field statistic	symbol
lensing potential (2D field)	$\phi(\boldsymbol{\theta})$, $\phi(\mathbf{x})$
gravitational potential (3D field)	$\psi(\mathbf{x}, \tau)$, $\psi(\boldsymbol{\theta}, \chi)$
CMB temperature fluctuations (2D field)	$T(\boldsymbol{\theta})$, $T(\mathbf{x})$

Table 2:   Notations of most common physical fields. Note that the lensing potential ϕ can refer to the CMB lensing potential (in Chapter 2 and 3) as well as the the lensing potential of weak galaxy lensing (Chapter 4).

To keep the notation short, we will sometimes drop the coordinates and write $Rs \equiv R_{\mathbf{xy}} s_{\mathbf{y}}$. For compactness we also denote

$$\int_{\mathbf{l}} \equiv \int \frac{\mathrm{d}\mathbf{l}}{(2\pi)^2} \quad \text{and} \quad \int_{\mathbf{k}} \equiv \int \frac{\mathrm{d}\mathbf{k}}{(2\pi)^3}. \tag{4}$$

Chapter 1

Introduction

In this chapter we provide a brief overview over the mathematical and physical concepts that form the basis of the research results presented in the subsequent chapters. We start by reviewing Bayesian statistics (Section 1.1) and information field theory (Section 1.2) before we turn to cosmology in Section 1.3. After a short recap of the standard ΛCDM model (Sections 1.3.1-1.3.3), we present the standard formalism to describe weak lensing by large-scale structure in Section 1.4, which we then specify to weak lensing of the cosmic microwave background (Section 1.5) and weak lensing of galaxies (Section 1.6). In Section 1.7 we outline the great potential of weak lensing measurements for constraining cosmological models.

1.1 Bayesian Statistics

The essence of Bayesian statistics lies in the interpretation of probabilities P as degrees of belief. This belief can change when additional information becomes available. The central theorem in Bayesian statistics is Bayes' theorem that describes how one's knowledge of the status of a variable s changes when additional information on it becomes available through the data d

$$P(s|d) = \frac{P(d|s)P(s)}{P(d)}. \tag{1.1}$$

$P(s|d)$ is called the posterior distribution or simply posterior. It expresses one's knowledge of s *after* the former knowledge has been updated by the data (hence the name). The knowledge one had *before* the update on the status of s is given by the prior distribution $P(s)$. The additional information that has become available through the data d is given by the likelihood $P(d|s)$ that expresses the probability of obtaining the observed realization of the data d given a fixed field configuration or status of s. Finally, $P(d)$ is called evidence and is defined by

$$P(d) = \int \mathcal{D}s \, P(d|s)P(s), \tag{1.2}$$

where the integration is over all possible states or configurations of s^1. It is a normalization that can often be neglected if one is only interested in estimating the moments of the posterior. It has, however, applications in model comparison: If two models α and β yield different prior probabilities $P(s|\alpha)$ and $P(s|\beta)$, their evidences $P(d|\alpha)$ and $P(d|\beta)$ will differ by a factor. This so called Bayes factor $\mathcal{B}$ can be used for model selection, i.e. one can discard one model in favor of another, if $\mathcal{B}$ is much larger or much smaller than 1. In that sense, the Bayes factor can be regarded as the Bayesian decision tool for models. Which values of $\mathcal{B}$ should result in abandoning one model in favor of another is a question of decision theory, i.e. it should depend on the cost of potentially making a wrong decision.

1.2   Information Field Theory (IFT)

In physical inference problems one is often interested in inferring the statistics and realizations of continuous physical fields, such as, e.g., the gravitational potential of objects or the temperature fluctuations in the cosmic microwave background. The discretization of these fields is often artificial and imposed by measurement devices and/or numerical analysis techniques. It is therefore natural to formulate inference problems in an abstract way that is as independent as possible of the pixelization scheme or basis functions and treats continuous fields mathematically as such. This allows to make use of the vast amount of mathematical techniques that have been developed for classical and quantum field theories and is the basic idea of information field theory (IFT)[55]. As a statistical field theory, IFT provides a framework for the application of Bayesian statistical inference on fields. Many inference methods have been derived in this framework, notably for problems with unknown signal correlation structure [54, 175, 56] and it has been successfully applied to inference problems in astrophysics and cosmology (see e.g. [50, 202, 174, 111, 64, 185]).

In the next sections, we will briefly introduce the formalism and standard notations of IFT (notably used in Chapters 2 and 4) by the example of a simple maximum a posteriori (MAP) problem that results in a Wiener Filter.

1.2.1   Wiener Filter Theory

To infer the most probable realization of some physical field s, one carries out a measurement that yields a discrete data vector d. This data is typically affected by some (measurement) noise n. Also, one rarely measures s directly. There is at least some operation in the measurement apparatus that converts the signal from the continuous field into the discretized data vector. In most cases there is an even more complicated relation between the underlying field of interest and the measurement data. In weak lensing of galaxies, for example, we can measure lensing only via its effect on galaxy shapes. In measurements of the CMB, we measure a convolution of the temperature field with the beam of the telescope.

---

[1]We use the most general notation here, for discretized quantities the integration transforms into a sum.

For linear measurement devices, the relation between unnoisy data and signal can be expressed in terms of a linear operator R. This *response operator* encodes all operations that translate the underlying field into unnoisy measurement data. R can take very complicated forms and is usually composed of some physical operation, e.g. lensing, plus some characteristics of the measurement process, e.g. a beam convolution. The application of R in continuous space reads

$$[Rs](\mathbf{x}) = \int d\mathbf{x}' \, R(\mathbf{x}, \mathbf{x}') s(\mathbf{x}'), \tag{1.3}$$

and its discretization is straightforward

$$[Rs]_i = \sum_j R_{ij} s_j. \tag{1.4}$$

Note that the last equation is still abstract and independent of the discretization or basis functions in which the problem is expressed.

The total data is the signal response Rs plus a typically independent noise contribution

$$d = Rs + n, \tag{1.5}$$

with n denoting the realization of the noise. Given measurement data d, one finds the most probable realization of s by maximizing the posterior $P(s|d)$. Following Bayes' theorem Eq. (1.1), this posterior can be expressed in terms of a prior distribution and a likelihood.

In nature, many processes lead to Gaussian-distributed quantities due to the central limit theorem. For example, the initial conditions for the mass distribution in the Universe are believed to result from the superposition of many random quantum fluctuations of the inflaton field. In the case of lensing, the total lensing deflection is a sum over many lensing events, which Gaussianize the statistics of the total deflection field. Even if the true distribution of a quantity is non-Gaussian, given only limited knowledge of it, such as its mean and the covariance, the principle of maximum entropy implies that the most ignorant estimate of the distribution i.e., the fit that adds the least additional information, is a normal distribution with this mean and covariance.

Because of this, we will often encounter inference problems where both noise statistics and the prior distribution are normally distributed. A Gaussian noise distribution implies a Gaussian likelihood with covariance equal to the noise covariance N,

$$P(d|s) = \int \mathcal{D}n \, \mathcal{G}\left(n|N\right) P(d|n, s) = \int \mathcal{D}n \, \mathcal{G}\left(n|N\right) \delta_{\mathrm{D}}\left[d - (Rs + n)\right]$$
$$= \mathcal{G}\left(d - Rs|N\right), \tag{1.6}$$

where $\int \mathcal{D}n$ denotes integration over all possible realizations of n.

Together with a Gaussian prior $\mathcal{G}(s|S)$ with covariance S, this yields a Gaussian posterior of the form

$$P(s|d) = \frac{1}{\sqrt{|2\pi D|}} \exp\left[-\frac{1}{2}(s - m)^\dagger D^{-1}(s - m)\right], \tag{1.7}$$

where we have defined $m = Dj$, with $j = R^\dagger N^{-1} d$, called the information source due to its dependence on the data, and $D = \left[S^{-1} + R^\dagger N^{-1} R\right]^{-1}$, the information propagator which propagates the information from the information source to our estimate of the underlying field $m = \hat{s}$. Finding the maximum of $P(s|d)$ is therefore a filter operation of the form

$$m = Dj = \left[S^{-1} + R^\dagger N^{-1} R\right]^{-1} R^\dagger N^{-1} d, \tag{1.8}$$

the so-called Wiener filter [235]. It involves an operator inversion that can only rarely be solved analytically (e.g. if there exists a basis in which all operators are diagonal). In most cases, one has to resort to numerical techniques, such as the conjugate gradient or steepest descent method to solve Eq. (1.8).

Note that the formulation in Eq. (1.8) is in signal space. This means that d gets translated into the space of the signal by application of $R^\dagger$ before the information propagator D, in which both terms, S^{-1} and $R^\dagger N^{-1} R$, are in signal space, is applied to it. The same filter operation can be equivalently formulated in data space [227],

$$m' = m = SR^\dagger \left[RSR^\dagger + N\right]^{-1} d. \tag{1.9}$$

Both formulations can be found in the literature.

1.2.2   Numerical IFT

For practical purposes, inference problems formulated in IFT have to be discretized for numerical implementation. To make this as simple and intuitive as possible and to keep the independence of the basis in which the inference problems are expressed, Selig et al. [201] have developed a numerical python package, named NIFTy[2]. NIFTy allows to implement problems formulated in the language of IFT in a coordinate and resolution independent way. It then adapts the computation internally to the chosen configuration. In particular, it consistently takes into account volume factors that appear, e.g., in matrix applications. Implementations in Chapters 2 and 4 make use of the NIFTy package.

1.3   Cosmology

1.3.1   Cosmological Model

Einstein's field equations, the central equations in general relativity, connect the curvature of space-time to the energy-momentum content of the Universe

$$R_{\mu\nu} - \frac{1}{2} g_{\mu\nu} R = \frac{8\pi G}{c^4} T_{\mu\nu} + \Lambda g_{\mu\nu}, \tag{1.10}$$

where $R_{\mu\nu}$ is the Ricci tensor, which (in a coordinate basis) can be fully described by second derivatives of the metric tensor $g_{\mu\nu}$. Its contraction, $R \equiv R^\mu_\mu$ is the Ricci scalar and $T_{\mu\nu}$ the

---

[2]`http://wwwmpa.mpa-garching.mpg.de/ift/nifty`

energy-momentum tensor. The constant Λ is called cosmological constant. Its value needs to be determined from observations (it can be zero). The cosmological constant is a priori only a mathematical freedom in the definition of the Einstein equation and its physical interpretation is not fully understood.

We make the standard assumption that the metric tensor of the observable Universe can be split into a background metric, whose evolution is guided by the cosmic mean energy density, plus small perturbations, $h_{\mu\nu}$, sourced by density fluctuations

$$g_{\mu\nu} = g_{\mu\nu}^{bg} + h_{\mu\nu}, \text{with } |h_{\mu\nu}| \ll 1. \tag{1.11}$$

Under the assumptions of statistical isotropy and homogeneity, space-time can be foliated into space-like hypersurfaces of constant coordinate time. This allows to write the background metric in the well known Robertson-Walker form, with line-element

$$\mathrm{d}s^2 = a^2(t) \left[-c^2 \mathrm{d}\tau^2 + \mathrm{d}\chi^2 + f_K^2(\chi)\mathrm{d}\omega^2 \right]. \tag{1.12}$$

To write Eq. (1.12), we have introduced a spherical symmetric coordinate system in which χ is the radial coordinate and $\mathrm{d}\omega$ the solid angle element. χ is also known as comoving distance, since it stays constant as the Universe expands. The function $f_K(\chi)$ depends on the curvature K of the space-like hypersurfaces and is given by

$$f_K(\chi) = \begin{cases} K^{-1/2} \sin\left(K^{1/2}\chi\right), & \text{if } K > 0 \\ \chi, & \text{if } K = 0 \\ |K|^{-1/2} \sinh\left(|K|^{1/2}\chi\right), & \text{if } K < 0. \end{cases} \tag{1.13}$$

$f_K(\chi)$ is called comoving angular diameter distance, for it is the comoving distance one infers by dividing the physical size of an object by its angular extent on the sky. The scale factor $a(t)$ is a function of the coordinate time that determines the homogeneous evolution of the energy densities in the Universe. The conformal time is defined by $\mathrm{d}\tau = \mathrm{d}t/a(t)$.

The time-evolution of the scale factor is found by solving the Friedmann equations, which are the Einstein equations Eq. (1.10) specialized to a Robertson-Walker metric and the energy-momentum tensor of the cosmic fluid,

$$\left(\frac{\dot{a}}{a}\right)^2 = \frac{8\pi G}{3}\rho - \frac{Kc^2}{a^2} + \frac{\Lambda c^2}{3} \tag{1.14}$$

$$\left(\frac{\ddot{a}}{a}\right) = -\frac{4\pi G}{3}\left(\rho + \frac{3p}{c^2}\right) + \frac{\Lambda c^2}{3}. \tag{1.15}$$

The initial value of a is fixed by demanding $a = 1$ today; the relative change of the scale factor, $\frac{\dot{a}}{a}$, is also known as Hubble parameter $H(a)$. The Hubble parameter today is often expressed in terms of the dimensionless constant h, $H(a{=}1){=}H_0{=}h\,100\,\mathrm{km}/(\mathrm{s\,Mpc})$. Measurements of H_0 determine the current value of $\dot{a}$. The expansion or contraction of space leads to a red- or blueshift of photons. The redshift z, defined by the relative difference between observed and emitted wavelength, is directly related to the scale factor

$$z \equiv \frac{\lambda_{\mathrm{obs}} - \lambda_{\mathrm{em}}}{\lambda_{\mathrm{em}}} = \frac{a_{\mathrm{obs}}}{a_{\mathrm{em}}} - 1. \tag{1.16}$$

The cosmic fluid consists of a radiation component with density $\rho_{\mathrm{rad}}(\tau) \propto a^{-4}$, a matter component with density $\rho_m(\tau) \propto a^{-3}$ and an energy density associated with the cosmological constant $\rho_\Lambda(\tau) = \mathrm{const}$. These densities are typically expressed in terms of dimensionless density parameters $\Omega_{i0} = \rho_i(a{=}1)/\rho_c(a{=}1)$, where the critical density ρ_c is the density required for a spatially flat Universe $\rho_c = 3H_0^2/(8\pi G)$. By analogy, one also defines a curvature density parameter $\Omega_K = -Kc^2/H_0^2$, which scales like a^{-2}. Current estimates for the density parameters from recent experiments and the Hubble parameter H_0 are listed in Table 1.1. A remarkable result of the recent cosmological observations is that the scale factor a increases faster with time than expected given the measured curvature, matter and radiation density. In the framework of general relativity, the observed accelerated expansion could be sourced by a cosmological constant, as well as by another, yet unknown energy component, or a mixture of both. It is also possible that this observation points towards a different theory of gravitation. Finding a profound physical explanation for the expansion is one of the greatest challenges for cosmology today.

H_0	Ω_{m0}	$\Omega_{\mathrm{rad}0}$	Ω_Λ	Ω_K
67.74 ± 0.49	0.3089 ± 0.0062	$(5.39 \pm 0.07) \times 10^{-5}$	0.6911 ± 0.0062	$0.0008^{+0.0040}_{-0.0039}$

Table 1.1: Current constraints on cosmological density parameters and the Hubble parameter derived from a combination of Planck data and external data sets. All values, except Ω_{r0}, were taken from the last column of Table 4 in Planck 2015 Results (XIII): Cosmological Parameters [182]. The radiation density was computed from the CMB mean temperature $T_0 = 2.7255K$, assuming that photons are the only relativistic species in the Universe today $\Omega_{\gamma 0} = \Omega_{\mathrm{rad}0}$.

Considering only scalar perturbations to the background metric[3] one arrives at a particularly simple form of the perturbed Robertson-Walker metric. In this so-called conformal Newtonian gauge [168, 153], the line-element reads

$$\mathrm{d}s^2 = a^2(t) \left[-\left(1 + 2\Psi/c^2\right) c^2 \mathrm{d}\tau^2 + \left(1 - 2\Phi/c^2\right) \left(\mathrm{d}\chi^2 + f_K^2(\chi)\mathrm{d}\omega^2\right) \right], \qquad (1.17)$$

where Φ and Ψ are two scalar degrees of freedom. For an isotropic stress-energy tensor, the Einstein equation enforces $\Phi = \Psi$ and Ψ can be identified with the Newtonian gravitational potential.

1.3.2 Structure Formation

Many observations on different scales imply that four fifth of the Universe's matter content consists of a non-electromagnetically interacting component, which only couples to gravity. This component is dubbed dark matter. The total matter density is the sum of the baryonic and dark matter densities $\Omega_m = \Omega_{dm} + \Omega_b$. Many direct searches for dark matter

---

[3]By doing so, we neglect free gravitational waves, and assume that the energy-momentum tensor of the cosmic fluid contains no significant vector or tensor parts.

particles are ongoing, but have not resulted in a firm detection yet (see e.g. [130, 160] for current reviews of the status of direct detections). Observations suggest that for structure formation, dark matter can be well modeled by a non-relativistic pressure-less fluid.

The standard cosmological model therefore assumes a cold (where cold refers to $\bar{v}_{dm} \ll c$) dark matter component (CDM) and a non-zero cosmological constant (Λ) and is referred to as ΛCDM cosmology.

In the Newtonian limit, the evolution of matter fluctuations in the cosmic mean density is guided by three non-linear coupled differential equations (on a homogeneously expanding background), well known from fluid dynamics

1. the continuity equation, which describes conservation of mass,

2. the Euler equation, describing conservation of momentum,

3. and the Poisson equation, which relates the mass density to the gravitational potential.

For components with non-negligible pressure, an equation of state must be added to close this set of equations.

Perturbations to the cosmic mean density are commonly expressed in terms of the density contrast $\delta(\mathbf{x}, a)$

$$\delta(\mathbf{x}, a) = \frac{\rho(\mathbf{x}, a) - \bar{\rho}(a)}{\bar{\rho}(a)}, \tag{1.18}$$

where $\mathbf{x}$ is a 3D position vector in comoving coordinates and we use a bar to indicate mean quantities. The initial density perturbations in the dark matter and baryons are small, $\delta_{dm} \approx 10^{-3}$ and $\delta_b \approx 10^{-5}$ at $z \approx 1100$, and normally distributed.

In the limit of $\delta \ll 1$ and negligible pressure, the set of differential equations listed above can be linearized and written as equations for the linear growth function $D_+(a)$, such that[4]

$$\delta(\mathbf{x}, a) = \frac{D_+(a)}{D_+(a_0)} \delta(\mathbf{x}, a_0) \tag{1.19}$$

For a matter-only Universe, which is a good approximation before dark energy starts to dominate the cosmic energy density, one can solve for $D_+(a)$ exactly and finds $D_+(a)=a$. In the presence of dark energy on finds $D(a) < a$, and the exact solution for D must be evaluated numerically [78, 148].

A Gaussian field with isotropic and homogeneous statistics is fully characterized by its mean and power spectrum. The mean overdensity, $\langle \delta(\mathbf{x}, a) \rangle = 0$, vanishes by construction. The matter power spectrum $P_\delta(k, a)$ is assumed to start out nearly scale invariant $P_{\text{initial}} \propto k^{n_s}$, where $n_s \approx 1$ [77, 241]. The subsequent evolution of this primordial spectrum can be expressed in term of a transfer function $T(k, a)$, $P(k, a) = T^2(k, a)P(k, a_{\text{initial}})$ [51, 52], which rescales the primordial power spectrum scale by scale to the late-time power spectrum. To accurately model this function one needs to take into account many physical

---

[4]D_+ denotes the relevant growing solution to the equations. The decaying solution is denoted D_-.

effects, such as, e.g., the scale dependent growth during an early radiation dominated phase, the coupling of baryons to radiation and dark matter, radiation and baryon pressure and the influence of massive neutrinos.

With the onset of matter domination, the simple rescaling,

$$P_\delta(k, a) = D_+^2(a)/D_+^2(a_0)P_\delta(k, a_0), \tag{1.20}$$

becomes a good approximation.

The normalization of the power spectrum is another parameter that needs to be measured from observations. It is commonly expressed in terms of the variance on scales of 8Mpc/h,

$$\sigma_8^2 = 4\pi \int \frac{k^2 \mathrm{d}k}{(2\pi)^3} \tilde{W}^2(k, R{=}8)P_\delta(k), \tag{1.21}$$

where $\tilde{W}(k, R{=}8)$ is the Fourier transform of a top hat with radius $R = 8$ Mpc/h. σ_8 is called the amplitude of matter fluctuations.

As structure grows, non-linear terms in the evolution equations become relevant. The non-linear evolution can to some extent be modeled in perturbation theory, i.e. by considering the next to leading order terms in δ (see [17] for an excellent review on the topic). However, this approximation breaks down on scales where the condition $\delta \ll 1$ is no longer satisfied. One consequence of non-linear terms is mode-coupling, e.g., the evolution of small scale modes depend on the large scale mode they reside on. Non-linear terms also give rise to higher-order cumulants in the distribution of the density contrast, e.g., at second order to a bispectrum $B_\delta(\mathbf{k}_1, \mathbf{k}_2, \mathbf{k}_3)$. Note that the density distribution must become non-Gaussian for the simple reason that the density contrast can become arbitrarily large but is physically limited from below, $\delta > -1$.

Non-linear corrections to the power spectrum can to some extent be modeled in the framework of the halo-model [217, 224]. In this thesis, we will refer to the linear power spectrum as P_δ or P_δ^{lin} and the corrected version as P_δ^{nl}.

1.3.3 Cosmic Microwave Background

The Universe is filled with a thermal photon background, whose phase-space distribution corresponds to a blackbody temperature of $2.73K$ and peaks at a wavelength in the microwave regime, hence the name cosmic microwave background (CMB). The CMB is a relic from ≈ 380 kyrs after the Big Bang, when photons and baryonic matter decoupled and the mean free path of photons became larger than the horizon. The CMB photons we receive today depict a redshifted snapshot (the redshift of the CMB is $z_{\mathrm{CMB}} \approx 1100$) of the spherical shell at the distance that light has traveled since the CMB was released. This shell is referred to as last scattering surface.

The CMB is almost spatially isotropic; deviations from the uniform temperature distribution are sourced by the small perturbations in the cosmic fluid at the time of decoupling and only occur at order 10^{-5}. These anisotropies are defined by

$$T(\boldsymbol{\theta}) \equiv \frac{T(\boldsymbol{\theta}) - \bar{T}}{\bar{T}}. \tag{1.22}$$

Denoting the fluctuations by T might seem confusing, but is generally not problematic since they are the primary focus of most CMB studies including the works in this thesis.[5]

The fluctuations in the cosmic microwave background are statistically isotropic and follow a Gaussian distribution. The CMB power spectrum can be modeled theoretically in perturbation theory and has been measured to high precision by a number of experiments from the largest scales down to arcmin scales. Comparing the measured spectrum to theoretical models provides the tightest constraints on most cosmological parameters today. In Fig. 1.1, we show the temperature power spectrum as measured by the Planck satellite together with the best ΛCDM fit to the data.
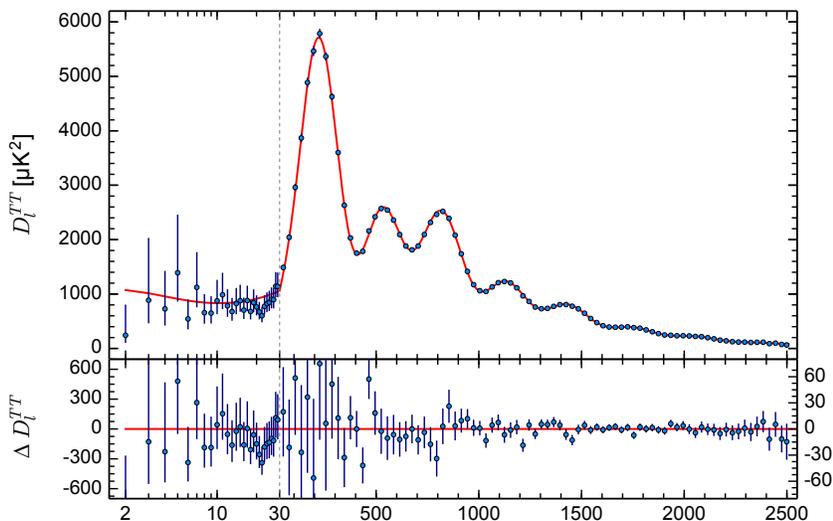
Figure 1.1: CMB temperature power spectrum $D_l^{TT} = l(l+1)C_l^{TT}/(2\pi)$ from the Planck 2015 data release [184]. The measurement is shown in blue dots and the ΛCDM fit, obtained from the full temperature plus low l polarization data, is plotted in red. The lower panel depicts the residuals.

Due to the distribution of hot and cold spots, the free electrons in the last scattering surface are exposed to quadrupole moments in the intensity of incoming radiation. Incoming photons interact with the electrons through Thomson scattering. This process polarizes the light depending on the angle between incoming and outgoing radiation. The net effect is a partial polarization of the CMB photons sourced by the presence of quadrupole moments in the temperature distribution around scattering electrons [187, 113, 26, 134](see also [102] and references therein).

---

[5]Sometimes $\Theta(\boldsymbol{\theta})$ is used instead of $T(\boldsymbol{\theta})$ to avoid confusion.

The polarization of a monochromatic photon is characterized by the Stokes parameters

$$I = A_x^2 + A_y^2 \qquad\qquad Q = A_x^2 - A_y^2 \tag{1.23}$$

$$U = 2A_x A_y \cos\left(\xi_x - \xi_y\right) \qquad V = 2A_x A_y \sin\left(\xi_x - \xi_y\right), \tag{1.24}$$

where A_x and A_y are the components of the amplitude of the electric field (the z-axis is chosen along the direction of propagation), and ξ_x, ξ_y their respective phase shift. I is the total intensity of the incoming light, the parameters Q and U capture the linear polarization, while V is needed to describe circular polarization. Since Thomson scattering produces only linearly polarized light, we can focus on Q and U to characterize the polarization state of CMB photons.

Q and U get mapped onto themselves after a rotation by π and constitute the components of a trace-less 2-tensor

$$P_{ab}(\boldsymbol{\theta}) = \frac{1}{2} \begin{pmatrix} Q(\boldsymbol{\theta}) & U(\boldsymbol{\theta}) \\ U(\boldsymbol{\theta}) & -Q(\boldsymbol{\theta}) \end{pmatrix}, \tag{1.25}$$

which can also be written as a complex number $P = |P|\mathrm{e}^{2i\varphi} = Q + \mathrm{i}U$.

The polarization tensor can be decomposed into coordinate independent gradient and curl components

$$\text{Gradient: } \nabla^2 E = \partial_a \partial_b P_{ab} \qquad \text{Curl: } \nabla^2 B = \epsilon_{ac} \partial_b \partial_c P_{ab}, \tag{1.26}$$

where ϵ_{ab} is the totally anti-symmetric tensor in 2D [239, 205, 119]. Referring to the gradient component as E-modes and to the curl componnents as B-modes is motivated by the analogy to electrostatics.

In a Fourier basis, E- and B-modes are related to the Stokes parameters by

$$E(\mathbf{l}) = \frac{1}{2} \frac{\left(l_x^2 - l_y^2\right) Q(\mathbf{l}) + 2l_x l_y U(\mathbf{l})}{l_x^2 + l_y^2} \tag{1.27}$$

$$B(\mathbf{l}) = \frac{1}{2} \frac{2l_x l_y Q(\mathbf{l}) - \left(l_x^2 - l_y^2\right) U(\mathbf{l})}{l_x^2 + l_y^2} \tag{1.28}$$

where $Q(\mathbf{l})$ and $U(\mathbf{l})$ are the Fourier coefficients of the Stokes parameter, and $\mathbf{l} = (l_x, l_y)$ the two-dimensional wave vector conjugate to $\boldsymbol{\theta}$. Expanding in a Fourier basis instead of a spherical harmonic basis is viable if one considers perturbations, whose angular extent on the sky is small compared to the 2-sphere and is known as flat sky approximation.

Curl and gradient components differ in their transformation under parity inversions. While the gradient component is invariant under parity inversions, the curl component changes sign. One can show that scalar perturbations in the density only produce gradient-like polarization patterns, while curl-like polarization requires tensor-like perturbations. Tensor-like perturbations in the metric describe gravitational waves (see e.g. [43, 205]). Inflation predicts a background of primordial gravitational waves, which - if present - is below the detection limit of current experiments. We will therefore assume $B(\mathbf{l}) \approx 0$ [43] in the remainder of this thesis.

Many modern CMB experiments measure the incident radiation by means of transition-edge bolometers, which are sensitive to the total incoming power only. For polarization measurements, polarization filter are placed in front of the detectors. This effectively halves the intensity of the incoming radiation. For the same integration time, a pure temperature measurement will receive twice as many photons as a polarization measurement. Consequently, the noise of the two measurements is related by [204]

$$(\sigma^N_{\mathrm{Pol}})^2 = 2(\sigma^N_{\mathrm{T}})^2. \tag{1.29}$$

1.4 Weak gravitational Lensing by Large-Scale Structure

The deflection of light rays by metric perturbations is called gravitational lensing, for it distorts the observed images of objects similarly to a lens. The formalism to describe this effect is well established and has been covered in a number of review articles and books [195, 12, 142, 188, 233].

The propagation of light rays is described by null geodesics. To quantify the effect of metric perturbations on the photon's path one can either solve for the spatial part of the perturbed geodesic equation or consider the equation of geodesic deviation, that describes how a light bundle evolves along the perturbed light path [191, 65, 200, 116].

In the Newtonian gauge, i.e. in the limit of small scalar perturbations to the background metric [cp. Eq. (1.17)], the comoving separation $\mathbf{x}(\boldsymbol{\theta}, \chi)$ of a light ray from a fiducial ray is given by

$$\mathbf{x}(\boldsymbol{\theta}, \chi) = f_K(\chi)\boldsymbol{\theta} - \frac{2}{c^2} \int_0^\chi \mathrm{d}\chi' f_K(\chi - \chi') \left[\nabla_\perp \psi[\mathbf{x}(\boldsymbol{\theta}, \chi'), \chi'] - \nabla_\perp \psi^{(0)}(\chi') \right], \tag{1.30}$$

where $\psi^{(0)}(\chi')$ denotes the Newtonian potential encountered by the fiducial ray, and $f_K(\chi)\boldsymbol{\theta}$ the separation of the light rays in the absence of any metric perturbations. Note that we integrate from the observer to the source and that $\boldsymbol{\theta}$ is the observed angular separation at $\chi = 0$. In the absence of lensing, the light would have traveled directly towards the observer and the two emission points of the rays would have been observed under an unlensed relative angle $\boldsymbol{\beta}$. To clarify the meaning of these angles, a sketch can be useful (Fig. 1.2)[6]: Consider an object at distance χ that emits two light rays from two different positions separated by the comoving distance $\boldsymbol{\beta} f_K(\chi)$. One of these light rays is emitted in the direction of the observer, the other in a slightly different direction. This second ray gets deflected towards the observer because it encounters a lens, i.e. a potential ψ at distance χ_{lens}. The lens changes its propagation direction by an angle $\hat{\boldsymbol{\alpha}}$. After the deflection, both light rays arrive at the observer at relative angle $\boldsymbol{\theta}$. The (naive) observer assigns the comoving separation $f_K(\chi)\boldsymbol{\theta}$ to the source positions of the rays.

---

[6]Where for simplicity we set $\psi^{(0)}(\chi') = 0$ and consider only a single lens plane.
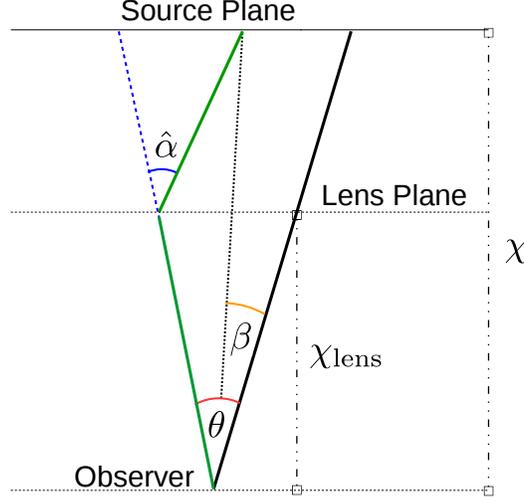
Figure 1.2: A sketch of the relevant angles in a lensing event: Two light rays (green and black solid lines) are emitted at the source plane at distance χ and arrive at the observer separated by an angle $\boldsymbol{\theta}$. At distance χ_{lens} the left ray has been deflected by the deflection angle $\hat{\boldsymbol{\alpha}}$. In the absence of lensing, the observer would receive the light from the two source position under the angle $\boldsymbol{\beta}$.

From the sketch in Fig. 1.2, we can easily deduce

$$f_K(\chi)\boldsymbol{\theta} - f_K(\chi)\boldsymbol{\beta} = f_K(\chi - \chi_{\text{lens}})\hat{\boldsymbol{\alpha}}$$

$$\Rightarrow \boldsymbol{\beta} = \boldsymbol{\theta} - \frac{f_K(\chi - \chi_{\text{lens}})}{f_K(\chi)}\hat{\boldsymbol{\alpha}}$$

$$\boldsymbol{\beta} \equiv \boldsymbol{\theta} + \boldsymbol{\alpha}, \tag{1.31}$$

where we have defined the reduced deflection angle $\boldsymbol{\alpha}$ in the last equation.[7] Comparing Eq. (1.31) with Eq. (1.30), we find

$$\boldsymbol{\alpha} = -\frac{2}{c^2} \int_0^\chi d\chi' \frac{f_K(\chi - \chi')}{f_K(\chi)} \left[\nabla_\perp \psi[\mathbf{x}(\boldsymbol{\theta}, \chi'), \chi'] - \nabla_\perp \psi^{(0)}(\chi') \right]. \tag{1.32}$$

The integral in Eq. (1.32) sums up all the deflections due to perturbations along the perturbed light-path and can, in the limit of small deflections, be solved iteratively. For most applications, however, the zeroth order result, in which the deflections are integrated along the unperturbed light path turns out to be an excellent approximation [211, 135, 66]. This so-called Born approximation is especially justified if one is only interested in the

---

[7]There exist different sign conventions for the reduced deflection angle in the literature. Since most of this thesis is dedicated to the study of CMB lensing, we use the convention that is prevalent in this field. In the other convention, which is more common in weak galaxy lensing, the last line in Eq. (1.31) would read $\boldsymbol{\beta} \equiv \boldsymbol{\theta} - \boldsymbol{\alpha}$.

statistics of the deflection field, since homogeneity and isotropy requires the statistics to be the same along any path.

With this approximation we derive at the final equation for the deflection angle

$$\boldsymbol{\alpha}(\boldsymbol{\theta}) = -\frac{2}{c^2} \int_0^\chi d\chi' \frac{f_K(\chi - \chi')}{f_K(\chi)f_K(\chi')} \nabla_{\boldsymbol{\theta}} \psi \left[f_K(\chi')\boldsymbol{\theta}, \chi' \right], \qquad (1.33)$$

where we have rewritten the spatial derivative in terms of the angular derivative on the sphere $\nabla_\perp = 1/f_K(\chi')\nabla_\theta$. Since all observations point towards a negligible curvature $K \approx 0$, we will specify all lens equations to a flat Universe in the remainder of this thesis. Defining the lensing efficiency

$$W\left(\chi', \chi\right) = \frac{\chi - \chi'}{\chi\chi'}, \qquad (1.34)$$

Eq. (1.33) simplifies to

$$\boldsymbol{\alpha}(\boldsymbol{\theta}) = -\frac{2}{c^2} \int_0^\chi d\chi' W(\chi', \chi) \nabla_{\boldsymbol{\theta}} \psi \left(f_K(\chi')\boldsymbol{\theta}, \chi' \right) \qquad (1.35)$$

and we can identify the lensing potential

$$\phi(\boldsymbol{\theta}) = -\frac{2}{c^2} \int_0^\chi d\chi' W(\chi', \chi) \psi \left(f_K(\chi')\boldsymbol{\theta}, \chi' \right). \qquad (1.36)$$

The lensing potential is therefore a weighted projection of all metric perturbations along the line of sight and the deflection angle can be written as the angular derivative of this 2-dimensional scalar field

$$\boldsymbol{\alpha}(\boldsymbol{\theta}) = \nabla_{\boldsymbol{\theta}} \phi(\boldsymbol{\theta}). \qquad (1.37)$$

Lensing conserves the surface brightness of an object, such that we can map the surface brightness distribution, I^s, at the source plane to the surface brightness distribution, I, at the observer

$$I(\boldsymbol{\theta}) = I^s \left[\boldsymbol{\beta}(\boldsymbol{\theta}) \right]. \qquad (1.38)$$

If the deflection changes only weakly over the extent of the source, this mapping can be linearized

$$I(\boldsymbol{\theta}) = I^s \left[\boldsymbol{\theta} + \mathcal{A}(\boldsymbol{\theta}_0)(\boldsymbol{\theta} - \boldsymbol{\theta}_0) \right], \qquad (1.39)$$

where the matrix $\mathcal{A}$ is given by

$$\mathcal{A}_{ij} = \frac{\partial \boldsymbol{\beta}_j}{\partial \boldsymbol{\theta}_i} = \delta_{ij} + \partial_i \boldsymbol{\alpha}_j = \delta_{ij} + \partial_i \partial_j \phi(\boldsymbol{\theta}), \qquad (1.40)$$

and we see that at first order the image distortions depends on the shear tensor of the lensing potential.

The trace of Eq. (1.40) is invariant under rotations, it describes isotropic stretching of the source image and defines the convergence κ

$$\text{tr}(\mathcal{A}) = 2 - (\partial_1^2 + \partial_2^2)\phi \equiv 2\left(1 - \kappa\right). \tag{1.41}$$

In the trace free part of $\mathcal{A}$, we can identify the shear components $\gamma_1 = \frac{1}{2}(\partial_1^2 - \partial_2^2)\phi$ and $\gamma_2 = \partial_1\partial_2\phi$

$$\mathcal{A}_{ij} - \frac{1}{2}\delta_{ij}\text{tr}(\mathcal{A}) = \begin{pmatrix} \gamma_1 & \gamma_2 \\ \gamma_2 & -\gamma_{1,} \end{pmatrix} \tag{1.42}$$

that can be combined to a complex field $\gamma = \gamma_1 + i\gamma_2 = |\gamma|e^{2\pi\varphi}$, which is mapped onto itself by a rotation about π (a spin-2 field).

We will consider two different applications of weak lensing in a cosmological context in this thesis: weak lensing of galaxies also known as cosmic shear and weak lensing of the cosmic microwave background. The lensing formalism that was derived in the previous section applies to both, but the characteristics of the sources and the lensing observables differ.

1.5   Weak gravitational Lensing of the CMB

Similarly to photons emitted by galaxies, photons of the cosmic microwave get deflected by large-scale structure [21, 40, 147, 35](see [142] for a review). In the presence of a deflection field $\boldsymbol{\alpha}(\boldsymbol{\theta})$, the temperature fluctuation observed in direction $\boldsymbol{\theta}$, has originally been emitted at position $\boldsymbol{\theta} + \boldsymbol{\alpha}(\theta)$

$$\tilde{T}(\boldsymbol{\theta}) = T\left[\boldsymbol{\theta} + \boldsymbol{\alpha}(\theta)\right], \tag{1.43}$$

where we use a tilde to indicate lensed quantities.

To good approximation $\boldsymbol{\alpha}(\boldsymbol{\theta}) = \nabla\phi(\theta)$ with the CMB lensing potential

$$\phi(\boldsymbol{\theta}) = -\frac{2}{c^2}\int_0^{\chi^*} \mathrm{d}\chi\, W(\chi, \chi^*)\psi(\boldsymbol{\theta}\chi, \chi), \tag{1.44}$$

where we have specialized Eq. (1.36) to $\chi = \chi*$, the comoving angular diameter distance to the last scattering surface.

The average lensing deflection is of the order of 2 arcmin, but its coherence scale, i.e. the typical correlation length of the deflection field, is of the order of degrees. This scale can be inferred from the CMB lensing power spectrum $C^{\phi\phi}$, which in Limber approximation [146, 152] can be written as a weighted integral over the matter power spectrum $P_\delta(k = l/\chi', z)$. The lensing power spectrum is depicted in Fig. 1.3. It peaks at scales $L \approx 50$, whereas the first peak in the CMB power spectrum is found at $l \approx 100$.

In Fig. 1.4 we illustrate the lensing effect by showing realizations of an unlensed CMB map, a lensing potential and the difference between the corresponding lensed and the unlensed CMB map. We do not show the lensed map since it would be hardly distinguishable from the unlensed one.
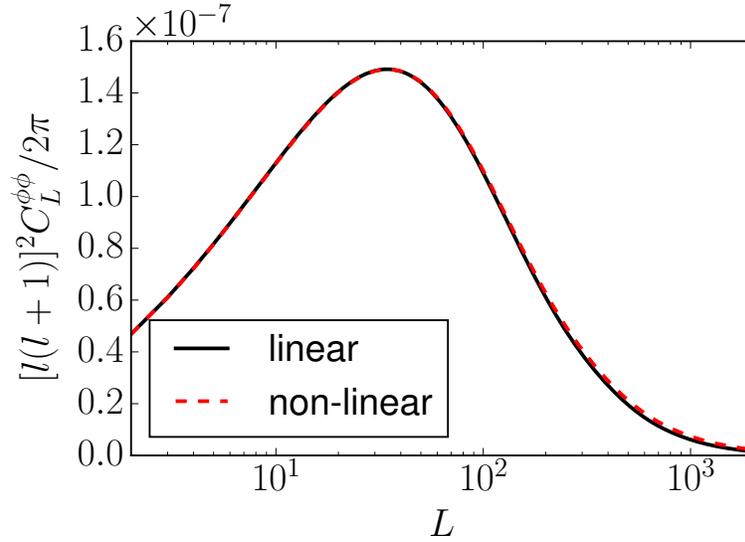
Figure 1.3: Power spectrum of the lensing deflection field in a standard ΛCDM Universe computed from a linear (black) and a non-linear matter power spectrum model (red). The curves were calculated with the publicly available CLASS code [23].

(a) Unlensed CMB Map   (b) Lensing Potential Map   (c) Lensed - Unlensed CMB Map
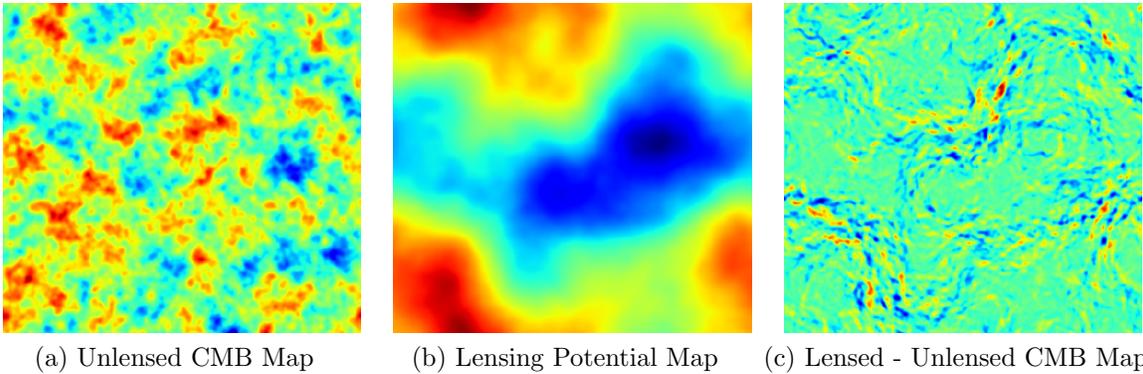
Figure 1.4: Realizations of an unlensed CMB map (left panel) and a lensing potential (middle panel) on a sky cut of size $(8.5 \times 8.5) \deg^2$. Lensing the CMB map with the deflection field obtained from the lensing potential yields a lensed CMB field which is not shown since it would be very difficult to distinguish unlensed and lensed realization by eye. It is more instructive to show the difference between the lensed and unlensed field (right panel). The maps were created with the quicklens package.[9]

For small deflections, Eq. (1.43) can be expanded in the deflection angle

$$\tilde{T}(\boldsymbol{\theta}) = T(\boldsymbol{\theta}) + \nabla^i T(\boldsymbol{\theta})\boldsymbol{\alpha}_i(\boldsymbol{\theta}) + \frac{1}{2}\nabla^i \nabla^j T(\boldsymbol{\theta})\boldsymbol{\alpha}_i(\boldsymbol{\theta})\boldsymbol{\alpha}_j(\boldsymbol{\theta}) + \mathcal{O}(\boldsymbol{\alpha}^3)$$

$$= T(\boldsymbol{\theta}) + \nabla^i T(\boldsymbol{\theta})\nabla_i\phi(\boldsymbol{\theta}) + \frac{1}{2}\nabla^i \nabla^j T(\boldsymbol{\theta})\nabla_i\phi(\boldsymbol{\theta})\nabla_j\phi(\boldsymbol{\theta}) + \mathcal{O}(\phi^3). \tag{1.45}$$

In a Fourier basis this becomes

$$\tilde{T}(\mathbf{l}) = T(\mathbf{l}) + \delta T(\mathbf{l}) + \delta^2 T(\mathbf{l}) + \mathcal{O}(\phi^3) \tag{1.46}$$

with, for example, the first order term

$$\delta T(\mathbf{l}) = -\int_{\mathbf{l}'} [\mathbf{l}' \cdot (\mathbf{l} - \mathbf{l}')]\, T(\mathbf{l}')\phi(\mathbf{l} - \mathbf{l}'). \tag{1.47}$$

Similarly to the temperature, lensing changes the CMB polarization pattern [240]. The deflected Stokes parameters are

$$\tilde{Q}(\mathbf{x}) = Q\left[\mathbf{x} + \boldsymbol{\alpha}(\mathbf{x})\right],\ \ \tilde{U}(\mathbf{x}) = U\left[\mathbf{x} + \boldsymbol{\alpha}(\mathbf{x})\right]. \tag{1.48}$$

Writing Eq. (1.48) in a series expansion in harmonic space and in terms of the gradient and curl components E and B, one finds that lensing transforms E-mode polarization into B-mode polarization [240].

The perturbed lensed temperature covariance is at first order

$$\langle \tilde{T}(\mathbf{l})\tilde{T}(\mathbf{l}')\rangle_{P(T)} = \delta_{\mathrm{D}}(\mathbf{l} - \mathbf{l}')\, C_l^{TT} - 2\left[\mathbf{l}' \cdot (\mathbf{l} - \mathbf{l}')\right]\phi(\mathbf{l} - \mathbf{l}')C_{l'}^{TT} + \mathcal{O}(\phi^2), \tag{1.49}$$

which is non-diagonal. For a fixed realization of the lensing potential, the lensing deflections correlate the temperature fluctuations at different scales. The fluctuations remain normally distributed but become statistically anisotropic.

Averaging over realizations of the CMB lensing potential under the assumptions that it follows an isotropic Gaussian distribution $\phi \leftarrow \mathcal{G}(\phi|C^{\phi\phi})$ and that unlensed temperature and lensing potential are statistically independent, yields a statistically isotropic CMB with power spectrum [203, 37]

$$C_l^{\tilde{T}\tilde{T}} = C_l^{TT} + C_l^{\delta T \delta T} + C_l^{T \delta^2 T} + \mathcal{O}(\phi^4), \tag{1.50}$$

where the two second order terms are given by

$$C^{\delta T \delta T} = \int_{\mathbf{l}'} [\mathbf{l}' \cdot (\mathbf{l} - \mathbf{l}')]^2\, C_{|\mathbf{l} - \mathbf{l}'|}^{\phi\phi} C_{l'}^{TT} \tag{1.51}$$

and

$$C_l^{T \delta^2 T} = -C_l^{TT} \int_{\mathbf{l}'} [\mathbf{l} \cdot \mathbf{l}']^2 C_{l'}^{\phi\phi}. \tag{1.52}$$

---

[9]`https://github.com/dhanson/quicklens`

These two terms almost cancel each other and what remains is only a change at the percent level for $l < 2000$ [203]: Lensing conserves the absolute power in the CMB, but slightly redistributed the power among different scales. A peak at a certain scale in the power spectrum implies the abundance of many hot and cold spots with a size corresponding to this scale. Lensing deflections can enhance or diminish the size of a spot. On average, this effect shuffles power from the peaks to the surrounding scales. On very small scales, where the CMB is well modeled as a smooth gradient, a lens can introduce extra power, e.g., by lensing photons from the colder end of the gradient to the hotter end and vice versa. This effect enhances the power in the tail of the power spectrum, which is almost featureless due to the imperfect coupling of photons to baryons. These two effects can be seen in the left panel of Fig. 1.5, where we overplot the unlensed temperature power spectrum by the lensed power spectrum for a standard cosmology. The polarization power spectra before and after lensing (assuming $B(\mathbf{l}) = 0$) are shown in the right panel.
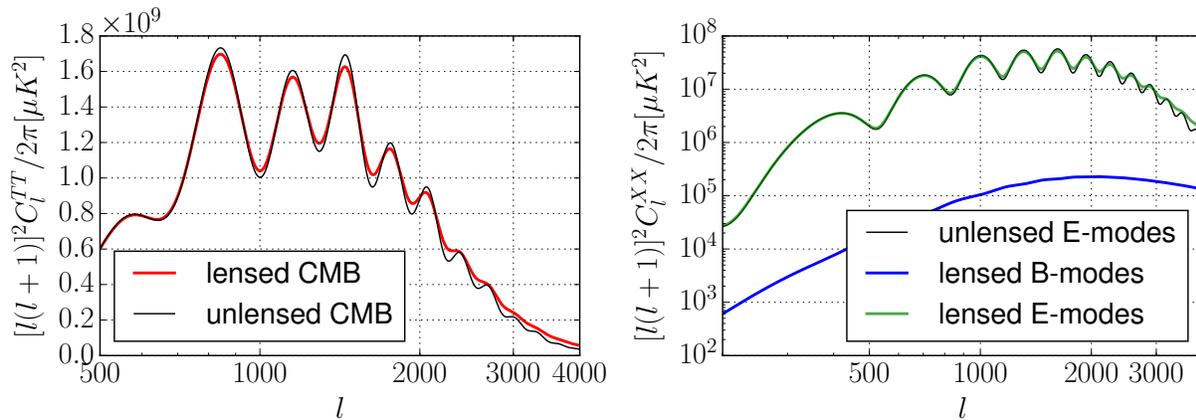
Figure 1.5: CMB power spectrum in a standard ΛCDM Universe before and after lensing by large-scale structure (computed with the publicly available CLASS code [23]). In the left plot, we plot the unlensed temperature power spectrum in black and the lensed spectrum in red. In the right panel, the unlensed E-mode power spectrum is plotted in black. Lensing partially transforms polarization E-modes into B-modes. The lensed E- and B-mode spectra are shown in green and blue.

Averaging over realizations of the lensing potential, also introduces higher order connected correlation functions in harmonic space [238, 95, 120]. Up to second order, the lensed temperature four-point function gets contributions from the following terms

$$\left\langle \tilde{T}\tilde{T}\tilde{T}\tilde{T} \right\rangle_{P(\phi),P(T)} = \langle TTTT \rangle + \langle \delta T \delta T T T \rangle + \langle \delta^2 T T T T \rangle + ... + O(\phi^4). \qquad (1.53)$$

By evaluation of these terms[10], one finds that the first and third term are completely disconnected, i.e. they can be written as products of two-point correlation functions,

---

[10]This involves applying Wick's theorem to the expectation values over the unlensed temperature.

while the second term contains connected terms that form a non-vanishing trispectrum. The effect of lensing on the average CMB fluctuations is therefore that it renders their distribution non-Gaussian by introducing higher-order cumulants.

1.5.1 CMB Lensing Reconstruction

One can get an estimate of the lensing potential from the temperature mode-coupling [207, 96, 97]. Specializing Eq. (1.49) to $\mathbf{l}' = \mathbf{l} - \mathbf{L}$, one finds

$$\langle \tilde{T}(\mathbf{l})\tilde{T}(\mathbf{l}-\mathbf{L})\rangle_{P(T)} = \delta_{\mathrm{D}}(\mathbf{L})\, C_l^{TT} - 2\left[(\mathbf{l}-\mathbf{L})\cdot\mathbf{L}\right]\, \phi(\mathbf{L})C_{|\mathbf{l}-\mathbf{L}|}^{TT} + \mathcal{O}(\phi^2)$$
$$\propto \phi(\mathbf{L}) \text{ for } \mathbf{L} > 0 \text{ and at order } \mathcal{O}(\phi). \tag{1.54}$$

Based on this observation, one can formulate a quadratic estimator for ϕ

$$\hat{\phi}(\mathbf{L}) = A_L \int_{\mathbf{l}} g(\mathbf{l},\mathbf{L})\tilde{T}_{\mathrm{expt}}(\mathbf{l})\tilde{T}_{\mathrm{expt}}^*(\mathbf{l}-\mathbf{L}), \tag{1.55}$$

where the weight $g(\mathbf{l},\mathbf{L}) \equiv g_{\mathbf{l},\mathbf{L}}$ is determined by requiring the variance of the estimator to be minimal

$$g(\mathbf{l},\mathbf{L}) = \frac{(\mathbf{L}-\mathbf{l})\cdot\mathbf{L}C_{|\mathbf{L}-\mathbf{l}|}^{TT} + \mathbf{l}\cdot\mathbf{L}C_l^{TT}}{2C_{l,\mathrm{expt}}^{\tilde{T}\tilde{T}}C_{|\mathbf{L}-\mathbf{l}|,\mathrm{expt}}^{\tilde{T}\tilde{T}}} \tag{1.56}$$

and the normalization A_L ensures that $\langle \hat{\phi}(\mathbf{L})\rangle_{P(T_{\mathrm{expt}})} = \phi(\mathbf{L})$,

$$A_L^{-1} = 2\int_{\mathbf{l}} g(\mathbf{l},\mathbf{L})\mathbf{l}\cdot\mathbf{L}C_l^{\tilde{T}\tilde{T}}, \tag{1.57}$$

where $\tilde{T}_{\mathrm{expt}}$ denotes the measured, noisy beam-deconvolved temperature fluctuations.

The two-point correlator of Eq. (1.55) can be used as an estimator of the lensing potential power spectrum

$$(2\pi)^2\delta_{\mathrm{D}}(\mathbf{L}+\mathbf{L}')\,C_L^{\hat{\phi}\hat{\phi}} = \langle\hat{\phi}(\mathbf{L})\hat{\phi}(\mathbf{L}')\rangle_{P(\phi,T)}$$
$$= A_L^2 \int_{\mathbf{l},\mathbf{l}'} g_{\mathbf{l},\mathbf{L}}\, g_{\mathbf{l}',\mathbf{L}'} \langle\tilde{T}_{\mathrm{expt}}(\mathbf{l})\tilde{T}_{\mathrm{expt}}(\mathbf{L}-\mathbf{l})\tilde{T}_{\mathrm{expt}}(\mathbf{l}')\tilde{T}_{\mathrm{expt}}(\mathbf{L}'-\mathbf{l}')\rangle_{P(\phi,T)}. \tag{1.58}$$

The estimator in Eq. (1.58) is sensitive to the lensed temperature four-point function. This is non-zero, even in the absence of lensing. From Eq. (1.53) we see that this estimator gets contributions from all even orders in ϕ. At second order, a total of six terms contribute to the lensed temperature four-point function[11], but not all of them, when inserted into the estimator Eq. (1.58) give rise to the desired power spectrum $C_L^{\phi\phi}$. As a consequence, the estimator is biased. Its expectation value is not equal to the lensing power spectrum. These

---

[11] Applying Wick's theorem to the expectation value over the unlensed temperature splits each term into a sum of three terms.

additional contributions, called reconstruction biases, can be evaluated in perturbation theory and subtracted. They are commonly denoted $N_L^{(n)}$, where n indicates their order in $C_L^{\phi\phi}$

$$\langle C_L^{\hat\phi\hat\phi} \rangle = N_L^{(0)} + C_L^{\phi\phi} + N_L^{(1)} + N_L^{(2)} + \mathcal{O}(\phi^6). \tag{1.59}$$

The $N_L^{(0)}$ bias is present even in the absence of lensing. It measures the amount of chance correlations in a Gaussian field that mimic the lensing effect. It is found to be equal to the normalization A_L. If we replace the unlensed power spectra in the weights $g_{\mathbf{l},\mathbf{L}}$ by the lensed one, A_L contains the contributions to the four-point function from all disconnected terms at arbitrary order[12] and the $N_L^{(0)}$ bias becomes an estimator for all disconnected bias terms. The $N_L^{(0)}$ bias dominates the signal over most scales. The $N_L^{(1)}$ bias is sourced by a contraction in the second term of Eq. (1.53) [121]. The $N_L^{(2)}$ bias can be nicely alleviated by replacing the unlensed power spectra by the lensed ones in Eq. (1.56) [143]. Fig. 1.6 depicts all lensing biases that have been taken into account in the CMB lensing analysis of the Planck experiment.
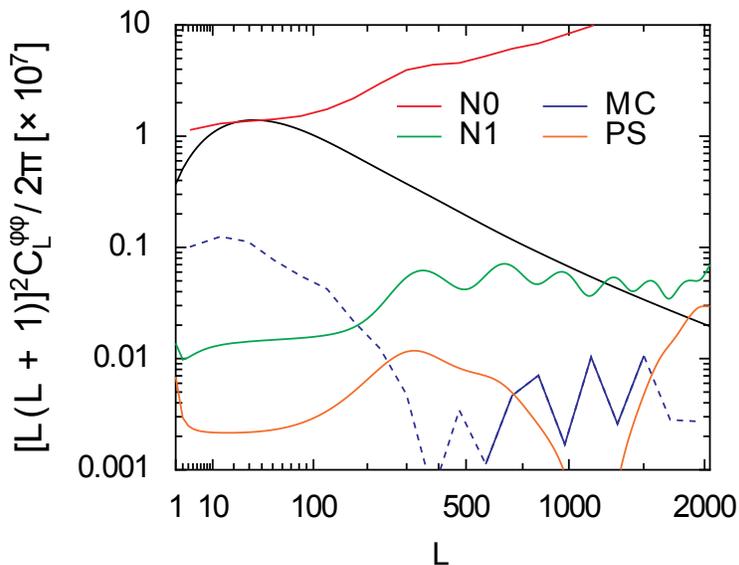
Figure 1.6: Noise Bias spectra for the combined temperature and polarization minimum variance estimator (figure taken from the Planck 2015 results (XV) gravitational lensing paper [183]). The fiducial ΛCDM power spectrum that has been used in the analysis is plotted in black.

In a real survey, masking and complicated noise and beam properties introduce mode-coupling, such that the expectation value of the quadratic estimator becomes non-zero $\langle \hat\phi_L \rangle_{P(T_{\mathrm{expt}})} \neq 0$ [75, 74]. In this case, one resorts to Monte Carlo simulations to estimate the spurious mean-field. Also an adapted bias-hardened estimator [171] that results in a smaller mean field has been proposed. For the power spectrum estimation Eq. (1.58), a

---

[12]depending on to what order the lensed temperature power spectrum is modeled

data dependent estimator for the disconnected noise bias $\hat{N}_L^{(0)}$ [189, 171] captures the effect of a statistically non-diagonal temperature covariance and reduces non-diagonal terms in the lensing power spectrum covariance [193]. Further biases are sourced by unresolved point sources $(N_L^{(PS)})$ and residual effects such as binning or errors in the calculation of $N_L^{(1)}$ $(N_L^{(MC)})$. $N_L^{(MC)}$ is determined from the comparison of reconstructed power spectra (corrected for all known biases) to the input power spectra in Monte Carlo simulations. In Fig. 1.7 we show a plot form the current Planck lensing paper depicting the current experimental status of lensing power spectrum measurements.
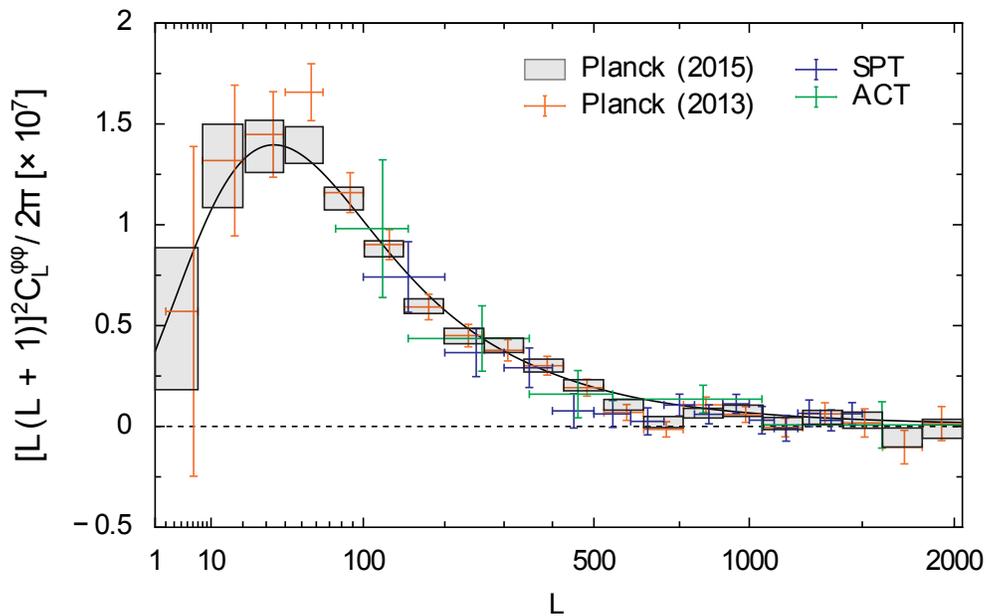
Figure 1.7: Reconstructed lensing potential power spectrum from the latest Planck data release (Figure taken from the Planck 2015 results (XV) gravitational lensing paper [183]). Grey boxes indicate the power spectrum as estimated from a combined minimum variance estimator for temperature and polarization data [183], the temperature-only estimation that was published in an earlier release [178] is shown in orange. Results from other ground-based experiments (South Pole Telescope (SPT) and Atacama Cosmology Telescope (ACT)) are plotted in green and blue [231, 45]. The fiducial ΛCDM power spectrum that has been used in the analysis is shown in black.

The estimator in Eq. (1.58) can be evaluated in complete analogy for all non-vanishing four-point correlators that combine E-, B- and temperature fluctuations, e.g. (EE,EE) or (TE,TE), with their own respective reconstruction biases [101, 173]. The resulting estimators can be added under the constraint of minimum variance to form a combined estimator.

1.5.2 Observational status and Relevance for this Thesis[13]

The CMB lensing signal was first detected by cross-correlating WMAP data with other tracers of large-scale structure [216, 89]. Measurements of the lensing power spectrum from CMB temperature data were then reported successively by the Atacama Cosmology Telescope (ACT) collaboration [46], the South Pole Telescope (SPT) collaboration [231], and the Planck Collaboration [178].

    The first polarization-based measurements of the CMB lensing power spectrum have recently been carried out with POLARBEAR [228], SPTPol [220], Planck [183] and ACT-Pol [213]. The ACTPol, SPT, and POLARBEAR collaborations have also reported detections from cross-correlating the reconstructed polarization lensing with a measurement of the cosmic infrared background [73, 3, 232]. With improving detectors and larger detector arrays, measurements of the CMB lensing effect have tremendously increased in precision; This rapid progress is expected to continue with future experiments (e.g. CMB-S4 or the Keck array [1, 221]). Exploiting this future data demands for an increasing accuracy of reconstruction techniques and theoretical modeling of the measurements. Improving the the theoretical modeling of CMB lensing analyses is the objective of Chapters 2 and 3.

1.6 Effect of weak Lensing by Large-Scale Structure on Galaxy Shapes

Lensing distorts the images of observed galaxies. Since the underlying galaxy shape is unknown, the effect can only be measured statistically: if a large enough number of galaxies get lensed by the same structure, their shapes will be correlated. This correlation can be measured and thus information about the lens properties inferred [22, 114](see e.g. [122, 188, 93] for recent reviews).

    The observed shape of galaxies is typically modeled as an ellipse, that is defined by its major and minor axis, a and b, and its orientation with respect to a chosen coordinate axis given by an angle φ. The source ellipticity can be expressed in terms of these quantities as

$$\epsilon_{\text{source}} = \left(\frac{a-b}{a+b}\right) e^{2\pi\varphi}. \tag{1.60}$$

Lensing changes the source ellipticity [131, 200, 115, 199]

$$\epsilon_{\text{obs}} = \frac{\epsilon_{\text{source}} + g}{1 + g^*\epsilon_{\text{source}}}, \tag{1.61}$$

where g is called the reduced shear and the asterisk denotes complex conjugation. g is defined by

$$g = \frac{\gamma}{1-\kappa}. \tag{1.62}$$

---

[13]adapted from [25]

For weak distortions $|\gamma| \ll 1$, $\kappa \ll 1$, the reduced shear is approximately the shear $g \approx \gamma$ [135] and Eq. (1.61) becomes

$$\epsilon_{\text{obs}} \approx \epsilon_{\text{source}} + g. \tag{1.63}$$

We will use this approximation in Chapter 4. If the intrinsic galaxy shapes are uncorrelated $\langle \epsilon_{\text{source}} \rangle = 0$, averaging over a large enough number of galaxies allows to measure the shear on the scale that corresponds to the area over which the average was performed. With an average intrinsic ellipticity of $\sigma_\epsilon \approx 0.3$ and shears of the order of a few percent, weak galaxy lensing surveys require large number counts to yield signal-to-noise ratios > 1.

The lensing potential and its moments for weak galaxy lensing are obtained by replacing the lensing kernel [Eq. (1.34)] by an effective kernel

$$W(\bar{\chi}, \chi') = \int_{\chi'}^{\text{inf}} d\chi'' \, n(\chi'') \frac{\chi'' - \chi'}{\chi'}, \tag{1.64}$$

where $n(\chi'') = n(z)\frac{dz}{d\chi''}$ is the redshift distribution function of the source galaxies. It can be obtained from photometric measurements of the galaxies' redshifts. Similarly to the CMB lensing power spectrum, the cosmic shear power spectra $(C_l^{\gamma\gamma} = C_l^{\kappa\kappa} = [l(l+1)]^2 C_l^{\phi\phi})$ can be modeled as a weighted integration over the matter power spectrum (only the weight changes due to the different integration kernel [Eq. (1.64)]) [114].

Galaxy lensing probes the integrated matter distribution over a wide range of scales and redshifts ($z \lesssim 2$). An accurate theoretical modeling of the galaxy lensing effect requires to take into account non-linear effects [106]. The importance of non-linear corrections to the lensing power spectrum can be estimated by replacing the linear matter power spectrum by the non-linear one in its calculation. This comparison is shown in Fig. 1.8. It implies that non-linear effects start to become important at relatively large scales (e.g. $l \gtrsim 50$). In addition, non-linear structure formation renders the statistics of the deflection field significantly non-Gaussian. Measuring the convergence bispectrum in addition to the power spectrum, for example, can help breaking parameters degeneracies [223].

Redshift- and thus time-resolution in weak galaxies measurements can be obtained by dividing the galaxy sample into redshift bins and computing the auto- and cross-spectra within and between these bins [208, 94] (Fig. 1.8 shows power and cross spectra for two different bins). Alternatively, one can measure the complete 3D power spectrum [79, 34, 128]. These methods can yield additional constraints on certain parameters but reach lower signal-to-noise levels due to the lower galaxy counts per spectrum and mode. They also rely on sufficiently accurate redshift measurements [155].

1.6.1 Observational Status and Relevance for this Thesis[14]

First firm statistical detections of cosmic shear were reported in 2000 by four different groups [11, 234, 118, 236]. Since then, the field has seen a tremendous increase in the

---

[14]adapted from the introduction in [24]
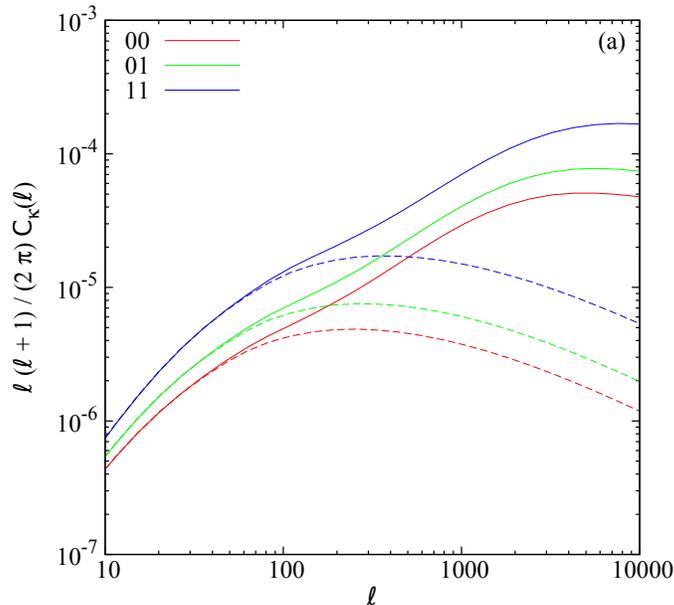
Figure 1.8:   The convergence auto- and cross-spectra for two redshift bins (z=[0.5,0.7], z=[0.9,1.1]) in a ΛCDM cosmology. Dashed lines were computed with a linear matter power spectrum, solid lines with a non-linear power spectrum model [224]. At most scales non-linear corrections must be taken into account for a correct interpretation of a measured lensing signal. The figure was taken from the cosmic shear review of Martin Kilbinger [122]

amount and quality of lensing data [198, 83, 47, 229, 107] as well as a notable improvement in analysis techniques [167, 129, 166, 243, 59, 194, 139, 15, 82, 124]. Cosmological parameters have been inferred from these data sets by comparing the power spectrum of the fully projected 2D shear field (or related quantities) to theoretical predictions [161, 110, 16, 123] as well as by assessing the shear auto- and cross-correlations in a number of redshift bins [196, 15, 87, 109, 81, 2]. Several authors have also investigated the additional constraining power that can be achieved by incorporating third-order statistics and/or shear peak counts and correlations [18, 223, 209, 48, 157, 158, 159, 85, 150, 112], which helps to break parameter degeneracies.

The full information content, however, lies in the three-dimensional non-linear shear field. 3D weak shear analysis methods have been proposed by a number of authors [79, 34, 128] and were recently applied to data from the Canada France Hawaii Telescope Lensing Survey (CFHTLenS) [127]. Furthermore, the measured shear field can be used for 3D reconstructions of the underlying density field. This can then be directly compared to models of structure formation and simplifies the cross correlation with other tracers of matter. Algorithms that invert the lens equation to obtain the density have been worked out by a number of authors [117, 100, 226]. Since this inversion is under-constrained, it requires some regularization method or choice of prior on the density field. Most of

the algorithms employ a Wiener filter (c.p. Section 1.2.1), which corresponds to a normal (Gaussian) prior, that can be complemented with information about galaxy clustering [214, 222].

In Chapter 4 we extend the work on tomographic reconstruction of the 3D matter distribution from weak galaxy lensing measurements and present a fully Bayesian reconstruction algorithm that uses a lognormal prior on the density field.

1.7 Why study weak Lensing by Large-Scale Structure

The study of weak lensing by large-scale structure is one of the most promising tools for obtaining a better understanding of the late-time Universe. Here, we briefly summarize the manifold potentials of weak lensing measurement in terms of constraining cosmological parameters in the ΛCDM model as well as possible extensions to it.

Measurements of weak lensing contain valuable information about the nature of dark energy, since lensing probes the amount of clustering at relatively low redshifts when dark energy starts to dominate. The primary effect of dark energy is to supress structure formation and thus the lensing signal. For example, CMB lensing can tighten constraints on the dark energy equation of state parameter w [215], but has limited potential for distinguishing between different dark energy models [30, 29]. This is because the CMB lensing kernel peaks at relatively high redshifts $z \approx 2$ and measures the integrated effect of a dark energy component. This is not the case for cosmic shear. Tomographic shear measurements allow to measure the clustering of matter at different redshifts and they can yield competative bounds on a possible time-variation of dark energy [98, 218, 104].

As a probe of structure formation, the lensing power spectrum is very sensitive to to a combination of the matter density Ω_{m0} and its clustering amplitude σ_8 [106, 18, 215].

Since measurements of galaxy lensing probe a wide range of scales, well down into the non-linear regime, they can also be used to constrain models of non-linear structure formation. Comparing the density distributions of the total matter inferred from lensing to the distribution of visible (i.e. with light interacting) matter provides exciting insights into the interplay of baryonic and dark matter components [76, 58]. It might thus shed light on the missing baryon problem (the fact that the directly observed density of baryonic matter is below the mean density inferred from indirect measures)(see e.g. [154]).

Lensing is also sensitive to a wide class of modified gravity models. Many of them can be parametrized such that the potentials Φ and Ψ in Eq. (1.17) differ. Light deflection is then governed by a combination of both potentials, while geodesics of non-relativistic matter are only sensitive to Ψ. This difference can be used to search for deviations from general relativity by testing the consistency of lensing measurements with other probes of clustering such as, e.g. redshift space distortions [242, 105, 6].

Mostly through the lensing efficiency W [Eq. (1.34)], the lensing signal is also sensitive to the spatial geometry [215]. In fact, adding gravitational lensing to the CMB likelihood significantly tightens the constraints on curvature from $\Omega_K = 0.052^{+0.03}_{-0.02}$ to $\Omega_K = -0.005^{+0.009}_{-0.007}$ [183].

Another yet poorly constrained constituent of the total energy budget are neutrinos. There exists experimental evidence of oscillations between neutrinos flavors, which implies that neutrinos are massive (see e.g. [156]). However, measurements of the oscillations only provide constraints on the difference between squared masses but not on an absolute scale. This can be inferred from cosmological observations: In the early Universe massive neutrinos start out as relativistic particles. As such, they contribute to the total radiation density. As the Universe expands, they get redshifted, become non-relativistic and start to behave like ordinary matter. The point of this transition depends on their mass. Relativistic particles have a different influence on structure formation than non-relativistic ones. Different neutrino masses thus lead to different structure formation histories which can be probed via weak lensing signals. Indeed, weak lensing turns out to be a very powerful probe for neutrino mass estimation [140, 67, 68]. To date, the tightest bound on the sum of neutrino masses has been reported by the Planck collaboration [183].

Chapter 2

A Maximum a Posteriori estimator for CMB Lensing

In this chapter we present a fully Bayesian approach to CMB lensing reconstruction, a maximum a posteriori (MAP) estimator for the lensing potential.

2.1 Introduction

The quadratic estimator (c.p. Section 1.5.1 and references therein) for lensing reconstruction from cosmic microwave background data is a well established tool that is also relatively easy to implement and has been used for many CMB lensing measurements. However, also the limitations of this estimator are well known: In the presence of masks and complicated beam and noise properties, it yields a spurious mean field, which has to be estimated from Monte Carlo simulations. The corresponding four-point estimator for the lensing power spectrum must further be corrected for a number of bias terms and the evaluation of these terms can be costly and inexact.

A maximum a posteriori estimator provides an elegant framework to consistently include masks, as well as noise and beam properties. This increases the computational cost of a MAP estimator compared to the standard quadratic estimator itself, but already includes some of the costly corrections to the latter. Since it is a fully probabilistic estimator, it also allows to consistently take into account uncertainties in the data model. A MAP estimator is also well suited for combining different data sets of tracers of large-scale structure. Finally, an alternative approach to the quadratic estimator is desirable, since it provides an important cross-check.

An optimally reconstructed map of the lensing potential is interesting, in particular, for delensing the measured CMB maps. From the unlensed maps one can infer tighter constraints on primordial physics, especially on the amplitude of primordial gravitational waves [62]. The gravitational wave signal is believed to have left imprints on the CMB polarization by the production of B-modes [205]. These primordial B-modes get partly obscured by the lensing induced B-modes [99]. The delensed CMB maps are obtained as

a biproduct of the MAP estimator for the lensing potential. Maps of the lensing potential can also be useful for cross-correlation measurements with other tracers of the dark or baryonic matter distribution [88, 149, 20, 125].

The maximum a posteriori estimator was first suggested by Hirata & Seljak in 2003 [91], but a numerical implementation for the application to real data sets with anisotropic noise, an anisotropic beam function and sky cuts, had not been published when the work on this thesis started. While taking first steps towards an implementation on the full sky, we were informed about direct competition by two groups and a first implementation of a temperature-based reconstruction in the flat sky approximation appeared soon after [8]. Only recently, the second group has published results of their implementation on the flat sky [33]. Due to this direct competition, it was decided to subordinate the work on this lensing reconstruction technique in favor of the other research projects that are part of this thesis.

We present here a rigorous derivation of the MAP estimator in the language of Information Field Theory (IFT) along with a description of its numerical implementation and the associated challenges. The abstract notation of IFT that we use is independent of the coordinate basis in which the problem is implemented. Depending on the experiment, CMB data can either require an implementation in flat or spherical coordinates. Since the method was initially aimed for the application to Planck data, we will primarily comment on the more complicated implementation on the sphere.

We start by introducing the operator notation used in this chapter in Section 2.2, before we turn to the derivation of the MAP estimator in two equivalent formulations in Section 2.3. In Section 2.4, we outline the necessary steps for an implementation on the sphere, starting with the lensing response operator in Section 2.4.1, followed by comments on the numerical caveats with spherical harmonic transforms in Section 2.4.2 and a description of the minimization algorithm that is needed to evaluate the estimator in Section 2.4.3. We conclude in Section 2.5.

2.2   Lensing of the CMB in Operator Notation

As outlined in Section 1.5, lensing corresponds to a remapping of the CMB temperature field. A measurement of the lensed CMB yields a data vector d that is a discrete set of temperature values d_i. Each of these data points contains the lensed, beam-convolved and pixelized temperature plus a statistically independent noise contribution n_i

$$d_i = \tilde{T}_i^{\text{conv}} + n_i. \tag{2.1}$$

Following the notation introduced in Section 1.2, we express the lensing operation in terms of a linear response operator, which we denote L^ϕ. It encapsulates the response of the continuous lensed temperature field $\tilde{T}$ to an unlensed field T for a fixed realization of the lensing potential ϕ, $\tilde{T} = L^\phi T$. Similarly, one can write the beam convolution as an operator B, that becomes diagonal in a harmonic basis if the beam is isotropic, and the pixel window function as an operator P, which in components reads $P_{ix} : d(\mathbf{x}) \to d_i$.

Realistic survey data will further have masked areas. The mask can be expressed as an operator M in configuration space, defined by

$$M_i = \begin{cases} 0, & \text{if } i \text{ in masked region} \\ 1, & \text{otherwise.} \end{cases} \tag{2.2}$$

With these definitions, the full data model for CMB lensing reads

$$d = MPBL^\phi T + n. \tag{2.3}$$

For a continuous temperature field, the lensing operation can be written as an integration

$$\tilde{T}(\mathbf{x}') = \int_\Omega d\mathbf{y}\, L^\phi\left(\mathbf{x}', \mathbf{y}\right) T\left(\mathbf{y}\right), \tag{2.4}$$

with

$$L^\phi(\mathbf{x}', \mathbf{y}) = \delta_D\left[\mathbf{x}' + \nabla\phi(\mathbf{x}') - \mathbf{y}\right]. \tag{2.5}$$

and the adjoint response is defined by

$$\begin{aligned} \left[L^\phi\right]^\dagger (\mathbf{y}, \mathbf{x}') f(\mathbf{x}') &= \int d\mathbf{x}'\, \delta_D\left[\mathbf{y} - \mathbf{x}' - \nabla\phi(\mathbf{x}')\right] f(\mathbf{x}') \\ &= \int d\mathbf{x}'\, \delta_D\left[\mathbf{y} - \mathbf{y}'(\mathbf{x}')\right] f(\mathbf{x}') \\ &= \int d\mathbf{y}'\, \left|\frac{\partial \mathbf{y}'(\mathbf{x}')}{\partial \mathbf{x}'}\right| \delta_D\left(\mathbf{y} - \mathbf{y}'\right) f\left[\mathbf{y}'^{-1}(\mathbf{x}')\right] \end{aligned} \tag{2.6}$$

where we have defined the unlensed coordinate $\mathbf{y}' = \mathbf{x}' + \nabla\phi(\mathbf{x}')$ and its inverse

$$\mathbf{y}'^{-1}\left[\mathbf{y}'(\mathbf{x}')\right] = \mathbf{x}'. \tag{2.7}$$

Integration over $\mathbf{y}'$ instead of $\mathbf{x}'$ introduces the Jacobi determinant

$$\left|\frac{\partial \mathbf{y}'(\mathbf{x}')}{\partial \mathbf{x}'}\right| = \left|\mathbb{1} + \frac{\partial \nabla\phi(\mathbf{x}')}{\partial \mathbf{x}'}\right| = \left|\delta_{ij} + \nabla_i\nabla_j\phi(\mathbf{x}')\right| = \left|\mathcal{A}(\mathbf{x}')\right|, \tag{2.8}$$

where we have identified the lensing distortion matrix $\mathcal{A}$ [c.p. Eq. (1.40)].

In the following, we will use R without the label ϕ to denote the complete lensing response, i.e. the lensing operation followed by the beam convolutions and the window function.[1]

$$R \equiv PBL^\phi \tag{2.9}$$

---

[1]We ignore the mask for notational simplicity, noting that including it does not change the general structure of the terms.

2.3 CMB Lensing Posterior

Different to the Wiener filter problem [c.p. Section 1.2.1], we are not only interested in inferring the underlying unlensed temperature field T, but primarily the lensing potential ϕ, which enters the lensing response. The CMB lensing posterior is therefore the joint probability of unlensed temperature and lensing potential given a CMB observation d. By application of Bayes theorem [Eq. (1.1)], this posterior can be expressed by the lensing likelihood times prior distributions of temperature and lensing potential.[2]

$$P(\phi, T|d) \propto P(d, \phi, T) = P(d|\phi, T)P(\phi, T) = P(d|\phi, T)P(\phi)P(T). \qquad (2.10)$$

The posterior distribution of the lensing potential alone is then found by marginalizing Eq. (2.10) over all realizations of the unlensed CMB

$$P(\phi|d) \propto \int \mathcal{D}T \, P(d|\phi, T)P(T)P(\phi). \qquad (2.11)$$

Evaluating this integral and maximizing the resulting posterior distribution requires the choice of suitable priors for the lensing potential and the unlensed temperature.

2.3.1 Prior Distributions and Noise Model

For both fields, unlensed temperature and lensing potential, Gaussian priors are well justified:

1. The lensing potential encapsulates the integrated effect of many metric perturbations along the line of sight. These metric perturbations seem to be well modeled by an initially Gaussian field, that also stays Gaussian over many scales and for most times. On small scales ($k \gtrsim 0.16$ Mpc^{-1} at $z = 0$), the metric perturbations acquire a non-Gaussian structure due to gravitational interactions. These Non-Gaussianities should be effectively Gaussianized by the integration. Deviations from a normally distributed lensing potential are expected to become detectable in future CMB experiments (see Chapter 3 and [169]). For future high-precision data and for estimates of the lensing potential power spectrum, it might therefore become necessary to model the effect of non-linear structure formation on $P(\phi)$. It is, however, unlikely that the

---

[2]To obtain the last expression in Eq. (2.10), we have assumed that lensing potential and temperature fluctuations are statistically sufficiently independent from each other, $P(\phi, T) = P(\phi)P(T)$. This assumption is justified over a wide range of scales. Correlations are introduced on the largest scales ($l < 100$) by the integrated Sachs-Wolf effect (iSW) [206] and on very small scales ($l > 2000$) due to the thermal SZ effect of galaxy cluster [41, 132]. In a Planck-like experiment most of the observed lensing effect comes from structures larger than typical cluster sizes. In lensing experiments that obtain significant lensing information from scales below $l \approx 2000$, the SZ contribution to the CMB map can be isolated by a suitable multi-frequency measurement. The iSW-induced correlations on the largest scales drop off very quickly and are strongly affected by cosmic variance, which allows to safely ignore them. In the future, both effects could be made part of a general response that incorporates all modifications to the CMB field that are caused by the structures along the line of sight.

maximum of the posterior, which we aim to reconstruct, will be significantly affected by these corrections. We also note that if the data is constraining enough, it will inform the resulting posterior $P(\phi|d)$ about non-Gaussianities.

2. Non-Gaussianities in the temperature fields can arrive from primordial and late-time physics. At late times these are sourced by second order effects such as the SZ- or iSW-effect. They also arises due to non-linearities in the Boltzmann equations that govern the evolution of the more or less tightly coupled fluids in the Universe [13]. Being second order, these effect are expected to be small on the scales of interest. In addition, they can be modeled and corrected for. Primordial non-Gaussianities could be imprinted by inflation (the exact shape depends on the inflationary model) but have so far not been detected [181, 179].

Given these arguments, we will model the lensing potential as an isotropic and homogeneous Gaussian field, with covariance $C^{\phi\phi}_{\mathbf{LL'}} \equiv \langle \phi(\mathbf{L})\phi^*(\mathbf{L'}) \rangle = (2\pi)^2 \delta_{\mathrm{D}}(\mathbf{L} - \mathbf{L'}) C^{\phi\phi}_L$ in harmonic space, where $C^{\phi\phi}_L$ denotes the CMB lensing power spectrum introduced in Section 1.5. Note that we use the same symbols for the full covariance and the power spectrum to keep the notation simple. The Gaussian prior for the lensing potential ϕ reads accordingly

$$P(\phi) = \mathcal{G}(\phi|C^{\phi\phi}) = \frac{1}{\sqrt{|2\pi C_{\phi\phi}|}} \exp\left[-\frac{1}{2}\phi^\dagger \left(C^{\phi\phi}\right)^{-1}\phi\right]. \tag{2.12}$$

Similarly, we take a Gaussian prior for the unlensed temperature, with covariance $C^{TT}_{\mathbf{ll'}} \equiv \langle T(\mathbf{l})T^*(\mathbf{l'}) \rangle = (2\pi)^2 \delta_{\mathrm{D}}(\mathbf{l} - \mathbf{l'}) C^{TT}_l$.

$$P(T) = \mathcal{G}(T|C^{TT}) = \frac{1}{\sqrt{|2\pi C^{TT}|}} \exp\left[-\frac{1}{2}T^\dagger \left(C^{TT}\right)^{-1}T\right]. \tag{2.13}$$

Finally, we also assume the noise to be Gaussian (which is a fair approximation after non-Gaussian foregrounds have been subtracted or masked)

$$P(n) = \mathcal{G}(n|N) = \frac{1}{\sqrt{|2\pi N|}} \exp\left[-\frac{1}{2}n^\dagger N^{-1}n\right], \tag{2.14}$$

where the noise covariance N is typically anisotropic and diagonal in data space.

2.3.2 Signal Space Posterior

When both fields of interest are kept fixed, the likelihood is entirely determined by the statistics of the noise

$$P(d|\phi, T) = P(n = d - RT|\phi, T) = \mathcal{G}(d - RT|N). \tag{2.15}$$

Inserting this and our priors on the temperature and deflection potential [Eqs. (2.13) and (2.12)] into the expression for the posterior, Eq. (2.11), we arrive at

$$P(\phi|d) \propto \int \mathcal{D}T \, \mathcal{G}(T|C^{TT}) \, \mathcal{G}(\phi|C^{\phi\phi}) \, \mathcal{G}(d - RT|N). \tag{2.16}$$

By quadratic completion, the expression in the integral can be reformulated to [3]

$$P(d, \phi) = \int \mathcal{D}T \ P(d|\phi, T)P(T|\phi)P(\phi) \tag{2.17}$$

$$\propto \exp\left\{-\frac{1}{2}\left[(T - Dj)^\dagger D^{-1}(T - Dj) - j^\dagger Dj + \phi^\dagger \left(C^{\phi\phi}\right)^{-1}\phi\right]\right\}, \tag{2.18}$$

where we have defined the information propagator $D = \left[\left(C^{TT}\right)^{-1} + R^\dagger N^{-1}R\right]^{-1}$ and the information source $j = R^\dagger N^{-1}d$ in analogy to Section 1.2.1. In this way, we see that the maximum of the probability $P(d, T|\phi) \propto P(T|d, \phi)$, i.e. the most probable realization of the unlensed temperature given ϕ, is the Wiener filter solution for the unlensed temperature

$$\max\left[P(d, T|\phi)\right] = \max\left[P(T|d, \phi)\right] = m = Dj. \tag{2.19}$$

The marginalization over T in Eq. (2.17) can be easily performed after a change of variable $(T - Dj) \to T$ and results in

$$P(d, \phi) \propto \sqrt{|D|} \exp\left\{-\frac{1}{2}\left[\phi^\dagger \left(C^{\phi\phi}\right)^{-1}\phi - j^\dagger Dj\right]\right\}. \tag{2.20}$$

From this we can read the expression for the negative log posterior

$$-\ln P(d|\phi) \widehat{=} -\frac{1}{2}\mathrm{Tr}(\ln D) - \frac{1}{2}j^\dagger Dj + \frac{1}{2}\phi^\dagger \left[C^{\phi\phi}\right]^{-1}\phi. \tag{2.21}$$

To find the most likely realization of the lensing potential, we solve for the fixed point of Eq. (2.21) by variation with respect to ϕ

$$-\frac{\delta}{\delta\phi}\ln P(d|\phi) = \frac{1}{2}\left(C^{\phi\phi}\right)^{-1}\phi - \frac{1}{2}j^\dagger D_{,\phi}\,j - 2j^\dagger Dj_{,\phi} - \frac{1}{2}\mathrm{Tr}(D_{,\phi}\,D^{-1}) \overset{!}{=} 0. \tag{2.22}$$

This expression involves functional derivatives of the information propagator and of the information source with respect to ϕ, indicated by a comma. Both of these derivatives can be expressed in terms of the functional derivative of the response operator. To see this, we first write

$$D_{,\phi} = -DD^{-1}_{,\phi}\,D \tag{2.23}$$

to shift the derivative on the inverse propagator, for which we have an analytic expression, and find

$$D^{-1}_{,\phi} = (R^\dagger N^{-1}R)_{,\phi} = R^\dagger_{,\phi}\,N^{-1}R + R^\dagger N^{-1}R_{,\phi}\,. \tag{2.24}$$

Likewise the derivative of the information source is

$$j_{,\phi} = (R^\dagger N^{-1}d)_{,\phi} = R^\dagger_{,\phi}\,N^{-1}d. \tag{2.25}$$

---

[3]In the following, we will only keep ϕ dependent terms. Terms independent of the lensing potential only change the normalization of the joint probability $P(d, \phi)$.

To evaluate Eq. (2.24) and Eq. (2.25) we require an analytic expression for the functional derivative of the response operator. The detailed derivation can be found in Appendix A, here we just quote the result

$$\frac{\delta}{\delta\phi(\mathbf{a})} [Rs]_j = P_{j\mathbf{y}'} B_{\mathbf{y}'\mathbf{x}'} \left[\nabla_{\mathbf{x}'} \delta_D(\mathbf{x}' - \mathbf{a}) \cdot \left[L^\phi \nabla s \right](\mathbf{x}') \right], \tag{2.26}$$

where s is a field in signal space and $\mathbf{x}'$ the coordinate of the lensed field $\tilde{s}(\mathbf{x}') = s[\mathbf{x}' + \nabla\phi(\mathbf{x}')]$. The dot indicates a point-wise product between two fields meaning that there is no contraction over $\mathbf{x}'$ in the expression in square brackets.

With this derivative at hand, we can expand the terms in Eq. (2.22) that belong to the likelihood

$$\begin{aligned}
-\frac{\delta}{\delta\phi} \ln P(\phi|d) = &- \nabla \left[B^\dagger P^\dagger \left(N^{-1} \right)^\dagger RDj \cdot L^\phi \nabla (Dj) \right] \\
&+ 2\nabla \left[L^{\phi\dagger} \nabla (Dj) \cdot B^\dagger P^\dagger \left(N^{-1} \right)^\dagger d \right] \\
&- \left\langle \nabla \left[B^\dagger P^\dagger \left(N^{-1} \right)^\dagger RDr \cdot L^\phi \nabla (Dr) \right] \right\rangle_{\mathcal{G}(r|D)} \\
= &\nabla \left[B^\dagger P^\dagger \left(N^{-1} \right)^\dagger RDj \cdot L^\phi \nabla (Dj) \right] \\
&- \left\langle \nabla \left[B^\dagger P^\dagger \left(N^{-1} \right)^\dagger RDr \cdot L^\phi \nabla (Dr) \right] \right\rangle_{\mathcal{G}(r|D)}. \tag{2.27}
\end{aligned}$$

The form of the last term, the derivative of the trace, requires some explication. To obtain it, we first rewrite

$$\begin{aligned}
\text{Tr}(D^{-1}D_{,\phi}) &= -\text{Tr}(D^{-1}DD_{,\phi}^{-1}D) \\
&= -\text{Tr}(D_{,\phi}^{-1}D), \tag{2.28}
\end{aligned}$$

and then use the identity

$$\text{Tr}(A) = \langle x \, A \, X^{-1} \, x \rangle_{\mathcal{G}(x|X)}, \tag{2.29}$$

for a Gaussian variable x with covariance X. In this specific case, we choose the Gaussian variable $r = (T - Dj)$ which has the Wiener filter covariance D and get

$$\text{Tr}(D_{,\phi}^{-1}D) = \langle r^\dagger D_{,\phi}^{-1}DD^{-1}r \rangle_{\mathcal{G}(r|D)} = \langle r^\dagger D_{,\phi}^{-1}r \rangle_{\mathcal{G}(r|D)}. \tag{2.30}$$

This form is convenient, since it can be evaluated numerically by sampling from $\mathcal{G}(r|D)$.

2.3.3 Data Space Posterior

Similarly to the Wiener filter, the posterior can be formulated in data space (c.p. Section 1.2.1). To arrive at the expressions corresponding to Eqs. (2.17) and (2.22) one starts out by writing the Gaussian likelihood $\mathcal{G}(d|C^{dd})$ in data space, with data covariance

$$C^{dd} = RC^{TT}R^\dagger + N. \tag{2.31}$$

Using the same Gaussian prior for the lensing potential as before, this results in a joint negative log posterior of the form

$$-\ln P(\phi, d) = \frac{1}{2} d^\dagger \left(C^{dd}\right)^{-1} d + \frac{1}{2} \ln |C^{dd}| + \frac{1}{2} \ln |C^{\phi\phi}| + \frac{1}{2} \phi^\dagger \left(C^{\phi\phi}\right)^{-1} \phi. \tag{2.32}$$

The functional derivative of (2.32) with respect to ϕ can be evaluated in an analogous manner to the signal space expression

$$\begin{aligned}
-\frac{\delta \ln P(d, \phi)}{\delta \phi} =& \nabla \left[L^\phi \nabla C^{TT} R^\dagger (C^{dd})^{-1} d \cdot B^\dagger P^\dagger (C^{dd})^{-1} d\right] - \frac{1}{2} \left(C^{\phi\phi}\right)^{-1} \phi \\
& - \left\langle \nabla \left[L^\phi \nabla C^{TT} R^\dagger \left(C^{dd}\right)^{-1} d \cdot B^\dagger P^\dagger \left(C^{dd}\right)^{-1} d\right]\right\rangle_{\mathcal{G}(d'|C^{dd})}
\end{aligned} \tag{2.33}$$

where we have applied the identity in Eq. (2.29) with $x = d'$ and $X = C^{dd}$ to express the derivative of the trace as an expectation value. The last term corresponds to the mean field contribution known from the quadratic estimator (c.p. Section 1.5.1).

Note that both formulations of the posterior contain a Wiener filter estimate of the unlensed CMB [c.p. Eq. (1.8) and Eq. (1.9)], which must be evaluated for the current estimate of the lensing potential. By this, one obtains the unlensed CMB maps as a byproduct of the minimization with respect to the lensing potential.[4]

2.3.4 Generalization to Polarization

So far, we have only referred to lensing of temperature fluctuations in this chapter, but additional lensing information is also available through polarization measurements and a generalization of the MAP estimator to include polarization data is possible [92]. This expands the data vector to $d \rightarrow d_T, d_U, d_Q$, where d_T is the temperature fluctuation data and d_Q and d_U are the vectors containing the measured Stokes parameters of the incoming photons (c.p. Section 1.3.3). In harmonic space, the polarization can be conveniently decomposed into a gradient component E that is invariant under a parity transformation and a curl component B that changes sign under reflection about one coordinate axis. Because of their different transformation properties, E and B polarization fields are uncorrelated by construction (if there are no significant parity violating interactions) and so are the temperature and the B field. This simplifies the covariance matrix of their joint Gaussian prior distribution to

$$\mathbf{C}_l = \begin{bmatrix} C^{TT} & C^{TE} & 0 \\ C^{ET} & C^{EE} & 0 \\ 0 & 0 & C^{BB} \end{bmatrix}, \tag{2.34}$$

---

[4]Note that this Wiener Filter estimate of the unlensed CMB should be used with caution, since it is not informed about the uncertainty of the current estimate of the lensing potential.

which is block diagonal with C^{XY} denoting the diagonal covariance of the fields X and Y. Perfectly isotropic noise would in addition result in a simple joint noise distribution

$$\mathbf{N}_l = \begin{bmatrix} N^{TT} & 0 & 0 \\ 0 & N^{EE} & 0 \\ 0 & 0 & N^{BB} \end{bmatrix}, \tag{2.35}$$

where N^{XX} are the diagonal covariances of the Gaussian random detector noise. This very simplistic noise model is often found in the literature but should only be used for crude signal to noise estimates. In a real experiment the noise structure is typically more complicated and the instrumental effects like imperfect polarization calibration as well as the incomplete sky coverage can cause leakage between T, E and B modes.

2.4 Implementation on the Sphere

A numerical implementation requires a discretization of the fields. Since the average deflection angle is of the order of ~ 2 arcmin, an accurate lensing scheme requires highly resolved CMB maps with an average pixel size of at most 1 arcmin^2. For a full sky experiment this resolution implies a map with at least $\sim 10^8$ pixels occupying ~ 1 Gb in memory.

For our implementation on the full sky we make use of the HEALPix pixelization scheme and software package [61]. This package was specially developed for the needs of CMB analyses and includes many tools for map manipulation and spherical harmonic transforms. A HEALPix map divides the sphere into pixels of equal area with pixel centers arranged on rings of constant latitude. An increase in resolution is achieved by dividing each pixel into four sub-pixels. The resolution of an healpix grid is characterized by the number nside=2^n, where n is a natural number. Table 2.1 summarizes the number of pixels, the resolution and maximum spherical wavenumber l for HEALPix nsides that yield maps with approximately arcmin resolution.

nside	number of pixels	resolution [arcmin]	maximal l	memory [Mb]
1024	$1.3e7$	3.44	3071	140
2048	$5e7$	1.71	6143	550
4096	$2e8$	0.86	12287	2200

Table 2.1: Properties of HEALPix maps with different nsides.

2.4.1 Implementation of the Lensing Response

A discretization of the lensing response L^ϕ poses the problem that a temperature at pixel i will generally not be shifted to the center of another pixel, i.e., the grid of new positions will be irregular. Mapping the lensed temperature again onto the pixel grid requires an interpolation scheme. This scheme should not introduce artificial features to the lensed

field and its statistics on the scales of interest. Also it should be sufficiently fast to apply and memory efficient.

We have further shown in Section 1.5 that the lensed temperature power spectrum is a convolution of the unlensed temperature with the lensing potential power spectrum - this is because lensing redistributes the power of the CMB field between different scales. To get accurate lensed power spectra to a scale L, we require a CMB map with $l_{\max} = L + \Delta L$, where ΔL is determined by the width of the convolution kernel (at first order this the lensing power spectrum itself $C_{|\mathbf{l}-\mathbf{L}|}^{\phi\phi}$) and the desired accuracy at L. Typical values for ΔL are $200 - 250$.

From these two arguments it is easily deduced that an accurate lensing schemes requires maps of higher resolution than the scales of interest together with an efficient interpolation scheme. A naive pixel-wise remapping scheme requires ~ 16 times more pixels than the base map corresponding to 4 times the base nside. In Fig. 2.1 we show results of a naive pixel-wise remapping for different nsides and list typical application times. For a CMB lensing reconstruction the lensing operator and its transpose have to be evaluated of the order of a few hundred times and constitute the computational bottleneck. To run a reconstruction within acceptable time scales on a cluster, parallelization of this operation is unavoidable.

Many lensing algorithms that meet the above criteria have been proposed in the literature for both flat and curved coordinates [44, 14, 151, 141, 70, 136] and are to some extend publicly available.[5]

Lensing Deflection on the Sphere

Taking the gradient of the lensing potential ϕ on the sphere yields the deflection vector $\boldsymbol{\alpha}$,

$$\nabla_{\mathbf{x}}\phi(\mathbf{x}) = \boldsymbol{\alpha}(\mathbf{x}) = \alpha \cos\delta\, \mathbf{e}_\theta + \alpha \sin\delta\, \mathbf{e}_\varphi, \tag{2.36}$$

that we have decomposed into the local spherical coordinate basis in the last expression. The temperature at unlensed position $\mathbf{x} = (\theta, \varphi)$ is shifted along a geodesic on the sphere defined by the direction of the tangent vector $\boldsymbol{\alpha}$ and with arc length $\alpha = |\boldsymbol{\alpha}|$. The endpoint $\mathbf{x}' = (\theta', \varphi + \Delta\varphi)$ of this shift can be found by applying spherical trigonometry. From the spherical cosine rule, we get [44, 36]

$$\cos(\theta') = \cos(\theta)\cos(\alpha) + \sin(\theta)\sin(\alpha)\cos(\delta) \tag{2.37}$$

and from the spherical sine rule

$$\sin(\Delta\varphi) = \sin(\alpha)\frac{\sin(\delta)}{\sin(\theta')}. \tag{2.38}$$

---

[5]e.g. `http://cosmologist.info/lenspix`,
`https://github.com/dhanson/quicklens`,
`http://www2.iap.fr/users/lavaux/software/flints.html`
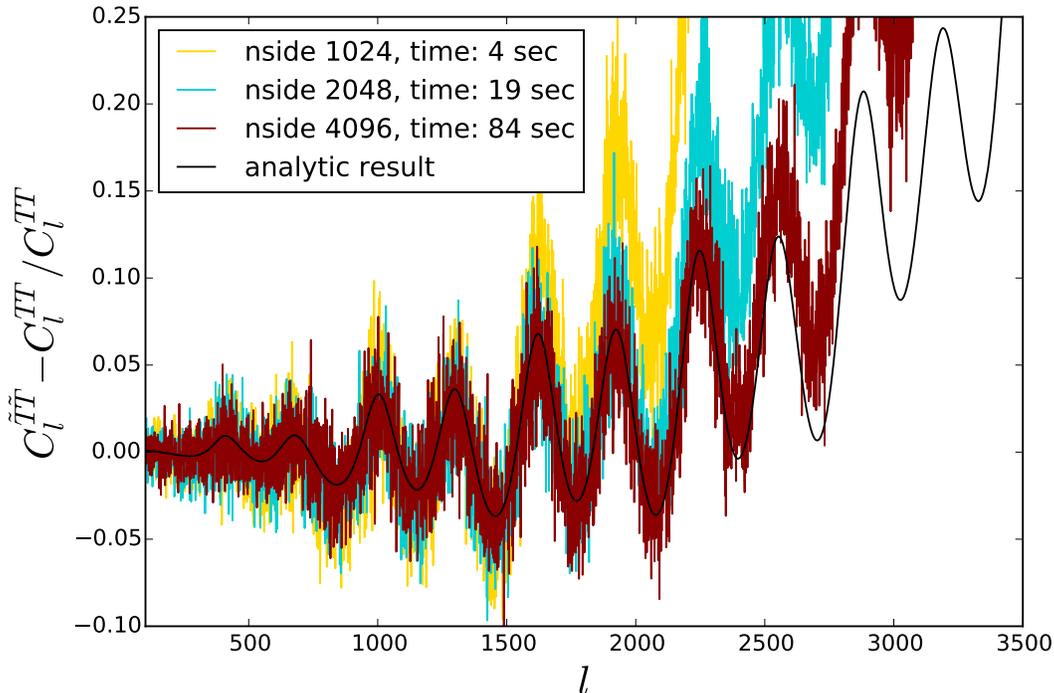
Figure 2.1: Relative differences between lensed and unlensed temperature power spectra. The lensing operation was performed by a naive pixel to pixel remapping, i.e. nearest grid point interpolation. We show results for different map resolutions (characterized by the nside parameter) and list the application times of the lensing operator for each case. The black line indicates the analytic result computed with CAMB[7] [144].

For polarization, the remapping operation becomes somewhat more complicated, since the polarization tensor $\mathcal{P}$ (c.p. Eq. (1.25) in Section 1.3.3) has to be parallel transported along the aforementioned geodesic. A naive remapping of the Stokes parameters $[Q(\mathbf{x}), U(\mathbf{x})] \rightarrow [Q(\mathbf{x}'), U(\mathbf{x}')]$ is not correct and would introduce spurious correlations [36]. Instead one needs to account for the change of the tangent basis

$$\tilde{\mathcal{P}}(\mathbf{x}') = \mathrm{e}^{[2i(\delta-\gamma)]}\mathcal{P}(\mathbf{x}),\tag{2.39}$$

where δ is as before the angle between the basis vector e_θ and $\boldsymbol{\alpha}$ at position $\mathbf{x}$ and γ the corresponding angle between $e_{\theta'}$ and $\boldsymbol{\alpha}$ at position $\mathbf{x}'$. The rotation angle $\delta' = \delta - \gamma$ is related to the deflection vector and the unlensed position by (see e.g. [141])

$$\tan(\delta') = \frac{\alpha \sin(\delta)}{d \sin(\alpha) \cot(\theta) + \alpha \cos(\delta)}.\tag{2.40}$$

2.4.2 Accuracy of Spherical Harmonic Transforms

While the prior distribution of the CMB and lensing potential can be analytically derived in harmonic space, but data, noise and in most cases the lensing operation are measured

and expressed in configuration space, we can not avoid to use harmonic transforms in a numerical implementation. The spherical harmonic transform used on the full sky is computationally more expensive than a Fourier transform, but can be efficiently implemented for the HEALPix grid [190]. The back transform (harmonic to configuration space) is a sum over a given set of spherical harmonic coefficients and spherical harmonics at fixed positions. This can be evaluated exactly. The forward transform (configuration to harmonic space), however, requires the integration over a sparsely sampled smooth function. This operation is in most cases ill-defined. It can only be evaluated exactly, if the function is strictly band limited, which is not the case for most physical fields. An increase in the accuracy of this operation can be reached at the cost of computation time by increasing the iteration of a weighting scheme that is used to approximate the integral [190]. In the HEALPix implementation used here, this iteration number is controlled by the parameter niter. In Fig. 2.2 we show the difference between an input CMB map at resolution nside=1024 and the same map after 5 back and 5 forward transformation. The difference map is divided by the standard deviation of the input map and the result plotted in units of percent. The error introduced by the transforms is significant and reaches values of up to $\sim 300\%$ for no iteration in the forward transform. Iterating once, yields smaller errors of up to $\sim 10\%$. Increasing niter to 3 yields no significant improvements in accuracy but roughly doubles the application time of the forward transform.

This problem can be elegantly alleviated by reconstructing the signal fields in spherical harmonic space. By doing so the backward harmonic transform becomes part of the response

$$d_i = R_{il}^{\text{new}} s_l = R_{ix} \mathcal{T}_{xl} s_l, \tag{2.41}$$

where $\mathcal{T}_{xl}$ denotes the backward harmonic transform and s_l is the signal field in harmonic space. If we, thus, acknowledge the transformation as part of the data model, we avoid its inverse $\mathcal{T}^{-1}$, since not the inverse but the adjoint $\mathcal{T}^\dagger$ will appear in the reconstruction. The adjoint operation is just as exact as the backward transform itself.

2.4.3 Minimizer

With analytic expressions for the negative log posterior and its derivative with respect to the field of interest at hand [Eq. (2.21) and (2.27) or Eq. (2.32) and (2.33)], we can initialize a minimizing algorithm, such as a steepest descent or conjugate descent. These algorithms typically need to evaluate the posterior and the gradient at the order of a few hundred times to converge to the minimum.

In each of these minimization steps, one needs to evaluate a Wiener Filter, either Dj [in the signal space formulation; c.p. Eq. (2.20)] or $C^{TT} R^\dagger \left(C^{dd}\right)^{-1} d$ [in the data space formulation; c.p. Eq. (2.32)]. These terms are non-trivial to compute since they involve the inversion of either the inverse lensing propagator $D^{-1} = R^\dagger N^{-1} R + (C^{TT})^{-1}$ or the data covariance $C^{dd} = R C^{TT} R^\dagger + N$. Both contain a noise covariance that is diagonal in configuration space and a signal covariance that is diagonal in harmonic space. The lensing operator introduces non-diagonal components in both configuration and harmonic space.

Mode-coupling is also soured by a mask or an isotropic beam function, such that there is no generic and easily computable basis in which all operators become diagonal.

This complicated structure inhibits or massively slows down the convergence of any inversion algorithm. A common technique to speed up the convergence of, e.g. a conjugate gradient, is to use a suitable preconditioner. This is an approximate inverse that is computationally efficient to compute and its application decreases the condition number of the matrix that one aims to invert. A smaller condition number leads to a faster convergence of the inversion algorithm. Since the noise contribution dominates on small scales and the signal dominated on large scales, a trivial global preconditioner such as S^{-1}/S or N/N^{-1} is not sufficient. One solution to this is to use a block preconditioner [57, 90], but better convergence rates can be obtained with a multigrid preconditioner [216]. In the block approach, the preconditioning matrix is split into a large scale part, where one inserts the full non-diagonal inverse for these scales and a small scale part, where an approximate inverse is inserted

$$\text{Precon}_{\text{block}} = \begin{bmatrix} X^{-1} & 0 \\ 0 & X^{-1}_{\text{approx}} \end{bmatrix}. \tag{2.42}$$

In the multigrid approach the problem is solved on increasingly finer grids using the solution of the coarser grid as a preconditioner in the next iteration. A completely alternative inversion method has been proposed by Elsner & Wandelt by introduction of a so called messenger field [53].

All of these methods have in common that they have free parameters which need to be chosen in order to optimally speed the convergence of the minimization. It is not to be expected that there exists a universal configuration that is optimal for every data set. In reality, the best minimization settings will depend on the specifics of the problem, i.e. the resolution, the shape of the masks and the noise.

2.5   Summary and Conclusions

In the above chapter, we have presented a full derivation of the joint probability distribution, $P(\phi, d)$, of the lensing potential ϕ and CMB data d, which is proportional to the lensing posterior $P(\phi|d)$ [Eq. (2.20)]. The expression has been derived under the assumption of a Gaussian unlensed temperature distribution and by imposing a Gaussian prior on the lensing potential, which are both well justified. Using this formula, together with the derived expression of its derivative with respect to ϕ [Eq. (2.27)], one can solve for the maximum of the distribution, which corresponds to the MAP estimate of the lensing potential.

This MAP estimate serves as an alternative to the commonly used quadratic estimator.[8]

We have further shown that the expressions for the negative log distribution and its derivative can be formulated in two equivalent ways, which we refer to as data and signal space formulation. This can be useful in the actual implementation were the minimization

---

[8]The quadratic estimator can be obtained from an approximation of the MAP estimator at linear order in ϕ [91].

in one formulation might be numerically more stable or faster in convergence than the other.

We have listed all the tools that are needed for an implementation of this estimator on the sphere and pointed out all the caveats that are known to us. The three major challenges in this type of lensing reconstruction are

1. memory usage and computational speed,

2. convergence of the minimization scheme and the operator inversions,

3. the convergence speed of the expectation value in the posterior derivative.

The first point is owed to the very small shifts that lensing introduces in the CMB field and the non-locality of the lensing operation in both harmonic and configuration space. Because of this, we need to resolve scales in the CMB field that are smaller than the smallest scales in the CMB data. In addition, the pixelization demands another non-local interpolation scheme in order to map the lensed field back onto the pixel grid.

The second point is due to the anisotropy that is introduced by lensing. The lensing operator will render diagonal operators like C^{TT} in harmonic space or N in data space non-diagonal by introducing correlations between modes or pixels. This is in fact the desired lensing signal that is exploited in the quadratic estimator. It will, however, slow down the convergence of the minimization. In real data, additional anisotropy can be introduced by an anisotropic beam and even more by a mask. Because of this, the minimizer (and preconditioner) settings must be carefully tuned to yield an acceptable convergence rate.

The minimization includes the evaluation of a peculiar term in the derivative of the posterior, that stems from the derivative of an operator determinant and can be rewritten as the negative expectation value of the first term that appears in the derivative. Carron & Lewis [33] have shown that the accuracy of the evaluation of this mean field constitutes the accuracy limit of the entire reconstruction. Sampling this expectation value is computationally expensive, since it involves solving the Wiener Filter for the unlensed temperature in every step, but can easily be parallelized.

Recent studies suggest that for current data sets the MAP estimator is compatible with the quadratic estimator. For future data, it can even be superior, e.g., by yielding better delensing efficiencies [33].

In the future, a Bayesian inference not only of the lensing potential itself, but of its power spectrum, would be interesting, since the standard power spectrum estimator is affected by many (known) biases, that have to be estimated independently before being subtracted. A Bayesian estimator would constitute a valuable crosscheck of these corrections.
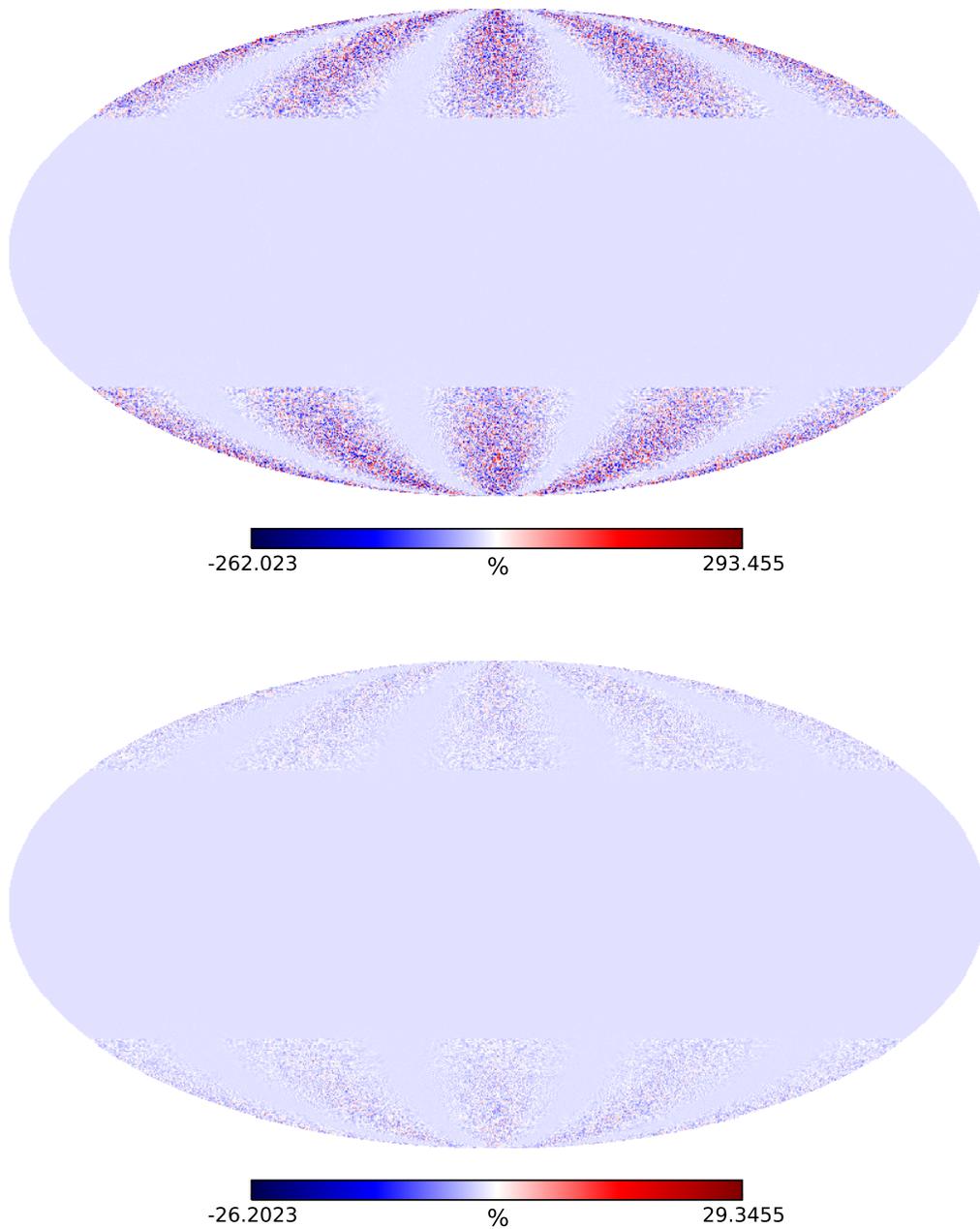
Figure 2.2: Difference between a CMB map after 5 forward and 5 backward spherical harmonic transforms and the original map before the transformations. We used a resolution of nside=1024 for this test and plot the difference in units of percent of the standard deviation of the original map. In the upper panel we have set the accuracy parameter niter to zero, yielding maximal errors of order $\sim 300\%$ around the poles. In the lower panel, we show the same difference for niter=1, which roughly doubles the computation time. Increasing niter to 3 yields no further improvements in accuracy.

Chapter 3

A new Bias to CMB Lensing Measurements

In this chapter we take a closer look at the standard CMB lensing reconstruction technique and ask if non-linear structure formation can have a significant impact on the measured CMB lensing power spectrum. The content of this chapter has been mostly taken from the corresponding publication [25]. Adaptations have been made in order to ease the understanding for non-CMB lensing experts.

3.1   Introduction

CMB lensing analyses commonly rely on the assumption of Gaussianity of both the unlensed CMB temperature field as well as the lensing potential. The lensing potential is a projection of the gravitational potential, which is known to become non-Gaussian at late times due to non-linear structure formation. However, the weighted projection, which sums up the effect of all fluctuations encountered on the photon geodesic, should suppress this non-Gaussianity by the central limit theorem (given a distance to the CMB of 14000 Mpc a CMB photon typically passes through $\mathcal{O}(50)$ structures of size 300 comoving Mpc, the scale at which the matter power spectrum peaks). The goal of our work is to test this intuitive argument quantitatively by abandoning the assumption of Gaussianity of the lensing potential and investigating the consequences of a nonzero bispectrum of the lensing potential on measurements of the lensing power spectrum. The main result is a new, typically negative, reconstruction bias $(N^{(3/2)})$ that contributes to the measured lensing power spectrum and must be corrected for. Following further tests of the importance of some of the neglected terms with analytics and simulations, this bias should be subtracted from future lensing 4-point measurements. It adds to known reconstruction power spectrum biases that arise for a Gaussian lensing potential and have been worked out in detail in [121, 72, 7].

While the effect of large-scale structure non-Gaussianity on lensing statistics has been computed in the context of galaxy weak lensing [49, 210, 135], it has not been analyti-

cally studied for CMB lensing reconstruction before. A number of works have tested CMB
lensing reconstruction on CMB maps lensed by non-Gaussian deflection fields computed
from N-body simulations [5, 231, 171, 10]. Some focused on estimating the impact of non-
linear structure formation on the lensing measurement, while many also included other
sources of biases, such as baryonic effects, survey boundaries and masking. In addition,
the primordial unlensed CMB may also be intrinsically non-Gaussian. A CMB bispectrum
induced by primordial non-Gaussianities of the local type has been studied as a signal on
its own (e.g. [133, 237, 145, 180]) and as a possible contaminant to CMB lensing measure-
ments [165]. Higher order corrections to the lensed temperature power spectrum have been
investigated analytically [164, 66] and in simulations [32, 31]. Related but different 4-point
CMB lensing biases were studied in [230, 176], caused by unresolved radio/infrared point
sources and galaxy clusters that add to CMB fluctuations.

This chapter is organized as follows. In Section 3.2 we briefly review the formalism
of CMB lensing and lensing measurements, introduce notation and conventions used in
this chapter and provide an analytic expression for the lensing bispectrum. The rigorous
derivation of the new reconstruction power bias is presented in Section 3.3 and results of
its numerical evaluation are given in Section 3.4. In Section 3.5 we provide an overview
of potential caveats in the numerical evaluation of the bias and present cross-checks that
were carried out to validate the results. An extension of the bias to CMB lensing cross-
correlation measurements is derived in Section 3.6. We conclude in Section 3.7. In a series
of appendices we provide details on the effect of the CMB lensing bispectrum on lensing
reconstruction in Fourier space, large-scale and squeezed limits and the generalization of
one of the contributing bias terms to polarization.

3.2   CMB Lensing and Reconstruction

3.2.1   CMB Lensing Model

As outlined in the introduction (Section 1.5), the lensed temperature $\tilde{T}$ can be approxi-
mated by perturbing in the lensing potential. We restrict ourselves to this series expansion
here, but note that this approximation is only accurate to about $5 - 10\%$ [142] and could
be improved by using the correlation function approach of [203] which is nonperturbative
in the deflection angle. Working under the flat-sky approximation valid on small scales
and truncating at second order in $\nabla\phi$, the perturbative series can be written as

$$\tilde{T}(\mathbf{x}) = T(\mathbf{x}) + \nabla T(\mathbf{x}) \cdot \nabla \phi(\mathbf{x}) + \frac{1}{2} \nabla_i \nabla_j T(\mathbf{x}) \, \nabla_i \phi(\mathbf{x}) \, \nabla_j \phi(\mathbf{x}) + \mathcal{O}(\phi^3), \qquad (3.1)$$

where we use the convention that the differential operator ∇ is only applied to the object
directly following it. In harmonic space, products turn into convolutions and gradients
correspond to multiplication with $-i\mathbf{l}$, so that

$$\tilde{T}(\mathbf{l}) = T(\mathbf{l}) + \delta T(\mathbf{l}) + \delta^2 T(\mathbf{l}) + \mathcal{O}(\phi^3) \qquad (3.2)$$

with $\mathcal{O}(\phi)$ correction

$$\delta T(\mathbf{l}) = - \int_{\mathbf{l}'} \mathbf{l}' \cdot (\mathbf{l} - \mathbf{l}') T(\mathbf{l}') \phi(\mathbf{l} - \mathbf{l}') \tag{3.3}$$

and $\mathcal{O}(\phi^2)$ correction

$$\delta^2 T(\mathbf{l}) = \frac{1}{2} \int_{\mathbf{l}'} \int_{\mathbf{l}''} [\mathbf{l}' \cdot \mathbf{l}''] [\mathbf{l}' \cdot (\mathbf{l} - \mathbf{l}' - \mathbf{l}'')] T(\mathbf{l}') \phi(\mathbf{l}'') \phi(\mathbf{l} - \mathbf{l}' - \mathbf{l}''). \tag{3.4}$$

All perturbations are linear in the unlensed temperature T.

3.2.2 CMB Lensing Statistics

Commonly the lensing potential is modeled as a statistically homogeneous and isotropic Gaussian random field, which is solely characterized by its power spectrum. This power spectrum is well described by a Limber projection of the power spectrum of matter fluctuations, $P_\delta(k, \eta)$,

$$C_L^{\phi\phi} = \int_0^{\chi_*} d\chi \frac{4W(\chi)^2}{\chi^2} \frac{\gamma(\chi)^2}{(L/\chi)^4} P_\delta(L/\chi; \chi), \tag{3.5}$$

where

$$\gamma(\chi) \equiv \frac{3}{2} \frac{H_0^2 \, \Omega_{\mathrm{m0}}}{c^2 a(\chi)}. \tag{3.6}$$

In this work we drop the assumption of Gaussianity and allow for a nonzero bispectrum of the lensing potential.

Similarly to the lensing power spectrum, the lensing bispectrum is a projection of the bispectrum of density perturbations $B_\delta(\mathbf{k}_1, \mathbf{k}_2, -\mathbf{k}_1 - \mathbf{k}_2; \chi)$:

$$B_\phi(\mathbf{l}_1, \mathbf{l}_2, \mathbf{l}_3) = - \int_0^{\chi_*} d\chi \, \chi^2 \, 8 \, W(\chi)^3 \frac{\gamma(\chi)^3}{(l_1 l_2 l_3)^2} B_\delta(l_1/\chi, l_2/\chi, l_3/\chi; \chi). \tag{3.7}$$

This follows by applying the Fourier space analogue of Limber's equation for bispectra (see e.g., [27, 223]). On very large scales, we expect the flat-sky and Limber approximations that we assume to break down. The lensing power spectrum is overestimated on large scales in the Limber approximation and the bispectrum could be affected similarly. We will therefore only consider multipoles $L > 100$.

The bispectrum of matter perturbations can be modeled by standard Eulerian perturbation theory, which gives at leading order in the linear matter overdensity (see e.g. [17] for a review),

$$B_\delta(\mathbf{k}_1, \mathbf{k}_2, \mathbf{k}_3; \eta) = 2 \, F_2(\mathbf{k}_1, \mathbf{k}_2) P_\delta(k_1, \eta) P_\delta(k_2, \eta) + (1 \leftrightarrow 3) + (2 \leftrightarrow 3). \tag{3.8}$$

This is quadratic in the linear matter power spectrum P_δ and involves the symmetrized kernel

$$F_2(\mathbf{k}_i, \mathbf{k}_j) = \frac{5}{7} + \frac{1}{2} \left(\frac{k_i}{k_j} + \frac{k_j}{k_i} \right) \hat{\mathbf{k}}_i \cdot \hat{\mathbf{k}}_j + \frac{2}{7} (\hat{\mathbf{k}}_i \cdot \hat{\mathbf{k}}_j)^2, \tag{3.9}$$

where $\hat{\mathbf{k}}_i = \mathbf{k}_i/|\mathbf{k}_i|$. The simple bispectrum model (3.8) is only accurate on relatively large scales that are under perturbative control (roughly $k \lesssim 0.07\,h/\mathrm{Mpc}$ at $z = 0$, see e.g., [138] for a recent study). It can be extended to smaller, non-linear scales by including higher-order (loop) corrections. A simpler phenomenological modification that extends the range of validity to slightly smaller scales can be obtained by replacing $P_\delta(k)$ with a matter power spectrum with non-linear corrections, $P_\delta^{\mathrm{nl}}(k)$, in Eq. (3.8) [197]. On smaller scales, that cannot be modeled analytically, one needs to resort to fitting formulae calibrated against simulations [197, 60].

3.2.3 Lensing Reconstruction

Lensing introduces a mode-coupling in the CMB fluctuations, which can be used to construct a quadratic lensing reconstruction estimator [207, 97], which can be written on the flat sky as (c.p. Section 1.5.1)

$$\hat{\phi}(\mathbf{L}) = A_L \int_{\mathbf{l}} g(\mathbf{l}, \mathbf{L}) \tilde{T}_{\mathrm{expt}}(\mathbf{l}) \tilde{T}_{\mathrm{expt}}(\mathbf{L} - \mathbf{l}), \qquad (3.10)$$

where $\tilde{T}_{\mathrm{expt}}$ are beam-deconvolved noisy temperature fluctuations. The observed temperature fluctuations are assumed to contain white noise and a Gaussian beam, so that the final power spectrum is

$$C_{l,\mathrm{expt}}^{\tilde{T}\tilde{T}} = C_l^{\tilde{T}\tilde{T}} + \sigma_N^2 \exp\left[l(l+1)\theta_{\mathrm{FWHM}}^2/(8\ln 2)\right], \qquad (3.11)$$

where the instrumental noise level is specified by σ_N^2 and the beam size is given in terms of the full width at half-maximum (FWHM) θ_{FWHM}. The weight $g(\mathbf{l}, \mathbf{L})$ (or short $g_{\mathbf{l},\mathbf{L}}$) in Eq. (3.10) is chosen such that the variance of the estimator is minimized [173, 143, 72];

$$g(\mathbf{l}, \mathbf{L}) = \frac{(\mathbf{L} - \mathbf{l}) \cdot \mathbf{L} C_{|\mathbf{L}-\mathbf{l}|}^{\tilde{T}\tilde{T}} + \mathbf{l} \cdot \mathbf{L} C_l^{\tilde{T}\tilde{T}}}{2 C_{l,\mathrm{expt}}^{\tilde{T}\tilde{T}} C_{|\mathbf{L}-\mathbf{l}|,\mathrm{expt}}^{\tilde{T}\tilde{T}}}. \qquad (3.12)$$

Note that $g(\mathbf{L} - \mathbf{l}, \mathbf{L}) = g(\mathbf{l}, \mathbf{L}) = g(-\mathbf{l}, -\mathbf{L})$. The normalization is given by

$$A_L^{-1} = 2 \int_{\mathbf{l}} g(\mathbf{l}, \mathbf{L}) \mathbf{l} \cdot \mathbf{L} C_l^{\tilde{T}\tilde{T}}. \qquad (3.13)$$

The power spectrum of the lensing reconstruction (3.10) involves the lensed temperature 4-point function,

$$\langle \hat{\phi}(\mathbf{L}) \hat{\phi}(-\mathbf{L}) \rangle = A_L^2 \int_{\mathbf{l}_1} \int_{\mathbf{l}_2} g_{\mathbf{l}_1,\mathbf{L}}\, g_{\mathbf{l}_2,\mathbf{L}} \langle \tilde{T}_{\mathrm{expt}}(\mathbf{l}_1)\, \tilde{T}_{\mathrm{expt}}(\mathbf{L} - \mathbf{l}_1)\, \tilde{T}_{\mathrm{expt}}(-\mathbf{l}_2)\, \tilde{T}_{\mathrm{expt}}(\mathbf{l}_2 - \mathbf{L}) \rangle. \qquad (3.14)$$

This 4-point function can be split into a disconnected part, obtained by contracting two pairs of lensed temperature fields with each other, and a connected part, given by the

full 4-point function minus the disconnected part. The disconnected part leads to the $N^{(0)}$ power spectrum bias, which would be present even for Gaussian temperature fluctuations in absence of lensing. It is called $N^{(0)}$ because it is of zeroth order in $C^{\phi\phi}$.[1] Note $N_L^{(0)} = A_L$ (a consequence of optimal weighting). The connected part of the 4-point function in Eq. (3.14) leads to the desired signal contribution $C_L^{\phi\phi}$. Additionally, it gives rise to the $N^{(1)}$ bias which is also of order $C^{\phi\phi}$ [121, 72, 7]. The expectation value of the measured lensing power spectrum is therefore[2]

$$\langle C_L^{\hat\phi\hat\phi}\rangle = N_L^{(0)} + C_L^{\phi\phi} + N_L^{(1)} + \mathcal{O}[(C^{\phi\phi})^3] \qquad \text{(Gaussian } \phi) \qquad (3.15)$$

if the lensing potential ϕ is assumed to be Gaussian. To obtain an unbiased estimator for the signal $C^{\phi\phi}$, the $N^{(0)}$ and $N^{(1)}$ biases are calculated (typically using simulations or simulation-data combinations) and subtracted from the measured lensing power.

3.3 The Effect of a non-vanishing Matter Bispectrum on standard Lensing Reconstruction

We now drop the assumption that the lensing potential ϕ is Gaussian. In this case, n-point functions with an odd number of lensing potentials no longer need to vanish, and n-point functions no longer need be determined by the Gaussian 2-point power spectrum $C^{\phi\phi}$ alone. We consider only a nonzero 3-point function or bispectrum, and ignore corrections from all higher-order n-point functions. This approximation is motivated by the specific non-Gaussianity generated by large-scale structure modes in the mildly non-linear regime relevant for CMB lensing. For simplicity we ignore the ISW effect and its induced correlations like $\langle T\phi\rangle$ and $\langle TT\phi\rangle$, but note that accounting for it may lead to additional biases that should be investigated in the future. We also assume that the unlensed CMB is a Gaussian field.

Allowing a nonzero lensing potential bispectrum B_ϕ, the lensed temperature 4-point function entering the expectation value for the measured lensing power spectrum (3.14) picks up additional contractions that would vanish for a Gaussian lensing potential. A new allowed contraction is, for example, of the form

$$\langle \tilde{T}\tilde{T}\tilde{T}\tilde{T}\rangle_{(\phi,T)} = \langle \delta T\delta T\delta TT\rangle + \cdots = \langle T_{,i}\phi_{,i}T_{,j}\phi_{,j}T_{,k}\phi_{,k}T\rangle + \cdots, \qquad (3.16)$$

where subscripts denote gradients $T_{,i} = \nabla_i T$ and $\phi_{,i} = \nabla_i \phi$.

In total, we can write down four qualitatively different contractions at order ϕ^3

$$\text{Type A: } \langle \delta T\delta T\,\delta T'T'\rangle \qquad \text{Type B: } \langle \delta^2 T\delta T\,T'T'\rangle$$
$$\text{Type C: } \langle \delta^2 TT\,\delta T'T'\rangle \qquad \text{Type D: } \langle \delta^3 TT\,T'T'\rangle. \qquad (3.17)$$

---

[1]We follow the common power-counting practice where only explicit appearances of $C^{\phi\phi}$ are counted that are not contained in lensing contributions to $C^{\tilde{T}\tilde{T}}$.

[2]An additional $N^{(2)}$ bias of order $(C^{\phi\phi})^2$ also arises, but we avoid it by using lensed CMB power spectra in the normalization A_L Eq. (3.13) and in the numerator of the weight g in Eq. (3.12) [72, 143].

The last two temperature fields are labeled with primes to indicate that they correspond to the second reconstruction field $\hat{\phi}(-\mathbf{L})$ in Eq. (3.14); quantities without primes correspond to the first reconstruction field $\hat{\phi}(\mathbf{L})$.

Each type of terms allows several Wick's theorem contractions. For example, for type A there are three contractions that we label A1, A2, and A3:

$$\langle T_{,i}\phi_{,i}T_{,j}\phi_{,j}\,T'_{,k}\phi'_{,k}T'\rangle_{A1} \;+\; \langle T_{,i}\phi_{,i}T_{,j}\phi_{,j}\,T'_{,k}\phi'_{,k}T'\rangle_{A2} \;+\; \langle T_{,i}\phi_{,i}T_{,j}\phi_{,j}\,T'_{,k}\phi'_{,k}T'\rangle_{A3}. \qquad (3.18)$$

Similarly, the type B term has three contractions B1, B2, and B3,

$$\langle T_{,ij}\phi_{,i}\phi_{,j}T_{,k}\phi_{,k}\,T'T'\rangle_{B1} \;+\; \langle T_{,ij}\phi_{,i}\phi_{,j}T_{,k}\phi_{,k}\,T'T'\rangle_{B2} \;+\; \langle T_{,ij}\phi_{,i}\phi_{,j}T_{,k}\phi_{,k}\,T'T'\rangle_{B3}, \qquad (3.19)$$

and the type C term has contributions C1, C2, and C3:

$$\langle T_{,ij}\phi_{,i}\phi_{,j}T\,T'_{,k}\phi'_{,k}T'\rangle_{C1} \;+\; \langle T_{,ij}\phi_{,i}\phi_{,j}T\,T'_{,k}\phi'_{,k}T'\rangle_{C2} \;+\; \langle T_{,ij}\phi_{,i}\phi_{,j}T\,T'_{,k}\phi'_{,k}T'\rangle_{C3}. \qquad (3.20)$$

Different to the contractions of type A-C, type D terms depend on $\delta^3 T$

$$\langle T_{,ijk}\phi_{,i}\phi_{,j}\phi_{,k}T\,T'T'\rangle_{D1} \;+\; \langle T_{,ijk}\phi_{,i}\phi_{,j}\phi_{,k}T\,T'T'\rangle_{D2} \;+\; \langle T_{,ijk}\phi_{,i}\phi_{,j}\phi_{,k}T\,T'T'\rangle_{D3}. \qquad (3.21)$$

All of these 12 terms contribute to the lensed temperature 4-point function and thus to the standard 4-point estimator for the CMB lensing power spectrum. They lead to a new bias $N_{L,\mathrm{tot}}^{(3/2)}$ of the measured 4-point lensing power spectrum,

$$\langle C_L^{\hat{\phi}\hat{\phi}}\rangle = N_L^{(0)} + C_L^{\phi\phi} + N_L^{(1)} + N_{L,\mathrm{tot}}^{(3/2)} + \mathcal{O}[(C^{\phi\phi})^{5/2}] \qquad \text{(non-Gaussian } \phi\text{).} \qquad (3.22)$$

We call the new non-Gaussian reconstruction bias $N^{(3/2)}$ because it scales like $\phi^3 \propto (C^{\phi\phi})^{3/2}$, and previously considered biases like $N^{(0)}$ and $N^{(1)}$ were labeled by the power of $C^{\phi\phi}$ they involve.

Not all of the 12 terms listed above contribute equally to $N^{(3/2)}$ and a close inspection allows us to identify the dominating ones. The generic recipe for inspecting the bias terms is:

- Insert the harmonic space expressions for $\delta^n T$ into one of the contraction in (3.17).

- Evaluate the expectation values over lensing potential and unlensed temperature, and apply Wick's theorem to split the unlensed temperature four-point functions into sums of products of 2-point functions [c.p. Eqs. (3.18-3.21)].

- Insert each of the resulting summands into Eq. (3.14).

- Multiply the result by its correct symmetry factor (E.g. the contraction $\langle \delta T \delta^2 T T' T'\rangle$ results in the same bias contribution as $\langle TT\delta T'\delta^2 T'\rangle$, etc.).

- Simplify as far as possible.

We refer the reader to Appendix B for the details of these calculations. In general, this procedure results in more or less coupled 6D integrals over unlensed temperature power spectra and the lensing bispectrum. Some of these integrals can be split into a product of three 2D integrals, some factorized into a 2D integral times a 4D integral and some can be shown to vanish identically (due to symmetry arguments).

After this inspection, we find that the $N^{(3/2)}$ bias gets contributions from the following non-vanishing terms

$$N_{\text{tot}}^{(3/2)} = \left(N_{A1}^{(3/2)} + N_{C1}^{(3/2)} \right) + N_{A2}^{(3/2)} + N_{A3}^{(3/2)} + N_{B2}^{(3/2)} + N_{B3}^{(3/2)} + N_{C2}^{(3/2)} + N_{C3}^{(3/2)}. \quad (3.23)$$

In this work, we evaluate the A1 and C1 terms numerically and focus on them in the main text. We focus on these terms both because they are expected to be among the largest and because they allow for numerical evaluation on reasonable timescales. In contrast, as discussed in Appendix B, the B1 term is zero, and the A2 and A3 terms are tightly coupled, which makes numerical evaluation difficult and time-consuming (the integrals are six-dimensional), but also suggests that these terms are small. Furthermore, the C2 term should be naturally accounted for in the (realization-dependent) calculations of the $N^{(0)}$ bias, which is included in modern lensing pipelines. We defer a full evaluation of the remaining B2, B3, and C3 terms to future work; we note that if they have a similar order of magnitude to $A1 + C1$, our approximate calculation might underestimate the true bias.

The A1 and C1 bias terms in Eqs. (3.18) and (3.20) have a simple intuitive interpretation: They arise because the *quadratic response* of the lensing reconstruction $\hat{\phi}(\mathbf{L})$ to the true lensing potential ϕ is correlated with the *linear response* of the lensing reconstruction $\hat{\phi}(-\mathbf{L})$ to the true lensing potential ϕ'. This correlation involves the 3-point correlation function $\langle \phi\phi\phi' \rangle$ of the true lensing potential, which is nonzero in presence of non-linear gravitational clustering.

We proceed by discussing these A1 and C1 terms, which contribute substantially to the total bias (3.23), in detail. Analytical expressions for the remaining bias contributions are given in Appendix B.

3.3.1 A1 Contribution to the $N^{(3/2)}$ Bias

We begin by computing the lensing bias from the contraction A1 in Eq. (3.18). This contraction is given by

$$\langle \delta T_{\mathbf{l}_1} \delta T_{\mathbf{l}_2} \delta T_{\mathbf{l}_3} T_{\mathbf{l}_4} \rangle_{A1} = -(2\pi)^2 \delta_D(\mathbf{l}_1 + \mathbf{l}_2 + \mathbf{l}_3 + \mathbf{l}_4) C_{l_4}^{TT} \left[(\mathbf{l}_3 + \mathbf{l}_4) \cdot \mathbf{l}_4 \right]$$

$$\times \int_{\mathbf{l}} \left[\mathbf{l} \cdot (\mathbf{l}_1 - \mathbf{l}) \right] \left[\mathbf{l} \cdot (\mathbf{l}_2 + \mathbf{l}) \right] C_l^{TT} B_\phi(\mathbf{l}_1 - \mathbf{l}, \mathbf{l}_2 + \mathbf{l}, -\mathbf{l}_1 - \mathbf{l}_2), \quad (3.24)$$

where we used the Fourier space expression Eq. (3.3) for the first order temperature change δT due to lensing, and contracted temperature and lensing fields as indicated for the A1

term in Eq. (3.18).[3] Inserting this into Eq. (3.14) yields the following A1 bias of the measured lensing power spectrum:

$$
\begin{aligned}
N_{A1}^{(3/2)}(L) &= -4A_L^2 S_L \int_{\mathbf{l}_1,\mathbf{l}} g_{\mathbf{l}_1,\mathbf{L}}\left[\mathbf{l}\cdot(\mathbf{l}_1-\mathbf{l})\right]\left[\mathbf{l}\cdot(\mathbf{L}-(\mathbf{l}_1-\mathbf{l}))\right] C_l^{TT} B_\phi(\mathbf{l}_1-\mathbf{l},\mathbf{L}-(\mathbf{l}_1-\mathbf{l}),-\mathbf{L}) \\
&= -4A_L^2 S_L \int_{\mathbf{l}_1,\mathbf{l}} g_{\mathbf{l}_1,\mathbf{L}}[(\mathbf{l}_1-\mathbf{l})\cdot\mathbf{l}][(\mathbf{l}_1-\mathbf{l})\cdot(\mathbf{L}-\mathbf{l})]C_{|\mathbf{l}_1-\mathbf{l}|}^{TT} B_\phi(\mathbf{l},\mathbf{L}-\mathbf{l},-\mathbf{L}). \quad (3.25)
\end{aligned}
$$

The prefactor S_L is an integral over the filtered unlensed CMB power spectrum,

$$
S_L = \int_{\mathbf{l}_2} g_{\mathbf{l}_2,\mathbf{L}}(\mathbf{l}_2\cdot\mathbf{L})C_{l_2}^{TT}, \quad (3.26)
$$

satisfying $S_L \approx 1/(2A_L)$ at leading order in $C^{\phi\phi}$. The prefactor of 4 in Eq. (3.25) stems from the four possibilities to arrange three temperatures perturbed to first order and one unperturbed temperature in a 4-point correlator. The second line in Eq. (3.25) follows by changing integration variables $\mathbf{l}\to\mathbf{l}_1-\mathbf{l}$.

3.3.2   C1 Contribution to the $N^{(3/2)}$ Bias

The C1 contraction defined in Eq. (3.20) is

$$
\begin{aligned}
\langle\delta^2 T_{\mathbf{l}_1} T_{\mathbf{l}_2}\delta T_{\mathbf{l}_3} T_{\mathbf{l}_4}\rangle_{C1} &= \frac{(2\pi)^2}{2}\delta_D(\mathbf{l}_1+\mathbf{l}_2+\mathbf{l}_3+\mathbf{l}_4)C_{l_2}^{TT}C_{l_4}^{TT}\left[(\mathbf{l}_3+\mathbf{l}_4)\cdot\mathbf{l}_4\right] \\
&\quad\times\int_{\mathbf{l}}(\mathbf{l}_2\cdot\mathbf{l})\left[\mathbf{l}_2\cdot(\mathbf{l}_1+\mathbf{l}_2-\mathbf{l})\right] B_\phi(\mathbf{l},\mathbf{l}_1+\mathbf{l}_2-\mathbf{l},-\mathbf{l}_1-\mathbf{l}_2). \quad (3.27)
\end{aligned}
$$

Inserting this in Eq. (3.14) gives the following C1 bias of the measured lensing power spectrum:

$$
N_{C1}^{(3/2)}(L) = 4A_L^2 S_L \int_{\mathbf{l}_1,\mathbf{l}} g_{\mathbf{l}_1,\mathbf{L}}(\mathbf{l}_1\cdot\mathbf{l})\left[\mathbf{l}_1\cdot(\mathbf{L}-\mathbf{l})\right] C_{l_1}^{TT} B_\phi(\mathbf{l},\mathbf{L}-\mathbf{l},-\mathbf{L}), \quad (3.28)
$$

We changed integration variables $\mathbf{l}_1\to\mathbf{L}-\mathbf{l}_1$, and we accounted for a symmetry factor 8 that arises because the resulting lensing bias does not change if we exchange $\mathbf{l}_1\leftrightarrow\mathbf{l}_2$, or $\mathbf{l}_3\leftrightarrow\mathbf{l}_4$, or both in Eq. (3.27).

3.3.3   Integral Expressions for fast numerical Evaluation

The A1 and C1 biases in Eqs. (3.25) and (3.28) involve four-dimensional integrals for every multipole L, which are computationally expensive to evaluate. Fortunately, however,

---

[3]For Gaussian instrument noise that is uncorrelated with the signal, all contributions to the four point correlator $\langle\tilde{T}_{\mathbf{l}_1}^{\mathrm{expt}}\tilde{T}_{\mathbf{l}_2}^{\mathrm{expt}}\tilde{T}_{\mathbf{l}_3}^{\mathrm{expt}}\tilde{T}_{\mathbf{l}_4}^{\mathrm{expt}}\rangle$ that involve instrument noise either vanish or contribute to the Gaussian noise bias. This justifies ignoring instrument noise in the calculation of the connected four point contributions to $N^{(3/2)}$.

the integrands of these 4D integrals can be rewritten in a product-separable form, which allows much faster numerical evaluation by multiplying 2D integrals. In Appendix C we demonstrate this and derive the following simply-evaluated expression for the C1 bias:

$$N_{C1}^{(3/2)}(L) = -4A_L^2 S_L \left[R_\parallel(L)\beta_\parallel(L) + R_\perp(L)\beta_\perp(L) \right], \tag{3.29}$$

where we defined the temperature integral $R_\parallel$ and integrated lensing bispectrum $\beta_\parallel$ as

$$R_\parallel(L) = \int_{\mathbf{l}_1} g(\mathbf{l}_1, \mathbf{L}) l_1^2 \cos^2(\mu_{\mathbf{l}_1}) C_{l_1}^{TT}, \tag{3.30}$$

$$\beta_\parallel(L) = \int_{\mathbf{l}} l \cos\mu_{\mathbf{l}} \left[l\cos\mu_{\mathbf{l}} - L \right] B_\phi(\mathbf{l}, \mathbf{L} - \mathbf{l}, -\mathbf{L}), \tag{3.31}$$

and similarly for the perpendicular component,

$$R_\perp(L) = \int_{\mathbf{l}_1} g(\mathbf{l}_1, \mathbf{L}) l_1^2 \sin^2(\mu_{\mathbf{l}_1}) C_{l_1}^{TT}, \tag{3.32}$$

$$\beta_\perp(L) = \int_{\mathbf{l}} l^2 \sin^2(\mu_{\mathbf{l}}) B_\phi(\mathbf{l}, \mathbf{L} - \mathbf{l}, -\mathbf{L}), \tag{3.33}$$

where $\cos\mu_{\mathbf{l}_1} = \mathbf{l}_1 \cdot \mathbf{L}/(l_1 L)$ and $\cos\mu_{\mathbf{l}} = \mathbf{l} \cdot \mathbf{L}/(lL)$. In Appendix C, we also derive a similar fast integral expression for the A1 bias.

3.3.4 Comparison of A1 and C1 Contributions to the $N^{(3/2)}$ Bias

The A1 bias of Eq. (3.25) and the C1 bias of Eq. (3.28) have a very similar structure. This makes sense because these biases arise from similar contractions in Eqs. (3.18) and (3.20). In the limit of Eq. (3.25) where the lensing multipole l is much lower than the temperature multipole l_1 (i.e., $l \ll l_1$ and $\mathbf{l}_1 - \mathbf{l} \approx \mathbf{l}_1$), the A1 and C1 biases cancel each other. The potential cancellation in this limit demands careful numerical evaluation of the A1 and C1 contributions to the $N^{(3/2)}$ bias. Numerically, we will find later that the range of reconstruction multipoles L where this cancellation is actually relevant depends strongly on experimental specifications. At very low reconstruction multipoles L, the cancellation helps to regularize the $N^{(3/2)}$ bias by canceling individually large A1 and C1 contributions with opposite sign.

3.4 Numerical Evaluation

3.4.1 Implementation

We continue by evaluating the expressions in (3.25) and (3.29) that follow from the type A1 and type C1 contractions. The integrals over the lensing bispectrum can be evaluated for any model of the lensing bispectrum. We evaluate them using the leading-order standard perturbation theory expression Eq. (3.7) with $P_\delta^{\rm lin}(k)$ replaced by the non-linear

matter power spectrum $P_\delta^{\rm nl}(k)$, which fits simulations slightly better than the leading-order bispectrum involving $P_\delta^{\rm lin}(k)$ (also see Section 3.5.3 for a discussion of the validity of this bispectrum model).

Small-scale temperature contributions to the integrals are suppressed by setting the experimental noise to an unphysically high value (irrespective of the experiment) for temperature multipoles $l \geq 3000$. This small-scale cutoff is often applied to real data to ensure the results are insensitive to astrophysical emission from dusty galaxies and the Sunyaev-Zeldovich effect which become relevant at these scales.

Representative experiment	Stage-IV (CMB-S4)	Stage-III (AdvancedACT-like)	Planck
$\theta_{\rm FWHM}$[arcmin]	1.0	1.4	7.0
$\sigma_N^{TT}[\mu{\rm Karcmin}]$	1.0	6.0	30.0
$f_{\rm sky}$	0.5	0.4	0.63

Table 3.1: Typical beam and noise specifications of current and future experiments. All resolution and noise dependent results shown are based on one of these configurations. The noise level stated in this table is for temperature measurements. For polarization we use $\sigma_N^{BB} = \sigma_N^{EE} = \sqrt{2}\sigma_N^{TT}$ (see also Eq. (1.29) in Section 1.3.3).

To evaluate the contributions to the $N^{(3/2)}$ bias we consider different experimental setups roughly corresponding to CMB Stage-III, Stage-IV, and Planck experiments. Beam width, noise levels and sky coverage for these representative classes of experiments are summarized in Table 3.1.

For the calculation of the fiducial power spectra of matter, CMB and lensing potential we use the publicly available CLASS code[4] [23]. The computation of non-linear corrections to the power spectrum of density fluctuations is based on the HALOFIT method [217, 224]. The underlying cosmology is a standard ΛCDM cosmology with Planck 2013 best fit parameters: $\omega_m = 0.311$, $\Omega_b = 0.049$, $h = 0.671$, $A_s = 2.215 \times 10^{-9}$, $n_s = 0.968$, and $T_{\rm CMB} = 2.7255$ K [177].

We next discuss results for lensing measurements from the CMB temperature fluctuations and include the contribution to $N^{(3/2)}$ from the sum of the two couplings A1 and C1. We then proceed with polarization measurements for which we only evaluate the C1 coupling because it is simpler to evaluate.

3.4.2   Results for A1 and C1 Contributions to the $N^{(3/2)}$ Bias for (TT, TT) Reconstruction

Fig. 3.1 shows the A1 and C1 contributions to the non-Gaussian reconstruction bias $N^{(3/2)}$ for the different classes of experiments summarized in Table 3.1. To assess the importance of the non-Gaussian biases, we also show in Fig. 3.2 the ratio of their sum to the lensing power spectrum signal.

---

[4]http://www.class-code.net/
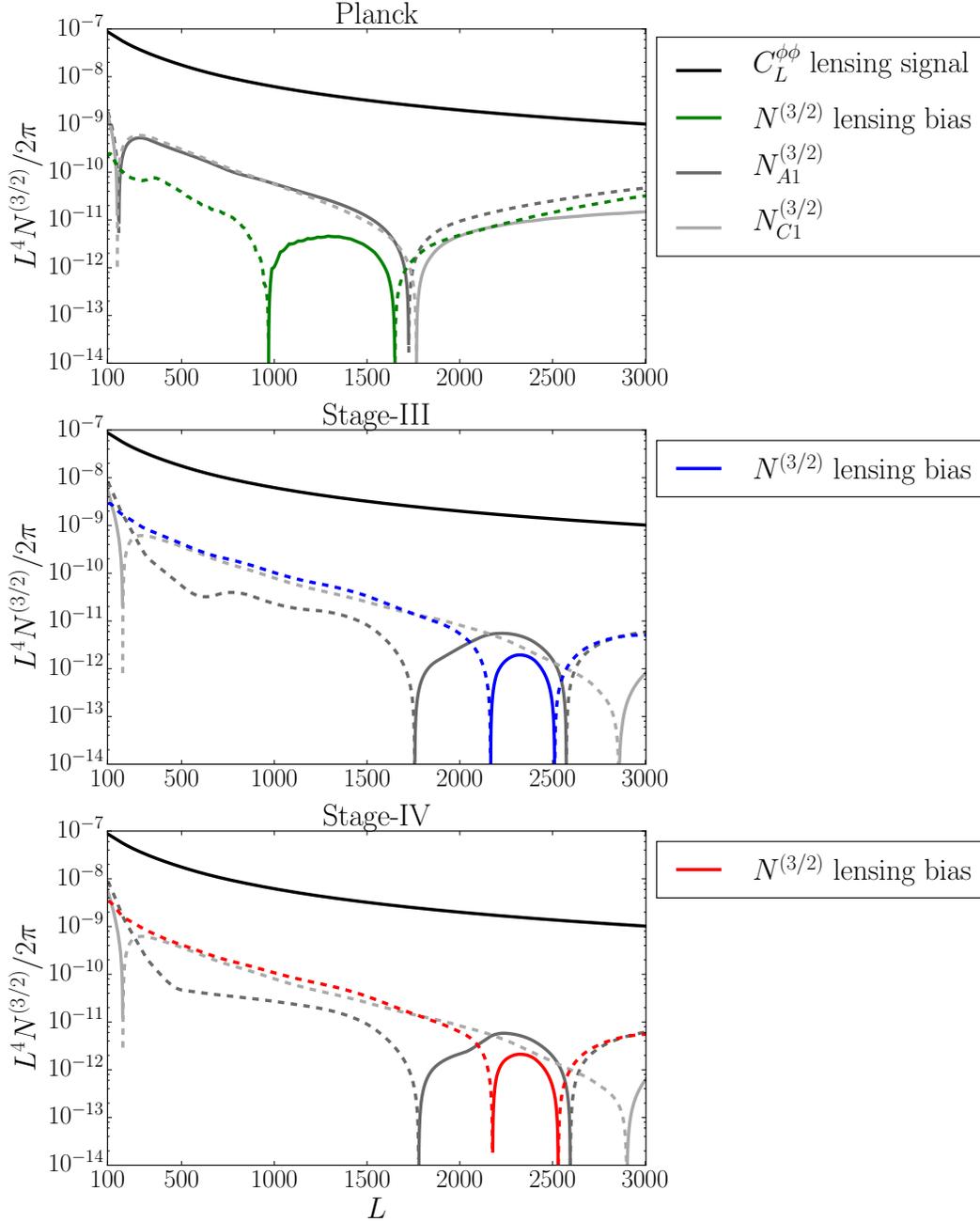
Figure 3.1: $N^{(3/2)}$ CMB lensing bias that arises in a temperature based lensing measurement. The signal lensing power spectrum $C^{\phi\phi}$ is shown for comparison (black). Different panels correspond to different experiment specifications summarized in Table 3.1. When negative, the absolute value of the functions are reported as dashed lines. The bias appears significant for Stage-III and Stage-IV experiments. We point out, that the bias plotted here is the sum of two out of many contributing terms to the total bias. These two terms, denoted type A1 and C1, are likely two of the largest terms.
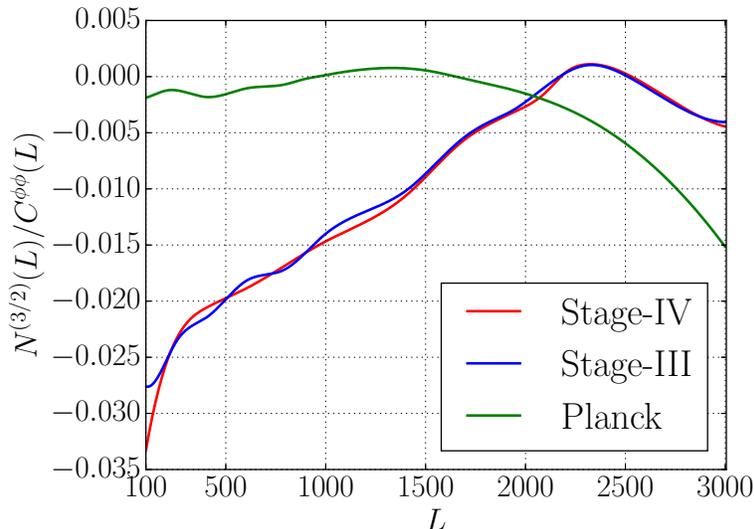
Figure 3.2:   Ratio of non-Gaussian $N^{(3/2)}$ bias over the signal lensing power spectrum $C^{\phi\phi}$ for a temperature based reconstruction. The bias reaches percent level over a wide range of multipoles for Stage-III and Stage-IV experiments.

For the high resolution Stage-III and Stage-IV experiments the bias is of order 0.5-2.5% of the signal, slowly decreasing towards smaller scales. The sign of the bias is negative over all relevant scales, i.e., it reduces the measured lensing power. For Planck, the bias appears nearly an order of magnitude smaller than in the high resolution case, typically entering at negligible levels well below one percent of the signal. This is the case because for Planck the A1 and C1 contributions to the bias partially cancel each other (see also the discussion at the end of Section 3.3). For Planck, the sign of the effect varies with angular scale.

The significance of the bias in each experiment depends on the statistical uncertainty of the measured lensing power spectrum. The Gaussian variance is given by

$$\sigma^2(L) = \frac{1}{f_{\text{sky}}} \frac{2}{(2L+1)} \left(N_L^{(0)} + C_L^{\phi\phi} + N_L^{(1)} \right)^2. \tag{3.34}$$

Fig. 3.3 shows the bias-to-noise ratio $N_{A1+C1}^{(3/2)}(L)/\sigma(L)$ if the measured lensing power spectrum is binned with bin width $\Delta L = 100$. The bias is significant in low-noise, high-resolution experiments such as CMB Stage-III or Stage-IV: If the bias is ignored, the measured lensing power spectrum will be biased low by $\sim 0.5\sigma - 1.5\sigma$ per bin for $L \sim 200 - 800$, for each bin of width $\Delta L = 100$. The total significance of this bias is $\sim 2.5\sigma$ for Stage-III and $\sim 3\sigma$ for Stage-IV.

The total bias is thus significant and should therefore be accounted for when performing (TT, TT) lensing reconstruction with CMB Stage-III or Stage-IV experiments. While Stage-IV will likely get most lensing information from polarization-based measurements so that the bias of temperature-based lensing measurements is less worrisome, a large
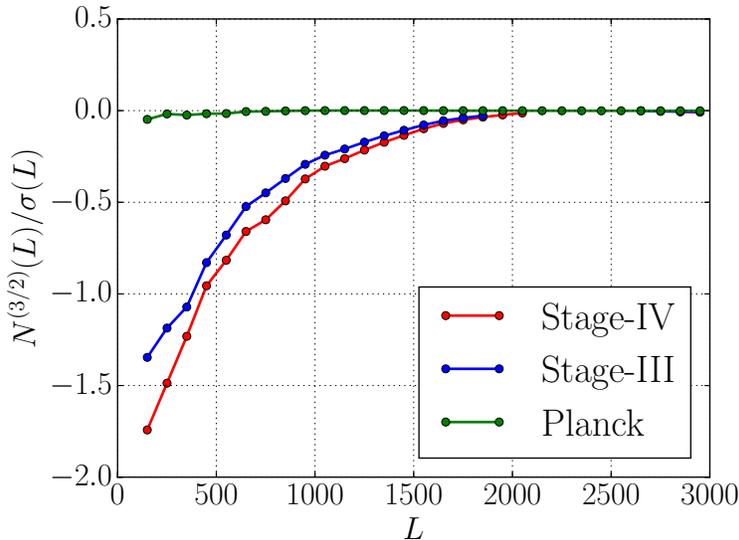
Figure 3.3: Ratio of $N^{(3/2)}$ bias over lensing power spectrum error $\sigma(L)$ on bandpowers of width $\Delta L = 100$. It can be seen that, while the bias appears negligible for Planck, it is a significant percent-level effect for Stage-III and Stage-IV experiments.

fraction of the lensing information from Stage-III experiments will come from (TT, TT) lensing measurements, so that accounting for the $N^{(3/2)}$ bias will be particularly important in this case. For Planck, however, the bias appears negligible (the significance of the total bias is only 0.06σ).

We emphasize that the above numbers just provide a rough estimate of the actual size of the $N^{(3/2)}$ bias because of the simplifying assumptions we made for the numerical evaluation. In particular, additional bias contributions from other contractions than A1 and C1 may be important for all experiments, and a more accurate model of the lensing bispectrum on small scales could change results for Stage-III and Stage-IV by an order one factor. We will discuss these caveats in more detail in Sections 3.5 and 3.7 below.

3.4.3 Results for C1 Contribution to the $N^{(3/2)}$ Bias for Polarization

We can generalize the $N^{(3/2)}$ bias to polarization-based measurements of the lensing power spectrum. In this work, we derive and evaluate the corresponding expressions for contributions from the coupling type C1 only (see Appendix D). The contribution from the coupling type A1 is numerically more expensive to evaluate and we defer its generalization to polarization to future work.

The left panel of Fig. 3.4 shows the C1 contribution to the bias from (EB, EB), (EE, EE), and (TT, TT) reconstruction for a Stage-IV experiment. On most relevant scales, the (TT, TT) and (EE, EE) biases are similar to each other, but the (EB, EB)

bias is much smaller. However, (EB, EB) reconstruction is also the combination which is expected to achieve the lowest error on the lensing measurement for future polarization-sensitive experiments like CMB Stage-IV. To assess the significance of the C1 bias contribution in this case, the right panel of Fig. 3.4 shows the bias divided by the reconstruction uncertainty for CMB Stage-IV and Planck (assuming Eq. (3.34) for the noise, and bin width $\Delta L = 100$). Despite the higher precision of (EB, EB) reconstruction, the bias still appears rather small, $0.1 - 0.3\sigma$ per L-bin of width $\Delta L = 100$.

We emphasize again that the bias is expected to change if contributions from the A1 and other contractions for polarization are included (like in the temperature-only case where the A1 contribution is rather important), and additional changes may arise from more accurate models for the matter bispectrum on small scales. Note also that the use of an iterative EB estimator could enhance the relative importance of the bias with respect to the lensing measurement error by roughly a factor of 3 for CMB Stage-IV, although the form of the bias may also be different for such a lensing estimator.

3.5 Discussion and Validation of the Calculations

In the following sections we discuss potential caveats in the evaluation of $N^{(3/2)}$ like its strong dependence on σ_8, cross-checks of our numerical implementation and assumptions made in the derivation and evaluation of $N^{(3/2)}$. Further, we explain how we have tested the influence of non-linear modes on the results and we comment on the sensitivity of the bias on the large-scale structure bispectrum model that is used. Some of our results have been derived for the C1 term only, but we expect them to apply similarly to the other relevant terms. We begin by discussing the scaling with σ_8.

3.5.1 Dependence of $N^{(3/2)}$ Bias on σ_8

Since the bispectrum of the lensing potential B_ϕ is quadratic in the power spectrum of the matter density, we expect the $N^{(3/2)}$ bias to scale with the fourth power of the normalization of matter fluctuations, σ_8. Thus relatively small changes of σ_8 lead to large changes of the $N^{(3/2)}$ bias. Computing the $N^{(3/2)}$ bias for a fiducial cosmology with slightly wrong σ_8 may therefore leave a significant residual bias. This may raise concerns because σ_8 is not very well known in practice. However, we found that the effect of σ_8 on the $N_{C1}^{(3/2)}$ bias is relatively well approximated by rescaling $N_{C1}^{(3/2)}$ with a scale-independent factor $(\sigma_8/\sigma_8^{\text{fiducial}})^4$. Therefore, the σ_8 dependence of the bias could easily be included when fitting cosmological parameters to data. This can in principle increase the precision of σ_8, because it includes information from the non-Gaussianity of the lensing potential ϕ (though more optimal methods for extracting this non-Gaussian information could be used instead).
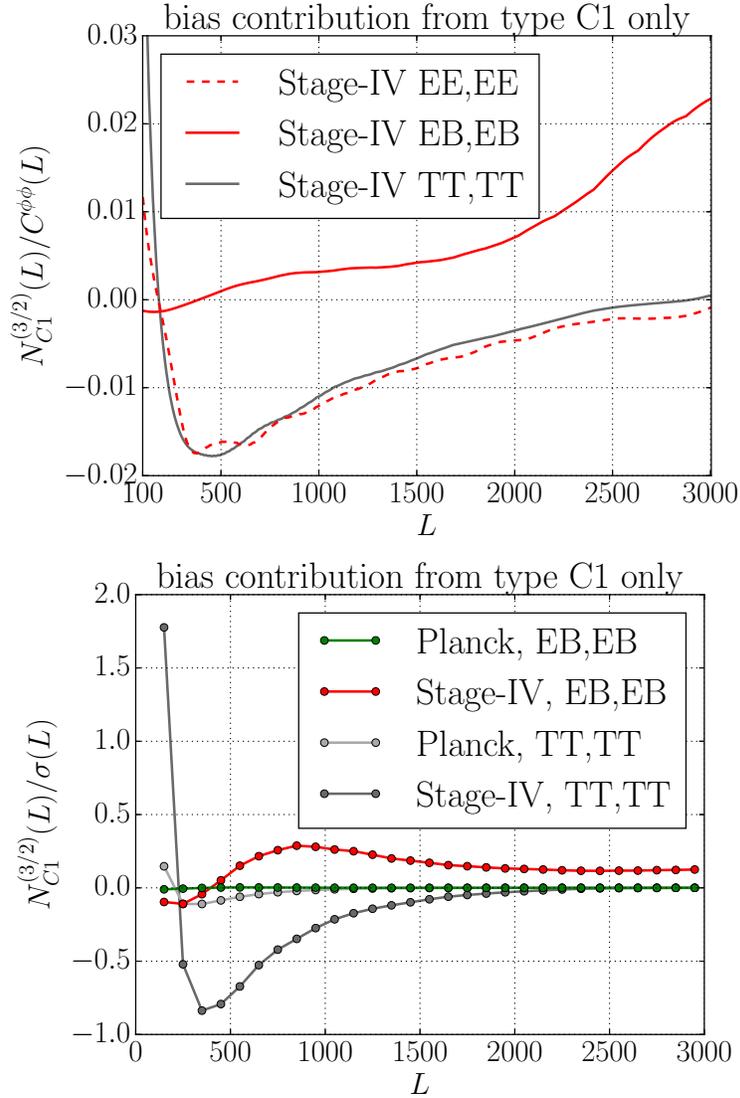
Figure 3.4:   Generalization of one of the bias contributions, from coupling type C1, to polarization-based measurements of the CMB lensing power spectrum (see Appendix D for details). All curves ignore the similar type A1 bias contribution. This provides some qualitative idea of how the bias changes for polarization, but should not be confused with the full expected lensing bias. A thorough quantification, which involves the evaluation of the remaining non-negligible term(s), is deferred to future work. In the upper panel, we show the C1 bias contribution for a Stage-IV experiment divided by the signal power spectrum for different estimators. In the lower panel, we divide the C1 bias contribution by the error on the lensing power spectrum measurement. In both panels the type C1 bias contribution for a temperature-based measurement is plotted for comparison. It can be seen that the C1 bias is less important for polarization lensing measurements using the EB estimator than it is for lensing measurements from temperature.

3.5.2 Cross-check with large-Lens and squeezed Bispectrum Limits

The numerical evaluation of the contributions to the $N^{(3/2)}$ bias involves several steps and relies on numerical approximations such as discretization schemes. Therefore, any of the computed results should be validated. Apart from code internal tests we have derived analytic large-lens and squeezed bispectrum limits for the various numerical integrals involved in evaluating $N^{(3/2)}$, evaluated them independently and compared them to full code results. These limits do not only provide a cross-check of the implementation, but are also useful to qualitatively understand the behavior and dependencies of the contributing terms. We have found excellent agreement between the analytic limits and our numerical calculations of the C1 contribution to the bias; for a detailed description of these tests we refer the reader to Appendix E.

3.5.3 Higher-order Corrections to the Matter Bispectrum

As discussed in Section 3.2.2, the simple model of Eq. (3.8) for the dark matter bispectrum from Eulerian standard perturbation theory at leading order is only valid for large-scale modes. It breaks down for small-scale modes that can have large overdensities $\delta \gg 1$ due to gravitational collapse. We use the simple leading-order model of Eq. (3.8) to get an approximate, conservative estimate of the expected size of the $N^{(3/2)}$ bias. In reality, higher-order (and ultimately non-perturbative) gravitational collapse on small scales generates a larger bispectrum that may lead to a larger $N^{(3/2)}$ lensing bias, especially for small-scale lenses (high L). For actual data analyses of experiments where the $N^{(3/2)}$ bias is relevant, fitting formulae for the matter bispectrum calibrated against N-body simulations should be used for more accurate predictions of the $N^{(3/2)}$ bias from small-scale modes. Our expressions for the lensing bias take an arbitrary matter bispectrum model as input so that it is straightforward to include more realistic bispectrum models. To get a rough estimate for the importance of small-scale modes on the $N^{(3/2)}$ bias, we compute the bias with the bispectrum set to zero if any of the contributing LSS modes is larger than a non-linear cutoff scale $k_{\mathrm{NL}}(z)$ defined by

$$\frac{k_{\mathrm{NL}}^3(z)P(k_{\mathrm{NL}}, z)}{2\pi^2} = 1, \tag{3.35}$$

and compare it to the full result. This test reveals that the contribution from these scales to the type C1 bias makes up $\sim 30\%$ of the signal at $L = 3000$ for CMB-S4 (and less for Stage-III and Planck experiments). Up to $L \sim 1000$ it lies below 10% for all experiments. At least up to this multipole range, the leading-order bispectrum (3.8) seems an acceptable approximation for the coupling of type C1. For the second coupling that we consider, type A1, we find somewhat different results. For a Planck-like experiment the contribution of small-scale modes at $L \sim 1000$ is of $\mathcal{O}(10\%)$ and thus similar to the type C1 term. For a Stage-IV experiment, however, these small modes contribute significantly even at lower
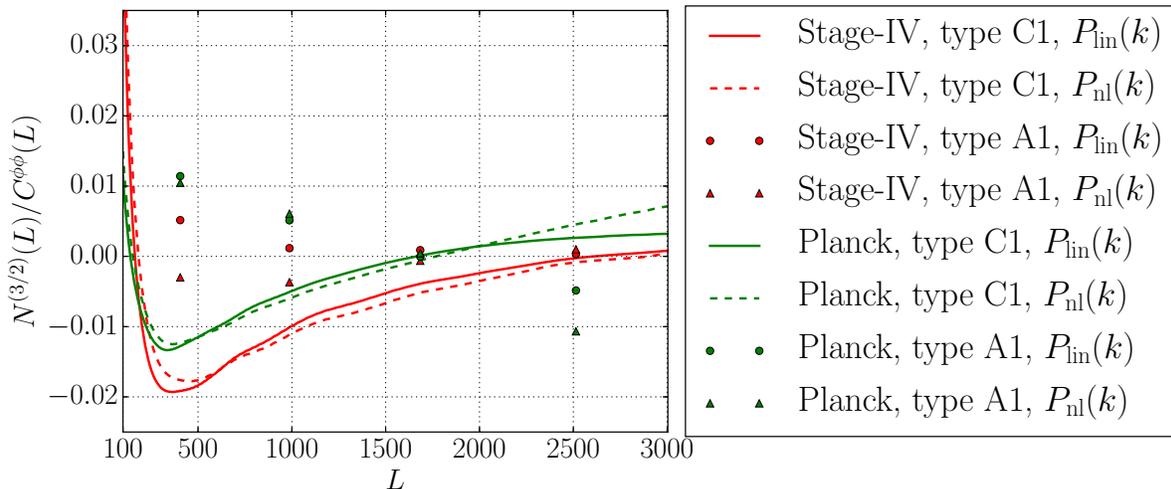
Figure 3.5: The fractional contribution of the non-linear bias from coupling type C1 (lines) and type A1 (symbols) (similar to the left panel in Fig. 3.2) computed from the standard Eulerian perturbation theory bispectrum at leading order and from a modified form where the linear matter power spectrum was replaced by a non-linear one (dashed lines). For the C1 contribution to the $N^{(3/2)}$ bias the standard leading-order bispectrum and the modified bispectrum (with enhanced non-linearity) give similar results at multipoles $L < 2000$. For the A1 contribution, which is computationally much more expensive to evaluate, the results are similar for Planck-like experiments, but for CMB Stage-IV higher-order corrections to the bispectrum seem to be important even at intermediate L.

multipoles. In particular, we find that the type A1 bias at $L = 1000$ has a different sign if modes smaller than the cutoff scale are excluded.

Another simple test of the impact of small-scale modes is obtained by comparing the $N^{(3/2)}$ bias evaluated with the standard perturbative bispectrum formula (3.8) and the bias computed from a modified bispectrum model where the linear matter power spectrum is replaced by the non-linear one, $P_{\rm lin} \to P_{\rm nl}$. This comparison is shown in Fig. 3.5. Lines indicate results for the type C1 contribution to the bias, symbols indicate the A1 contribution. The C1 bias contribution changes by $\mathcal{O}(10\%)$ or less for lensing multipoles $L < 2000$ if the non-linear instead of linear matter power spectrum is used. At higher multipoles $L > 2000$ the change can be larger.

For the similar A1 contribution to the bias we restrict this test to a few points (indicated by markers), because evaluation is much more computationally expensive. In this case, we find that the importance of non-linear corrections strongly depends on the experimental specifications. For a Planck-like experiment, the corrections seem similarly small as for the type C1 term. For a CMB Stage-IV experiment, however, the modification of the matter power spectrum leads to a significant change of the bias even at intermediate L.

We conclude that for high resolution experiments the leading-order perturbation theory

bispectrum model may not be sufficient for obtaining an exact estimate of the size of the $N^{(3/2)}$ bias, but instead can only provide an approximate estimate. For Planck, however, the leading-order model appears to be accurate. A thorough quantification of the bias for Stage-III and Stage-IV experiments requires a more accurate modeling of the LSS bispectrum for small LSS modes. This could be achieved by using fitting formulae for the matter bispectrum calibrated by numerical N-body simulations (e.g., [197, 60, 138, 137]).

3.5.4 Prospects for Comparison with Results from numerical Simulations

The derived form of the non-linear bias relies on the validity of certain assumptions, including e.g., the validity of the bispectrum approximation, the domination of the two contributions of type A1 and C1 to the bias over all other contributions, and the negligibility of non-linear corrections that are higher than third order in the lensing potential. An independent test of their correctness could be obtained by a comparison with N-body simulations that provide a full non-linear lensing potential and do not rely on a perturbative approach. We defer an analysis of the non-linear bias in CMB lensing simulations based on N-body simulations to future work.

3.6 Cross-correlation of CMB Lensing with an external LSS Tracer

While our paper focuses on the auto-power spectrum of the quadratic lensing reconstruction, $\langle \hat{\phi}\hat{\phi} \rangle$, it is also worthwhile to cross-correlate the lensing reconstruction $\hat{\phi}$ with other external LSS tracers ϕ_{ext} like the cosmic infrared background, galaxy weak lensing, galaxy or quasar catalogs, or Lyman-alpha observations; see e.g., [216, 89, 212, 71, 149, 73, 3, 232]. The cross-correlation $\langle \hat{\phi}\phi_{\text{ext}} \rangle$ between the quadratic CMB lensing reconstruction $\hat{\phi}$ and the external LSS tracer ϕ_{ext} then picks up a similar bias arising from the large-scale structure bispectrum generated by non-linear structure formation. In this section we compute this cross-spectrum bias similarly to the calculations above, under the assumption that the observed external LSS tracer is uncorrelated with the unlensed CMB.

The bias of the cross-spectrum induced by a nonzero LSS bispectrum is caused by the correlation of the external LSS tracer with the second order response of the reconstructed lensing potential to the true lensing potential. Similarly to the A1 and C1 contributions to the auto-spectrum bias in Eqs. (3.18) and (3.20), this bias to the cross-spectrum follows schematically from two contractions 'A1cross' and 'C1cross':

$$\langle \tilde{T}\tilde{T}\phi_{\text{ext}} \rangle_{\mathcal{O}[(C^{\phi\phi})^{3/2}]} = \langle \delta T \delta T \phi_{\text{ext}} \rangle + 2\langle \delta^2 T T \phi_{\text{ext}} \rangle \tag{3.36}$$

$$= \langle T_{,i}\phi_{,i}T_{,j}\phi_{,j}\,\phi_{\text{ext}} \rangle_{A1\text{cross}} + 2\langle T_{,ij}\phi_{,i}\phi_{,j}T\,\phi_{\text{ext}} \rangle_{C1\text{cross}}. \tag{3.37}$$

These are all contractions allowed for the cross-spectrum, so that the full expectation value

of the cross-spectrum up to fifth order in LSS perturbations is

$$\langle C_L^{\hat{\phi}\phi_{\text{ext}}}\rangle = C_L^{\phi\phi_{\text{ext}}} + N_{A1\text{cross}}^{(3/2)}(L) + N_{C1\text{cross}}^{(3/2)}(L) + \mathcal{O}(\phi^5), \tag{3.38}$$

where the new bispectrum-induced biases are

$$N_{A1\text{cross}}^{(3/2)}(L) = -A_L \int_{\mathbf{l},\mathbf{l}_1} g(\mathbf{l}_1, \mathbf{L})[(\mathbf{l}_1 - \mathbf{l})\cdot\mathbf{l}][(\mathbf{l}_1 - \mathbf{l})\cdot(\mathbf{L} - \mathbf{l})]C_{|\mathbf{l}_1 - \mathbf{l}|}^{TT} B_{\phi\phi_{\text{ext}}}(\mathbf{l}, \mathbf{L} - \mathbf{l}, -\mathbf{L}) \tag{3.39}$$

and

$$N_{C1\text{cross}}^{(3/2)}(L) = A_L \int_{\mathbf{l},\mathbf{l}_1} g(\mathbf{l}_1, \mathbf{L})(\mathbf{l}_1 \cdot \mathbf{l})[\mathbf{l}_1 \cdot (\mathbf{L} - \mathbf{l})]C_{l_1}^{TT} B_{\phi\phi_{\text{ext}}}(\mathbf{l}, \mathbf{L} - \mathbf{l}, -\mathbf{L}). \tag{3.40}$$

Here, $B_{\phi\phi_{\text{ext}}}$ is the mixed bispectrum between two CMB lensing modes and one external LSS tracer.

The cross-spectrum biases (3.39) and (3.40) are similar to the A1 and C1 auto-spectrum biases in Eqs. (3.25) and (3.28). Indeed, if the external tracer were equal to the true lensing potential modulo uncorrelated noise, $\phi_{\text{ext}} = \phi + n$, the cross biases would be half the auto-spectrum biases at leading order in the lensing potential power:

$$N_{A1\text{cross}}^{(3/2)}(L) \approx \frac{1}{2}N_{A_1}^{(3/2)}(L) \qquad \text{and} \qquad N_{C1\text{cross}}^{(3/2)}(L) \approx \frac{1}{2}N_{C_1}^{(3/2)}(L). \tag{3.41}$$

In practice, the external LSS tracer is typically different from the lensing potential, e.g., because of different redshift kernels, so that the cross-bias should be evaluated with the full Eqs. (3.39) and (3.40). Fast-to-evaluate expressions for these biases take the same form as those for the A1 and C1 auto-spectrum biases if the lensing bispectrum is replaced by the mixed lensing-lensing-tracer bispectrum $B_{\phi\phi_{\text{ext}}}$. We note that for lower-redshift tracers, the non-linearity is enhanced, so that cross-correlation biases may be larger than the biases for CMB lensing alone.

3.7 Summary and Conclusions

In this chapter, we have investigated the effect of large-scale structure non-Gaussianity on CMB lensing reconstruction. The bispectrum of the CMB lensing potential generated by non-linear structure formation leads to a bias of the measured CMB lensing power spectrum that has been neglected so far. We call the bias $N^{(3/2)}$ because it involves $\phi^3 \sim (C^{\phi\phi})^{3/2}$. For an unbiased measurement, this bias must be calculated and subtracted from measured lensing power spectra. We derive an analytical expression for this lensing bias, which splits into several contributions that involve the CMB power spectrum and the dark matter bispectrum.

The magnitude of the $N^{(3/2)}$ bias depends on experiment specifications and field combinations used for the lensing reconstruction. For CMB Stage-III and Stage-IV experiments, we find that the lensing power spectrum measurements are biased low by 0.5-2.5% (for

Planck, the bias is at a negligible sub-percent level) if temperature data is used. For future experiments, this negative bias will shift measurements of the lensing power spectrum by multiple standard deviations and must thus be accounted for. For Stage-III a large fraction of the lensing signal-to-noise is expected from the temperature-based reconstruction, so accounting for the bias is particularly important in this case. We focus on temperature-only lensing reconstructions, but we demonstrate for one of the bias contributions how it can be straightforwardly generalized to polarization-based reconstructions.

Our first results on this non-Gaussian bias, including the expected size of the bias, rely on a number of simplifying assumptions that should be tested in future work:

1. Some contributions to the non-Gaussian lensing bias involve high-dimensional integrals that are computationally challenging to evaluate. Therefore, for numerical evaluations, we consider only two bias contributions that can be evaluated in reasonable timescales. They arise from particular contractions denoted type A1 (Eq. (3.25)) which contributes to $\langle \delta T \delta T \delta TT \rangle$, and type C1 (Eq. (3.28)) which contributes to $\langle \delta^2 TT \delta TT \rangle$. Intuitively, we suspect that these two contributions to $N^{(3/2)}$ are among the largest contributions, because they have relatively simple, separable forms in Fourier space. For all other bias contributions we present analytical expressions but do not evaluate them numerically in the present work. Future work should check if these additional bias contributions are relevant, e.g., by performing the required numerical integrations or by comparing against estimates of the same non-Gaussian lensing bias from ray-traced N-body simulations.

2. While our analytical expressions can take arbitrary matter bispectrum models as their input, our numerical evaluations assume a simple matter bispectrum model that follows from leading-order Eulerian standard perturbation theory. While this is valid in the regime where only large-scale lensing modes contribute, more accurate results for the non-Gaussian lensing bias can be obtained by using more accurate matter bispectrum models on small scales. Our tests indicate that such corrections are likely small for Planck but significant for future CMB Stage-III or Stage-IV experiments.

3. Our analytical expressions follow by perturbing lensed CMB fluctuations in the lensing deflection angle. This perturbative expansion does not converge well on all scales, although corrections from nonperturbative approaches are typically less than 10%. Again, the accuracy of this approximation should be checked in the future.

4. Our calculation for the lensing potential bispectrum B_ϕ induced by non-linear structure formation assumes the flat sky approximation and Limber's projection. This is valid on intermediate and small scales, but breaks down on very large scales. We therefore restrict the discussion of the bias to multipoles $L \geq 100$. Although it would be interesting to extend our result to the full sky, we note that CMB experiments have most lensing information at multipoles $L \geq 100$.

Apart from testing each of the above assumptions in more detail, there are various other directions to extend and generalize our work in the future. For example, while we regard the non-Gaussianity of the lensing potential and the induced lensing power bias as a *nuisance*, it could equally well be regarded as a new *signal*. Pushing this further, one could envision other estimators to extract information from the non-Gaussianity of the lensing potential, e.g., by measuring the skewness or bispectrum of the reconstructed lensing potential, as investigated very recently by Namikawa [170]. We leave such exciting extensions to future studies. We also note that we have assumed the standard quadratic lensing estimator when deriving the $N^{(3/2)}$ bias. However, future polarization-sensitive experiments like CMB Stage-IV will benefit significantly from likelihood-based lensing estimators [91, 33] (c.p. Chapter 2); the impact of large-scale structure non-Gaussianity on these estimators should be considered.

More generally, accounting for the bispectrum and non-linearity of large-scale structure is just one of many possible extensions to refine theoretical modeling of CMB lensing. While leading-order modeling of CMB lensing is often rather accurate, the highly increased sensitivity of upcoming CMB Stage-III and Stage-IV experiments may require additional modeling corrections that should be investigated in the future.

While finalizing this work, Namikawa [170] pointed out that the CMB lensing bispectrum can also be regarded as a potential future signal from the CMB 6-point function rather than a bias of lensing 4-point measurements. While our papers are complementary in most parts, they both demonstrate the future importance of the non-Gaussianity of the CMB lensing potential. We checked that our theoretical CMB lensing bispectrum from leading-order standard perturbation theory agrees with [170].

Chapter 4

Bayesian 3D Density Reconstruction from Cosmic Shear

In this chapter, we turn to the analysis of a weak galaxy lensing, for which we propose and test a new Bayesian reconstruction algorithm. Given weak cosmic shear data, i.e. measured galaxy shapes, this algorithm returns an estimate of the 3-dimensional matter distribution between the galaxy sample and the observer. This chapter contains an updated and slightly adapted version of the corresponding publication [24].

4.1 Introduction

The inversion of the lens-equation, i.e. the inference of the matter distribution that causes the observed lensed galaxy shapes, is an ill-constrained problem and requires regularization. In Bayesian statistics this regularization is elegantly provided by the prior distribution, i.e. our best knowledge of the matter distribution prior to the lensing measurement. Previous studies have used a Gaussian prior for obtaining an estimate of the 3D matter density field [214, 222]. We aim to extend the work on tomographic lensing reconstructions by designing a fully Bayesian reconstruction algorithm that uses a lognormal prior on the density distribution.

   The algorithm is designed to reconstruct the 3D cosmic density fluctuation field $\delta(\mathbf{x}, \tau)$ from weak galaxy lensing data, i.e. a measurement of galaxy ellipticities at different (photometrically measured) redshifts. Its derivation is based on the language of information field theory [55] (c.p. Section 1.2), which has already been used to address similar tomography problems [64]. We do not make use of the flat-sky approximation i.e. lines of sight are allowed to be non-perpendicular to a fixed 3D coordinate grid. Further, we do not bin the data into pixels but take each galaxy into account as an individual contribution to the likelihood. This allows us to incorporate distance uncertainties of individual galaxies instead of sample redshift distributions.

   In contrast to a normal prior for the density field, as it has often been assumed before, a lognormal prior automatically enforces the strict positivity of the field and allows to

capture some of the non-Gaussian features that are imprinted on the density distribution by non-linear structure formation. Hubble was the first to notice that galaxy number counts could be well approximated by a lognormal distribution [103]. Characterizing the matter overdensities in the Universe as a lognormal field was first assessed by Coles & Jones in 1991 [42]. Subsequent studies showed that a logarithmic mapping of the non-linear matter distribution can partly re-Gaussianize the field, and that non-linear features in the matter power spectrum can be reproduced by a lognormal transformation of the linear matter power spectrum [172, 63]. A lognormal prior has already been used and shown to be superior to a Gaussian one in Bayesian algorithms that reconstruct the large-scale matter distribution from the observed galaxy distribution [55, 126, 108]. Lognormal distributions have also already been considered in the context of weak lensing: Analyses of ray-tracing simulations and the Dark Energy Survey (DES) Science Verification data showed that the 1-point distribution function of the lensing convergence is better described by a lognormal than a Gaussian model [225, 39]. Also the cosmic shear covariance can be modeled to better accuracy under the assumption that the underlying convergence field follows a lognormal distribution instead of a Gaussian one [84].

Bayesian inference methods are widely used in weak shear analyses, most prominently in the context of shear measurements from galaxy images [167, 19, 194]. Recently, notable effort has been put into developing a fully Bayesian analysis pipeline that propagates all uncertainties consistently from the raw image to the inferred cosmological parameters [4, 80].

This chapter is organized as follows: This introduction is followed by a short section, Sec. 4.2, in which we briefly introduce the notations and coordinate systems that will be used in the derivation of the formalism. Our lognormal prior model for the density is described in detail in Sec. 4.3. In Sec. 4.4, we present the data model, i.e. the lensing formalism that connects the data from a cosmic shear measurement to the underlying density field and give a brief overview over its implementation in Sec. 4.5. The maximum a posteriori estimator that is used to infer the matter distribution is introduced in Sec. 4.6 and extended to include redshift uncertainties of individual sources in Sec. 4.7. In Sec. 4.8, we show results of the density reconstruction on increasingly realistic mock data. We conclude this work with a summary and discussion in Sec. 3.7.

4.2 Coordinate Systems and notational Conventions

We work with three different types of coordinate systems. First, we use three-dimensional purely spatial comoving coordinates $\mathbf{x} = (x_0, x_1, x_2)$ at fixed comoving lookback time τ, that, combined with the time coordinate, form the four-dimensional coordinate system $(\mathbf{x}, \tau)$.

Second, we use a 3D comoving coordinate system on the light cone of an observer at the origin. Vectors on the light cone are marked by a prime, e.g. $\mathbf{x}'$. Since $\mathbf{x}'$-coordinates implicitly define a comoving lookback time $\tau(\mathbf{x}') = |\mathbf{x}'|/c$ (where c denotes the speed of light), we omit spelling out the time explicitly and write $A(\mathbf{x}') = A(\mathbf{x}', \tau)$ for any quantity

A that is defined on the light cone. The operation that links quantities on the light cone to their corresponding quantities in 4D space-time can be encoded in a projection operator with kernel

$$\mathcal{C}_{\mathbf{x}'(\mathbf{x},\tau)} = \delta_{\mathrm{D}}\left(\mathbf{x}' - \mathbf{x}\right)\delta_{\mathrm{D}}\left(\tau - |\mathbf{x}|/c\right). \tag{4.1}$$

Third, we employ a set of coordinate systems on the light cone, in which each system is orientated such that one axis points into the direction of a source galaxy. These line of sight coordinate systems are centered on the observer and spanned by the vectors $(\hat{\mathbf{r}}_0^i, \hat{\mathbf{r}}_1^i, \hat{\mathbf{r}}_2^i)$, where $\hat{\mathbf{r}}_0^i(\mathbf{x}')$ points into the direction of the ith source galaxy and the normal vectors $(\hat{\mathbf{r}}_1^i, \hat{\mathbf{r}}_2^i)$ span the two-dimensional plane perpendicular to $\hat{\mathbf{r}}_0^i$. The radial comoving distance of each galaxy from the observer is denoted $r^i = |\mathbf{r}^i| \equiv |\mathbf{r}_0^i|$. The transformation from the light cone system into the line of sight (LOS) system of a source galaxy i is achieved by a rotation of the x_0'-axis into the ith line of sight, while x_1' and x_2' get aligned with the image coordinates of the galaxy observation. We denote the corresponding transformation operators $\mathcal{R}^i{}_{\mathbf{rx}'}$.

4.3 Prior Model

The comoving density $\rho(\mathbf{x}, \tau)$ can be split into its time-independent spatial mean $\bar{\rho}$, and a perturbation $\delta\rho(\mathbf{x}, \tau) = \bar{\rho}\,\delta(\mathbf{x}, \tau)$. The fractional overdensity $\delta(\mathbf{x}, \tau)$ is commonly modeled as a homogeneous, isotropic Gaussian field with zero mean and power spectrum $P_\delta(k, \tau)$. This is an excellent description at early times where fluctuations are very small, as, e.g., shown by observations of the cosmic microwave background radiation (CMB). At linear level, valid for $\delta \ll 1$, the time evolution of the density field can be described by

$$\begin{aligned}
\rho(\mathbf{x}, \tau) &= \bar{\rho}\left[1 + \delta(\mathbf{x}, \tau)\right] \\
&= \bar{\rho}\left[1 + \int_{\mathbf{y}} D(|\mathbf{x} - \mathbf{y}|, \tau, \tau_0)\varphi(\mathbf{y}, \tau_0)\right] \\
&= \bar{\rho}\left[1 + D_{\mathbf{xy}}(\tau, \tau_0)\varphi_{\mathbf{y}}(\tau_0)\right].
\end{aligned} \tag{4.2}$$

In the last expression we have introduced the short-hand notation for integrals that we already used in the previous chapters: repeated indices are integrated over if they do not appear on both sides of the equation. In Eq. (4.2), $D(|\mathbf{x} - \mathbf{y}|, \tau, \tau_0)$ is the integration kernel of a linear homogeneous and isotropic, but possibly scale-dependent, growth operator. The field φ is an isotropic and homogeneous random field whose values are drawn from a multivariate normal distribution with mean $\bar{\varphi}$ and covariance Φ,

$$\varphi \hookleftarrow \mathcal{G}(\varphi|\bar{\varphi}, \Phi). \tag{4.3}$$

Here, it describes the three dimensional density fluctuations at time τ_0 and is translated to other times τ by the growth operation $D_{\mathbf{xy}}(\tau, \tau_0)$. This implies $\bar{\varphi} = 0$ for this linear Gaussian model.

The description Eq. (4.2) breaks down when $\delta \not\ll 1$ such that non-linearities become important. A possible way to account for non-linearities is to include higher-order terms

from a perturbation series expansion of the full non-linear evolution equations. However, a further shortcoming of the model (4.2) is that it allows arbitrarily negative density contrasts, which physically can not be smaller than -1. To obtain a strictly positive density field, we instead modify Eq. (4.2) by an exponential:

$$\rho(\mathbf{x}, \tau) = \bar{\rho} \left[1 + \delta(\mathbf{x}, \tau) \right] = \bar{\rho} \exp \left[D_{\mathbf{xy}}(\tau, \tau_0) \varphi_{\mathbf{y}}(\tau_0) \right]. \tag{4.4}$$

Since the expectation value of the density $\rho(\mathbf{x}, \tau)$ must equal $\bar{\rho}$, the mean of φ must be set to

$$\bar{\varphi}_{\mathbf{x}}(\tau) = -\frac{1}{2} D_{\mathbf{xy}}^{-1}(\tau, \tau_0) \left[D(\tau, \tau_0) \Phi(\tau_0) D(\tau, \tau_0) \right]_{\mathbf{yy}}, \tag{4.5}$$

for every time τ. Note that we integrate over the index $\mathbf{y}$ in this expression, i.e. the diagonal of the composite operator in square brackets is treated as a field.

For a local growth operator, $D_{\mathbf{xy}}(\tau, \tau_0) = D(\tau, \tau_0) \delta_{\mathrm{D}}(\mathbf{x} - \mathbf{y})$, this mean correction simplifies to

$$\bar{\varphi}_{\mathbf{x}}(\tau) = -\frac{1}{2} D(\tau, \tau_0) \hat{\Phi}_{\mathbf{x}}(\tau_0), \tag{4.6}$$

where we defined $\hat{\Phi}_{\mathbf{x}}(\tau_0) \equiv \Phi_{\mathbf{xx}}(\tau_0)$.

The Gaussian field φ and the growth operator D can be related to known quantities. To see this, consider the expansion of the Fourier modes of δ in Eulerian perturbation theory (see e.g. [17]),

$$\delta(\mathbf{k}, \tau) = \sum_{n=1} D^{(n)}(\tau) \delta^{(n)}(\mathbf{k}), \tag{4.7}$$

where $\delta^{(n)}$ are convolutions of n initial fields $\delta(\mathbf{k}, \tau_0)$ with an integration kernel that changes from order to order. The first term in this series is $D^{(1)}(\tau)/D^{(1)}(\tau_0) \delta_0(\mathbf{k}, \tau_0)$, where $D^{(1)}(\tau)$ is the growing solution to the linearized growth equation [148] (c.p. Section 1.3.2).

We use this analogy to motivate the simplest possible form of the growth operation in the lognormal model and write

$$D_{\mathbf{xy}}(\tau) = \delta_{\mathrm{D}}(\mathbf{x} - \mathbf{y}) D^{(1)}(\tau) \tag{4.8}$$

where we have set $D^{(1)}(\tau_0) = 1$. This approximation erases any a-priori assumption of scale-dependent growth and mode-coupling of the log field φ. Such a simplification is viable since the model in Eq. (4.8) describes only our prior assumptions about the density field ρ. The algorithm will find the most probable realization of φ for a fixed growth operator D given the data. If a scale-dependence is favored by the data, it will be recovered, at least partially, in the estimate of φ.

Our algorithm also allows to incorporate a more general growth operation at the expense of computation time and memory usage. The application of the most general $D_{\mathbf{xy}}(\tau)$ generates a four-dimensional field: three-dimensional spatial comoving volumes for every time-slice τ. This very large volume is then restricted to a three-dimensional cut by application of the light cone operator defined in Eq. (4.1). The prior model for the matter overdensity on the light cone then becomes

$$\delta_{\mathbf{x}'} = \mathcal{C}_{\mathbf{x}'(\mathbf{x}, \tau)} \exp \left[D_{\mathbf{xy}}(\tau) \varphi_{\mathbf{y}}(\tau) \right] - 1. \tag{4.9}$$

Applying a complicated, non-diagonal growth operation on all time slices separately before constructing the light cone is numerically not feasable in the current implementation if one wants to resolve a sufficiently large observational volume down to the mildly non-linear scales.

The simplest form of D, Eq. (4.8), that depends only on time can be applied to the light cone directly

$$\delta_{\mathbf{x}'} = \exp\left[D_{\mathbf{x}'\mathbf{y}'}\varphi_{\mathbf{y}'}\right] - 1. \tag{4.10}$$

For this work, we use the growth operator in Eq. (4.8) with the usual linear growth factor and leave extension of this model to future work.

4.4 Data Model

In this section we establish the analytic relation between the signal field φ, the field of overdensities δ that we aim to reconstruct, and the data that is obtained from a weak lensing measurement.

Weak galaxy lensing surveys produce galaxy image ellipticities that can be quantified, e.g., by a complex number $\epsilon = \epsilon_1 + i\epsilon_2$. For an ellipse with major axis a, minor axis b, and position angle η (relative to the x-axis of the chosen coordinate grid), ϵ is defined as

$$\epsilon = (a - b)/(a + b)\exp(2\mathrm{i}\eta). \tag{4.11}$$

We use the common approximation that the components of the intrinsic source galaxy ellipticity $\boldsymbol{\epsilon}^{\mathrm{s}} = (\epsilon_1^{\mathrm{s}}, \epsilon_2^{\mathrm{s}})$, which define the shape that would be observed in the absence of lensing[1], follow a global bivariate Gaussian distribution with zero mean and variance σ_ϵ^2 per component:

$$\boldsymbol{\epsilon}^{\mathrm{s}} \hookleftarrow \mathcal{G}(\boldsymbol{\epsilon}^{\mathrm{s}}|\,0, N^{\mathrm{s}}), \qquad N_{ij}^{\mathrm{s}} = \delta_{ij}\sigma_\epsilon^2. \tag{4.12}$$

This approximation has shortcomings (see e.g. [166]), but serves for the proof of our concept, since we create the mock data on which we test the algorithm with exactly this shape noise model. In the future, more elaborated (Bayesian hierarchical) shear estimators, that, e.g., take into account galaxy properties, can be incorporated into the algorithm [167, 194, 19].

Lensing distorts the galaxy images in shape and size. If the distortion is small, i.e. in the limit of weak lensing, the relation between intrinsic source ellipticity and observed ellipticity can be linearized and simplifies to [200]

$$\epsilon = g + \epsilon^{\mathrm{s}}, \tag{4.13}$$

where g is the reduced shear. The reduced shear combines the effect of anisotropic lensing distortions, encoded in the shear $\gamma = \gamma_1 + i\gamma_2$, and the isotropic distortion, encoded in the convergence κ

$$g = \frac{\gamma}{1 - \kappa} \approx \gamma. \tag{4.14}$$

---

[1]We use vector notation, e.g. $\boldsymbol{\epsilon}$, to denote the tuple of real and imaginary part (ϵ_1, ϵ_2) of a complex number $\epsilon = \epsilon_1 + i\epsilon_2$.

If $\kappa \ll 1$, which is often the case for galaxy lensing, the reduced shear can be approximated by the shear itself $g \approx \gamma$.

The shear and convergence at angular position $\boldsymbol{\theta}$ are related to the lensing potential ϕ by

$$\gamma_1(\boldsymbol{\theta}) = \frac{1}{2}\left(\partial_1^2 - \partial_2^2\right)\phi(\boldsymbol{\theta}); \qquad \gamma_2(\boldsymbol{\theta}) = \partial_1\partial_2\phi(\boldsymbol{\theta}); \qquad \kappa(\boldsymbol{\theta}) = \frac{1}{2}(\partial_1^2 + \partial_2^2)\phi(\boldsymbol{\theta}). \qquad (4.15)$$

Using the Born approximation, that is assuming that the lensing deflections can be summed along the unperturbed photon geodesic, the lensing potential can be written as a weighted projection of the peculiar Newtonian gravitational potential ψ along the line of sight. For a source at LOS distance r^i, this integration reads

$$\phi(\boldsymbol{\theta}) = \frac{2}{c^2} \int_0^{r^i} \mathrm{d}r \, \frac{r^i - r}{rr^i} \psi(r, r\theta_1, r\theta_2), \qquad (4.16)$$

where we have assumed a spatially flat Universe. Applying the angular derivatives in Eq. (4.15) to the expression for the lensing potential in Eq. (4.16), we get

$$\partial_k\partial_l\phi(\boldsymbol{\theta}) = \frac{2}{c^2} \int_0^{r^i} \mathrm{d}r \, W(r; r^i)\partial_{r_k}\partial_{r_l}\psi\left(r, r\theta_1, r\theta_2\right), \qquad (4.17)$$

where $k, l \in (1, 2)$, and the lensing efficiency

$$W(r; r^i) = \frac{r(r^i - r)}{r^i}. \qquad (4.18)$$

In practice the distance to the source r^i cannot be determined directly but follows from the photometrically measured redshift z^i. Photometrically measured redshifts are associated with a relatively high error, $\sigma_z/(1 + z) \approx 0.03 - 0.06$ [86]. In its most simple form the algorithm ignores this uncertainty. We will use this simplified model to validate the functionality of the algorithm in terms of reconstructing non-linear structures in the lognormal approximation. Redshift uncertainties will be included later in Section 4.7.

The lensing shear is completely determined by the second derivatives of the lensing potential perpendicular to the LOS. The tidal tensor $\partial_{r_k}\partial_{r_l}\phi(\mathbf{r})$ along the LOS of the ith source galaxy is obtained by rotating the tidal tensor on the global coordinate grid $\mathbf{x}'$

$$T_{ij}(\mathbf{x}') = \partial_{x'_i}\partial_{x'_j}\psi(\mathbf{x}'), \qquad i, j \in (0, 1, 2), \qquad (4.19)$$

into the specific coordinate system (with coordinates $\mathbf{r}^i$) that points into the direction of this ith galaxy and projecting it onto the $(r_1^i - r_2^i)$-plane perpendicular to the LOS.

The last relation required to connect the data to the density fluctuations is Poisson's equation. It relates the potential $\phi(\mathbf{x}')$ to the density fluctuations $\delta(\mathbf{x}')$,

$$\nabla^2\psi(\mathbf{x}') = \frac{3}{2}\Omega_\mathrm{m}H_0^2\frac{\delta(\mathbf{x}')}{a(|\mathbf{x}'|/\mathrm{c})}, \qquad (4.20)$$

where H_0 denotes the Hubble constant (parametrized by $h = H_0/(100\,\mathrm{km\,s^{-1}Mpc^{-1}})$ in our test simulations), and $a(|\mathbf{x}'|/\mathrm{c}) = a(\tau)$ denotes the scale factor at the time τ corresponding to LOS distance $r^i(x')$.

4.5   Implementation

The implementation, not only of the data model, but of the entire algorithm, is based on NIFTy [201], a versatile software package for the development of inference algorithms. We further compute cosmology-dependent quantities, like power spectra and distance-redshift relations, with the publicly available CLASS code[2] [23]. To summarize the data model we introduce short-hand notations for each operation in terms of operators.

In its most general form, the prior and data model, that connect the Gaussian field φ with a data vector of N_s measured source ellipticities, are as follows: The growth operator $D_{\mathbf{xy}}(\tau)$ imprints a growth structure on the Gaussian field. The resulting four-dimensional field is plugged into the exponential of $E(\cdot) = \exp(\cdot) - 1$ [see Eq. (4.4)] to obtain the fractional overdensity $\delta_{\mathbf{x}}(\tau)$. The overdensity induces the potential $\psi_{\mathbf{y}}(\tau)$ by the Poisson equation, that we encode in the operator $\mathcal{P}_{\mathbf{yx}}(\tau) \equiv \Delta^{-1}3/2\Omega_\mathrm{m}H_0^2/a(|\mathbf{x}|/\mathrm{c})$ [Eq. (4.20)] and which can be solved efficiently in Fourier space. The resulting gravitational potential is restricted to the light cone of the observer by the light cone operator $\mathcal{C}_{\mathbf{y}'(\mathbf{y},\tau)}$ [Eq. (4.1)]. We compute the tidal tensor on the light cone [(Eq. (4.19)] by application of a global differentiation operator, which we denote $\mathcal{T}_{\mathbf{z}'\mathbf{y}'}$. The tidal tensor is then rotated into each galaxy's LOS coordinate system by a rotation operator, $\mathcal{R}^i_{\mathbf{rz}'}$. An integration operator $\mathcal{I}_{j\mathbf{r}}$, which applies the integration in Eq. (4.17), integrates the components of each of the resulting N_s tidal tensors along the unperturbed photon geodesic. For this operator, we use an adapted version of the implementation that was already successfully applied in a similar reconstruction method [64]. The application of $\mathcal{I}_{j\mathbf{r}}$ yields derivatives of the lensing potential for each galaxy location. From this we can compute the shear components by a linear operator $\mathcal{L}_{ij}$ that comprises the equations in Eq. (4.15). Rotation and integration map the three dimensional continuous signal space into the discrete space (two shear components for every galaxy) of the data. The shear components are thus automatically computed at the locations of the galaxies.

In the simplified implementation that we use for this work, we avoid the 4D coordinate grid $(\mathbf{x}, \tau)$ and work on the three-dimensional light cone from the beginning. In the prior, we model the Gaussian log-density φ with the power spectrum of matter fluctuations today $P_\mathrm{lin}(k, a{=}1)$, where a denotes the scale factor. The growth operator is diagonal in configuration space and only a function of comoving distance to the observer $D_{\mathbf{x}'\mathbf{y}'} = D^{(1)}(\tau)\delta_\mathrm{D}(\mathbf{x}' - \mathbf{y}')$, where $D^{(1)}(\tau)$ is the growing solution of the linearized growth equation. The Poisson operator is split into two parts. First, a multiplication with $3/2\,\Omega_\mathrm{m}H_0^2/a(|\mathbf{x}'|/\mathrm{c})$, i.e. an operation that is diagonal in configuration space. Second, the inverse Laplace operation Δ^{-1}, which is diagonal in Fourier space. The inverse Laplacian in the Poisson equation is a non-local operation that should strictly be applied to 3D

---

[2]http://class-code.net/

spatial volumes at fixed time. Here, we apply it on the light cone noting that the induced error in radial direction should be small (roughly of order a^2) if we apply the first part of the Poisson operator first and if $D^{(1)}(\tau)$ is approximately proportional to the scale factor. In this case, the first order term of the exponential expression

$$\exp\left(D_{\mathbf{x'y'}}\varphi_{\mathbf{y'}}\right) - 1 = D_{\mathbf{x'y'}}\varphi_{\mathbf{y'}} + \mathcal{O}(\varphi^2) \approx a(|\mathbf{x'}|)\delta_{\mathrm{D}}(\mathbf{x'} - \mathbf{y'})\varphi_{\mathbf{y'}} + \mathcal{O}(\varphi^2), \qquad (4.21)$$

and therefore the first order time dependence of the overdensity field will partly be canceled by the $1/a$ in the Poisson equation before the inverse Laplacian rescales the field. This cancellation corresponds to the commonly known fact that the comoving gravitational potential is constant in a matter dominated Universe.

After computing the six independent entries of the tidal shear tensor, we integrate each of its components along the LOS. Only after the integration we rotate the resulting tensors into their LOS coordinate systems and project out all entries which are not in the plane perpendicular to $\mathbf{r}$. This change of order allows to efficiently combine three operations, which are 1) the rotation into the LOS, 2) projecting out non-perpendicular components of the tidal tensor, and 3) the computation of shear components and convergence, in a single linear operation. We denote the corresponding operator $\mathcal{G}$ (Gamma-Projection-Rotation).

For one data point the implemented data model in operator notation reads

$$d_i = \boldsymbol{\epsilon}_i = [R(\varphi)]_i + \boldsymbol{\epsilon}_i^{\mathrm{s}} + \mathbf{n}_i = \mathcal{G}_{ij}\mathcal{I}_{j\mathbf{r'}}\mathcal{T}_{\mathbf{r'z'}}\mathcal{P}_{\mathbf{z'y'}}\left[\exp\left(D_{\mathbf{y'x'}}\varphi_{\mathbf{x'}}\right) - 1_{\mathbf{y'}}\right] + \boldsymbol{\epsilon}_i^{\mathrm{s}} + \mathbf{n}_i. \qquad (4.22)$$

The total data vector d has dimensions $2 \times N_s$, i.e. two ellipticity components for each of the N_s source galaxies. We use the letter R to encode the total response of the data to a signal φ, i.e. the composite action of all operators. We have also added an experimental noise $\mathbf{n}$ here for completeness. In general this will be subdominant to the shape noise $\boldsymbol{\epsilon}^{\mathrm{s}}$ and we ignore it in the following. Note, however, that the formalism allows for an incorporation of several independent noise sources.

4.6   MAP Estimator

Our aim is to obtain a maximum a posteriori (MAP) estimate of the signal field φ. The posterior distribution is related to the likelihood and the prior by Bayes' theorem (c.p. Section 1.1)

$$P(\varphi|d) = \frac{P(d|\varphi)P(\varphi)}{P(d)}. \qquad (4.23)$$

The prior probability $P(\varphi)$ is modeled as a Gaussian distribution with covariance Φ. In a first simple approximation Φ can be taken to be diagonal in Fourier space with the usual power spectrum of matter overdensities $P_\delta^{\mathrm{lin}}(k, a)$.

To obtain the likelihood, we marginalize over all realizations of the shape noise

$$P(d|\varphi) = \int \mathcal{D}\boldsymbol{\epsilon}^{\mathrm{s}}\, P\left(d|\varphi, \boldsymbol{\epsilon}^{\mathrm{s}}\right) P\left(\boldsymbol{\epsilon}^{\mathrm{s}}\right) = \mathcal{G}\left[d|R(\varphi), N\right], \qquad (4.24)$$

where the covariance N of the shape noise was defined in Eq. (4.12) and we neglect any other sources of measurement noise. With this, the negative log-posterior becomes

$$- \ln P(\varphi|d) \,\hat{=}\, \frac{1}{2} \left[d - R(\varphi)\right]^\dagger N^{-1} \left[d - R(\varphi)\right] + \frac{1}{2} \left(\varphi - \bar{\varphi}\right)^\dagger \Phi^{-1} \left(\varphi - \bar{\varphi}\right), \tag{4.25}$$

where we have dropped most terms that are independent of the field of interest, φ.

The maximum of the posterior distribution is found by minimizing the expression in Eq. (4.25). Note that the posterior distribution is not Gaussian. Due to the exponential in the response R it is not quadratic in φ. To find the minimum of the negative log-posterior we apply a Newton-like minimization scheme [28]. This requires the derivative of the negative log-posterior with respect to φ

$$- \frac{\delta \ln P(\varphi|d)}{\delta \varphi_\mathbf{u}} = \left[d - R(\varphi)\right]_i N_{ij}^{-1} \mathcal{G}_{jk} \mathcal{I}_{k\mathbf{r'}} \mathcal{T}_{\mathbf{r'z'}} \mathcal{P}_{\mathbf{z'y'}} \left[\exp(D_{\mathbf{y'x'}}\varphi_{\mathbf{x'}}) \cdot D_{\mathbf{y'u}}\right]$$
$$+ \Phi_{\mathbf{uq}}^{-1} \left(\varphi - \bar{\varphi}\right)_\mathbf{q}, \tag{4.26}$$

where the dot denotes a point-wise product in position space, i.e. $(\alpha \cdot \beta)_\mathbf{x} = \alpha_\mathbf{x}\beta_\mathbf{x}$.

4.7 Redshift-marginalized Likelihood and Posterior

We can take into account the source redshift uncertainty by generalizing the marginalized likelihood in Eq. (4.24) to include the probability of the source redshifts z_s given their measured photometric redshifts z_photo. This probability is given by the posterior redshift distribution function $P(z^s|z_\mathrm{photo})$, where z^s and z_photo are vectors of the redshifts of all sources. Including this redshift posterior in the likelidood yields,

$$P(d|\varphi) = \int \mathcal{D}\boldsymbol{\epsilon}^\mathrm{s} \int \mathcal{D}z^s \, P(d|\varphi, \boldsymbol{\epsilon}^\mathrm{s}, z^s) P(\boldsymbol{\epsilon}^\mathrm{s}) P(z^s|z_\mathrm{photo})$$
$$= \int \mathcal{D}z^s \, \mathcal{G}[d|R^{z^s}(\varphi), N] P(z^s|z_\mathrm{photo}). \tag{4.27}$$

In most cases, this integration cannot be done analytically and the resulting distribution will in general not be Gaussian. Here, we restrict the analysis to a Gaussian approximation of the marginalized likelihood, that we characterize by the first and second central moment of the full distribution.

To obtain them, we need to calculate $\langle d \rangle_{P(d|\varphi)}$ and $\langle dd^\dagger \rangle_{P(d|\varphi)}$. For the expectation

value of the data, we obtain

$$
\langle d \rangle_{P(d|\varphi)} = \int \mathcal{D}z^s \int \mathcal{D}d \, d \, \mathcal{G}[d|R^{z^s}(\varphi), N] \, P(z^s|z_{\text{photo}})
$$

$$
= \int \mathcal{D}z^s \, R^{z^s}(\varphi) \, P(z^s|z_{\text{photo}})
$$

$$
\langle d_i \rangle_{P(d|\varphi)} = \mathcal{G}_{ij} \left[\int dz^s \, P(z^s|z_{\text{photo}}) \mathcal{I}_{j\mathbf{r}}^{z^s} \right] \bar{R}(\varphi)_{\mathbf{r}} \tag{4.28}
$$

$$
= \mathcal{G}_{ij} \left[\int_0^\infty dr \int_r^\infty dr^j \, W(r, r^j) P(z_j^s|z_{\text{photo}_j}) \frac{dz_j^s}{dr^j} \right] \bar{R}(\varphi)_{\mathbf{r}}
$$

$$
\equiv \left[\mathcal{G}\bar{\mathcal{I}}\bar{R} \right](\varphi)_i \equiv \tilde{R}(\varphi)_i, \tag{4.29}
$$

where $\bar{I}$ denotes the redshift averaged integration operator defined in the square brackets in the first line of Eq. (4.29) and we have introduced $\bar{R}(\cdot) \equiv \mathcal{TP}\left(\exp\left[D(\cdot)\right] - 1\right)$ to summarize the action of all source-redshift independent operators.

The second moment is

$$
\langle dd^\dagger \rangle_{P(d|\varphi)} = N + \langle (R(\varphi))(R(\varphi))^\dagger \rangle_{P(z|z_{\text{ph}})}. \tag{4.30}
$$

Non-diagonal elements of the second term in Eq. (4.30) read

$$
\langle ((R(\varphi))_i (R(\varphi))_j) \rangle_{P(z|z_{\text{ph}})} = \langle (R(\varphi))_i \rangle_{P(z|z_{\text{ph}})} \langle (R(\varphi))_j \rangle_{P(z|z_{\text{ph}})} = (\tilde{R}\varphi)_i (\tilde{R}\varphi)_j \tag{4.31}
$$

and diagonal elements are

$$
\langle (R(\varphi))_i (R(\varphi))_i \rangle_{P(z|z_{\text{ph}})} =
$$

$$
\mathcal{G}_{ij}\mathcal{G}_{ij} \left[\int_0^\infty dr \int_0^\infty dr' \int_{\max(r,r')}^\infty dr^j \, W(r, r^j) W(r', r^j) P(z_j^s|z_{\text{photo}_j}) \frac{dz^j}{dr^j} \right] \bar{R}(\varphi)_{\mathbf{r}} \, \bar{R}(\varphi)_{\mathbf{r}'}
$$

$$
\equiv \mathcal{G}_{ij}\mathcal{G}_{ij}\tilde{\mathcal{I}}_{j\mathbf{r},\mathbf{r}'} \bar{R}(\varphi)_{\mathbf{r}} \, \bar{R}(\varphi)_{\mathbf{r}'}, \tag{4.32}
$$

where the new operator $\tilde{\mathcal{I}}$ denotes the squared average of the integration operator, i.e. the square brackets in the first line of Eq. (4.32).

The Gaussian approximation to the likelihood is then $\mathcal{G}[d|\tilde{R}(\varphi), \tilde{N}]$, where $\tilde{N} = N + Q$ and Q is

$$
Q = \langle (R(\varphi))_i (R(\varphi))_j \rangle_{P(z|z_{\text{ph}})} - \langle (\tilde{R}\varphi)_i \rangle_{P(z|z_{\text{ph}})} \langle (\tilde{R}\varphi)_j \rangle_{P(z|z_{\text{ph}})}
$$

$$
= \langle (R(\varphi))_i (R(\varphi))_i \rangle_{P(z|z_{\text{ph}})} - (\tilde{R}\varphi)_i (\tilde{R}\varphi)_i. \tag{4.33}
$$

This expression is still signal-dependent and we approximate it further by replacing φ by its posterior mean $\langle \varphi \rangle_{P(\varphi|d)}$. Since this mean depends on $\tilde{N}$, the resulting set of equations must be solved iteratively.

4.8   Validation and Tests

To validate the implementation and assess the goodness of the tomographic reconstruction, we perform a number of increasingly realistic tests, which we denote tests A, B and C. In tests of type A we employ a homogeneous source distribution over the entire box. These tests are the least realistic ones and serve to validate the correctness of the implementation. Test B uses a realistic source distribution and test C adds realistic shape noise.

In all of these tests, we place the observer in the center of the bottom of the computational box[3] and resolve the underlying and reconstructed overdensity fields with 128^3 pixels. Depending on the test, we allow the physical sizes of the box to differ. The current pixel resolution is limited due to computation time and memory usage. A higher resolution will be accessible after parallelization and adaption of the code for the usage on a high-performance cluster.

The minimization is achieved through 300 steps of an LBFGS algorithm [28] followed by a steepest descent algorithm. The latter is set to have reached convergence if the maximal pixelwise relative difference between two subsequent field estimates is smaller than 10^{-4} for three iteration in a row. If the steepest descent does not converge within 200 iterations, the same combination of LBFGS and steepest descent minimizers is started once more. We find that, at latest in this second run, all of our example reconstructions meet the convergence criterium. In the current serial implementation, the entire minimization takes between 1 day (for idealized tests at fixed redshifts) and 6 days (for a realistic source distribution and shape noise) on a single processor with 2.6 Ghz.[4]

Most of the tests are based on mock data that we create by applying the data model described in Sec. 4.4 to non-linear density fields obtained from N-body simulations. For tests at fixed redshifts we use snapshots of the Millennium-XXL simulation [9] from which we take the entire volume of size $[3h^{-1}\,\mathrm{Gpc}]^3$ and smooth the density fields to fit the desired resolution of 128^3 pixels. For more realistic test cases we construct a light cone of size $[500h^{-1}\,\mathrm{Mpc}, 500h^{-1}\,\mathrm{Mpc}, 4000h^{-1}\,\mathrm{Mpc}]$ by joining snapshots of the Millennium Run [219]. The Millennium box measures $500h^{-1}\,\mathrm{Mpc}$ along each side and we shift it every time $500h^{-1}\,\mathrm{Mpc}$ in the z-direction have been constructed. This procedure ensures that a LOS is unlikely to hit the same structure repeatedly. In the resulting light cone we achieve a resolution of $3.9h^{-1}\,\mathrm{Mpc}$ in the x- and y-directions corresponding to mildly non-linear scales and reach a redshift of $z = 2.2$ in the z-direction. Since we use 128^3 pixel to resolve the light cone box, the physical size of the pixels is longer along the z-axis, meaning that we obtain a poorer resolution in this direction.

Both the Millennium-XXL and the Millennium simulation use a flat ΛCDM cosmology

---

[3]This position is not fixed by the algorithm. For a reconstruction from a survey that covers a significant fraction of the sky, the observer can be placed in the center of the box, for example.

[4]Due to small but necessary corrections to the code, we had to rerun the last test less than 6 days before the hand-in date. Because of this time-constraint the minimization in the test of type C, which is shown here, was truncated after only 100 LBFGS and 20 stepest descent iterations. By the time of hand-in, another 100+20 steps had been completed but the result seemed to be affected by strong numerical instabilities. The reason for these instabilities has to be investigated in the future.

with $\Omega_{\mathrm{m}} = 0.25$ and $h = 0.73$.

4.8.1   Tests A: Simple Geometry

In this series of tests we distribute 500 000 sources evenly in the box and slightly beyond ($\pm 100 h^{-1}\,\mathrm{Mpc}$). We place sources outside of the reconstructed volume in order to increase the area in which we can recover the underlying density field with high resolution. The quality of the reconstruction decreases with increasing distance to the observer because of increasing distances between lines of sight and a decreasing number of background sources that help to break the LOS degeneracy of the lensing kernel. We further only add unphysically low, negligible shape noise in this first test set.

We perform three different tests of type A for which we create data from increasingly realistic input fields:

1) A self-consistency test, where we create an overdensity field from a random realization of the Gaussian field φ [Eq. (4.3)] in a cubic box of side length $1000 h^{-1}\,\mathrm{Mpc}$. We then apply the implemented data model and use the algorithm to recover this input field. We do not show any results from this test, since they would not provide any additional insights compared to tests A2 and A3, but simply state that we can recover the input field with high fidelity which means that the implementation is in itself consistent.

2) A test in which we create shears from overdensity fields taken from an N-body simulation at fixed redshifts. We use three different snapshots at individual redshifts $z = 1$, $z = 0.25$ and $z = 0$. This allows to assess the algorithm's ability to recover increasingly non-linear fields. In each case, we compare the lognormal reconstruction to a Wiener filter (WF) reconstruction, which uses the same data model and source distribution but a Gaussian prior on the overdensity field δ. Comparisons between input and reconstructed fields in each case are shown in Fig. 4.1. The resolution of the reconstruction decreases with distance to the observer. This is because 1) the density of lines of sight decreases 2) there are less sources behind the point we want to reconstruct 3) the information from these sources is suppressed by the shape of the integration kernel. In all cases, the lognormal reconstruction is superior in capturing the highest values of the density field and avoids unphysically low density contrasts below -1. Table 4.1 summarizes pixelwise quadratic differences and the pixel-wise Pearson correlation between underlying and reconstructed fields. In Table 4.2 we compare the minimal and maximal values in the reconstructions to the extremal values in the true density field. For all redshifts tested the lognormal prior yields higher correlations with the original field than the Gaussian prior. It also better reconstructs the maximal values. The difference between lognormal and WF reconstruction increases as the input field becomes more non-linear. This is also reflected in the 1-point probability distribution functions (PDFs), which we show in Fig. 4.2. While the Wiener Filter PDF is closer to symmetric in all cases, we can capture more of the skewness of the input field by applying the lognormal prior. An notable feature of the 1-point PDFs is that the maximum value is slightly biased in both reconstructions. The distributions of the reconstructions peak at zero, i.e. at their mean, while the underlying field peaks below. This is a feature of both priors since they prefer the mean density (or a zero density

contrast) if the data does not contain enough information on the density.

redshifts	$\langle(\hat{\delta}-\delta)^2\rangle/\sigma_\delta^2$		$\sqrt{\langle\hat{\delta}\delta\rangle/(\sigma_\delta\sigma_{\hat{\delta}})}$	
	lognormal	WF	lognormal	WF
1.	0.66	0.69	0.58	0.56
0.25	0.73	0.77	0.52	0.49
0.0	0.73	0.77	0.53	0.48
light cone	0.65	0.73	0.61	0.51

Table 4.1: Quantitative comparison of reconstruction methods for tests A2 and A3. We compare the lognormal to the Gaussian prior in terms of the mean square pixel-wise difference (first column) and the Pearson-correlation coefficient (second column) between the reconstruction and the underlying field (which we denote $\hat{\delta}$ and δ, respectively).

redshifts	$\max(\hat{\delta})$, $\max(\delta)$			$\min(\hat{\delta})$, $\min(\delta)$		
	lognormal	WF	N-body	lognormal	WF	N-body
1.	4.22	2.95	4.92	-0.63	-0.91	-0.79
0.25	7.38	5.00	8.49	-0.77	-1.28	-0.87
0.0	8.32	5.55	10.26	-0.99	-1.57	-0.89
light cone	32.90	20.81	70.20	-0.98	-4.28	-0.92

Table 4.2: Quantitative comparison of reconstruction methods for tests A2 and A3. We compare the minimal and maximal values of the underlying and reconstructed fields (δ and $\hat{\delta}$, respectively).

3) A test similar to A2 but with a redshift dependent density field constructed from different snapshots. The physical size of the box spans $[500h^{-1}\,\mathrm{Mpc}]^2$ in the $(x-y)$-plane and $4000h^{-1}\,\mathrm{Mpc}$ into the z-direction corresponding to a maximum redshift of $z = 2.2$.[5] Results of test A3 are shown in Fig. 4.3 and Fig. 4.4. The quantitative comparison between the lognormal and the corresponding WF run is listed in the last rows of Tables 4.1 and 4.2, labeled "light cone". We find a similar match between the underlying and reconstructed fields as in tests A2 and again a superiority of the lognormal prior over the Wiener Filter reconstruction in terms of correlation coefficients, pixel-wise differences and extremal values. The distributions of the pixel-wise matching between input and reconstructions in the upper panel of Fig. 4.4 imply that the lognormal prior is more likely to reconstruct

---

[5]The light cone is constructed by merging planes from different snapshots along the z-direction of the box, but the algorithm assumes that the distance and redshift increase in radial direction from the observer. This leads to a mismatch between the distance to a (source) position assumed by the algorithm and the distance or rather redshift that this position corresponds to in the simulation. The distance in the simulation is $\cos\theta$ times the distance assumed by the algorithm, where θ is the angle between the LOS and the z-axis. This mismatch should only become relevant for relatively large angles $\theta > \pi/2$. Lines of sight with such angles only cover a minor fraction of the box and we therefore expect the test to not be severely affected by this approximation.

$$-1 \qquad \ln[1+\delta] \qquad 1$$
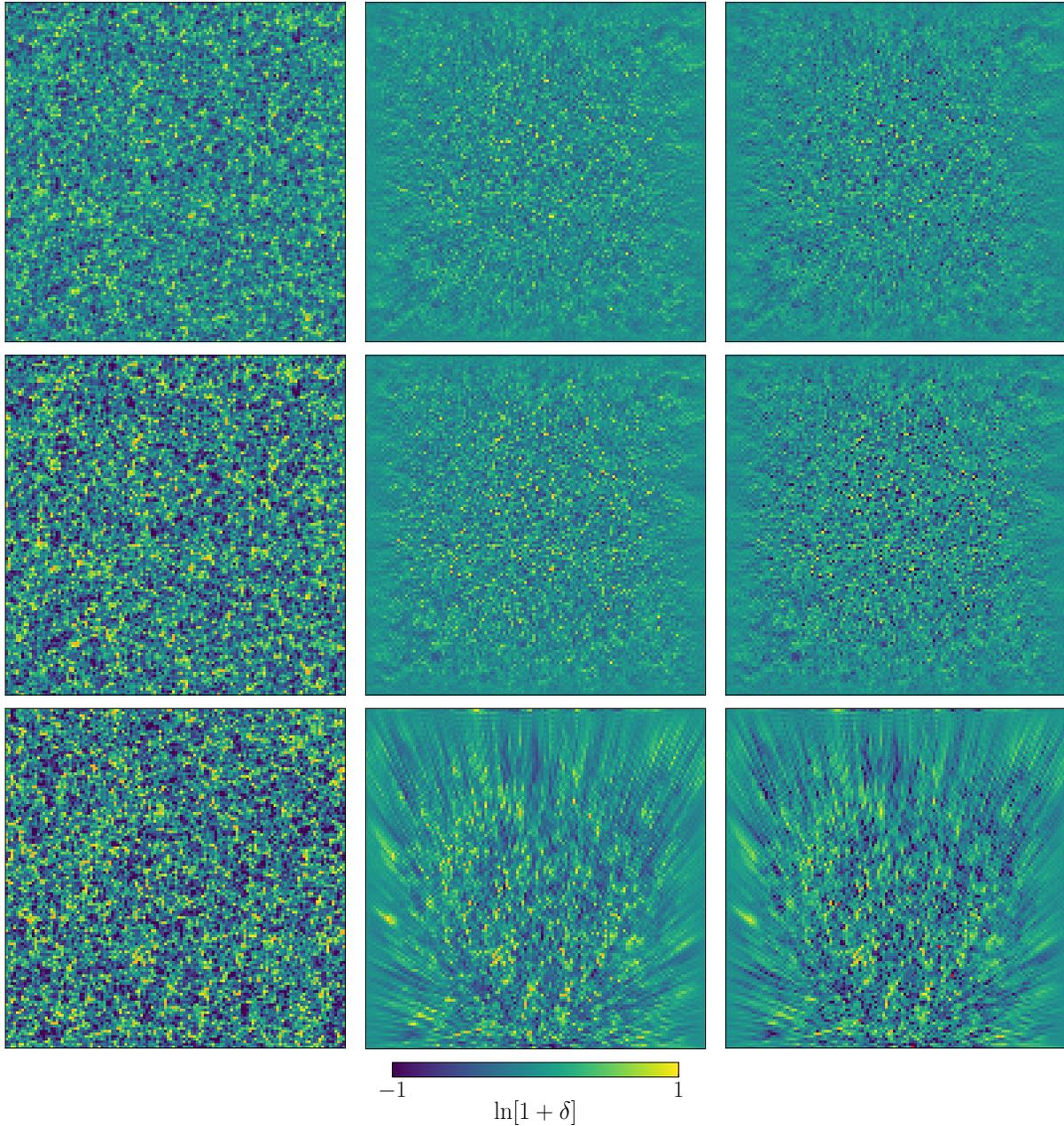
Figure 4.1: Qualitative comparison of reconstruction methods in the test series A2, for which we create mock data from individual simulation snapshots, apply a homogeneous source distribution and add negligible shape noise. We show central slices through the 3-dimensional fields. The observer is located in the center of the $(x-y)$-plane at the origin of the z-axis. The redshift of the snapshot decreases from top to bottom, $z = [1, 0.25, 0.]$. In the two upper rows we show the $(x-y)$ plane at $z = \max(z)/2$, in the last row the $(x-z)$-plane at $y = \max(y)/2$. The fields are from left to right: the overdensity field from the simulation, its reconstruction with a lognormal prior and its reconstruction with a Gaussian prior (Wiener filter). We plot $\ln[1+\delta]$ and mark unphysical negative densities in the Wiener Filter reconstruction in red.
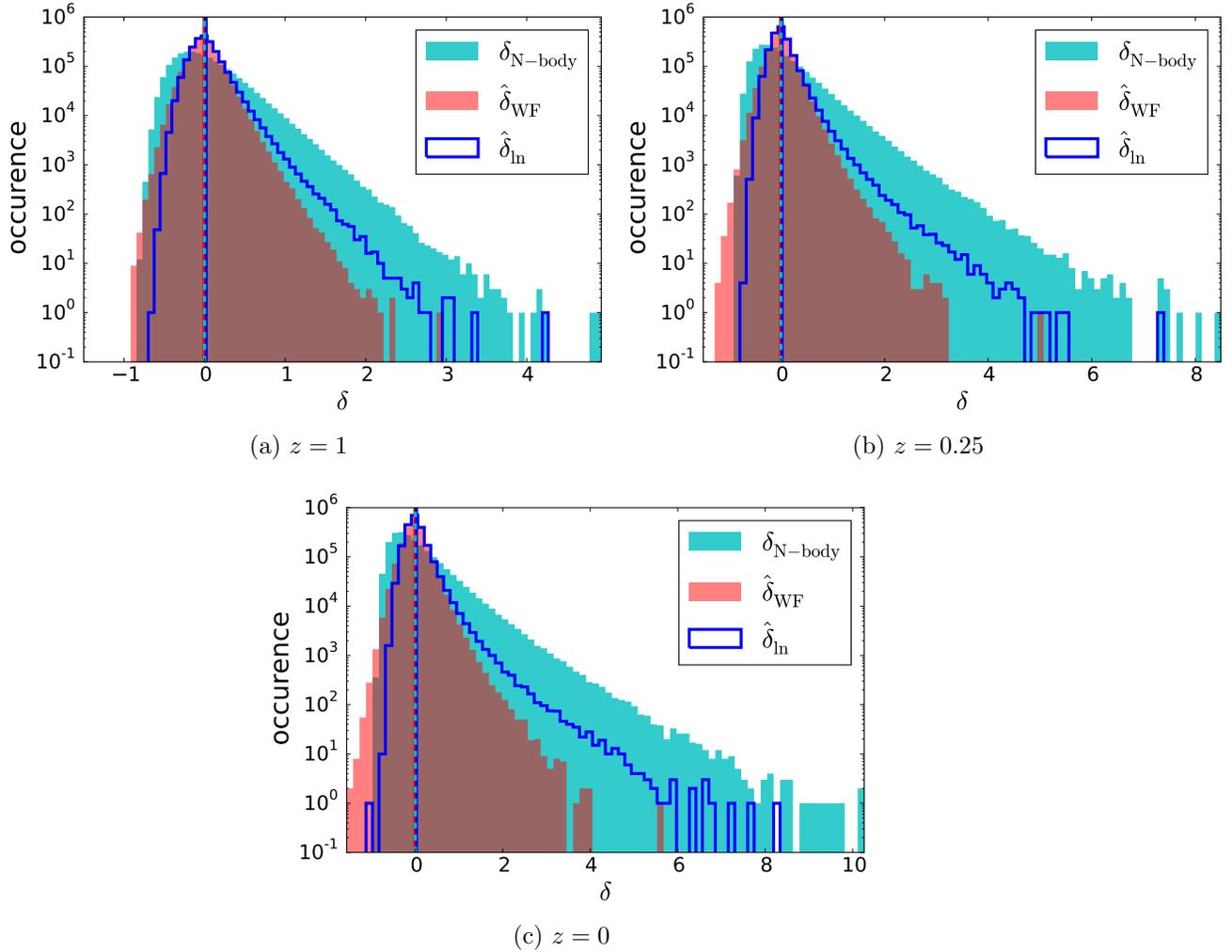
Figure 4.2: 1-point PDFs of the simulated density contrasts (in cyan) and their Wiener filter and lognormal reconstructions (red and dark blue) in tests on mock data created from different snapshots of an N-body simulation with a homogeneous source distribution and negligible shape noise (A2). The PDF of the lognormal reconstruction is slightly more skewed than the Wiener filter PDF, which is closer to symmetric in all cases. Both the Wiener filter and the lognormal reconstruction are slightly biased in the position of the peak, however, the mean values of both reconstructions agree well with the mean value of the underlying density. The mean values of the density contrast are indicated by vertical lines in the same color as their corresponding distribution. We also find that the Wiener filter produces unphysical density contrasts below -1 in the snapshots at redshift $z = 0.25$ and $z = 0$.

overdensities correctly, while the Wiener Filter is better in tracing the underdensities. The full distributions in the lower panel of the same Figure suggest that the reconstruction of low densities with the Wiener Filter is a consequence of allowing negative densities in this model: The Gaussian prior does not only permit negative densities in the reconstructed density field but even encourages them due to its symmetry. Because of this, it supports the assignment of low densities to to poorly constrained regions. At these places the reconstructed values sometimes coincide by chance with the real values (low density regions tend to have lower signal-to-noise). The lognornal prior refrains from reconstructing very low densities in regions with low signal-to-noise, since they are not significantly requested by the data.

4.8.2   Test B: Realistic Survey Geometry

In the test of type B, we employ a realistic survey geometry and source distribution. We use input overdensities from the same light cone as in test A3 to generate mock data and place sources in a cone that spans 7.15^o. The sources are distributed according to a distribution function of form

$$n(z) = z^{\alpha}\exp[-(z/z_0)^{\beta}], \tag{4.34}$$

where we fit α, β, and z_0 to the publicly available source distribution of the CFHTLenS survey[6]. The resulting source distribution function is shown in the left panel of Fig. 4.5. The fit does not exactly match the survey distribution, but the similarity is sufficient for this test. We then draw $\Omega[\text{armcin}^2]\rho_s[\text{gal/arcmin}^2]$ source positions from this distribution, where Ω is the angular opening area of the cone in arcmin^2 and ρ_s the source density of the survey, which we choose to be $\rho_s = 11\,\text{gal/arcmin}^2$ corresponding to the source density in CFHTLenS. A scatter plot of the resulting spatial source distribution is shown in the right panel of Fig. 4.5. The reconstructions are depicted in Fig. 4.6.

We find that the superiority of the lognormal model remains with a realistic background galaxy distribution. If we restrict our analysis to the region that is covered by the observational cone, we find that the distribution of the reconstructed field values closely follows the underlying density distribution if we apply the lognormal prior. The Gaussian prior produces negative densities (Fig. 4.7), but seems better in reconstructing low densities. However, this apparent superiority seems spurious since it also affect regions, where the algorithm gets little information from the data, e.g. at large distances from the observer (c.p Fig. 4.6).

4.8.3   Test C: Realistic Shape Noise

In the last test of our test series, we add realistic shape noise with variance $\sigma_{\epsilon}^2 = 0.25$ to the mock data on the light cone. This value is close to the value in CFHTLenS, $\sigma_{\epsilon}^2 = 0.279$ [81]. Compared to test B, we use the same opening angle of 7.15^o but use a slightly higher galaxy density of $15\,\text{gal/arcmin}^2$. We show results of this final test in Figures 4.8 and 4.9. The

---

[6]http://www.cfhtlens.org/astronomers/cosmological-data-products
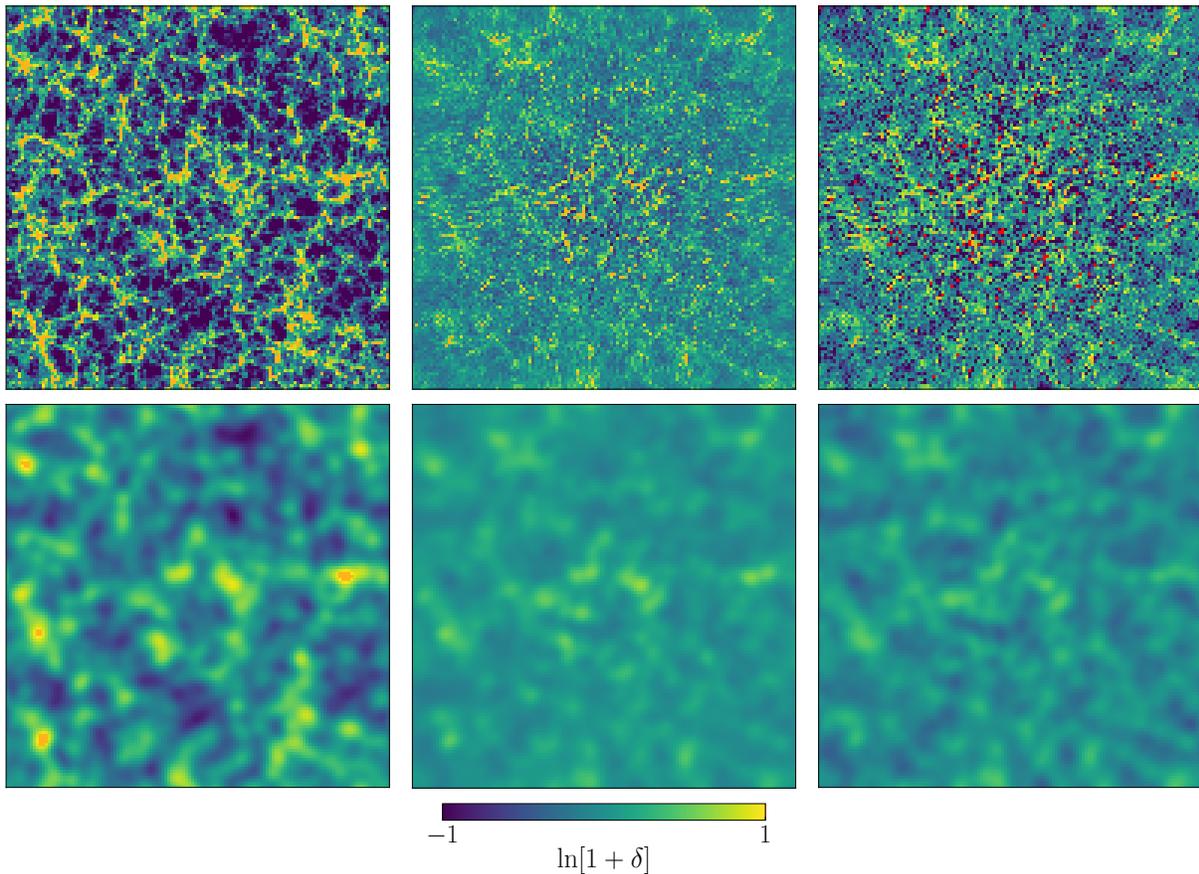
Figure 4.3:   Qualitative comparison of reconstruction methods in test A 3. For this test, we create mock data from a simulated density field on a light cone, use a homogeneous source distribution and add only negligible shape noise. The fields are from left to right: the underlying overdensity field from the simulation, the reconstructed overdensity field using a lognormal prior and the reconstructed overdensity using a Gaussian prior (Wiener filter). We show the 32nd (out of 128) $(x - y)$-plane of the reconstruction box in each panel. The observer is located in the center of the $(x - y)$-plane at the origin of the z-axis. Note that we plot $\ln[1 + \delta]$ and mark negative densities in red. In the second row, we show a smoothed version of the fields. The smoothing was performed on the density constrast with a Gaussian kernel of width $\sigma = 8h^{-1}\,\mathrm{Mpc}$, $\delta \to \delta_{R=8}$, and we plot $\ln[\delta_{R=8} + 1]$.
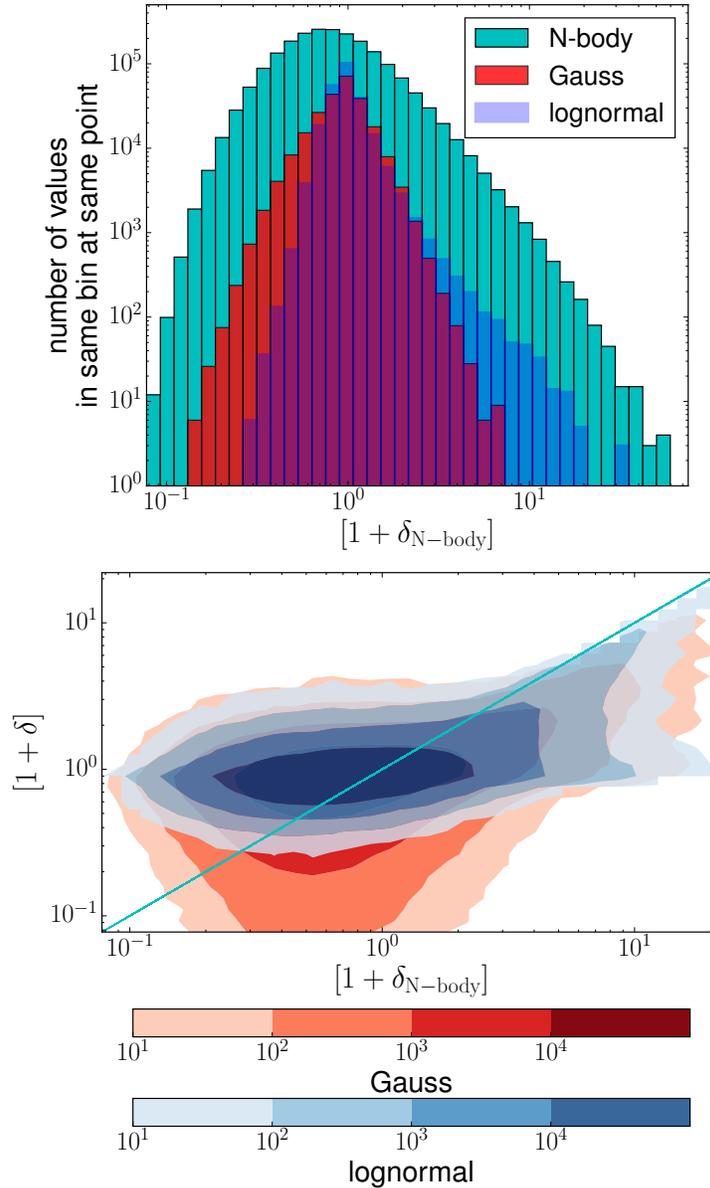
Figure 4.4:   Comparison of reconstruction methods in test A3: In the upper panel, we have binned the underlying density into 40 bins of equal width (0.17) in ln-space and count the points in the reconstructions whose density lies in the same bin at the same location. The total number of points in a density bin in the original density field is shown for comparison in the background (cyan). This plot suggests that the lognormal model is better in capturing overdensities, while the WF reconstruction is more likely to coincide with the real underdensities. In the lower panel, we plot the full distributions of the reconstructions against the underlying density. A perfect reconstruction would follow the diagonal. At points that are poorly constrained, both reconstructions should prefer values around the horizontal, which corresponds to the mean density. The Gaussian prior is more likely to yield lower densities, since it favors a symmetric density distribution.
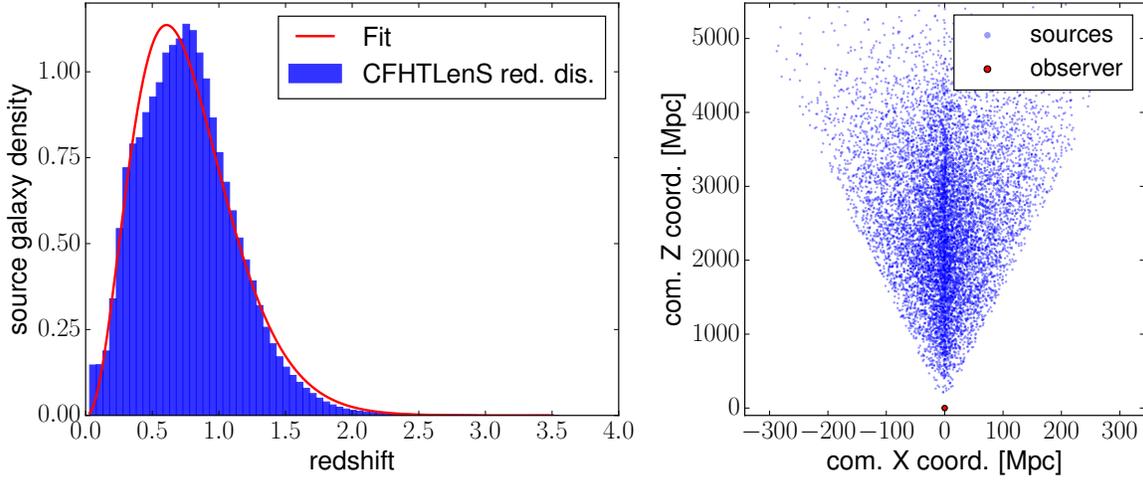
Figure 4.5:   The source redhsift distribution used for test B: In the left panel, we show the histogramm of source redshifts from CFHTLenS and our fit to this distribution of the form given in Eq. (4.34). The right panel depicts the projected 3D scatter plot of the galaxy sample that is drawn from the fit and used in test B (we only show every 200th source).
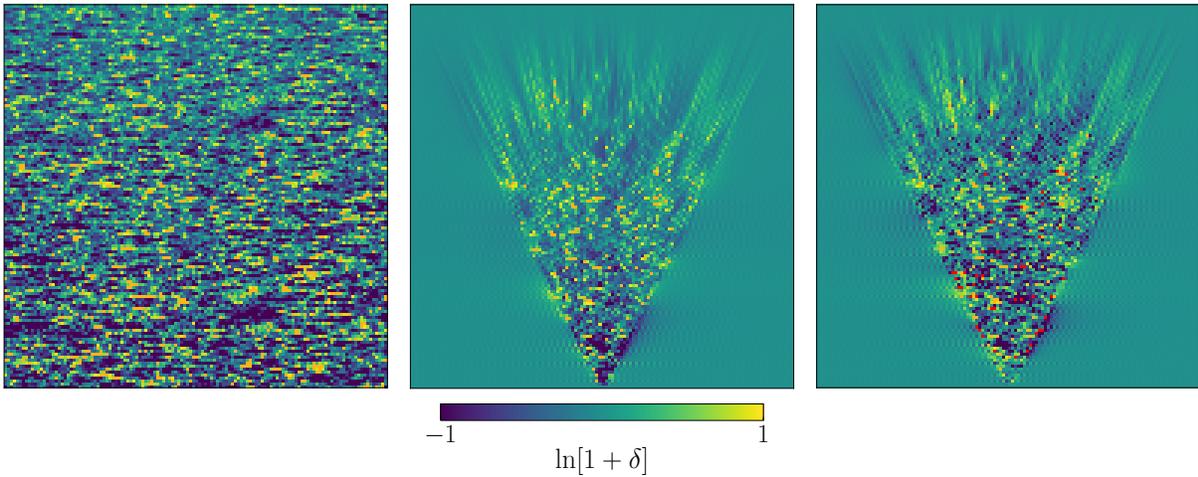
Figure 4.6:   Results of test B, reconstructions of a redshift-dependent density field on the observer's light cone from mock data with a realistic source distribution but negligible shape noise. We show central slices through the y-axis of the underlying field, $\ln[\delta_{\mathrm{N-Body}} + 1]$, in the left, the lognormal reconstruction, $\ln[\hat{\delta}_{\mathrm{ln}} + 1]$, in the middle and the Wiener Filter reconstruction, $\ln[\hat{\delta}_{\mathrm{WF}} + 1]$ in the right panel. Negative densities are marked in red. The apparent anisotropy of the fields stems from the fact that we have squeezed them in the z-direction. We use square pixels in the plot, while their physical size is eight times larger in the z-direction than in the x-direction.
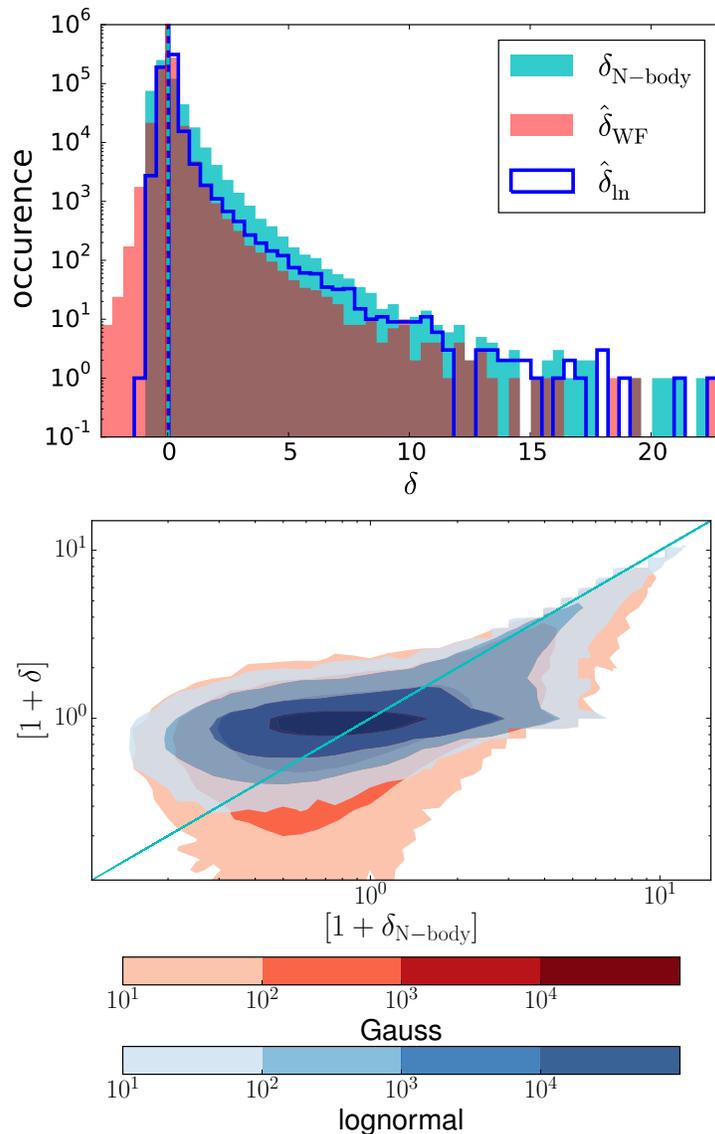
Figure 4.7:   Results of test B, reconstructions from mock data with a CFHTLenS-like source distribution. We have restricted the analysis to the field values that lie within the observed cone. In the upper panel we show the 1-point PDFs of the fields with mean values indicated by vertical lines in the same color as their corresponding distribution. The lower plot shows the density distributions of the reconstructions against the underlying density. The lognormal model is better in tracing the highest values of the true density distribution, while the Wiener Filter often prefers lower densities than the lognormal prior, especially at positions where the data is little constraining.
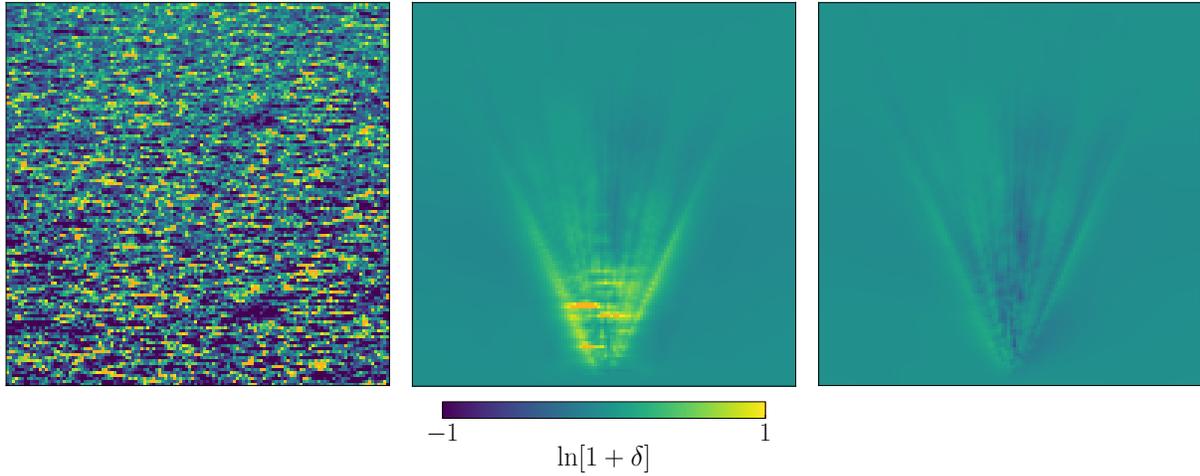
Figure 4.8: Results of test C, reconstructions from CFHTLenS-like mock data with realistic shape noise. In the left panel we show the underlying density field on the central slice through the y-axis. The central and middle panel depict the corresponding slices through the lognormal and WF reconstructions, respectively. The test reveals that current data is only poorly constraining on the smaller scales. The Wiener Filter finds very little contrast, while the lognormal reconstruction slightly overestimates the presence of overdensities. Both are significantly affected by the line of sight degeneracy.

test reveals that the lognormal model is still better in reconstructing overdensities in this realistic, CFHTLenS-like configuration, while the Wiener Filter better traces the underdense regions. Both reconstructions exhibit a strong line of sight degeneracy, which is why a slice-wise comparison of the input and reconstructed maps does not reveal many common features. Due to time-constraints, we stopped the minimzation in this test after only 100 iterations of the LBFGS and 20 steps of the steepest descent algorithm. Both minimizers failed to significantly reduce the negative log posterior during these steps. An inspection of the posterior gradient in each LBFGS step reveals that its absolute value is close to monotonically decreasing in the Wiener Filter reconstruction, while it is rather irregularly evolving in the lognormal case. When trying to converge further in the lognormal reconstruction, we also encounter significant numerical instabilites. These could be due to the code finding a local minimum, different from the global one, or shortcomings in our data model. To test the first assumption in the future, we will examine the stability of the current estimate by including a Monte-Carlo step that adds randomly drawn and downweighted realizations from the prior distribution to the current estimate. Alternatively, we could choose different starting points. Currently, we initialize the minimizer with zero density contrast.
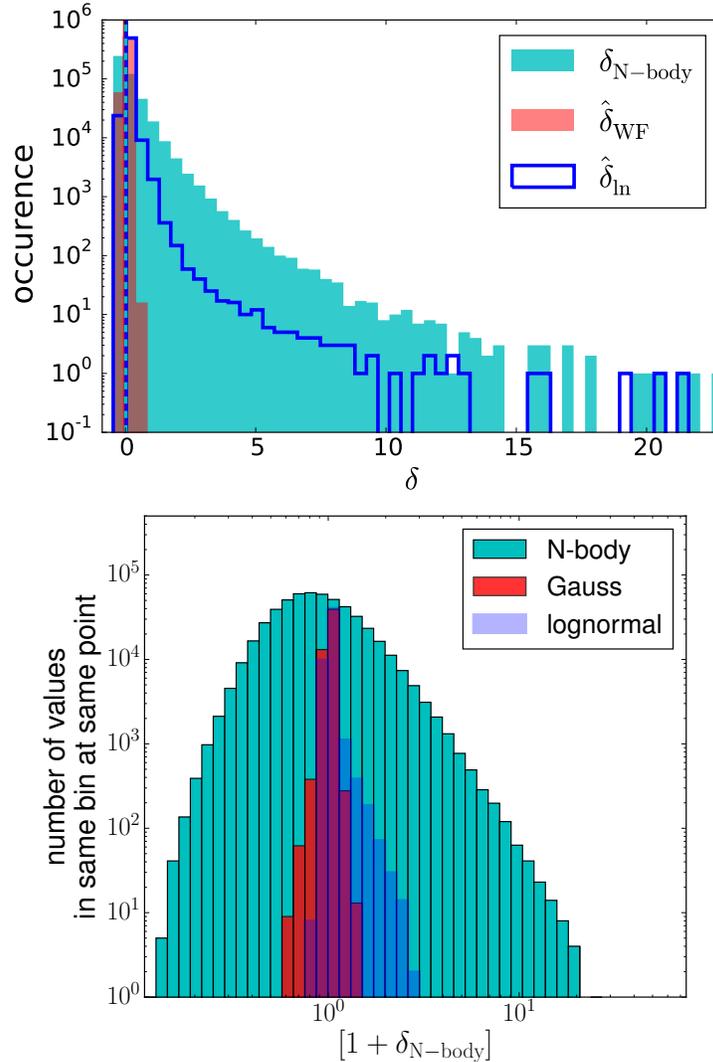
Figure 4.9:   Results of test C, reconstructions from mock data with a CFHTLenS-like source distribution and realistic shape noise. We have restricted the analysis to the field values that lie within the observed cone. In the upper panel we show the 1-point PDFs of the fields with mean values indicated by vertical lines in the same color as their corresponding distribution, in the lower panel, we count the pixels in which the reconstructed densities coincide with the original density field (i.e. lie within the same density bin). Similarly to the test with low shape noise, we find that the Wiener Filter traces the underdensities slightly better, while the lognormal prior is more likely to reconstruct overdensities correctly.

4.9   Conclusions

In this chapter, we have presented a novel, fully Bayesian, lensing tomography algorithm that reconstructs the three-dimensional matter distribution from measurements of individual galaxy shapes. The main difference to existing lensing reconstruction methods lies in the use of a lognormal prior on the density field instead of a Gaussian one. The lognormal model is an improvement over the Gaussian approximation in two ways: First, it enforces the strict positivity of the density while a Gaussian prior allows unphsical, negative densities. Second, it incorporates an a priori knowledge of the presence of odd moments in the matter distribution, which arise as a consequence of non-linear structure formation. These corrections are relevant since the cosmic shear signal probes structures down to scales that lie well in the non-linear regime. We note that the lognormal distribution does not describe the exact distribution of non-linearly evolved overdensities. However, since it is only used as a prior, it will be updated by the information contained in the data. In regions with high signal-to-noise, this prior model only supports the high-fidelity reconstruction. In less well constrained regions it prevents unphysical features in the reconstructed field.

To assess the differences between a reconstruction with a lognormal and a Gaussian prior (the latter corresponds to a Wiener filter), we have applied the algorithm with both priors to increasingly realistic mock data sets. Those data sets were produced by applying the algorithm's inherent data model to non-linearly evolved densities from N-body simulations. In tests with negligible shape noise, but a realistic CFHTLenS-like source distribution, we find that our reconstruction method is superior to the Wiener filter: It avoids negative densities that are present in the Wiener filter reconstructions. It is better in reconstructing the highest local peaks in the density field, and it leads to a higher point-wise correlation between the true underlying density and its reconstruction. When we reconstruct from CFHTLenS-like mock data with realistic shape noise, we find that both reconstructions show a strong line of sight degeneracy and that the Wiener Filter estimate exhibits very little contrast, while the lognormal model slightly overestimates the presence of high density values. This overestimation seems to be due to numerical instabilities. The exact reason for these instabilities has to be investigated in the future.

The Bayesian formulation also allows for an easy and consistent integration of other sources of information or uncertainties. In this work we show how photometric redshift uncertainties can be included, but leave the implementation for future work. The algorithm can further be complemented with models of intrinsic alignments or extended to use the clustering of galaxies as an additional source of information on the underlying matter distribution. Finally, it can be combined with existing Bayesian methods for shear estimation from galaxy surveys, yielding a complete Bayesian analysis pipeline. The outcome of an improved 3D reconstruction can then, for example, be used for measurements of the cross-correlation with other tracers of matter or for studying higher order field statistics.

In this chapter, we have proven that the algorithm yields better density reconstructions than existing methods in idealized test cases. In the future, a parallelized implementation of the algorithm, that can handle larger data sets, should be tested on realistic mock data of current and future surveys. These tests will reveal for which survey characteristics this

new algorithm can achieve a significant improvement over existing methods.

Chapter 5

Conclusion & Outlook

Weak lensing of the cosmic microwave background and of galaxies are both exceptionally promising cosmological probes since they are sensitive to the yet poorly constrained late-time evolution of our Universe, comparably little affected by model assumptions (since lensing measures the matter distribution directly) and can be measured over a wide range of scales and redshifts. Moreover, current and upcoming surveys will yield a vast amount of unprecedentedly precise data in these fields.

High precision data demands for very accurate analysis techniques and many of the assumptions that standard analyses are based on cease to be valid for current or future experiments. The increasing number of data sets also creates the need for methods that consistently combine the data obtained from different experiments and probes. Such a combination should allow to make use of the full information content while propagating uncertainties consistently. In this thesis we have addressed these demands by deriving new analysis methods for weak lensing measurements in a Bayesian framework, as well as by computing corrections to standard analysis techniques.

In Chapter 2 we have derived and outlined the implementation of a maximum a posteriori estimator for the CMB lensing potential from CMB data. This work has remained at a preliminary stage and unpublished because of direct competition by two groups and their corresponding publications [8, 33]. Especially the latest publication provides a functioning estimator for realistic data sets in the flat-sky approximation. Because of this we have put a particular emphasis on describing the caveats and specialities of an implementation on the full, curved sky. The next generation CMB data sets will be provided by ground-based experiments, for which the flat-sky approximation should be sufficient. A full sky implementation should be aimed at once the next generation CMB satellite probes are in reach (e.g. LiteBird with anticipated launch in 2025-2027 [162]).

An exciting extension of this method would be a joint estimator for the realization of the lensing potential and its power spectrum. The power spectrum estimate could then be used for cosmological parameter estimates by comparison to theory power spectra. In another extension the cosmological parameter inference could be made part of the reconstruction algorithm. The standard estimator for the CMB lensing power spectrum is a biased estimator and the bias terms need to be evaluated independently and subtracted.

They depend on the fiducial cosmology and some must be estimated with Monte Carlo simulations. An alternative estimator for the power spectrum would constitute a valuable cross check for this standard technique. Note, however, that it will likely be numerically as costly to evaluate as the four-point estimator with its corrections since the corrections must be in some way inherent to any estimator.

An estimator for the power spectrum could also be extended to cross-spectra with other tracers of large-scale structure. Instead of cross-correlating two maps, such an estimator would combine two data sets in a joint estimator that finds the most probable realizations of the lensing potential and, e.g. a Compton y-map, plus their auto- and cross-spectra. In such a framework uncertainties of the two field reconstructions could be propagated consistently to the estimates of the spectra.

In Chapter 3 we have described a new bias to the standard four-point estimator for the CMB lensing power spectrum. This bias is sourced by the matter bispectrum, which arises as a consequence of nonlinear structure formation. According to our estimate of the magnitude of the bias, it should be significant for current Stage-III experiments. In its evaluation we had to make a number of assumptions, and we stated in the conclusion to this chapter that these have to be validated in the future. Since the publication of this work, we have evaluated the bias for an improved fitting formula for the bispectrum (calibrated on N-body simulations) and found that this greatly enhances its significance, in particular on small scales. However, this enhancement seems to be almost canceled by the post-Born corrections to the bispectrum, which have recently been evaluated [186] and turn out to have opposite sign to the bispectrum induced by structure formation. An updated estimate of the bias will be published along with an independent measurement from ray-tracing simulations, which currently seems to confirm our analytical results but still needs to be tested thoroughly. The same kind of bias should also be evaluated for cross-correlation measurements where it could be even more significant.

We note that the significance of this bias suggests that deviations from Gaussianity should in the future also be accounted for in the MAP estimator of Chapter 2: The estimate of the lensing potential inferred from this estimator can be non-Gaussian if one employs a Gaussian prior, but it will be suboptimal, if we do not make use of our complete prior knowledge.

Finally, in Chapter 4 we have presented a MAP estimator that infers the 3D large-scale mass distribution inferred from lensed galaxy shape measurements. This MAP estimator is different to existing ones, in particular since it takes into account non-linear corrections to the density distribution by employing a lognormal prior on the density field. In a series of tests we have compared the result of this lognormal reconstruction to a Wiener Filter, which uses a Gaussian prior on the density field. We found that in the low noise regime the lognormal MAP estimator yields reconstructions that are closer to the true underlying field in terms of, e.g. pixel-wise difference or extremal values. Moreover it enforces positive densities, while the Wiener filter allows unphysical negative densities. For current data sets with realistic noise levels, however, both methods seem competitive. In the future, this estimator should be extended to include other tracers of the large-scale structure, such as the clustering of galaxies. It can also be used for cross-correlation studies, in the same

way as it was outlined above for the estimator for CMB lensing.

We conclude that Bayesian inference algorithms offer an exciting framework for consistently bundling information into joint inference algorithms. We have taken first steps towards such analysis pipelines, outlined a road map for future extensions and pointed out possible caveats.

Appendix A

Functional Derivative of the Lensing Response Operator

In this appendix we give a detailed derivation of the analytical form of the functional derivative of the response operator that appears in Chapter 2. To do this, we first write the response operator in a Fourier basis

$$
\tilde{s}(\mathbf{x}') = L^\phi_{\mathbf{x}'\mathbf{y}} s_\mathbf{y} = \int \mathrm{d}\mathbf{y}\, \delta_\mathrm{D}\left[\mathbf{x}' + \phi(\mathbf{x}') - \mathbf{y}\right] s(\mathbf{y})
$$
$$
= \int \mathrm{d}\mathbf{k}\, \mathrm{e}^{-i\mathbf{k}[\mathbf{x}'+\nabla\phi(\mathbf{x}')]} \int \mathrm{d}\mathbf{y}\, \mathrm{e}^{i\mathbf{k}\mathbf{y}} s(\mathbf{y}). \tag{A.1}
$$

Taking the functional derivative of the last expression with respect to the lensing potential at position $\mathbf{a}$, gives (assuming periodic boundary conditions)

$$
\frac{\delta}{\delta\phi_\mathbf{a}}\left[L^\phi_{\mathbf{x}'\mathbf{y}} s_\mathbf{y}\right] = \int \mathrm{d}\mathbf{k}\, \frac{\delta}{\delta\phi(\mathbf{a})} \mathrm{e}^{i\mathbf{k}[\mathbf{x}'+\nabla\phi(\mathbf{x}')]} \int \mathrm{d}\mathbf{y}\, \mathrm{e}^{-i\mathbf{k}\mathbf{y}} s(\mathbf{y})
$$
$$
= \int \mathrm{d}\mathbf{k}\, \nabla_{\mathbf{x}'}\left[\delta_\mathrm{D}\left(\mathbf{x}'-\mathbf{a}\right)\right] \cdot (i\mathbf{k}) \mathrm{e}^{i\mathbf{k}[\mathbf{x}'+\nabla\phi(\mathbf{x}')]} \int \mathrm{d}\mathbf{y}\, \mathrm{e}^{-i\mathbf{k}\mathbf{y}} s(\mathbf{y})
$$
$$
= \int \mathrm{d}\mathbf{k} \int \mathrm{d}\mathbf{y}\, \left[\nabla_{\mathbf{x}'}\delta_\mathrm{D}\left(\mathbf{x}'-\mathbf{a}\right)\right] \mathrm{e}^{i\mathbf{k}[\mathbf{x}'+\nabla\phi(\mathbf{x}')]} \cdot \left[-\nabla_\mathbf{y} \mathrm{e}^{-i\mathbf{k}\mathbf{y}}\right] s(\mathbf{y})
$$
$$
= \left[\nabla_{\mathbf{x}'}\delta_\mathrm{D}\left(\mathbf{x}'-\mathbf{a}\right)\right] \cdot \left[\int \mathrm{d}\mathbf{k}\, \mathrm{e}^{i\mathbf{k}[\mathbf{x}'+\nabla\phi(\mathbf{x}')]} \int \mathrm{d}\mathbf{y}\, \mathrm{e}^{-i\mathbf{k}\mathbf{y}} \nabla_\mathbf{y} s(\mathbf{y})\right]
$$
$$
= \left[\nabla_{\mathbf{x}'}\delta_\mathrm{D}\left(\mathbf{x}'-\mathbf{a}\right)\right] \cdot \left[L^\phi_{\mathbf{x}'\mathbf{y}} \nabla_\mathbf{y} s(\mathbf{y})\right]. \tag{A.2}
$$

In the last expression, we have again identified the configuration space formulation of the lensing response operator. The resulting expression is not only correct in flat space, but also on the sphere.[1]

---

[1]One could have equivalently derived the derivative by expressing the delta function in a spherical harmonic basis or by taking the derivative of the delta function in configuration space.

The derivative of the delta function that relates the position of the lensing potential **a** with the observing direction $\mathbf{x}'$ can be evaluated in the the context of a complete expression, e.g. $j^\dagger D_{,\phi} j$, which appears in the signal space posterior [Eq. (2.21)]. Keeping track of the correct coordinates in the derivative of such an expression, requires to take into account the beam function B and the pixel window function P. The total response (without mask) is

$$R_{j\mathbf{y}} = P_{j\mathbf{y}'} B_{\mathbf{y}'\mathbf{x}'} L^\phi_{\mathbf{x}'\mathbf{y}}, \tag{A.3}$$

and its derivative

$$(L^\phi_{\mathbf{x}'\mathbf{y}})_{,\phi} \to (R_{j\mathbf{y}})_{,\phi} = P_{j\mathbf{y}'} B_{\mathbf{y}'\mathbf{x}'} \left[\nabla_{\mathbf{x}'} \delta_{\mathrm{D}} (\mathbf{x}' - \mathbf{a}) \cdot \left(L^\phi_{\mathbf{x}'\mathbf{y}} \nabla_{\mathbf{y}} \right) \right]. \tag{A.4}$$

Inserting this into the terms that appear in the posterior, one finds, e.g.

$$
\begin{aligned}
j^\dagger D_{,\phi} j = & -j^\dagger D D^{-1}_{,\phi} D j \\
= & -2 j^\dagger D [R^\dagger N^{-1} R_{,\phi}] D j \\
= & -2 j_{\mathbf{x}} D_{\mathbf{xy}'} \left[R_{\mathbf{y}'i} N^{-1}_{ij} (R_{i\mathbf{y}})_{,\phi} \right] D_{\mathbf{yz}'} j_{\mathbf{z}'} \\
= & -2 j_{\mathbf{x}} D_{\mathbf{xy}'} R_{\mathbf{y}'i} N^{-1}_{ij} P_{j\mathbf{z}} B_{\mathbf{zx}'} \left[\nabla_{\mathbf{x}'} \delta_{\mathrm{D}} (\mathbf{x}' - \mathbf{a}) \cdot L^\phi_{\mathbf{x}'\mathbf{y}} \nabla_{\mathbf{y}} \right] D_{\mathbf{yz}'} j_{\mathbf{z}'} \\
= & -2 j_{\mathbf{x}} D_{\mathbf{xy}'} R_{\mathbf{y}'i} N^{-1}_{ij} P_{j\mathbf{z}} B_{\mathbf{zx}'} \\
& \left[\nabla_{\mathbf{x}'} \left(\delta_{\mathrm{D}} (\mathbf{x}' - \mathbf{a}) \cdot L^\phi_{\mathbf{x}'\mathbf{y}} \nabla_{\mathbf{y}} \right) - \delta_{\mathrm{D}} (\mathbf{x}' - \mathbf{a}) \cdot \nabla_{\mathbf{x}'} L^\phi_{\mathbf{x}'\mathbf{y}} \nabla_{\mathbf{y}} \right] D_{\mathbf{yz}'} j_{\mathbf{z}'} \\
= & \, 2 j_{\mathbf{x}} D_{\mathbf{xy}'} R_{\mathbf{y}'i} N^{-1}_{ij} P_{j\mathbf{z}} \\
& \left\{ \nabla_{\mathbf{x}'} B_{\mathbf{zx}'} \left[\delta_{\mathrm{D}} (\mathbf{x}' - \mathbf{a}) \cdot L^\phi_{\mathbf{x}'\mathbf{y}} \nabla_{\mathbf{y}} \right] + B_{\mathbf{zx}'} \left[\delta_{\mathrm{D}} (\mathbf{x}' - \mathbf{a}) \cdot \nabla_{\mathbf{x}'} L^\phi_{\mathbf{x}'\mathbf{y}} \nabla_{\mathbf{y}} \right] \right\} D_{\mathbf{yz}'} j_{\mathbf{z}'} \\
= & \, 2 j_{\mathbf{x}} D_{\mathbf{xy}'} R_{\mathbf{y}'i} N^{-1}_{ij} P_{j\mathbf{z}} \left[\nabla_{\mathbf{a}} B_{\mathbf{za}} \cdot L^\phi_{\mathbf{ay}} \nabla_{\mathbf{y}} + B_{\mathbf{za}} \cdot \nabla_{\mathbf{a}} L^\phi_{\mathbf{ay}} \nabla_{\mathbf{y}} \right] D_{\mathbf{yz}'} j_{\mathbf{z}'} \\
= & \, 2 \nabla \left[B^\dagger P^\dagger N^{-1} R D j \cdot L^\phi \nabla (D j) \right], \tag{A.5}
\end{aligned}
$$

where we have expressed the beam function in configuration space for notational convenience $B_{\mathbf{y}'\mathbf{x}'} \equiv \mathcal{F}^\dagger_{\mathbf{y}'\mathbf{k}} B_{\mathbf{kk}'} \mathcal{F}_{\mathbf{k}'\mathbf{x}'}$.

Appendix B

Detailed Evaluation of the individual Contributions to the Lensing Bispectrum Bias

B.1 Bias from Terms of Type A

We begin by computing the lensing bias from the contraction type A. For the type A1 contraction, we obtain

$$\langle \delta T_{\mathbf{l}_1} \delta T_{\mathbf{l}_2} \delta T_{\mathbf{l}_3} T_{\mathbf{l}_4} \rangle_{A1} = - (2\pi)^2 \delta_{\mathrm{D}}(\mathbf{l}_1 + \mathbf{l}_2 + \mathbf{l}_3 + \mathbf{l}_4) C_{l_4}^{TT} \left[(\mathbf{l}_3 + \mathbf{l}_4) \cdot \mathbf{l}_4 \right]$$
$$\times \int_{\mathbf{l}} \left[\mathbf{l} \cdot (\mathbf{l}_1 - \mathbf{l}) \right] \left[\mathbf{l} \cdot (\mathbf{l}_2 + \mathbf{l}) \right] C_l^{TT} B_\phi(\mathbf{l}_1 - \mathbf{l}, \mathbf{l}_2 + \mathbf{l}, -\mathbf{l}_1 - \mathbf{l}_2). \quad \text{(B.1)}$$

Inserting this 4-point function into Eq. (3.14) yields the A1 bias to the measured lensing power spectrum,

$$N_{A1}^{(3/2)}(L) = -4A_L^2 S_L \int_{\mathbf{l}_1,\mathbf{l}} g_{\mathbf{l}_1,\mathbf{L}} [(\mathbf{l}_1 - \mathbf{l}) \cdot \mathbf{l}][(\mathbf{l}_1 - \mathbf{l}) \cdot (\mathbf{L} - \mathbf{l})] C_{|\mathbf{l}_1 - \mathbf{l}|}^{TT} B_\phi(\mathbf{l}, \mathbf{L} - \mathbf{l}, -\mathbf{L}). \quad \text{(B.2)}$$

The prefactor of 4 is a symmetry factor that arises from the four identical possibilities to place three first order perturbed temperature contributions, δT, and one unlensed contribution, T, in the temperature 4-point correlator. S_L denotes an integral over the filtered unlensed CMB power spectrum,

$$S_L = \int_{\mathbf{l}_2} g_{\mathbf{l}_2,\mathbf{L}}(\mathbf{l}_2 \cdot \mathbf{L}) C_{l_2}^{TT}, \quad \text{(B.3)}$$

which corresponds to half the inverse normalization $S_L \approx 1/(2A_L)$ at leading order in $C^{\phi\phi}$. Spelling out the A2 contraction, we find

$$\langle \delta T_{\mathbf{l}_1} \delta T_{\mathbf{l}_2} \delta T_{\mathbf{l}_3} T_{\mathbf{l}_4} \rangle_{A2} = - (2\pi)^2 \delta_D(\mathbf{l}_1 + \mathbf{l}_2 + \mathbf{l}_3 + \mathbf{l}_4) C_{l_4}^{TT} \left[\mathbf{l}_4 \cdot (\mathbf{l}_2 + \mathbf{l}_4) \right]$$
$$\times \int_{\mathbf{l}} C_l^{TT} \left[\mathbf{l} \cdot (\mathbf{l}_1 - \mathbf{l}) \right] \left[\mathbf{l} \cdot (\mathbf{l} + \mathbf{l}_3) \right] B_\phi(\mathbf{l}_1 - \mathbf{l}, \mathbf{l} + \mathbf{l}_3, \mathbf{l}_2 + \mathbf{l}_4), \quad \text{(B.4)}$$

resulting in the bias

$$
N_{A2}^{(3/2)}(L) = -4A_L^2 \int_{\mathbf{l}_1 \mathbf{l}_2} g_{\mathbf{l}_1,\mathbf{L}} g_{\mathbf{l}_2,\mathbf{L}} [(\mathbf{l}_2 - \mathbf{l}_1) \cdot (\mathbf{l}_2 - \mathbf{L})] C_{|\mathbf{L}-\mathbf{l}_2|}^{TT}
$$
$$
\times \int_{\mathbf{l}} [(\mathbf{l}_1 - \mathbf{l}) \cdot \mathbf{l}][(\mathbf{l}_1 - \mathbf{l}) \cdot (\mathbf{l}_1 - \mathbf{l}_2 - \mathbf{l})] C_{|\mathbf{l}_1-\mathbf{l}|}^{TT} B_\phi(\mathbf{l}, (\mathbf{l}_1 - \mathbf{l}_2) - \mathbf{l}, -(\mathbf{l}_1 - \mathbf{l}_2)), \quad \text{(B.5)}
$$

where we have again included a symmetry factor of 4. The integrand involves functions that depend on different combinations of $\mathbf{l}_1$, $\mathbf{l}_2$, and $\mathbf{l}$, leading to a tightly coupled 6D integral for every L. The $N^{(3/2)}$ bias from the A3 contraction is found to be equal the A2 contraction by noting that the bias is invariant under exchanging $\mathbf{l}_1 \leftrightarrow \mathbf{L} - \mathbf{l}_1$ in Eq. (3.14).

B.2 Bias Contributions from Terms of Type B

Terms of type B are of the form $\langle \delta^2 T \delta T T' T' \rangle$ with both perturbed temperatures coupling to the same quadratic estimator $\hat{\phi}$ in the four point estimator $\langle \hat{\phi} \hat{\phi}' \rangle$. There are 4 possibilities to form such a term, resulting in a symmetry factor of 4. The CMB lensing bias sourced by the B1 contraction vanishes for $L > 0$,

$$
N_{B1}^{(3/2)}(L) = 0. \tag{B.6}
$$

The B2 contraction is

$$
\langle \delta^2 T_{\mathbf{l}_1} \delta T_{\mathbf{l}_2} T_{\mathbf{l}_3} T_{\mathbf{l}_4} \rangle_{B2} = -\frac{(2\pi)^2}{2} \delta_D(\mathbf{l}_1 + \mathbf{l}_2 + \mathbf{l}_3 + \mathbf{l}_4) C_{l_3}^{TT} C_{l_4}^{TT}
$$
$$
\times \int_{\mathbf{l}} [\mathbf{l}_3 \cdot (\mathbf{l} - \mathbf{l}_1 - \mathbf{l}_3)] [\mathbf{l}_3 \cdot \mathbf{l}] [(\mathbf{l}_1 + \mathbf{l}_2 + \mathbf{l}_3) \cdot (\mathbf{l}_3 + \mathbf{l}_1)] B_\phi(\mathbf{l}, \mathbf{l}_1 + \mathbf{l}_3 - \mathbf{l}, -\mathbf{l}_1 - \mathbf{l}_3). \quad \text{(B.7)}
$$

Together with the similar $B3$ contraction, this results in the lensing bias

$$
N_{B2}^{(3/2)}(L) + N_{B3}^{(3/2)}(L) = -2A_L^2 \int_{\mathbf{l}_1,\mathbf{l}_2} g_{\mathbf{l}_1,\mathbf{L}} g_{\mathbf{l}_2,\mathbf{L}} [(\mathbf{L} - \mathbf{l}_2) \cdot (\mathbf{l}_1 - \mathbf{l}_2)] C_{l_2}^{TT} C_{|\mathbf{L}-\mathbf{l}_2|}^{TT}
$$
$$
\times \int_{\mathbf{l}} [\mathbf{l}_2 \cdot (\mathbf{l} - (\mathbf{l}_1 - \mathbf{l}_2))] (\mathbf{l}_2 \cdot \mathbf{l}) B_\phi(\mathbf{l}, (\mathbf{l}_1 - \mathbf{l}_2) - \mathbf{l}, -(\mathbf{l}_1 - \mathbf{l}_2)) + (\mathbf{l}_2 \leftrightarrow \mathbf{L} - \mathbf{l}_2). \quad \text{(B.8)}
$$

B.3 Biases from Terms of type C

The C1 contraction defined in Eq. (3.20) reads

$$
\langle \delta^2 T_{\mathbf{l}_1} T_{\mathbf{l}_2} \delta T_{\mathbf{l}_3} T_{\mathbf{l}_4} \rangle_{C1} = \frac{(2\pi)^2}{2} \delta_D(\mathbf{l}_1 + \mathbf{l}_2 + \mathbf{l}_3 + \mathbf{l}_4) C_{l_2}^{TT} C_{l_4}^{TT} [(\mathbf{l}_3 + \mathbf{l}_4) \cdot \mathbf{l}_4]
$$
$$
\times \int_{\mathbf{l}} (\mathbf{l}_2 \cdot \mathbf{l}) [\mathbf{l}_2 \cdot (\mathbf{l}_1 + \mathbf{l}_2 - \mathbf{l})] B_\phi(\mathbf{l}, \mathbf{l}_1 + \mathbf{l}_2 - \mathbf{l}, -\mathbf{l}_1 - \mathbf{l}_2). \quad \text{(B.9)}
$$

Inserting this into Eq. (3.14) gives the following C1 bias of the measured lensing power spectrum:

$$N_{C1}^{(3/2)}(L) = 4A_L^2 S_L \int_{l_1,l} g_{l_1,\mathbf{L}}(\mathbf{l}_1 \cdot \mathbf{l})\,[\mathbf{l}_1 \cdot (\mathbf{L} - \mathbf{l})]\,C_{l_1}^{TT} B_\phi(\mathbf{l}, \mathbf{L} - \mathbf{l}, -\mathbf{L}), \tag{B.10}$$

where the integral S_L was defined in Eq. (B.3). Eq. (B.10) takes into account a symmetry factor of 8 that arises because the resulting lensing bias does not change if we exchange $\mathbf{l}_1 \leftrightarrow \mathbf{l}_2$, or $\mathbf{l}_3 \leftrightarrow \mathbf{l}_4$, or both in Eq. (3.27).

The C2 contraction in Eq. (3.20) is given by

$$\langle \delta^2 T_{l_1} T_{l_2} \delta T_{l_3} T_{l_4} \rangle_{C2} = \langle \delta^2 T_{l_1} \delta T_{l_3} \rangle \langle T_{l_2} T_{l_4} \rangle. \tag{B.11}$$

This involves the correction $\langle \delta^2 T \delta T \rangle$ of the lensed temperature power spectrum generated by a nonzero lensing bispectrum (another correction would be $\langle \delta^3 T T \rangle$). Based on analytical [164] and numerical investigations this correction is expected to be small. Further, it should be automatically accounted for when using realization-dependent subtraction of the Gaussian $N^{(0)}$ bias which is common in modern lensing pipelines. We do not investigate this term here further. The C3 contraction is given by

$$\langle \delta^2 T_{l_1} T_{l_2} \delta T_{l_3} T_{l_4} \rangle_{C3} = -\frac{(2\pi)^2}{2} \delta_D(\mathbf{l}_1 + \mathbf{l}_2 + \mathbf{l}_3 + \mathbf{l}_4)$$
$$\times \int_{l_2'} [\mathbf{l}_4 \cdot (\mathbf{l}_1 + \mathbf{l}_4 - \mathbf{l}_2')]\,[\mathbf{l}_4 \cdot \mathbf{l}_2']\,[\mathbf{l}_2 \cdot (\mathbf{l}_1 + \mathbf{l}_4)]\,C_{l_2}^{TT} C_{l_4}^{TT} B_\phi(\mathbf{l}_2', \mathbf{l}_1 + \mathbf{l}_4 - \mathbf{l}_2', -(\mathbf{l}_1 + \mathbf{l}_4))$$
$$\tag{B.12}$$

The induced bias of the measured lensing power spectrum is

$$N_{C3}^{(3/2)}(L) = -\frac{8}{2} A_L^2 \int_{l_1,l_2} g_{l_1,\mathbf{L}} g_{l_2,\mathbf{L}}\,[(\mathbf{l}_1 - \mathbf{L}) \cdot (\mathbf{l}_1 + \mathbf{l}_2 - \mathbf{L})]\,C_{|\mathbf{L}-l_1|}^{TT} C_{|l_2-\mathbf{L}|}^{TT}$$
$$\times \int_l [(\mathbf{l}_2 - \mathbf{L}) \cdot (\mathbf{l} - \mathbf{l}_1 - \mathbf{l}_2 + \mathbf{L})]\,[(\mathbf{l}_2 - \mathbf{L}) \cdot \mathbf{l}]\,B_\phi(\mathbf{l}, -\mathbf{l}_2 + \mathbf{L} - \mathbf{l}_1, \mathbf{l}_1 + \mathbf{l}_2 - \mathbf{L} - \mathbf{l}),$$
$$\tag{B.13}$$

where we have accounted for all possibilities to place the (perturbed) temperatures in the four-point correlator by including a symmetry factor of 8. Changing integration variables $\mathbf{l}_1 \to \mathbf{L} - \mathbf{l}_1$ and $\mathbf{l}_2 \to \mathbf{L} - \mathbf{l}_2$, we obtain

$$N_{C3}^{(3/2)}(L) = 4A_L^2 \int_{l_1,l_2} g_{l_1,\mathbf{L}} g_{l_2,\mathbf{L}}\,[\mathbf{l}_1 \cdot (\mathbf{L} - \mathbf{l}_1 - \mathbf{l}_2)]\,C_{l_1}^{TT} C_{l_2}^{TT}$$
$$\times \int_l [\mathbf{l}_2 \cdot (\mathbf{l} - (\mathbf{L} - \mathbf{l}_1 - \mathbf{l}_2))]\,(\mathbf{l}_2 \cdot \mathbf{l}) B_\phi(\mathbf{l}, (\mathbf{L} - \mathbf{l}_1 - \mathbf{l}_2) - \mathbf{l}, -(\mathbf{L} - \mathbf{l}_1 - \mathbf{l}_2)), \tag{B.14}$$

where we used $g_{l,\mathbf{L}} = g_{\mathbf{L}-l,\mathbf{L}}$.

B.4 Bias from Terms of Type D

The last type of coupling, type D, involves the lensed temperature perturbed to third order in ϕ. It picks up the three-point function of the components of the lensing deflection at the same location $\langle \alpha_i(\mathbf{x})\alpha_j(\mathbf{x})\alpha_k(\mathbf{x})\rangle$. This correlation must vanish by statistical isotropy [164]. To verify this analytically, we note that each contractions of type D can be written as

$$\langle \delta^3 T_{\mathbf{l}_1} T_{\mathbf{l}_2} T_{\mathbf{l}_3} T_{\mathbf{l}_4}\rangle = -\frac{1}{6}\zeta(\mathbf{l}_1)\langle T_{\mathbf{l}_1} T_{\mathbf{l}_2} T_{\mathbf{l}_3} T_{\mathbf{l}_4}\rangle_{(T)}, \tag{B.15}$$

where we defined

$$\zeta(\mathbf{l}_1) \equiv \int_{\mathbf{L}} (\mathbf{l}_1 \cdot \mathbf{L}) \int_{\mathbf{l}} (\mathbf{l}_1 \cdot \mathbf{l})[\mathbf{l}_1 \cdot (\mathbf{l} - \mathbf{L})] B_\phi(\mathbf{l}, \mathbf{L} - \mathbf{l}, -\mathbf{L}). \tag{B.16}$$

The integral over $\mathbf{l}$ is the same as that already encountered in Eq. (B.10). Using the same trick of Eq. (C.2) to make the integral separable leads to

$$\zeta(\mathbf{l}_1) = l_1^3 \int_{\mathbf{L}} \left[\cos^3(\mu_{\mathbf{L}})\beta_\|(L) + \cos\mu_{\mathbf{L}}\sin^2(\mu_{\mathbf{L}})\beta_\perp(L) \right] = 0, \tag{B.17}$$

where $\cos\mu_{\mathbf{L}} = \cos\mu_{\mathbf{l}_1} = \hat{\mathbf{l}}_1 \cdot \hat{\mathbf{L}}$. This vanishes after performing the angular integration over $\mu_{\mathbf{L}}$.

Appendix C

Bias Integral Expressions for faster numerical Evaluation

The A1 and C1 biases in Eqs. (B.2) and (B.10) involve four-dimensional integrals for every multipole L, which are computationally expensive to evaluate. Fortunately, however, the integrands of these 4D integrals can be rewritten in a product-separable form, which allows much faster numerical evaluation by multiplying 2D integrals. The next two subsections will show this explicitly for the C1 and A1 contributions to the bias, with the final results given by Eqs. (3.29) and (C.15), which have a simple form.

C.1 Fast Expression for C1 Bias by Separation of Integrals

We start with the C1 contribution to the $N^{(3/2)}$ bias because it is somewhat simpler to speed up than the A1 contribution. The C1 contribution given by Eq. (B.10) involves a 4D integral over $\mathbf{l}_1$ and $\mathbf{l}$ for every value of L, which is computationally expensive. To separate the integrand, we rewrite scalar products between wavevectors using the angle addition theorem for the cosine: If we define $\cos\mu_{\mathbf{l}_1} = \mathbf{l}_1 \cdot \mathbf{L}/(l_1 L)$ and $\cos\mu_{\mathbf{l}} = \mathbf{l} \cdot \mathbf{L}/(lL)$, then the angle between $\mathbf{l}_1$ and $\mathbf{l}$ is $\mu_{\mathbf{l}_1} - \mu_{\mathbf{l}}$, so that

$$\mathbf{l}_1 \cdot \mathbf{l} = l_1 l \cos(\mu_{\mathbf{l}_1} - \mu_{\mathbf{l}}) = l_1 l \left[\cos(\mu_{\mathbf{l}_1})\cos(\mu_{\mathbf{l}}) + \sin(\mu_{\mathbf{l}_1})\sin(\mu_{\mathbf{l}})\right]. \tag{C.1}$$

Then, using basic trigonometric identities we obtain for the expression in the integrand of Eq. (B.10)

$$\begin{aligned}
\left[\mathbf{l}_1 \cdot (\mathbf{l} - \mathbf{L})\right]\left[\mathbf{l}_1 \cdot \mathbf{l}\right] = l_1^2 l \Big\{ &\cos^2(\mu_{\mathbf{l}_1}) \cos\mu_{\mathbf{l}} \left[l \cos\mu_{\mathbf{l}} - L\right] \\
&+ \cos\mu_{\mathbf{l}_1} \sin\mu_{\mathbf{l}_1} \sin\mu_{\mathbf{l}} \left[2l \cos\mu_{\mathbf{l}} - L\right] \\
&+ \sin^2(\mu_{\mathbf{l}_1}) \, l \sin^2(\mu_{\mathbf{l}}) \Big\},
\end{aligned} \tag{C.2}$$

which is a sum of terms that are separable in μ_{l_1} and μ_l as desired. The first term on the right hand side of Eq. (C.2) involves $l_{1,\|}^2 = (\mathbf{l_1} \cdot \hat{\mathbf{L}})^2 = l_1^2 \cos^2(\mu_{l_1})$ which measures the component of the temperature multipole $\mathbf{l_1}$ along the reconstruction multipole $\mathbf{L}$. The third term involves $l_{1,\perp}^2 = l_1^2 \sin^2(\mu_{l_1})$ which measures the component of the temperature multipole $\mathbf{l_1}$ perpendicular to the reconstruction multipole $\mathbf{L}$. The second term in Eq. (C.2) is a cross term involving a product of these two components, $l_{1,+}^2 = l_{1,\|} l_{1,\perp}$. Using Eq. (C.2), the C1 contribution (B.10) to the $N^{(3/2)}$ bias therefore turns into the following simple form of Eq. (3.29):

$$N_{C1}^{(3/2)}(L) \quad = -4A_L^2 S_L \left[R_\|(L)\beta_\|(L) + R_\perp(L)\beta_\perp(L) \right], \tag{C.3}$$

where we defined the temperature integral $R_\|$ and integrated lensing bispectrum $\beta_\|$ as

$$R_\|(L) \quad = \int_{l_1} g_{l_1,\mathbf{L}} l_1^2 \cos^2(\mu_{l_1}) C_{l_1}^{TT}, \tag{C.4}$$

$$\beta_\|(L) \quad = \int_l l \cos \mu_l \left[l \cos \mu_l - L \right] B_\phi(\mathbf{l}, \mathbf{L} - \mathbf{l}, -\mathbf{L}), \tag{C.5}$$

and similarly for the perpendicular component,

$$R_\perp(L) \quad = \int_{l_1} g_{l_1,\mathbf{L}} l_1^2 \sin^2(\mu_{l_1}) C_{l_1}^{TT}, \tag{C.6}$$

$$\beta_\perp(L) \quad = \int_l l^2 \sin^2(\mu_l) B_\phi(\mathbf{l}, \mathbf{L} - \mathbf{l}, -\mathbf{L}). \tag{C.7}$$

The cross term from the second line of Eq. (C.2) yields $R_+ \beta_+ = 0$; see Appendix C.1.1. We will use Eq. (3.29) for numerically evaluating the C1 contribution to the $N^{(3/2)}$ bias, because it only involves 2D integrals that are much faster to evaluate than the 4D integral in Eq. (B.10).

A slightly simpler approximate expression follows by noting that $S_L \approx 1/(2A_L)$ at leading order in $C^{\phi\phi}$:

$$N_{C1}^{(3/2)}(L) \approx -2A_L \left[R_\|(L)\beta_\|(L) + R_\perp(L)\beta_\perp(L) \right]. \tag{C.8}$$

C.1.1   Vanishing Cross-Integrals

The fast expression (3.29) for the type C1 bias has an additional contribution $\beta_+ R_+$, where

$$R_+(\mathbf{L}) = \int_{l_1} g_{l_1,\mathbf{L}} l_1^2 \cos \mu_{l_1} \sin \mu_{l_1} C_{l_1}^{TT} = 0 \tag{C.9}$$

$$\beta_+(\mathbf{L}) = \int_l l \sin \mu_l \left[2l \cos \mu_l - L \right] B_\phi(\mathbf{l}, \mathbf{L} - \mathbf{l}, -\mathbf{L}) = 0. \tag{C.10}$$

Here we show that both integrals R_+ and β_+ vanish. We start by writing out the weight in Eq. (C.9),

$$R_+(\mathbf{L}) = \int_\mathbf{l} \frac{\mathbf{l}\cdot\mathbf{L}C_l^{\tilde{T}\tilde{T}} + (\mathbf{L}-\mathbf{l})\cdot\mathbf{L}C_{|\mathbf{L}-\mathbf{l}|}^{\tilde{T}\tilde{T}}}{2C_{l,\mathrm{expt}}^{\tilde{T}\tilde{T}}C_{|\mathbf{L}-\mathbf{l}|,\mathrm{expt}}^{\tilde{T}\tilde{T}}} l^2 \cos\mu_\mathbf{l} \sin\mu_\mathbf{l} C_l^{TT}. \tag{C.11}$$

Choosing a coordinate system where the x-axis is aligned with $\mathbf{L}$ gives $\mathbf{l}\cdot\mathbf{L} = l_x L$, $l\cos\mu_\mathbf{l} = l_x$ and $l\sin\mu_\mathbf{l} = l_y$, so that

$$\begin{aligned}
R_+(L) =& \frac{1}{(2\pi)^2} \int_{-\infty}^\infty \mathrm{d}l_x\, l_x \int_{-\infty}^\infty \mathrm{d}l_y\, l_y C_{(l_x^2+l_y^2)^{1/2}}^{TT} \\
&\times \frac{l_x L C_{(l_x^2+l_y^2)^{1/2}}^{\tilde{T}\tilde{T}} + (L^2 - l_x L)C_{(L^2+l_x^2+l_y^2-2Ll_x)^{1/2}}^{\tilde{T}\tilde{T}}}{2C_{(l_x^2+l_y^2)^{1/2},\mathrm{expt}}^{\tilde{T}\tilde{T}} C_{(L^2+l_x^2+l_y^2-2Ll_x)^{1/2},\mathrm{expt}}^{\tilde{T}\tilde{T}}} \\
=& 0. \tag{C.12}
\end{aligned}$$

The integrand changes sign under $l_y \to -l_y$ so that the integral over l_y vanishes and thus $R_+ = 0$. Although we chose a particular coordinate system aligned with $\mathbf{L}$ to show this, the fact that $R_+ = 0$ is coordinate-independent (in coordinate-independent terms, the 2D integral can be split into two 1D integrals parallel and perpendicular to $\mathbf{L}$; the latter integral vanishes). Note that $R_\parallel$ and $R_\perp$ do not vanish because they involve even powers of l_x and l_y in the integrand. Following the same line of argument the very similar integral of type R_+^{BE} can be shown to be zero.

To show $\beta_+ = 0$ we proceed similarly. Choosing a coordinate system with x-axis aligned with $\mathbf{L}$ and writing Eq. (C.10) in components,

$$\begin{aligned}
\beta_+(L) =& \frac{1}{(2\pi)^2} \int_{-\infty}^\infty \mathrm{d}l_x \int_{-\infty}^\infty \mathrm{d}l_y\, l_y (2l_x - L) B_\phi\left((l_x^2+l_y^2)^{1/2}, (L^2+l_x^2+l_y^2-2Ll_x)^{1/2}, L\right) \\
=& 0. \tag{C.13}
\end{aligned}$$

The integral over l_y vanishes again because the integrand changes sign under $l_y \to -l_y$.

We also confirmed numerically that R_+ and β_+ vanish by evaluating the integrals in Eqs. (C.9) and (C.10) directly.

C.2 Fast Expression for A1 Bias by evaluating Fourier-space Convolution as position-space Product

Numerical evaluation of the 4D integral appearing in the A1 contribution of Eq. (B.2) to the $N^{(3/2)}$ bias can also be accelerated by suitably rewriting the integral. The idea is that, for fixed $\mathbf{l}$, the integral over $\mathbf{l}_1$ in Eq. (B.2) is a convolution in Fourier space, which can be evaluated efficiently as a product in position space (similarly to References [192] and [163]

which used the same idea to accelerate large-scale structure perturbation theory integrals). This gives the following fast expression for the A1 bias of Eq. (B.2):[1]

$$N_{A1}^{(3/2)}(L) = 4A_L^2 S_L \int \mathrm{d}^2\mathbf{r}\, \xi_g(\mathbf{r}, \mathbf{L}) \left[\bar{\beta}_\parallel(\mathbf{r}, \mathbf{L}) \bar{\xi}_\parallel^{TT}(\mathbf{r}) + \bar{\beta}_\perp(\mathbf{r}, \mathbf{L}) \bar{\xi}_\perp^{TT}(\mathbf{r}) \right]. \tag{C.15}$$

The structure of this is very similar to the fast expression for the C1 term given by Eq. (3.29), but it involves a 2D $\mathbf{r}$-integral over the following 2D Fourier transforms:

$$\xi_g(\mathbf{r}, \mathbf{L}) = \int_{\mathbf{l}_1} e^{i\mathbf{l}_1 \cdot \mathbf{r}}\, g_{\mathbf{l}_1, \mathbf{L}}, \tag{C.16}$$

and

$$\bar{\beta}_\parallel(\mathbf{r}, \mathbf{L}) = \int_{\mathbf{l}} e^{-i\mathbf{l}\cdot\mathbf{r}}\, l\cos\mu_{\mathbf{l}}(l\cos\mu_{\mathbf{l}} - L)B_\phi(\mathbf{l}, \mathbf{L} - \mathbf{l}, -\mathbf{L}) \tag{C.17}$$

$$\bar{\beta}_\perp(\mathbf{r}, \mathbf{L}) = \int_{\mathbf{l}} e^{-i\mathbf{l}\cdot\mathbf{r}}\, (l)^2 \sin^2(\mu_{\mathbf{l}})B_\phi(\mathbf{l}, \mathbf{L} - \mathbf{l}, -\mathbf{L}), \tag{C.18}$$

which satisfies $\bar{\beta}_n(0, \mathbf{L}) = \beta_n(\mathbf{L})$. We also defined temperature correlation functions

$$\bar{\xi}_\parallel^{TT}(\mathbf{r}) = \int_{\mathbf{l}} e^{-i\mathbf{l}\cdot\mathbf{r}}\, l^2 \cos^2(\mu_{\mathbf{l}}) C_l^{TT} \tag{C.19}$$

$$= \frac{1}{2\pi} \left[\frac{1}{r} \int_0^\infty \mathrm{d}l\, l^2 J_1(lr) C_l^{TT} - \cos^2(\nu_{\mathbf{L}}) \int_0^\infty \mathrm{d}l\, l^3 J_2(lr) C_l^{TT} \right], \tag{C.20}$$

$$\bar{\xi}_\perp^{TT}(\mathbf{r}) = \int_{\mathbf{l}} e^{-i\mathbf{l}\cdot\mathbf{r}}\, l^2 \sin^2(\mu_{\mathbf{l}}) C_l^{TT} = \frac{1}{2\pi} \int_0^\infty \mathrm{d}l\, l^3 J_0(lr) C_l^{TT} - \bar{\xi}_\parallel^{TT}(\mathbf{r}, \mathbf{L}). \tag{C.21}$$

On the right hand sides, 2D Fourier transforms reduce to 1D Hankel transforms by using the cosine angle addition theorem to express $\cos\mu_{\mathbf{l}} = \hat{\mathbf{l}}\cdot\hat{\mathbf{L}}$ in terms of $\cos\nu_{\mathbf{L}} = \hat{\mathbf{L}}\cdot\hat{\mathbf{r}}$ and $\cos\nu_{\mathbf{l}} = \hat{\mathbf{l}}\cdot\hat{\mathbf{r}}$ (similarly to Eq. (C.1)). The angular integrals then lead to Bessel functions of the first kind, J_n. The 1D Hankel transforms can be evaluated efficiently with 1D FFTs using e.g., FFTLog [69]. A somewhat slower but still feasible approach is to evaluate the 2D Fourier transforms on a grid using 2D FFTs.

---

[1]This follows by introducing $\mathbf{l} = \mathbf{l}_1 - \mathbf{l}'$ in Eq. (B.2) with a Dirac delta,

$$\int_{\mathbf{l}_1, \mathbf{l}'} g_{\mathbf{l}_1, \mathbf{L}} C_{|\mathbf{l}_1 - \mathbf{l}'|}^{TT} [(\mathbf{l}_1 - \mathbf{l}')\cdot\mathbf{l}'][(\mathbf{l}_1 - \mathbf{l}')\cdot(\mathbf{L} - \mathbf{l}')] B_\phi(\mathbf{l}', \mathbf{L} - \mathbf{l}', -\mathbf{L})$$

$$= \int_{\mathbf{l}_1, \mathbf{l}, \mathbf{l}'} (2\pi)^2 \delta_D(\mathbf{l} - \mathbf{l}_1 + \mathbf{l}') g_{\mathbf{l}_1, \mathbf{L}} C_l^{TT}(\mathbf{l}\cdot\mathbf{l}')[\mathbf{l}\cdot(\mathbf{L} - \mathbf{l}')] B_\phi(\mathbf{l}', \mathbf{L} - \mathbf{l}', -\mathbf{L}), \tag{C.14}$$

expanding the Dirac delta in plane waves, and separating the scalar products using Eq. (C.2).

Appendix D

$N^{(3/2)}$ Type C1 Bias for polarization-based Lensing Reconstructions

The $N^{(3/2)}$ bias also exists for polarization-based lensing reconstructions. In this paper, we show how to generalize the non-Gaussian bias from the coupling type C1 (Eq. (3.20)) to reconstructions from arbitrary field combinations but leave a generalization of other contributing terms to future work. The results for the single coupling do not provide a proper quantitative estimate of the general bias, but give some idea of the qualitative changes and other terms can be derived in a similar fashion.

D.1 General polarization-based Lensing Reconstruction

We first consider the most general case where the lensing potential is reconstructed from two placeholder fields W and X that can each be T, E or B, and from two potentially different fields Y and Z that can again each be T, E, or B, and then the cross-spectrum of these reconstructions is used to estimate the lensing power, i.e., we consider $\langle \hat{\phi}^{WX} \hat{\phi}^{YZ} \rangle$ where $W, X, Y, Z \in \{T, E, B\}$ throughout this section.

Lensing changes the CMB fields according to

$$\tilde{X}(\mathbf{l}) = X(\mathbf{l}) + \delta X(\mathbf{l}) + \delta^2 X(\mathbf{l}), \tag{D.1}$$

where in absence of primordial gravitational waves [95, 101]

$$\delta X(\mathbf{l}) = -\int_{\mathbf{l}_1} \bar{X}(\mathbf{l}_1)\phi(\mathbf{l}-\mathbf{l}_1)h_X(\mathbf{l}_1,\mathbf{l})(\mathbf{l}-\mathbf{l}_1)\cdot\mathbf{l}_1 \tag{D.2}$$

$$\delta^2 X(\mathbf{l}) = -\frac{1}{2}\int_{\mathbf{l}_1,\mathbf{l}_2} \bar{X}(\mathbf{l}_1)\phi(\mathbf{l}_2)\phi(\mathbf{l}-\mathbf{l}_1-\mathbf{l}_2)h_X(\mathbf{l}_1,\mathbf{l})(\mathbf{l}_1\cdot\mathbf{l}_2)\left[(\mathbf{l}_1+\mathbf{l}_2-\mathbf{l})\cdot\mathbf{l}_1\right]. \tag{D.3}$$

To simplify the notation we also defined

$$\bar{T} \equiv T, \qquad \bar{E} \equiv E, \qquad \bar{B} \equiv E, \tag{D.4}$$

and

$$h_X(\mathbf{l}_1, \mathbf{l}) \equiv \begin{cases} 1 & \text{if } X = T, \\ \cos(2(\varphi_{\mathbf{l}_1} - \varphi_{\mathbf{l}})) & \text{if } X = E, \\ \sin(2(\varphi_{\mathbf{l}_1} - \varphi_{\mathbf{l}})) & \text{if } X = B, \end{cases} \tag{D.5}$$

which satisfies $h_X(\mathbf{l}_1, \mathbf{l}) = h_X(-\mathbf{l}_1, -\mathbf{l})$ and $h_X(\mathbf{l}_1, \mathbf{l}) = h_X(\mathbf{l}_1, -\mathbf{l}) = h_X(-\mathbf{l}_1, \mathbf{l})$.

The general lensing reconstruction estimator is [101]

$$\hat{\phi}^{WX}(\mathbf{L}) = A_L^{WX} \int_{\mathbf{l}} g_{WX}(\mathbf{l}, \mathbf{L}) \tilde{W}_{\text{expt}}(\mathbf{l}) \tilde{X}^*_{\text{expt}}(\mathbf{l} - \mathbf{L}), \tag{D.6}$$

with normalization

$$A_L^{WX} = \left[\int_{\mathbf{l}} f_{WX}(\mathbf{l}, \mathbf{L} - \mathbf{l}) g_{WX}(\mathbf{l}, \mathbf{L}) \right]^{-1} \tag{D.7}$$

and weight

$$g_{WX}(\mathbf{l}, \mathbf{L}) = \frac{C_{l,\text{expt}}^{\tilde{X}\tilde{X}} C_{|\mathbf{L}-\mathbf{l}|,\text{expt}}^{\tilde{W}\tilde{W}} f_{WX}(\mathbf{l}, \mathbf{L} - \mathbf{l}) - C_{l,\text{expt}}^{\tilde{W}\tilde{X}} C_{|\mathbf{L}-\mathbf{l}|,\text{expt}}^{\tilde{W}\tilde{X}} f_{WX}(\mathbf{L} - \mathbf{l}, \mathbf{l})}{C_{l,\text{expt}}^{\tilde{W}\tilde{W}} C_{|\mathbf{L}-\mathbf{l}|,\text{expt}}^{\tilde{X}\tilde{X}} C_{l,\text{expt}}^{\tilde{X}\tilde{X}} C_{|\mathbf{L}-\mathbf{l}|,\text{expt}}^{\tilde{W}\tilde{W}} - (C_{l,\text{expt}}^{\tilde{W}\tilde{X}} C_{|\mathbf{L}-\mathbf{l}|,\text{expt}}^{\tilde{W}\tilde{X}})^2}, \tag{D.8}$$

where f_{WX} is defined by $\langle \tilde{W}(\mathbf{l}) \tilde{X}(\mathbf{L} - \mathbf{l}) \rangle_{\text{CMB}} = f_{WX}(\mathbf{l}, \mathbf{L} - \mathbf{l}) \phi(\mathbf{L})$ and can be found in [101]. We assume a slightly modified form where unlensed spectra are replaced by lensed ones [72] to avoid the $N^{(2)}$ bias. Note that $f_{WX}(\mathbf{l}, \mathbf{L} - \mathbf{l}) = f_{XW}(\mathbf{L} - \mathbf{l}, \mathbf{l})$ and thus

$$g_{WX}(\mathbf{l}, \mathbf{L}) = g_{XW}(\mathbf{L} - \mathbf{l}, \mathbf{L}). \tag{D.9}$$

D.1.1 C1 Bias Contribution for general polarization-based Reconstruction

The type C contribution to the $N^{(3/2)}$ bias of the general reconstruction power $\langle \hat{\phi}^{WX} \hat{\phi}^{YZ} \rangle$ is

$$N_{WX,YZ}^{(3/2),\text{typeC}}(L) = A_L^{WX} A_L^{YZ} \int_{\mathbf{l}_1, \mathbf{l}_2} g_{WX}(\mathbf{l}_1, \mathbf{L}) g_{YZ}(\mathbf{l}_2, \mathbf{L}) \mathcal{T}_{WX,YZ}^{\text{typeC}}(\mathbf{l}_1, \mathbf{L} - \mathbf{l}_1, -\mathbf{l}_2, \mathbf{l}_2 - \mathbf{L}), \tag{D.10}$$

where the trispectrum is given by all contributions to $\langle \tilde{W}\tilde{X}\tilde{Y}\tilde{Z} \rangle_c$ that are of type C form $\langle \delta^2 W X \delta Y Z \rangle_c \sim$ '2010'. There are 8 such terms: 2010, 2001, 0210, 0201, 1020, 0120, 1002 and 0102, where '0' denotes the position of unperturbed fields and '1' and '2' that of first and second order perturbed fields. Let us denote the integral over the 2010 term by

$$U_{WX,YZ}(L) \equiv \int_{\mathbf{l}_1, \mathbf{l}_2} g_{WX}(\mathbf{l}_1, \mathbf{L}) g_{YZ}(\mathbf{l}_2, \mathbf{L}) \mathcal{T}_{WX,YZ}^{\text{typeC1}}(\mathbf{l}_1, \mathbf{L} - \mathbf{l}_1, -\mathbf{l}_2, \mathbf{l}_2 - \mathbf{L}) \tag{D.11}$$

$$= \int_{\mathbf{l}'_1, \mathbf{l}'_2} g_{WX}(\mathbf{L} - \mathbf{l}'_1, \mathbf{L}) g_{YZ}(\mathbf{L} - \mathbf{l}'_2, \mathbf{L}) \mathcal{T}_{WX,YZ}^{\text{typeC1}}(\mathbf{L} - \mathbf{l}'_1, \mathbf{l}'_1, \mathbf{l}'_2 - \mathbf{L}, -\mathbf{l}'_2), \tag{D.12}$$

where we changed integration variables in the second line. Using Eq. (D.9), $\mathcal{T}(-\mathbf{l}_1, -\mathbf{l}_2, -\mathbf{l}_3, -\mathbf{l}_4) = \mathcal{T}(\mathbf{l}_1, \mathbf{l}_2, \mathbf{l}_3, \mathbf{l}_4)$ and substitution of integration variables, the 8 type C terms contributing to Eq. (D.10) can be written simply by permuting field labels of U:

$$
\begin{aligned}
N_{WX,YZ}^{(3/2),\text{typeC}}(L) = &A_L^{WX} A_L^{YZ} \big[U_{WX,YZ}(L) + U_{WX,ZY}(L) + U_{XW,YZ}(L) + U_{XW,ZY}(L) \\
&+ U_{YZ,WX}(L) + U_{YZ,XW}(L) + U_{ZY,WX}(L) + U_{ZY,XW}(L) \big].
\end{aligned}
\tag{D.13}
$$

It remains to calculate $U_{WX,YZ}$. Extending Eq. (3.27) to the general polarization case, the connected 4-point function of coupling type C due to the 2010 contraction is

$$
\begin{aligned}
\langle \delta^2 W_{\mathbf{l}_1} X_{\mathbf{l}_2} \delta Y_{\mathbf{l}_3} Z_{\mathbf{l}_4} \rangle_c = &\frac{(2\pi)^2}{2} \delta_D(\mathbf{l}_1 + \mathbf{l}_2 + \mathbf{l}_3 + \mathbf{l}_4) C_{l_2}^{\bar{W}X} C_{l_4}^{\bar{Y}Z} h_W(-\mathbf{l}_2, \mathbf{l}_1) h_Y(-\mathbf{l}_4, \mathbf{l}_3) \\
&\times [(\mathbf{l}_3 + \mathbf{l}_4) \cdot \mathbf{l}_4] \int_{\mathbf{l}'} (\mathbf{l}' \cdot \mathbf{l}_2) [(\mathbf{l}_1 + \mathbf{l}_2 - \mathbf{l}') \cdot \mathbf{l}_2] B_\phi(\mathbf{l}', \mathbf{l}_1 + \mathbf{l}_2 - \mathbf{l}', \mathbf{l}_3 + \mathbf{l}_4) \\
&+ (\mathbf{l}_2 \leftrightarrow \mathbf{l}_4, X \leftrightarrow Z),
\end{aligned}
\tag{D.14}
$$

where the permutation in the last line is obtained by simultaneously replacing every $\mathbf{l}_2$ by $\mathbf{l}_4$, every $\mathbf{l}_4$ by $\mathbf{l}_2$, every X by Z and every Z by X in the first two lines (in particular, this permutation involves $C_{l_4}^{\bar{W}Z} C_{l_2}^{\bar{Y}X}$). We ignore this permutation in the last line of Eq. (D.14) from now on because it is expected to lead to more tightly coupled terms that should be subdominant; we call the dominant first two lines 'typeC1'. For the multipole arguments required for Eq. (D.12) we get

$$
\begin{aligned}
\langle \delta^2 W_{\mathbf{L}-\mathbf{l}_1} X_{\mathbf{l}_1} \delta Y_{\mathbf{l}_2-\mathbf{L}} Z_{-\mathbf{l}_2} \rangle_c^{\text{typeC1}} = &\frac{(2\pi)^2}{2} \delta_D(\mathbf{0}) C_{l_1}^{\bar{W}X} C_{l_2}^{\bar{Y}Z} h_W(-\mathbf{l}_1, \mathbf{L} - \mathbf{l}_1) h_Y(\mathbf{l}_2, \mathbf{l}_2 - \mathbf{L})(\mathbf{L} \cdot \mathbf{l}_2) \\
&\times \int_{\mathbf{l}'} (\mathbf{l}' \cdot \mathbf{l}_1) [(\mathbf{L} - \mathbf{l}') \cdot \mathbf{l}_1] B_\phi(\mathbf{l}', \mathbf{L} - \mathbf{l}', -\mathbf{L}).
\end{aligned}
\tag{D.15}
$$

Thus,

$$
\begin{aligned}
U_{WX,YZ}(L) = &\frac{1}{2} \int_{\mathbf{l}_1, \mathbf{l}_2} g_{WX}(\mathbf{L} - \mathbf{l}_1, \mathbf{L}) g_{YZ}(\mathbf{L} - \mathbf{l}_2, \mathbf{L}) C_{l_1}^{\bar{W}X} C_{l_2}^{\bar{Y}Z} h_W(-\mathbf{l}_1, \mathbf{L} - \mathbf{l}_1) h_Y(\mathbf{l}_2, \mathbf{l}_2 - \mathbf{L}) \\
&\times (\mathbf{L} \cdot \mathbf{l}_2) \int_{\mathbf{l}} [\mathbf{l}_1 \cdot (\mathbf{L} - \mathbf{l})] [\mathbf{l}_1 \cdot \mathbf{l}] B_\phi(\mathbf{l}, \mathbf{L} - \mathbf{l}, -\mathbf{L}).
\end{aligned}
\tag{D.16}
$$

The weights in the last integral can be expressed in the separable form of Eq. (3.29). Then,

$$
U_{WX,YZ}(L) = -\frac{1}{2} \left[\int_{\mathbf{l}_2} g_{ZY}(\mathbf{l}_2, \mathbf{L}) h_Y(\mathbf{l}_2, \mathbf{l}_2 - \mathbf{L})(\mathbf{L} \cdot \mathbf{l}_2) C_{l_2}^{\bar{Y}Z} \right] \sum_{n \in \{\|, +, \perp\}} R_n^{WX}(\mathbf{L}) \beta_n(\mathbf{L})
\tag{D.17}
$$

where β_n integrals are the same as in Eqs. (3.31), (3.33), and we defined

$$
R_\|^{WX}(\mathbf{L}) = \int_{\mathbf{l}_1} g_{XW}(\mathbf{l}_1, \mathbf{L}) l_1^2 \cos^2(\mu_{\mathbf{l}_1}) h_W(-\mathbf{l}_1, \mathbf{L} - \mathbf{l}_1) C_{l_1}^{\bar{W}X}
\tag{D.18}
$$

$$
R_+^{WX}(\mathbf{L}) = \int_{\mathbf{l}_1} g_{XW}(\mathbf{l}_1, \mathbf{L}) l_1^2 \sin(\mu_{\mathbf{l}_1}) \cos(\mu_{\mathbf{l}_1}) h_W(-\mathbf{l}_1, \mathbf{L} - \mathbf{l}_1) C_{l_1}^{\bar{W}X}
\tag{D.19}
$$

$$
R_\perp^{WX}(\mathbf{L}) = \int_{\mathbf{l}_1} g_{XW}(\mathbf{l}_1, \mathbf{L}) l_1^2 \sin^2(\mu_{\mathbf{l}_1}) h_W(-\mathbf{l}_1, \mathbf{L} - \mathbf{l}_1) C_{l_1}^{\bar{W}X}.
\tag{D.20}
$$

When evaluating h_W numerically, the angle $2(\varphi_{\mathbf{l}_1} - \varphi_{\mathbf{L}-\mathbf{l}_1})$ can be obtained brute-force from the components of 2D vectors $\mathbf{l}_1$ and $\mathbf{L}$. [1] In the special case of a temperature-only based measurement we recover the previously derived results with $R_n^{TT} = R_n$. The final $N_{C1}^{(3/2)}$ bias for polarization is obtained by plugging Eq. (D.17) into Eq. (D.13)

$$N_{WX,YZ}^{(3/2),\text{typeC1}}(L) = -\frac{1}{2} A_L^{WX} A_L^{YZ} S_L^{YZ} \sum_{n \in \{\|,+,\perp\}} R_n^{WX}(\mathbf{L}) \beta_n(\mathbf{L}) + 7 \text{ perms in } W, X; Y, Z$$

$$(D.21)$$

where the permutations denote those written out in Eq. (D.13). We also defined

$$S_L^{YZ} \equiv \left[\int_{\mathbf{l}_2} g_{ZY}(\mathbf{l}_2, \mathbf{L}) h_Y(\mathbf{l}_2, \mathbf{l}_2 - \mathbf{L})(\mathbf{L} \cdot \mathbf{l}_2) C_{l_2}^{\bar{Y}Z} \right]. \tag{D.22}$$

One can show that $S_L^{YZ} + S_L^{ZY} = A_L^{-1}$ to first order in $C^{\phi\phi}$. This identity also holds for field combinations where one of the S_L^{YZ} terms is zero (e.g., S_L^{EB}).

Eq. (D.21) involves the same integrals β_n over the lensing bispectrum B_ϕ as the temperature reconstruction bias. The 2D integrals over CMB power spectra R_n^{WX} have a similar form as for the temperature-only case, with slightly different weights in the integrands. For $(WX, YZ) = (TT, TT)$ the general bias formula $N_{WX,YZ}^{(3/2),\text{typeC1}}(L)$ simplifies to the expression derived for the temperature Eq. (3.29).

D.1.2   C1 Bias Contribution for (EB, EB) Reconstruction

The special case of (EB, EB)-reconstruction is expected to have relatively high signal-to-noise in comparison with the other polarization-based lensing estimators. In this case, we have $W = Y = E$ and $X = Z = B$ so that the $N^{(3/2)}$ bias becomes

$$N_{EB,EB}^{(3/2),\text{typeC1}}(L) =$$
$$- (A_L^{EB})^2 \sum_{n \in \{\|,+,\perp\}} \beta_n(\mathbf{L}) \left[S_L^{EB} R_n^{EB}(\mathbf{L}) + S_L^{EB} R_n^{BE}(\mathbf{L}) + S_L^{BE} R_n^{EB}(\mathbf{L}) + S_L^{BE} R_n^{BE}(\mathbf{L}) \right].$$

$$(D.23)$$

We can further simplify Eq. (D.23) by noting that $R_n^{EB} = 0$ and $S_L^{EB} = 0$ (which follows from $C_l^{EB} = 0$) and obtain

$$N_{EB,EB}^{(3/2),\text{typeC1}}(L) = -(A_L^{EB})^2 S_L^{BE} \sum_{n \in \{\|,+,\perp\}} \beta_n(\mathbf{L}) R_n^{BE}(\mathbf{L}), \tag{D.24}$$

where R_n^{BE} are integrals over the E-mode power spectrum given by Eqs. (D.18)-(D.20), and β_n are integrated lensing bispectra computed earlier in Eqs. (3.31), (3.33).

---

[1] Explicitly, defining angles with respect to the x-axis, we have $\varphi_{\mathbf{l}_1} = \arccos\left[l_{1,x} / \sqrt{l_{1,x}^2 + l_{1,y}^2} \right]$ and $\varphi_{\mathbf{L}-\mathbf{l}_1} = \arccos\left[(L_x - l_{1,x}) / \sqrt{(L_x - l_{1,x})^2 + (L_y - l_{1,y})^2} \right]$.

Appendix E

Low-L, large-scale Lens and squeezed Limits

In this section we consider certain limits where the $N^{(3/2)}$ bias simplifies, e.g., the limit of reconstructing large-scale lenses from small-scale temperature fluctuations, or the squeezed limit of the lensing bispectrum. This is useful to understand the qualitative behavior of the bias and check the robustness of numerical evaluations. We first discuss the C1 term in Eq. (3.20), and then the A1 term in Eq. (3.18).

E.1   Limit of C1 Contribution to $N^{(3/2)}$ Bias

We first consider the limit of reconstructing large-scale lensing modes $\phi(\mathbf{L})$ from temperature fluctuations $T(\mathbf{l})$ on much smaller scales, i.e., $L \ll l$. Taylor expanding $|\mathbf{l} - \mathbf{L}|$ around l yields for the lensing reconstruction weight

$$
\lim_{L \ll l} g_{\mathbf{l},\mathbf{L}} = \frac{L^2}{2} \frac{C_l^{\tilde{T}\tilde{T}}}{(C_{l,\text{expt}}^{\tilde{T}\tilde{T}})^2} \left\{ \left[1 + \frac{\mathrm{d} \ln C_l^{\tilde{T}\tilde{T}}}{\mathrm{d} \ln l} \cos^2 \mu_{\mathbf{l}} \right] \right.
$$
$$
\left. + \frac{L}{l} \left[\frac{\mathrm{d} \ln C_l^{\tilde{T}\tilde{T}}}{\mathrm{d} \ln l} \frac{\mathrm{d} \ln C_{l,\text{expt}}^{\tilde{T}\tilde{T}}}{\mathrm{d} \ln l} \cos^3 \mu_{\mathbf{l}} - \frac{\mathrm{d} \ln \left(\frac{C_l^{\tilde{T}\tilde{T}}}{C_{l,\text{expt}}^{\tilde{T}\tilde{T}}} \right)}{\mathrm{d} \ln l} \cos \mu_{\mathbf{l}} \right] \right\}, \qquad \text{(E.1)}
$$

where $\cos \mu_{\mathbf{l}} = \mathbf{l} \cdot \mathbf{L}/(lL)$. The terms in the first square brackets of Eq. (E.1) are of order $(L/l)^0$ and involve only even powers of $\cos \mu_{\mathbf{l}}$, while the second square bracket is of order $(L/l) \ll 1$ and involves only odd powers of $\cos \mu_{\mathbf{l}}$.

Using this, we can compute the large-lens limit of $R_{\parallel}$ defined in Eq. (3.30). The terms

in the second square brackets vanish upon angular integration so that

$$
\begin{aligned}
\lim_{L \to 0} R_\parallel(L) &= \frac{L^2}{8\pi} \int \mathrm{d}l_1 l_1^3 \frac{C_{l_1}^{TT} C_{l_1}^{\tilde{T}\tilde{T}}}{(C_{l_1,\mathrm{expt}}^{\tilde{T}\tilde{T}})^2} \left[1 + \frac{3}{4} \frac{\mathrm{d}\ln C_{l_1}^{\tilde{T}\tilde{T}}}{\mathrm{d}\ln l_1} \right] + \mathcal{O}\left((L/l_1)^2 \right) \\
&\approx \frac{3L^2}{32\pi} \int \mathrm{d}l_1 l_1^3 \left(\frac{C_{l_1}^{\tilde{T}\tilde{T}}}{C_{l_1,\mathrm{expt}}^{\tilde{T}\tilde{T}}} \right)^2 \left[\frac{\mathrm{d}\ln l_1^{4/3} C_{l_1}^{\tilde{T}\tilde{T}}}{\mathrm{d}\ln l_1} \right] + \mathcal{O}\left((L/l_1)^2 \right).
\end{aligned}
\tag{E.2}
$$

The power spectrum ratio in the integrand is unity on scales where the temperature power spectrum is signal-dominated and gets exponentially suppressed when it becomes noise-dominated. The l_1^3 weight upweights high l_1 in the signal-dominated regime but cannot compete against the exponential fall-off in the noise-dominated regime. These two factors are thus maximal at the highest l_1 that are still signal-dominated. In this regime, typically $l_1 \sim$ few thousand, the derivative is mostly negative, so that the overall large-lens limit of $R_\parallel$ is negative. Its amplitude is determined by the multipole at which the temperature power becomes noise dominated, i.e., it is very sensitive to the noise and beam specifications of the experiment under consideration.

The large-lens limit of $R_\perp$ reads

$$
\begin{aligned}
\lim_{L \to 0} R_\perp(L) &= \frac{L^2}{8\pi} \int \mathrm{d}l_1 \, l_1^3 \frac{C_{l_1}^{TT} C_{l_1}^{\tilde{T}\tilde{T}}}{\left(C_{l_1,\mathrm{expt}}^{\tilde{T}\tilde{T}} \right)^2} \left[1 + \frac{1}{4} \frac{\mathrm{d}\ln C_{l_1}^{\tilde{T}\tilde{T}}}{\mathrm{d}\ln l_1} \right] + \mathcal{O}\left((L/l_1)^2 \right). \\
&\approx \frac{L^2}{32\pi} \int \mathrm{d}l_1 \, l_1^3 \left(\frac{C_{l_1}^{\tilde{T}\tilde{T}}}{C_{l_1,\mathrm{expt}}^{\tilde{T}\tilde{T}}} \right)^2 \frac{\mathrm{d}\ln(l_1^4 C_{l_1}^{\tilde{T}\tilde{T}})}{\mathrm{d}\ln l_1} + \mathcal{O}\left((L/l_1)^2 \right).
\end{aligned}
\tag{E.3}
$$

which has the same structure as the expression that was derived for $R_\parallel$, the only difference being a suppression of the derivative term by a factor of 3. It is thus similarly sensitive to beam and noise specifications as $R_\parallel$, but smaller, since the dominant contribution stems from the derivative.

Additionally to the R_n integrals the $N_{C1}^{(3/2)}$ bias involves β_n integrals over the lensing bispectrum defined in Eqs. (3.31) and (3.33). One limit where these simplify is the squeezed limit of the lensing bispectrum, where the reconstructed lensing mode is on much larger scales than the other two internal lensing modes, i.e., $L \ll l \approx |\mathbf{l} - \mathbf{L}|$ and

$$
\begin{aligned}
\lim_{L \ll l} B_\phi(L, l, -\cos\mu_{\mathbf{l}}) = \int_0^{\chi_*} \mathrm{d}\chi \frac{W(\chi)^3}{\chi^4} \frac{\gamma^3(\chi)}{(L/\chi)^2 (l/\chi)^4} \left(1 + 2\frac{L}{l}\cos\mu_{\mathbf{l}} \right) \\
\times \lim_{L \ll l} B_\delta(L/\chi, l/\chi, -\cos\mu_{\mathbf{l}}; \chi),
\end{aligned}
\tag{E.4}
$$

where we insert the squeezed limit of the matter bispectrum (e.g., [38])

$$
\begin{aligned}
\lim_{k_1 \ll k_2} B_\delta(k_1, k_2, \cos\mu_{\mathbf{l}}) = P_{k_1}(\chi) P_{k_2}(\chi) \Big[\frac{13}{7} + \cos^2\mu_{\mathbf{l}} \left(\frac{8}{7} - \frac{\partial \ln P_{k_2}(\chi)}{\partial \ln k_2} \right) \\
+ \frac{k_1}{k_2} \left(\frac{8}{7} - \frac{8}{7}\cos^2\mu_{\mathbf{l}} + \left(\frac{3}{7}\frac{\partial \ln P_{k_2}(\chi)}{\partial \ln k_2} - 1 \right)\cos\mu_{\mathbf{l}} + \left(\frac{4}{7}\frac{\partial \ln P_{k_2}(\chi)}{\partial \ln k_2} + 1 \right)\cos^3\mu_{\mathbf{l}} \right) \Big],
\end{aligned}
\tag{E.5}
$$

assuming that limits in l translate to limits in k in the Limber approximation. In this approximation the angle $\mu_{\mathbf{l}}$ between $\mathbf{L}$ and $\mathbf{l}$ is the same as between the 3D modes $\vec{k}_1$ and $\vec{k}_2{}^1$.

Using Eq. (E.4) in the expression for $\beta_\parallel$ we find for the contribution from squeezed bispectrum configurations

$$
\begin{aligned}
\lim_{L \ll l} \beta_\parallel(L) &= \int_1 l \left(l \cos^2(\mu_{\mathbf{l}}) - L \cos(\mu_{\mathbf{l}}) \right) \lim_{L \ll l} B_\phi(L, l, -\cos\mu_{\mathbf{l}}) \\
&= \int_1 l^2 \left(\cos^2(\mu_{\mathbf{l}}) - \frac{L}{l} \cos(\mu_{\mathbf{l}}) \right) \int_0^{\chi*} \mathrm{d}\chi W(\chi)^3 \chi^2 \frac{\gamma^3(\chi)}{L^2 l^4} \left(1 + 2\frac{L}{l} \cos\mu_{\mathbf{l}} \right) \\
&\quad \times \lim_{L \ll l} B_\delta(L/\chi, l/\chi, -\cos\mu_{\mathbf{l}}; \chi),
\end{aligned}
\tag{E.6}
$$

Upon angular integration the squared cosine picks up all terms that are even in the cosine. This includes all contributions of order $\mathcal{O}((\frac{L}{l})^0)$,

$$
\lim_{L \ll l} \beta_\parallel(L) = \frac{1}{L^2} \int_0^{\chi*} \mathrm{d}\chi W(\chi)^3 \chi^2 \gamma^3(\chi)
\tag{E.7}
$$

$$
\times \int \frac{\mathrm{d}\ln l}{4\pi} \left[\frac{13}{7} + \frac{3}{4} \left(\frac{8}{7} - n(l, \chi) \right) + \frac{2}{7} \frac{L}{l} \right] P_{L/\chi}(\chi) P_{l/\chi}(\chi),
\tag{E.8}
$$

where we defined the spectral index of the matter power spectrum

$$
n(l, \chi) = \frac{\partial \ln P_{l/\chi}(\chi)}{\partial \ln(l/\chi)}.
\tag{E.9}
$$

The squeezed limit of $\beta_\perp$ is

$$
\begin{aligned}
\lim_{L \ll l} \beta_\perp(L) &= \int_1 l^2 \sin^2(\mu_{\mathbf{l}}) \lim_{L \ll l} B_\phi(L, l, -\cos\mu_{\mathbf{l}}) \\
&= \frac{1}{L^2} \int_0^{\chi*} \mathrm{d}\chi W(\chi)^3 \chi^2 \gamma^3(\chi)
\end{aligned}
\tag{E.10}
$$

$$
\times \int \frac{\mathrm{d}\ln l}{4\pi} \left[\frac{13}{7} + \frac{1}{4} \left(\frac{8}{7} - n(l, \chi) \right) + \frac{6}{7} \frac{L}{l} \right] P_{L/\chi}(\chi) P_{l/\chi}(\chi),
\tag{E.11}
$$

which is similar to the limit of $\beta_\parallel$ but smaller since the zeroth order term in round brackets gets suppressed by a factor of 3 (the first order term is enhanced by the same factor). The limits of both integrals, $\beta_\perp$ and $\beta_\parallel$, are positive for any realistic value of the spectral index n. This agrees with the results obtained by numerical integration over the full bispectrum.

In Fig. E.1 we plot $\beta_\parallel$ and $\beta_\perp$ and their squeezed limits. Since the squeezed configuration excludes triangle configurations with small and comparable side lengths, the squeezed limits do not coincide with the full integrals at low L. For a valid comparison, the numerical result has to be restricted to squeezed configurations. After this modification they agree with the analytically derived limits.
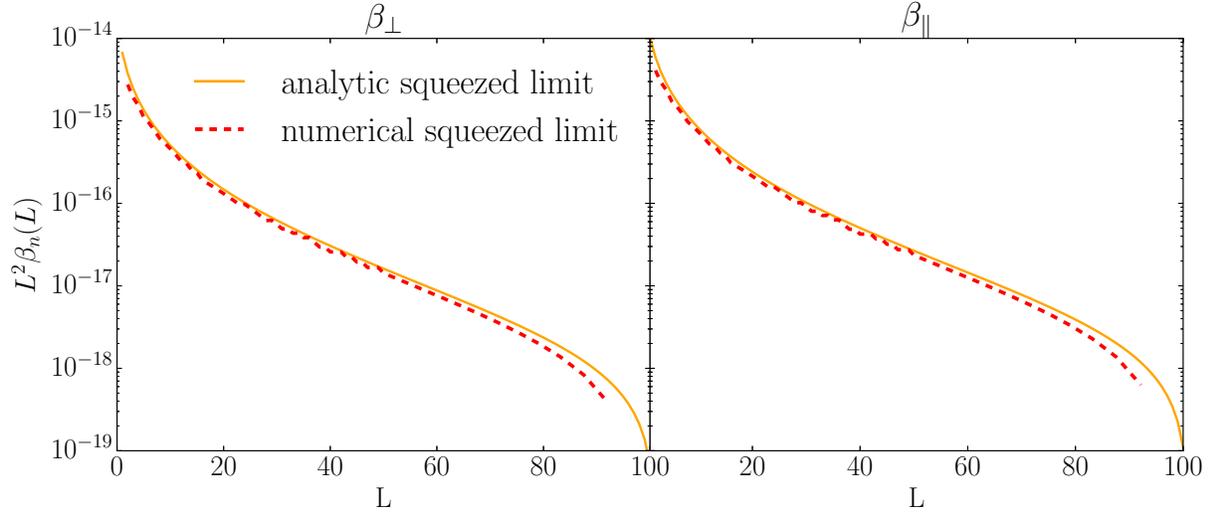
Figure E.1:   Integrals of type $\beta_{\parallel}$ and $\beta_{\perp}$ calculated numerically with a restriction to squeezed triangle configurations ($l/L>100$) and their analytic squeezed limits [Eq. (E.7), (E.10)].
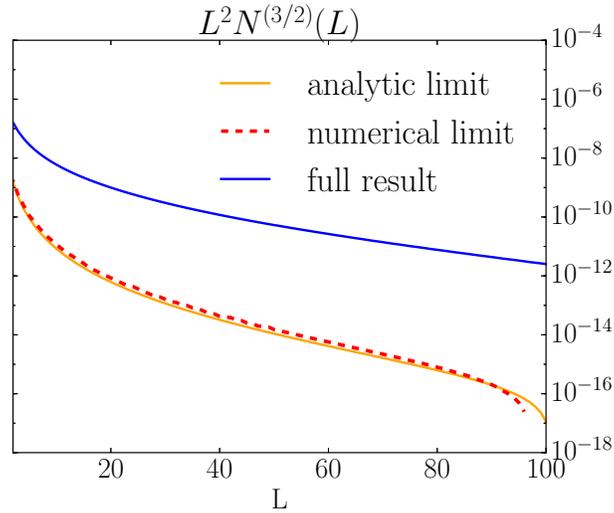
Figure E.2:   The large-lens and squeezed limit of $\lim_{L\to0} -2A_L\beta_{\parallel}(L)R_{\parallel}(L)$ [Eq. (E.14)], the dominant contribution to $N_{C1}^{(3/2)}$ for small L. Since we take the limit where only squeezed triangle configurations contribute to the lensing or matter bispectrum, we also have to restrict the numerical evaluation to squeezed triangle configurations to find agreement.

To obtain the large-lens and squeezed limit of the $N^{(3/2)}$ bias we also need the large-scale limit of A_L which is [72]

$$\lim_{L\to 0} A_L = \frac{8\pi}{L^4} \left[\sum_l (2l+1) \left(\frac{C_l^{\tilde{T}\tilde{T}}}{C_{l,\text{expt}}^{\tilde{T}\tilde{T}}} \right)^2 D_l \right]^{-1}, \tag{E.12}$$

where

$$D_l = 1 + \frac{\mathrm{d}\ln C_l^{TT}}{\mathrm{d}\ln l} + \frac{3}{8} \left(\frac{\mathrm{d}\ln C_l^{TT}}{\mathrm{d}\ln l} \right)^2. \tag{E.13}$$

Putting all these results together we obtain for the large-lens and squeezed limit of $N^{(3/2)}$ (which is dominated by the $\beta_\| R_\|$ term)

$$\lim_{L\to 0} -2A_L R_\|(L)[\beta_\|(L)]_{\text{squeezed}} = -2 \left[\sum_l (2l+1) \left(\frac{C_l^{\tilde{T}\tilde{T}}}{C_{l,\text{expt}}^{\tilde{T}\tilde{T}}} \right)^2 D_l \right]^{-1}$$

$$\times \left[\sum_{l_1} \frac{(l_1)^3}{(L+1)^2} \left(\frac{C_{l_1}^{\tilde{T}\tilde{T}}}{C_{l_1,\text{expt}}^{\tilde{T}\tilde{T}}} \right)^2 \frac{\mathrm{d}\ln(l^2 C_{l_1}^{\tilde{T}\tilde{T}})}{\mathrm{d}\ln l_1} \right] \lim_{L\to 0} [\beta_\|(L)]_{\text{squeezed}}. \tag{E.14}$$

The comparison with the full result is shown in Fig. E.2. For $\lim_{L\to 0}[\beta_\|(L)]_{\text{squeezed}}$ we use the squeezed limit of $\beta_\|$ which we obtain in two ways: (1) by evaluating the analytic limit given in Eq. (E.7), and (2) by restricting the full numerical result to squeezed triangle configurations of the bispectrum.

---

[1]Note that the integrals over the lensing bispectrum (Eqs.3.33 and 3.31) integrate over $B_\phi(\vec{l}, \vec{L}-\vec{l}, -\vec{L})$. The minus sign in front of the bispectrum's third argument, $\vec{L}$, induces a minus sign in front of $\cos\mu_{\vec{l}}$ when inserting the squeezed limit of the matter bispectrum into these integrals.

Bibliography

[1] K. N. Abazajian, P. Adshead, Z. Ahmed, S. W. Allen, D. Alonso, K. S. Arnold, C. Baccigalupi, J. G. Bartlett, N. Battaglia, B. A. Benson, C. A. Bischoff, J. Borrill, V. Buza, E. Calabrese, R. Caldwell, J. E. Carlstrom, C. L. Chang, T. M. Crawford, F.-Y. Cyr-Racine, F. De Bernardis, T. de Haan, S. di Serego Alighieri, J. Dunkley, C. Dvorkin, J. Errard, G. Fabbian, S. Feeney, S. Ferraro, J. P. Filippini, R. Flauger, G. M. Fuller, V. Gluscevic, D. Green, D. Grin, E. Grohs, J. W. Henning, J. C. Hill, R. Hlozek, G. Holder, W. Holzapfel, W. Hu, K. M. Huffenberger, R. Keskitalo, L. Knox, A. Kosowsky, J. Kovac, E. D. Kovetz, C.-L. Kuo, A. Kusaka, M. Le Jeune, A. T. Lee, M. Lilley, M. Loverde, M. S. Madhavacheril, A. Mantz, D. J. E. Marsh, J. McMahon, P. D. Meerburg, J. Meyers, A. D. Miller, J. B. Munoz, H. N. Nguyen, M. D. Niemack, M. Peloso, J. Peloton, L. Pogosian, C. Pryke, M. Raveri, C. L. Reichardt, G. Rocha, A. Rotti, E. Schaan, M. M. Schmittfull, D. Scott, N. Sehgal, S. Shandera, B. D. Sherwin, T. L. Smith, L. Sorbo, G. D. Starkman, K. T. Story, A. van Engelen, J. D. Vieira, S. Watson, N. Whitehorn, and W. L. Kimmy Wu. CMB-S4 Science Book, First Edition. *ArXiv e-prints*, October 2016, 1610.02743.

[2] T. Abbott, F. B. Abdalla, S. Allam, A. Amara, J. Annis, R. Armstrong, D. Bacon, M. Banerji, A. H. Bauer, E. Baxter, M. R. Becker, A. Benoit-Lévy, R. A. Bernstein, G. M. Bernstein, E. Bertin, J. Blazek, C. Bonnett, S. L. Bridle, D. Brooks, C. Bruderer, E. Buckley-Geer, D. L. Burke, M. T. Busha, D. Capozzi, A. Carnero Rosell, M. Carrasco Kind, J. Carretero, F. J. Castander, C. Chang, J. Clampitt, M. Crocce, C. E. Cunha, C. B. D'Andrea, L. N. da Costa, R. Das, D. L. DePoy, S. Desai, H. T. Diehl, J. P. Dietrich, S. Dodelson, P. Doel, A. Drlica-Wagner, G. Efstathiou, T. F. Eifler, B. Erickson, J. Estrada, A. E. Evrard, A. Fausti Neto, E. Fernandez, D. A. Finley, B. Flaugher, P. Fosalba, O. Friedrich, J. Frieman, C. Gangkofner, J. Garcia-Bellido, E. Gaztanaga, D. W. Gerdes, D. Gruen, R. A. Gruendl, G. Gutierrez, W. Hartley, M. Hirsch, K. Honscheid, E. M. Huff, B. Jain, D. J. James, M. Jarvis, T. Kacprzak, S. Kent, D. Kirk, E. Krause, A. Kravtsov, K. Kuehn, N. Kuropatkin, J. Kwan, O. Lahav, B. Leistedt, T. S. Li, M. Lima, H. Lin, N. MacCrann, M. March, J. L. Marshall, P. Martini, R. G. McMahon, P. Melchior, C. J. Miller, R. Miquel, J. J. Mohr, E. Neilsen, R. C. Nichol, A. Nicola, B. Nord, R. Ogando, A. Palmese, H. V. Peiris, A. A. Plazas, A. Refregier, N. Roe, A. K. Romer, A. Roodman, B. Rowe, E. S. Rykoff, C. Sabiu, I. Sadeh, M. Sako, S. Samuroff, E. Sanchez, C. Sánchez, H. Seo, I. Sevilla-Noarbe, E. Sheldon, R. C. Smith, M. Soares-Santos, F. Sobreira, E. Suchyta,

M. E. C. Swanson, G. Tarle, J. Thaler, D. Thomas, M. A. Troxel, V. Vikram, A. R. Walker, R. H. Wechsler, J. Weller, Y. Zhang, J. Zuntz, and Dark Energy Survey Collaboration. Cosmology from cosmic shear with Dark Energy Survey Science Verification data. *Physical Review D*, 94(2):022001, July 2016, 1507.05552.

[3] P. A. R. Ade, Y. Akiba, A. E. Anthony, K. Arnold, M. Atlas, D. Barron, D. Boettger, J. Borrill, C. Borys, S. Chapman, Y. Chinone, M. Dobbs, T. Elleflot, J. Errard, G. Fabbian, C. Feng, D. Flanigan, A. Gilbert, W. Grainger, N. W. Halverson, M. Hasegawa, K. Hattori, M. Hazumi, W. L. Holzapfel, Y. Hori, J. Howard, P. Hyland, Y. Inoue, G. C. Jaehnig, A. Jaffe, B. Keating, Z. Kermish, R. Keskitalo, T. Kisner, M. Le Jeune, A. T. Lee, E. M. Leitch, E. Linder, M. Lungu, F. Matsuda, T. Matsumura, X. Meng, N. J. Miller, H. Morii, S. Moyerman, M. J. Myers, M. Navaroli, H. Nishino, H. Paar, J. Peloton, D. Poletti, E. Quealy, G. Rebeiz, C. L. Reichardt, P. L. Richards, C. Ross, K. Rotermund, I. Schanning, D. E. Schenck, B. D. Sherwin, A. Shimizu, C. Shimmin, M. Shimon, P. Siritanasak, G. Smecher, H. Spieler, N. Stebor, B. Steinbach, R. Stompor, A. Suzuki, S. Takakura, A. Tikhomirov, T. Tomaru, B. Wilson, A. Yadav, O. Zahn, and Polarbear Collaboration. Evidence for Gravitational Lensing of the Cosmic Microwave Background Polarization from Cross-Correlation with the Cosmic Infrared Background. *Physical Review Letters*, 112(13):131302, April 2014, 1312.6645.

[4] J. Alsing, A. Heavens, A. H. Jaffe, A. Kiessling, B. Wandelt, and T. Hoffmann. Hierarchical cosmic shear power spectrum inference. *Monthly Notices of the Royal Astronomical Society*, 455:4452–4466, February 2016, 1505.07840.

[5] A. Amblard, C. Vale, and M. White. Weak lensing of the CMB by large-scale structure. *New Astronomy*, 9:687–704, October 2004, astro-ph/0403075.

[6] L. Amendola, M. Kunz, and D. Sapone. Measuring the dark side (with weak lensing). *Journal of Cosmology and Astroparticle Physics*, 4:013, April 2008, 0704.2421.

[7] E. Anderes. Decomposing CMB lensing power with simulation. *Physical Review D*, 88(8):083517, October 2013, 1301.2576.

[8] E. Anderes, B. D. Wandelt, and G. Lavaux. Bayesian Inference of CMB Gravitational Lensing. *The Astrophysical Journal*, 808:152, August 2015, 1412.4079.

[9] R. E. Angulo, V. Springel, S. D. M. White, A. Jenkins, C. M. Baugh, and C. S. Frenk. Scaling relations for galaxy clusters in the Millennium-XXL simulation. *Monthly Notices of the Royal Astronomical Society*, 426:2046–2062, November 2012, 1203.3216.

[10] C. Antolini, Y. Fantaye, M. Martinelli, C. Carbone, and C. Baccigalupi. N-body lensed CMB maps: lensing extraction and characterization. *Journal of Cosmology and Astroparticle Physics*, 2:039, February 2014, 1311.7112.

[11] D. J. Bacon, A. R. Refregier, and R. S. Ellis. Detection of weak gravitational lensing by large-scale structure. *Monthly Notices of the Royal Astronomical Society*, 318:625–640, October 2000, astro-ph/0003008.

[12] M. Bartelmann and P. Schneider. Weak gravitational lensing. *Physics Reports*, 340:291–472, January 2001, astro-ph/9912508.

[13] N. Bartolo, S. Matarrese, and A. Riotto. Non-Gaussianity and the Cosmic Microwave Background Anisotropies. *Advances in Astronomy*, 2010:157079, 2010, 1001.3957.

[14] S. Basak, S. Prunet, and K. Benabed. Simulating weak lensing on CMB maps. *ArXiv e-prints*, November 2008, 0811.1677.

[15] J. Benjamin, L. Van Waerbeke, C. Heymans, M. Kilbinger, T. Erben, H. Hildebrandt, H. Hoekstra, T. D. Kitching, Y. Mellier, L. Miller, B. Rowe, T. Schrabback, F. Simpson, J. Coupon, L. Fu, J. Harnois-Déraps, M. J. Hudson, K. Kuijken, E. Semboloni, S. Vafaei, and M. Velander. CFHTLenS tomographic weak lensing: quantifying accurate redshift distributions. *Monthly Notices of the Royal Astronomical Society*, 431:1547–1564, May 2013, 1212.3327.

[16] Jonathan Benjamin, Catherine Heymans, Elisabetta Semboloni, Ludovic Van Waerbeke, Henk Hoekstra, Thomas Erben, Michael D. Gladders, Marco Hetterscheidt, Yannick Mellier, and H. K. C. Yee. Cosmological constraints from the 100-deg2 weak-lensing survey. *Monthly Notices of the Royal Astronomical Society*, 381(2):702, 2007.

[17] F. Bernardeau, S. Colombi, E. Gaztañaga, and R. Scoccimarro. Large-scale structure of the Universe and cosmological perturbation theory. *Physics Reports*, 367:1–248, September 2002, astro-ph/0112551.

[18] F. Bernardeau, L. van Waerbeke, and Y. Mellier. Weak lensing statistics as a probe of Ω and power spectrum. *Astronomy and Astrophysics*, 322:1–18, June 1997, astro-ph/9609122.

[19] G. M. Bernstein and R. Armstrong. Bayesian lensing shear measurement. *Monthly Notices of the Royal Astronomical Society*, 438:1880–1893, February 2014, 1304.1843.

[20] F. Bianchini, P. Bielewicz, A. Lapi, J. Gonzalez-Nuevo, C. Baccigalupi, G. de Zotti, L. Danese, N. Bourne, A. Cooray, L. Dunne, S. Dye, S. Eales, R. Ivison, S. Maddox, M. Negrello, D. Scott, M. W. L. Smith, and E. Valiante. Cross-correlation between the CMB Lensing Potential Measured by Planck and High-z Submillimeter Galaxies Detected by the Herschel-Atlas Survey. *The Astrophysical Journal*, 802:64, March 2015, 1410.4502.

[21] A. Blanchard and J. Schneider. Gravitational lensing effect on the fluctuations of the cosmic background radiation. *Astronomy and Astrophysics*, 184:1–6, October 1987.

[22] R. D. Blandford, A. B. Saust, T. G. Brainerd, and J. V. Villumsen. The distortion of distant galaxy images by large-scale structure. *Monthly Notices of the Royal Astronomical Society*, 251:600–627, August 1991.

[23] D. Blas, J. Lesgourgues, and T. Tram. The Cosmic Linear Anisotropy Solving System (CLASS). Part II: Approximation schemes. *Journal of Cosmology and Astroparticle Physics*, 7:34, July 2011, 1104.2933.

[24] V. Böhm, S. Hilbert, M. Greiner, and T. A. Enßlin. Bayesian weak lensing tomography: Reconstructing the 3D large-scale distribution of matter with a lognormal prior. *ArXiv e-prints*, January 2017, 1701.01886.

[25] V. Böhm, M. Schmittfull, and B. D. Sherwin. Bias to CMB lensing measurements from the bispectrum of large-scale structure. *Physical Review D*, 94(4):043519, August 2016, 1605.01392.

[26] J. R. Bond and G. Efstathiou. The statistics of cosmic background radiation fluctuations. *Monthly Notices of the Royal Astronomical Society*, 226:655–687, June 1987.

[27] A. Buchalter, M. Kamionkowski, and A. H. Jaffe. The Angular Three-Point Correlation Function in the Quasi-linear Regime. *The Astrophysical Journal*, 530:36–52, February 2000, astro-ph/9903486.

[28] R. H. Byrd, P. Lu, J. Nocedal, and C. Zhu. A Limited Memory Algorithm for Bound Constrained Optimization. *SIAM Journal on Scientific and Statistical Computing*, 16:1190, August 1995, 1104.2933.

[29] E. Calabrese, R. de Putter, D. Huterer, E. V. Linder, and A. Melchiorri. Future CMB constraints on early, cold, or stressed dark energy. *Physical Review D*, 83(2):023011, January 2011, 1010.5612.

[30] E. Calabrese, A. Slosar, A. Melchiorri, G. F. Smoot, and O. Zahn. Cosmic microwave weak lensing data as a test for the dark universe. *Physical Review D*, 77(12):123531, June 2008, 0803.2309.

[31] M. Calabrese, C. Carbone, G. Fabbian, M. Baldi, and C. Baccigalupi. Multiple lensing of the cosmic microwave background anisotropies. *Journal of Cosmology and Astroparticle Physics*, 3:049, March 2015, 1409.7680.

[32] C. Carbone, C. Baccigalupi, M. Bartelmann, S. Matarrese, and V. Springel. Lensed CMB temperature and polarization maps from the Millennium Simulation. *Monthly Notices of the Royal Astronomical Society*, 396:668–679, June 2009, 0810.4145.

[33] J. Carron and A. Lewis. Maximum a posteriori CMB lensing reconstruction. *ArXiv e-prints*, April 2017, 1704.08230.

[34] P. G. Castro, A. F. Heavens, and T. D. Kitching. Weak lensing analysis in three dimensions. *Physical Review D*, 72(2):023516, July 2005, astro-ph/0503479.

[35] L. Cayon, E. Martinez-Gonzalez, and J. L. Sanz. Gravitational lensing and the cosmic microwave background. *The Astrophysical Journal*, 403:471–475, February 1993.

[36] A. Challinor and G. Chon. Geometry of weak lensing of CMB polarization. *Physical Review D*, 66(12):127301, December 2002, astro-ph/0301064.

[37] A. Challinor and A. Lewis. Lensed CMB power spectra from all-sky correlation functions. *Physical Review D*, 71(10):103010, May 2005, astro-ph/0502425.

[38] C.-T. Chiang, C. Wagner, F. Schmidt, and E. Komatsu. Position-dependent power spectrum of the large-scale structure: a novel method to measure the squeezed-limit bispectrum. *Journal of Cosmology and Astroparticle Physics*, 5:048, May 2014, 1403.3411.

[39] L. Clerkin, D. Kirk, M. Manera, O. Lahav, F. Abdalla, A. Amara, D. Bacon, C. Chang, E. Gaztañaga, A. Hawken, B. Jain, B. Joachimi, V. Vikram, T. Abbott, S. Allam, R. Armstrong, A. Benoit-Lévy, G. M. Bernstein, R. A. Bernstein, E. Bertin, D. Brooks, D. L. Burke, A. C. Rosell, M. Carrasco Kind, M. Crocce, C. E. Cunha, C. B. D'Andrea, L. N. da Costa, S. Desai, H. T. Diehl, J. P. Dietrich, T. F. Eifler, A. E. Evrard, B. Flaugher, P. Fosalba, J. Frieman, D. W. Gerdes, D. Gruen, R. A. Gruendl, G. Gutierrez, K. Honscheid, D. J. James, S. Kent, K. Kuehn, N. Kuropatkin, M. Lima, P. Melchior, R. Miquel, B. Nord, A. A. Plazas, A. K. Romer, A. Roodman, E. Sanchez, M. Schubnell, I. Sevilla-Noarbe, R. C. Smith, M. Soares-Santos, F. Sobreira, E. Suchyta, M. E. C. Swanson, G. Tarle, and A. R. Walker. Testing the lognormality of the galaxy and weak lensing convergence distributions from Dark Energy Survey maps. *Monthly Notices of the Royal Astronomical Society*, August 2016, 1605.02036.

[40] S. Cole and G. Efstathiou. Gravitational lensing of fluctuations in the microwave background radiation. *Monthly Notices of the Royal Astronomical Society*, 239:195–200, July 1989.

[41] S. Cole and N. Kaiser. Sunyaev-Zel'dovich fluctuations in the cold dark matter scenario. *Monthly Notices of the Royal Astronomical Society*, 233:637–648, August 1988.

[42] P. Coles and B. Jones. A lognormal model for the cosmological mass distribution. *Monthly Notices of the Royal Astronomical Society*, 248:1–13, January 1991.

[43] R. Crittenden, R. L. Davis, and P. J. Steinhardt. Polarization of the Microwave Background Due to Primordial Gravitational Waves. *The Astrophysical Journall*, 417:L13, November 1993, astro-ph/9306027.

[44] S. Das and P. Bode. A Large Sky Simulation of the Gravitational Lensing of the Cosmic Microwave Background. *The Astrophysical Journal*, 682:1–13, July 2008, 0711.3793.

[45] S. Das, T. Louis, M. R. Nolta, G. E. Addison, E. S. Battistelli, J. R. Bond, E. Calabrese, D. Crichton, M. J. Devlin, S. Dicker, J. Dunkley, R. Dünner, J. W. Fowler, M. Gralla, A. Hajian, M. Halpern, M. Hasselfield, M. Hilton, A. D. Hincks, R. Hlozek, K. M. Huffenberger, J. P. Hughes, K. D. Irwin, A. Kosowsky, R. H. Lupton, T. A. Marriage, D. Marsden, F. Menanteau, K. Moodley, M. D. Niemack, L. A. Page, B. Partridge, E. D. Reese, B. L. Schmitt, N. Sehgal, B. D. Sherwin, J. L. Sievers, D. N. Spergel, S. T. Staggs, D. S. Swetz, E. R. Switzer, R. Thornton, H. Trac, and E. Wollack. The Atacama Cosmology Telescope: temperature and gravitational lensing power spectrum measurements from three seasons of data. *Journal of Cosmology and Astroparticle Physics*, 4:014, April 2014, 1301.1037.

[46] S. Das, B. D. Sherwin, P. Aguirre, J. W. Appel, J. R. Bond, C. S. Carvalho, M. J. Devlin, J. Dunkley, R. Dünner, T. Essinger-Hileman, J. W. Fowler, A. Hajian, M. Halpern, M. Hasselfield, A. D. Hincks, R. Hlozek, K. M. Huffenberger, J. P. Hughes, K. D. Irwin, J. Klein, A. Kosowsky, R. H. Lupton, T. A. Marriage, D. Marsden, F. Menanteau, K. Moodley, M. D. Niemack, M. R. Nolta, L. A. Page, L. Parker, E. D. Reese, B. L. Schmitt, N. Sehgal, J. Sievers, D. N. Spergel, S. T. Staggs, D. S. Swetz, E. R. Switzer, R. Thornton, K. Visnjic, and E. Wollack. Detection of the Power Spectrum of Cosmic Microwave Background Lensing by the Atacama Cosmology Telescope. *Physical Review Letters*, 107(2):021301, July 2011, 1103.2124.

[47] J. T. A. de Jong, K. Kuijken, D. Applegate, K. Begeman, A. Belikov, C. Blake, J. Bout, D. Boxhoorn, H. Buddelmeijer, A. Buddendiek, M. Cacciato, M. Capaccioli, A. Choi, O. Cordes, G. Covone, M. Dall'Ora, A. Edge, T. Erben, J. Franse, F. Getman, A. Grado, J. Harnois-Deraps, E. Helmich, R. Herbonnet, C. Heymans, H. Hildebrandt, H. Hoekstra, Z. Huang, N. Irisarri, B. Joachimi, F. Köhlinger, T. Kitching, F. La Barbera, P. Lacerda, J. McFarland, L. Miller, R. Nakajima, N. R. Napolitano, M. Paolillo, J. Peacock, B. Pila-Diez, E. Puddu, M. Radovich, A. Rifatto, P. Schneider, T. Schrabback, C. Sifon, G. Sikkema, P. Simon, W. Sutherland, A. Tudorica, E. Valentijn, R. van der Burg, E. van Uitert, L. van Waerbeke, M. Velander, G. V. Kleijn, M. Viola, and W.-J. Vriend. The Kilo-Degree Survey. *The Messenger*, 154:44–46, December 2013.

[48] J. P. Dietrich and J. Hartlap. Cosmology with the shear-peak statistics. *Monthly Notices of the Royal Astronomical Society*, 402:1049–1058, February 2010, 0906.3512.

[49] S. Dodelson, C. Shapiro, and M. White. Reduced shear power spectrum. *Physical Review D*, 73(2):023009, January 2006, astro-ph/0508296.

[50] Sebastian Dorn, Maksim Greiner, and Torsten A. Enßlin. All-sky reconstruction of the primordial scalar potential from wmap temperature data. *Journal of Cosmology and Astroparticle Physics*, 2015(02):041, 2015.

[51] D. J. Eisenstein and W. Hu. Baryonic Features in the Matter Transfer Function. *The Astrophysical Journal*, 496:605–614, March 1998, astro-ph/9709112.

[52] D. J. Eisenstein and W. Hu. Power Spectra for Cold Dark Matter and Its Variants. *The Astrophysical Journal*, 511:5–15, January 1999, astro-ph/9710252.

[53] F. Elsner and B. D. Wandelt. Fast Wiener filtering of CMB maps. *ArXiv e-prints*, November 2012, 1211.0585.

[54] T. A. Enßlin and M. Frommert. Reconstruction of signals with unknown spectra in information field theory with parameter uncertainty. *Physical Review D*, 83(10):105014, May 2011, 1002.2928.

[55] T. A. Enßlin, M. Frommert, and F. S. Kitaura. Information field theory for cosmological perturbation reconstruction and nonlinear signal analysis. *Physical Review D*, 80(10):105005, November 2009, 0806.3474.

[56] T. A. Enßlin and J. Knollmüller. Correlated signal inference by free energy exploration. *ArXiv e-prints*, December 2016, 1612.08406.

[57] H. K. Eriksen, I. J. O'Dwyer, J. B. Jewell, B. D. Wandelt, D. L. Larson, K. M. Górski, S. Levin, A. J. Banday, and P. B. Lilje. Power Spectrum Estimation from High-Resolution Maps by Gibbs Sampling. *The Astrophysical Journals*, 155:227–241, December 2004, astro-ph/0407028.

[58] S. Foreman, M. R. Becker, and R. H. Wechsler. Cosmic shear as a probe of galaxy formation physics. *Monthly Notices of the Royal Astronomical Society*, 463:3326–3338, December 2016, 1605.09056.

[59] M. Gentile, F. Courbin, and G. Meylan. A simple fitting method (gfit) for galaxy shape measurement in weak lensing surveys. *ArXiv e-prints*, November 2012, 1211.4847.

[60] H. Gil-Marín, C. Wagner, F. Fragkoudi, R. Jimenez, and L. Verde. An improved fitting formula for the dark matter bispectrum. *Journal of Cosmology and Astroparticle Physics*, 2:47, February 2012, 1111.4477.

[61] K. M. Górski, E. Hivon, A. J. Banday, B. D. Wandelt, F. K. Hansen, M. Reinecke, and M. Bartelmann. HEALPix: A Framework for High-Resolution Discretization and Fast Analysis of Data Distributed on the Sphere. *The Astrophysical Journal*, 622:759–771, April 2005, astro-ph/0409513.

[62] D. Green, J. Meyers, and A. van Engelen. CMB Delensing Beyond the B Modes. *ArXiv e-prints*, September 2016, 1609.08143.

[63] M. Greiner and T. A. Enßlin. Log-transforming the matter power spectrum. *Astronomy and Astrophysics*, 574:A86, February 2015, 1312.1354.

[64] M. Greiner, D. H. F. M. Schnitzeler, and T. A. Enßlin. Tomography of the Galactic free electron density with the Square Kilometer Array. *Astronomy and Astrophysics*, 590:A59, May 2016, 1512.03480.

[65] J. E. Gunn. On the Propagation of Light in Inhomogeneous Cosmologies. I. Mean Effects. *The Astrophysical Journal*, 150:737, December 1967.

[66] S. Hagstotz, B. M. Schäfer, and P. M. Merkel. Born-corrections to weak lensing of the cosmic microwave background temperature and polarization anisotropies. *Monthly Notices of the Royal Astronomical Society*, 454:831–838, November 2015, 1410.8452.

[67] A. C. Hall and A. Challinor. Probing the neutrino mass hierarchy with cosmic microwave background weak lensing. *Monthly Notices of the Royal Astronomical Society*, 425:1170–1184, September 2012, 1205.6172.

[68] J. Hamann, S. Hannestad, and Y. Y. Y. Wong. Measuring neutrino masses with a future galaxy survey. *Journal of Cosmology and Astroparticle Physics*, 11:052, November 2012, 1209.1043.

[69] A. J. S. Hamilton. Uncorrelated modes of the non-linear power spectrum. *Monthly Notices of the Royal Astronomical Society*, 312:257–284, February 2000, astro-ph/9905191.

[70] S. Hamimeche and A. Lewis. Likelihood analysis of CMB temperature and polarization power spectra. *Physical Review D*, 77(10):103013, May 2008, 0801.0554.

[71] N. Hand, A. Leauthaud, S. Das, B. D. Sherwin, G. E. Addison, J. R. Bond, E. Calabrese, A. Charbonnier, M. J. Devlin, J. Dunkley, T. Erben, A. Hajian, M. Halpern, J. Harnois-Déraps, C. Heymans, H. Hildebrandt, A. D. Hincks, J.-P. Kneib, A. Kosowsky, M. Makler, L. Miller, K. Moodley, B. Moraes, M. D. Niemack, L. A. Page, B. Partridge, N. Sehgal, H. Shan, J. L. Sievers, D. N. Spergel, S. T. Staggs, E. R. Switzer, J. E. Taylor, L. Van Waerbeke, C. Welker, and E. J. Wollack. First measurement of the cross-correlation of CMB lensing and galaxy lensing. *Physical Review D*, 91(6):062001, March 2015, 1311.6200.

[72] D. Hanson, A. Challinor, G. Efstathiou, and P. Bielewicz. CMB temperature lensing power reconstruction. *Physical Review D*, 83(4):043005, February 2011, 1008.4403.

[73] D. Hanson, S. Hoover, A. Crites, P. A. R. Ade, K. A. Aird, J. E. Austermann, J. A. Beall, A. N. Bender, B. A. Benson, L. E. Bleem, J. J. Bock, J. E. Carlstrom, C. L.

Chang, H. C. Chiang, H.-M. Cho, A. Conley, T. M. Crawford, T. de Haan, M. A. Dobbs, W. Everett, J. Gallicchio, J. Gao, E. M. George, N. W. Halverson, N. Harrington, J. W. Henning, G. C. Hilton, G. P. Holder, W. L. Holzapfel, J. D. Hrubes, N. Huang, J. Hubmayr, K. D. Irwin, R. Keisler, L. Knox, A. T. Lee, E. Leitch, D. Li, C. Liang, D. Luong-Van, G. Marsden, J. J. McMahon, J. Mehl, S. S. Meyer, L. Mocanu, T. E. Montroy, T. Natoli, J. P. Nibarger, V. Novosad, S. Padin, C. Pryke, C. L. Reichardt, J. E. Ruhl, B. R. Saliwanchik, J. T. Sayre, K. K. Schaffer, B. Schulz, G. Smecher, A. A. Stark, K. T. Story, C. Tucker, K. Vanderlinde, J. D. Vieira, M. P. Viero, G. Wang, V. Yefremenko, O. Zahn, and M. Zemcov. Detection of B-Mode Polarization in the Cosmic Microwave Background with Data from the South Pole Telescope. *Physical Review Letters*, 111(14):141301, October 2013, 1307.5830.

[74] D. Hanson, A. Lewis, and A. Challinor. Asymmetric beams and CMB statistical anisotropy. *Physical Review D*, 81(10):103003, May 2010, 1003.0198.

[75] D. Hanson, G. Rocha, and K. Górski. Lensing reconstruction from Planck sky maps: inhomogeneous noise. *Monthly Notices of the Royal Astronomical Society*, 400:2169–2173, December 2009, 0907.1927.

[76] J. Harnois-Déraps, L. van Waerbeke, M. Viola, and C. Heymans. Baryons, neutrinos, feedback and weak gravitational lensing. *Monthly Notices of the Royal Astronomical Society*, 450:1212–1223, June 2015, 1407.4301.

[77] E. R. Harrison. Fluctuations at the threshold of classical cosmology. *Phys. Rev. D*, 1:2726–2730, May 1970.

[78] D. J. Heath. The growth of density perturbations in zero pressure Friedmann-Lemaitre universes. *Monthly Notices of the Royal Astronomical Society*, 179:351–358, May 1977.

[79] A. Heavens. 3D weak lensing. *Monthly Notices of the Royal Astronomical Society*, 343:1327–1334, August 2003, astro-ph/0304151.

[80] A. Heavens, J. Alsing, A. Jaffe, T. Hoffmann, A. Kiessling, and B. Wandelt. Bayesian hierarchical modelling of weak lensing - the golden goal. *ArXiv e-prints*, February 2016, 1602.05345.

[81] C. Heymans, E. Grocutt, A. Heavens, M. Kilbinger, T. D. Kitching, F. Simpson, J. Benjamin, T. Erben, H. Hildebrandt, H. Hoekstra, Y. Mellier, L. Miller, L. Van Waerbeke, M. L. Brown, J. Coupon, L. Fu, J. Harnois-Déraps, M. J. Hudson, K. Kuijken, B. Rowe, T. Schrabback, E. Semboloni, S. Vafaei, and M. Velander. CFHTLenS tomographic weak lensing cosmological parameter constraints: Mitigating the impact of intrinsic galaxy alignments. *Monthly Notices of the Royal Astronomical Society*, 432:2433–2453, July 2013, 1303.1808.

[82] C. Heymans and A. Heavens. Reducing and constraining the intrinsic galaxy alignment contamination to weak lensing measurements. *ArXiv Astrophysics e-prints*, October 2003, astro-ph/0310495.

[83] C. Heymans, L. Van Waerbeke, L. Miller, T. Erben, H. Hildebrandt, H. Hoekstra, T. D. Kitching, Y. Mellier, P. Simon, C. Bonnett, J. Coupon, L. Fu, J. Harnois Déraps, M. J. Hudson, M. Kilbinger, K. Kuijken, B. Rowe, T. Schrabback, E. Semboloni, E. van Uitert, S. Vafaei, and M. Velander. CFHTLenS: the Canada-France-Hawaii Telescope Lensing Survey. *Monthly Notices of the Royal Astronomical Society*, 427:146–166, November 2012, 1210.0032.

[84] S. Hilbert, J. Hartlap, and P. Schneider. Cosmic shear covariance: the log-normal approximation. *Astronomy and Astrophysics*, 536:A85, December 2011, 1105.3980.

[85] S. Hilbert, L. Marian, R. E. Smith, and V. Desjacques. Measuring primordial non-Gaussianity with weak lensing surveys. *Monthly Notices of the Royal Astronomical Society*, 426:2870–2888, November 2012, 1204.4530.

[86] H. Hildebrandt, T. Erben, K. Kuijken, L. van Waerbeke, C. Heymans, J. Coupon, J. Benjamin, C. Bonnett, L. Fu, H. Hoekstra, T. D. Kitching, Y. Mellier, L. Miller, M. Velander, M. J. Hudson, B. T. P. Rowe, T. Schrabback, E. Semboloni, and N. Benítez. CFHTLenS: improving the quality of photometric redshifts with precision photometry. *Monthly Notices of the Royal Astronomical Society*, 421:2355–2367, April 2012, 1111.4434.

[87] H. Hildebrandt, M. Viola, C. Heymans, S. Joudaki, K. Kuijken, C. Blake, T. Erben, B. Joachimi, D. Klaes, L. Miller, C. B. Morrison, R. Nakajima, G. Verdoes Kleijn, A. Amon, A. Choi, G. Covone, J. T. A. de Jong, A. Dvornik, I. Fenech Conti, A. Grado, J. Harnois-Déraps, R. Herbonnet, H. Hoekstra, F. Köhlinger, J. McFarland, A. Mead, J. Merten, N. Napolitano, J. A. Peacock, M. Radovich, P. Schneider, P. Simon, E. A. Valentijn, J. L. van den Busch, E. van Uitert, and L. Van Waerbeke. KiDS-450: cosmological parameter constraints from tomographic weak gravitational lensing. *Monthly Notices of the Royal Astronomical Society*, 465:1454–1498, February 2017, 1606.05338.

[88] J. C. Hill and D. N. Spergel. Detection of thermal SZ-CMB lensing cross-correlation in Planck nominal mission data. *Journal of Cosmology and Astroparticle Physics*, 2:030, February 2014, 1312.4525.

[89] C. M. Hirata, S. Ho, N. Padmanabhan, U. Seljak, and N. A. Bahcall. Correlation of CMB with large-scale structure. II. Weak lensing. *Physical Review D*, 78(4):043520, August 2008, 0801.0644.

[90] C. M. Hirata, N. Padmanabhan, U. Seljak, D. Schlegel, and J. Brinkmann. Cross-correlation of CMB with large-scale structure: Weak gravitational lensing. *Physical Review D*, 70(10):103501, November 2004, astro-ph/0406004.

[91] C. M. Hirata and U. Seljak. Analyzing weak lensing of the cosmic microwave background using the likelihood function. *Physical Review D*, 67(4):043001, February 2003, astro-ph/0209489.

[92] C. M. Hirata and U. Seljak. Reconstruction of lensing from the cosmic microwave background polarization. *Physical Review D*, 68(8):083002, October 2003, astro-ph/0306354.

[93] H. Hoekstra and B. Jain. Weak Gravitational Lensing and Its Cosmological Applications. *Annual Review of Nuclear and Particle Science*, 58:99–123, November 2008, 0805.0139.

[94] W. Hu. Power Spectrum Tomography with Weak Lensing. *The Astrophysical Journall*, 522:L21–L24, September 1999, astro-ph/9904153.

[95] W. Hu. Weak lensing of the CMB: A harmonic approach. *Physical Review D*, 62(4):043007, August 2000, arXiv:astro-ph/0001303.

[96] W. Hu. Angular trispectrum of the cosmic microwave background. *Physical Review D*, 64(8):083005, October 2001, arXiv:astro-ph/0105117.

[97] W. Hu. Mapping the Dark Matter through the Cosmic Microwave Background Damping Tail. *The Astrophysical Journall*, 557:L79–L83, August 2001, arXiv:astro-ph/0105424.

[98] W. Hu. Dark energy and matter evolution from lensing tomography. *Physical Review D*, 66(8):083515, October 2002, astro-ph/0208093.

[99] W. Hu. Dark synergy: Gravitational lensing and the CMB. *Physical Review D*, 65(2):023003, January 2002, astro-ph/0108090.

[100] W. Hu and C. R. Keeton. Three-dimensional mapping of dark matter. *Physical Review D*, 66(6):063506, September 2002, astro-ph/0205412.

[101] W. Hu and T. Okamoto. Mass Reconstruction with Cosmic Microwave Background Polarization. *The Astrophysical Journal*, 574:566–574, August 2002, arXiv:astro-ph/0111606.

[102] W. Hu and M. White. A CMB polarization primer. *New Astronomy*, 2:323–344, October 1997, astro-ph/9706147.

[103] E. Hubble. The Distribution of Extra-Galactic Nebulae. *The Astrophysical Journal*, 79:8, January 1934.

[104] D. Huterer. Weak lensing and dark energy. *Physical Review D*, 65(6):063001, March 2002, astro-ph/0106399.

[105] B. Jain and P. Zhang. Observational tests of modified gravity. *Physical Review D*, 78(6):063503, September 2008, 0709.2375.

[106] Bhuvnesh Jain and Uroš Seljak. Cosmological model predictions for weak lensing: Linear and nonlinear regimes. *The Astrophysical Journal*, 484(2):560, 1997.

[107] M. Jarvis, E. Sheldon, J. Zuntz, T. Kacprzak, S. L. Bridle, A. Amara, R. Armstrong, M. R. Becker, G. M. Bernstein, C. Bonnett, C. Chang, R. Das, J. P. Dietrich, A. Drlica-Wagner, T. F. Eifler, C. Gangkofner, D. Gruen, M. Hirsch, E. M. Huff, B. Jain, S. Kent, D. Kirk, N. MacCrann, P. Melchior, A. A. Plazas, A. Refregier, B. Rowe, E. S. Rykoff, S. Samuroff, C. Sánchez, E. Suchyta, M. A. Troxel, V. Vikram, T. Abbott, F. B. Abdalla, S. Allam, J. Annis, A. Benoit-Lévy, E. Bertin, D. Brooks, E. Buckley-Geer, D. L. Burke, D. Capozzi, A. Carnero Rosell, M. Carrasco Kind, J. Carretero, F. J. Castander, J. Clampitt, M. Crocce, C. E. Cunha, C. B. D'Andrea, L. N. da Costa, D. L. DePoy, S. Desai, H. T. Diehl, P. Doel, A. Fausti Neto, B. Flaugher, P. Fosalba, J. Frieman, E. Gaztanaga, D. W. Gerdes, R. A. Gruendl, G. Gutierrez, K. Honscheid, D. J. James, K. Kuehn, N. Kuropatkin, O. Lahav, T. S. Li, M. Lima, M. March, P. Martini, R. Miquel, J. J. Mohr, E. Neilsen, B. Nord, R. Ogando, K. Reil, A. K. Romer, A. Roodman, M. Sako, E. Sanchez, V. Scarpine, M. Schubnell, I. Sevilla-Noarbe, R. C. Smith, M. Soares-Santos, F. Sobreira, M. E. C. Swanson, G. Tarle, J. Thaler, D. Thomas, A. R. Walker, and R. H. Wechsler. The DES Science Verification weak lensing shear catalogues. *Monthly Notices of the Royal Astronomical Society*, 460:2245–2281, August 2016, 1507.05603.

[108] J. Jasche, F. S. Kitaura, C. Li, and T. A. Enßlin. Bayesian non-linear large-scale structure inference of the Sloan Digital Sky Survey Data Release 7. *Monthly Notices of the Royal Astronomical Society*, 409:355–370, November 2010, 0911.2498.

[109] M. J. Jee, J. A. Tyson, S. Hilbert, M. D. Schneider, S. Schmidt, and D. Wittman. Cosmic Shear Results from the Deep Lens Survey. II. Full Cosmological Parameter Constraints from Tomography. *The Astrophysical Journal*, 824:77, June 2016, 1510.03962.

[110] M. J. Jee, J. A. Tyson, M. D. Schneider, D. Wittman, S. Schmidt, and S. Hilbert. Cosmic Shear Results from the Deep Lens Survey. I. Joint Constraints on Ω_M and σ_8 with a Two-dimensional Analysis. *The Astrophysical Journal*, 765:74, March 2013, 1210.2732.

[111] H. Junklewitz, M. R. Bell, M. Selig, and T. A. Enßlin. RESOLVE: A new algorithm for aperture synthesis imaging of extended emission in radio astronomy. *Astronomy and Astrophysics*, 586:A76, February 2016, 1311.5282.

[112] T. Kacprzak, D. Kirk, O. Friedrich, A. Amara, A. Refregier, L. Marian, J. P. Dietrich, E. Suchyta, J. Aleksić, D. Bacon, M. R. Becker, C. Bonnett, S. L. Bridle,

C. Chang, T. F. Eifler, W. G. Hartley, E. M. Huff, E. Krause, N. MacCrann, P. Melchior, A. Nicola, S. Samuroff, E. Sheldon, M. A. Troxel, J. Weller, J. Zuntz, T. M. C. Abbott, F. B. Abdalla, R. Armstrong, A. Benoit-Lévy, G. M. Bernstein, R. A. Bernstein, E. Bertin, D. Brooks, D. L. Burke, A. Carnero Rosell, M. Carrasco Kind, J. Carretero, F. J. Castander, M. Crocce, C. B. D'Andrea, L. N. da Costa, S. Desai, H. T. Diehl, A. E. Evrard, A. F. Neto, B. Flaugher, P. Fosalba, J. Frieman, D. W. Gerdes, D. A. Goldstein, D. Gruen, R. A. Gruendl, G. Gutierrez, K. Honscheid, B. Jain, D. J. James, M. Jarvis, K. Kuehn, N. Kuropatkin, O. Lahav, M. Lima, M. March, J. L. Marshall, P. Martini, C. J. Miller, R. Miquel, J. J. Mohr, R. C. Nichol, B. Nord, A. A. Plazas, A. K. Romer, A. Roodman, E. S. Rykoff, E. Sanchez, V. Scarpine, M. Schubnell, I. Sevilla-Noarbe, R. C. Smith, M. Soares-Santos, F. Sobreira, M. E. C. Swanson, G. Tarle, D. Thomas, V. Vikram, A. R. Walker, Y. Zhang, and DES Collaboration. Cosmology constraints from shear peak statistics in Dark Energy Survey Science Verification data. *Monthly Notices of the Royal Astronomical Society*, 463:3653–3673, December 2016, 1603.05040.

[113] N. Kaiser. Small-angle anisotropy of the microwave background radiation in the adiabatic theory. *Monthly Notices of the Royal Astronomical Society*, 202:1169–1180, March 1983.

[114] N. Kaiser. Weak gravitational lensing of distant galaxies. *The Astrophysical Journal*, 388:272–286, April 1992.

[115] N. Kaiser. Nonlinear cluster lens reconstruction. *The Astrophysical Journall*, 439:L1–L3, January 1995, astro-ph/9408092.

[116] N. Kaiser. Weak Lensing and Cosmology. *The Astrophysical Journal*, 498:26–42, May 1998, astro-ph/9610120.

[117] N. Kaiser and G. Squires. Mapping the dark matter with weak gravitational lensing. *The Astrophysical Journal*, 404:441–450, February 1993.

[118] N. Kaiser, G. Wilson, and G. A. Luppino. Large-Scale Cosmic Shear Measurements. *ArXiv Astrophysics e-prints*, March 2000, astro-ph/0003338.

[119] M. Kamionkowski, A. Kosowsky, and A. Stebbins. Statistics of cosmic microwave background polarization. *Physical Review D*, 55:7368–7388, June 1997, astro-ph/9611125.

[120] M. Kesden, A. Cooray, and M. Kamionkowski. Weak lensing of the CMB: Cumulants of the probability distribution function. *Physical Review D*, 66(8):083007, October 2002, arXiv:astro-ph/0208325.

[121] M. Kesden, A. Cooray, and M. Kamionkowski. Lensing reconstruction with CMB temperature and polarization. *Physical Review D*, 67(12):123507, June 2003, astro-ph/0302536.

[122] M. Kilbinger. Cosmology with cosmic shear observations: a review. *Reports on Progress in Physics*, 78(8):086901, July 2015, 1411.0115.

[123] M. Kilbinger, L. Fu, C. Heymans, F. Simpson, J. Benjamin, T. Erben, J. Harnois-Déraps, H. Hoekstra, H. Hildebrandt, T. D. Kitching, Y. Mellier, L. Miller, L. Van Waerbeke, K. Benabed, C. Bonnett, J. Coupon, M. J. Hudson, K. Kuijken, B. Rowe, T. Schrabback, E. Semboloni, S. Vafaei, and M. Velander. CFHTLenS: combined probe cosmological model comparison using 2D weak gravitational lensing. *Monthly Notices of the Royal Astronomical Society*, 430:2200–2220, April 2013, 1212.3338.

[124] L. J. King and P. Schneider. Separating cosmic shear from intrinsic galaxy alignments: Correlation function tomography. *Astronomy and Astrophysics*, 398:23–30, January 2003, astro-ph/0209474.

[125] D. Kirk, Y. Omori, A. Benoit-Lévy, R. Cawthon, C. Chang, P. Larsen, A. Amara, D. Bacon, T. M. Crawford, S. Dodelson, P. Fosalba, T. Giannantonio, G. Holder, B. Jain, T. Kacprzak, O. Lahav, N. MacCrann, A. Nicola, A. Refregier, E. Sheldon, K. T. Story, M. A. Troxel, J. D. Vieira, V. Vikram, J. Zuntz, T. M. C. Abbott, F. B. Abdalla, M. R. Becker, B. A. Benson, G. M. Bernstein, R. A. Bernstein, L. E. Bleem, C. Bonnett, S. L. Bridle, D. Brooks, E. Buckley-Geer, D. L. Burke, D. Capozzi, J. E. Carlstrom, A. C. Rosell, M. C. Kind, J. Carretero, M. Crocce, C. E. Cunha, C. B. D'Andrea, L. N. da Costa, S. Desai, H. T. Diehl, J. P. Dietrich, P. Doel, T. F. Eifler, A. E. Evrard, B. Flaugher, J. Frieman, D. W. Gerdes, D. A. Goldstein, D. Gruen, R. A. Gruendl, K. Honscheid, D. J. James, M. Jarvis, S. Kent, K. Kuehn, N. Kuropatkin, M. Lima, M. March, P. Martini, P. Melchior, C. J. Miller, R. Miquel, R. C. Nichol, R. Ogando, A. A. Plazas, C. L. Reichardt, A. Roodman, E. Rozo, E. S. Rykoff, M. Sako, E. Sanchez, V. Scarpine, M. Schubnell, I. Sevilla-Noarbe, G. Simard, R. C. Smith, M. Soares-Santos, F. Sobreira, E. Suchyta, M. E. C. Swanson, G. Tarle, D. Thomas, R. H. Wechsler, and J. Weller. Cross-correlation of gravitational lensing from DES Science Verification data with SPT and Planck lensing. *Monthly Notices of the Royal Astronomical Society*, 459:21–34, June 2016, 1512.04535.

[126] F.-S. Kitaura, J. Jasche, and R. B. Metcalf. Recovering the non-linear density field from the galaxy distribution with a Poisson-lognormal filter. *Monthly Notices of the Royal Astronomical Society*, 403:589–604, April 2010, 0911.1407.

[127] T. D. Kitching, A. F. Heavens, J. Alsing, T. Erben, C. Heymans, H. Hildebrandt, H. Hoekstra, A. Jaffe, A. Kiessling, Y. Mellier, L. Miller, L. van Waerbeke, J. Benjamin, J. Coupon, L. Fu, M. J. Hudson, M. Kilbinger, K. Kuijken, B. T. P. Rowe, T. Schrabback, E. Semboloni, and M. Velander. 3D cosmic shear: cosmology from CFHTLenS. *Monthly Notices of the Royal Astronomical Society*, 442:1326–1349, August 2014, 1401.6842.

[128] T. D. Kitching, A. F. Heavens, and L. Miller. 3D photometric cosmic shear. *Monthly Notices of the Royal Astronomical Society*, 413:2923–2934, June 2011, 1007.2953.

[129] T. D. Kitching, L. Miller, C. E. Heymans, L. van Waerbeke, and A. F. Heavens. Bayesian galaxy shape measurement for weak lensing surveys - II. Application to simulations. *Monthly Notices of the Royal Astronomical Society*, 390:149–167, October 2008, 0802.1528.

[130] M. Klasen, M. Pohl, and G. Sigl. Indirect and direct search for dark matter. *Progress in Particle and Nuclear Physics*, 85:1–32, November 2015, 1507.03800.

[131] C. S. Kochanek. Inverting Cluster Gravitational Lenses. *Monthly Notices of the Royal Astronomical Society*, 247:135, November 1990.

[132] E. Komatsu and T. Kitayama. Sunyaev-Zeldovich Fluctuations from Spatial Correlations between Clusters of Galaxies. *The Astrophysical Journall*, 526:L1–L4, November 1999, astro-ph/9908087.

[133] E. Komatsu, A. Kogut, M. R. Nolta, C. L. Bennett, M. Halpern, G. Hinshaw, N. Jarosik, M. Limon, S. S. Meyer, L. Page, D. N. Spergel, G. S. Tucker, L. Verde, E. Wollack, and E. L. Wright. First-Year Wilkinson Microwave Anisotropy Probe (WMAP) Observations: Tests of Gaussianity. *The Astrophysical Journals*, 148:119–134, September 2003, astro-ph/0302223.

[134] A. Kosowsky. Cosmic microwave background polarization. *Annals of Physics*, 246:49–85, February 1996, astro-ph/9501045.

[135] E. Krause and C. M. Hirata. Weak lensing power spectra for precision cosmology. Multiple-deflection, reduced shear, and lensing bias corrections. *Astronomy and Astrophysics*, 523:A28, November 2010, 0910.3786.

[136] G. Lavaux and B. D. Wandelt. Fast and Optimal Cosmic Microwave Background Lensing Using Statistical Interpolation on the Sphere. *The Astrophysical Journals*, 191:32–42, November 2010, 1003.4984.

[137] A. Lazanu, T. Giannantonio, M. Schmittfull, and E. P. S. Shellard. Characterising the matter bispectrum of large-scale structure: halo models, perturbation theory and a three-shape model. *ArXiv e-prints*, November 2015, 1511.02022.

[138] Andrei Lazanu, Tommaso Giannantonio, Marcel Schmittfull, and E. P. S. Shellard. Matter bispectrum of large-scale structure: Three-dimensional comparison between theoretical models and numerical simulations. *Phys. Rev.*, D93(8):083517, 2016, 1510.04075.

[139] Alexie Leauthaud, Richard Massey, Jean-Paul Kneib, Jason Rhodes, David E. Johnston, Peter Capak, Catherine Heymans, Richard S. Ellis, Anton M. Koekemoer, Oliver Le Fèvre, Yannick Mellier, Alexandre Réfrégier, Annie C. Robin, Nick Scoville, Lidia Tasca, James E. Taylor, and Ludovic Van Waerbeke. Weak gravitational lensing with cosmos: Galaxy selection and shape measurements. *The Astrophysical Journal Supplement Series*, 172(1):219, 2007.

[140] J. Lesgourgues, L. Perotto, S. Pastor, and M. Piat. Probing neutrino masses with CMB lensing extraction. *Physical Review D*, 73(4):045021, February 2006, arXiv:astro-ph/0511735.

[141] A. Lewis. Lensed CMB simulation and parameter estimation. *Physical Review D*, 71(8):083008, April 2005, astro-ph/0502469.

[142] A. Lewis and A. Challinor. Weak gravitational lensing of the CMB. *Physics Reports*, 429:1–65, June 2006, arXiv:astro-ph/0601594.

[143] A. Lewis, A. Challinor, and D. Hanson. The shape of the CMB lensing bispectrum. *Journal of Cosmology and Astroparticle Physics*, 3:18, March 2011, 1101.2234.

[144] Antony Lewis, Anthony Challinor, and Anthony Lasenby. Efficient computation of CMB anisotropies in closed FRW models. *Astrophys. J.*, 538:473–476, 2000, astro-ph/9911177.

[145] M. Liguori, A. Yadav, F. K. Hansen, E. Komatsu, S. Matarrese, and B. Wandelt. Temperature and polarization CMB maps from primordial non-Gaussianities of the local type. *Physical Review D*, 76(10):105016, November 2007, 0708.3786.

[146] D. N. Limber. The Analysis of Counts of the Extragalactic Nebulae in Terms of a Fluctuating Density Field. *The Astrophysical Journal*, 117:134, January 1953.

[147] E. V. Linder. Analysis of gravitationally lensed microwave background anisotropies. *Monthly Notices of the Royal Astronomical Society*, 243:353–361, April 1990.

[148] E. V. Linder and A. Jenkins. Cosmic structure growth and dark energy. *Monthly Notices of the Royal Astronomical Society*, 346:573–583, December 2003, astro-ph/0305286.

[149] J. Liu and J. C. Hill. Cross-correlation of Planck CMB lensing and CFHTLenS galaxy weak lensing maps. *Physical Review D*, 92(6):063517, September 2015, 1504.05598.

[150] J. Liu, A. Petri, Z. Haiman, L. Hui, J. M. Kratochvil, and M. May. Cosmology constraints from the weak lensing peak counts and the power spectrum in CFHTLenS data. *Physical Review D*, 91(6):063507, March 2015, 1412.0757.

[151] T. Louis, S. Næss, S. Das, J. Dunkley, and B. Sherwin. Lensing simulation and power spectrum estimation for high-resolution CMB polarization maps. *Monthly Notices of the Royal Astronomical Society*, 435:2040–2047, November 2013, 1306.6692.

[152] M. Loverde and N. Afshordi. Extended Limber approximation. *Physical Review D*, 78(12):123506, December 2008, 0809.5112.

[153] C.-P. Ma and E. Bertschinger. Cosmological Perturbation Theory in the Synchronous and Conformal Newtonian Gauges. *The Astrophysical Journal*, 455:7, December 1995, astro-ph/9506072.

[154] Y.-Z. Ma, L. Van Waerbeke, G. Hinshaw, A. Hojjati, D. Scott, and J. Zuntz. Probing the diffuse baryon distribution with the lensing-tSZ cross-correlation. *Journal of Cosmology and Astroparticle Physics*, 9:046, September 2015, 1404.4808.

[155] Z. Ma, W. Hu, and D. Huterer. Effects of Photometric Redshift Uncertainties on Weak-Lensing Tomography. *The Astrophysical Journal*, 636:21–29, January 2006, astro-ph/0506614.

[156] M. Maltoni, T. Schwetz, M. Tórtola, and J. W. F. Valle. Status of global fits to neutrino oscillations. *New Journal of Physics*, 6:122, September 2004, hep-ph/0405172.

[157] L. Marian, S. Hilbert, R. E. Smith, P. Schneider, and V. Desjacques. Measuring Primordial Non-gaussianity Through Weak-lensing Peak Counts. *The Astrophysical Journall*, 728:L13, February 2011, 1010.5242.

[158] L. Marian, R. E. Smith, S. Hilbert, and P. Schneider. Optimized detection of shear peaks in weak lensing maps. *Monthly Notices of the Royal Astronomical Society*, 423:1711–1725, June 2012, 1110.4635.

[159] L. Marian, R. E. Smith, S. Hilbert, and P. Schneider. The cosmological information of shear peaks: beyond the abundance. *Monthly Notices of the Royal Astronomical Society*, 432:1338–1350, June 2013, 1301.5001.

[160] T. Marrodán Undagoitia and L. Rauch. Dark matter direct-detection experiments. *Journal of Physics G Nuclear Physics*, 43(1):013001, January 2016, 1509.08767.

[161] R. Massey, J. Rhodes, A. Leauthaud, P. Capak, R. Ellis, A. Koekemoer, A. Réfrégier, N. Scoville, J. E. Taylor, J. Albert, J. Bergé, C. Heymans, D. Johnston, J.-P. Kneib, Y. Mellier, B. Mobasher, E. Semboloni, P. Shopbell, L. Tasca, and L. Van Waerbeke. COSMOS: Three-dimensional Weak Lensing and the Growth of Structure. *The Astrophysical Journals*, 172:239–253, September 2007, astro-ph/0701480.

[162] T. Matsumura, Y. Akiba, J. Borrill, Y. Chinone, M. Dobbs, H. Fuke, A. Ghribi, M. Hasegawa, K. Hattori, M. Hattori, M. Hazumi, W. Holzapfel, Y. Inoue, K. Ishidoshiro, H. Ishino, H. Ishitsuka, K. Karatsu, N. Katayama, I. Kawano, A. Kibayashi, Y. Kibe, K. Kimura, N. Kimura, K. Koga, M. Kozu, E. Komatsu, A. Lee, H. Matsuhara, S. Mima, K. Mitsuda, K. Mizukami, H. Morii, T. Morishima, S. Murayama, M. Nagai, R. Nagata, S. Nakamura, M. Naruse, K. Natsume, T. Nishibori, H. Nishino, A. Noda, T. Noguchi, H. Ogawa, S. Oguri, I. Ohta, C. Otani, P. Richards, S. Sakai, N. Sato, Y. Sato, Y. Sekimoto, A. Shimizu, K. Shinozaki, H. Sugita, T. Suzuki, A. Suzuki, O. Tajima, S. Takada, S. Takakura, Y. Takei, T. Tomaru, Y. Uzawa, T. Wada, H. Watanabe, M. Yoshida, N. Yamasaki, T. Yoshida, and K. Yotsumoto. Mission Design of LiteBIRD. *Journal of Low Temperature Physics*, 176:733–740, September 2014, 1311.2847.

[163] J. E. McEwen, X. Fang, C. M. Hirata, and J. A. Blazek. FAST-PT: a novel algorithm to calculate convolution integrals in cosmological perturbation theory. *ArXiv e-prints*, March 2016, 1603.04826.

[164] P. M. Merkel and B. M. Schäfer. Gravitational lensing of the cosmic microwave background by non-linear structures. *Monthly Notices of the Royal Astronomical Society*, 411:1067–1076, February 2011, 1007.1408.

[165] P. M. Merkel and B. M. Schäfer. The interplay of CMB temperature lensing power reconstruction with primordial non-Gaussianity of local type. *Monthly Notices of the Royal Astronomical Society*, 429:444–451, February 2013, 1206.2851.

[166] L. Miller, C. Heymans, T. D. Kitching, L. van Waerbeke, T. Erben, H. Hildebrandt, H. Hoekstra, Y. Mellier, B. T. P. Rowe, J. Coupon, J. P. Dietrich, L. Fu, J. Harnois-Déraps, M. J. Hudson, M. Kilbinger, K. Kuijken, T. Schrabback, E. Semboloni, S. Vafaei, and M. Velander. Bayesian galaxy shape measurement for weak lensing surveys - III. Application to the Canada-France-Hawaii Telescope Lensing Survey. *Monthly Notices of the Royal Astronomical Society*, 429:2858–2880, March 2013, 1210.8201.

[167] L. Miller, T. D. Kitching, C. Heymans, A. F. Heavens, and L. van Waerbeke. Bayesian galaxy shape measurement for weak lensing surveys - I. Methodology and a fast-fitting algorithm. *Monthly Notices of the Royal Astronomical Society*, 382:315–324, November 2007, 0708.2340.

[168] V. F. Mukhanov, H. A. Feldman, and R. H. Brandenberger. Theory of cosmological perturbations. *Physics Reports*, 215:203–333, June 1992.

[169] T. Namikawa. CMB lensing bispectrum from nonlinear growth of the large scale structure. *Physical Review D*, 93(12):121301, June 2016, 1604.08578.

[170] T. Namikawa. CMB Lensing Bispectrum from Nonlinear Growth of the Large Scale Structure. *ArXiv e-prints*, April 2016, 1604.08578.

[171] T. Namikawa, D. Hanson, and R. Takahashi. Bias-hardened CMB lensing. *Monthly Notices of the Royal Astronomical Society*, 431:609–620, May 2013, 1209.0091.

[172] M. C. Neyrinck, I. Szapudi, and A. S. Szalay. Rejuvenating the Matter Power Spectrum: Restoring Information with a Logarithmic Density Mapping. *The Astrophysical Journall*, 698:L90–L93, June 2009, 0903.4693.

[173] T. Okamoto and W. Hu. Cosmic microwave background lensing reconstruction on the full sky. *Physical Review D*, 67(8):083002, April 2003, arXiv:astro-ph/0301031.

[174] N. Oppermann, H. Junklewitz, M. Greiner, T. A. Enßlin, T. Akahori, E. Carretti, B. M. Gaensler, A. Goobar, L. Harvey-Smith, M. Johnston-Hollitt, L. Pratley,

D. H. F. M. Schnitzeler, J. M. Stil, and V. Vacca. Estimating extragalactic Faraday rotation. *Astronomy and Astrophysics*, 575:A118, March 2015, 1404.3701.

[175] N. Oppermann, M. Selig, M. R. Bell, and T. A. Enßlin. Reconstruction of Gaussian and log-normal fields with spectral smoothness. *Physical Review E*, 87(3):032136, March 2013, 1210.6866.

[176] S. J. Osborne, D. Hanson, and O. Doré. Extragalactic foreground contamination in temperature-based CMB lens reconstruction. *Journal of Cosmology and Astroparticle Physics*, 3:024, March 2014, 1310.7547.

[177] Planck Collaboration, P. A. R. Ade, N. Aghanim, C. Armitage-Caplan, M. Arnaud, M. Ashdown, F. Atrio-Barandela, J. Aumont, C. Baccigalupi, and A. J. Banday et al. Planck 2013 results. XVI. Cosmological parameters. *Astronomy and Astrophysics*, 571:A16, November 2014, 1303.5076.

[178] Planck Collaboration, P. A. R. Ade, N. Aghanim, C. Armitage-Caplan, M. Arnaud, M. Ashdown, F. Atrio-Barandela, J. Aumont, C. Baccigalupi, and A. J. Banday et al. Planck 2013 results. XVII. Gravitational lensing by large-scale structure. *Astronomy and Astrophysics*, 571:A17, November 2014, 1303.5077.

[179] Planck Collaboration, P. A. R. Ade, N. Aghanim, C. Armitage-Caplan, M. Arnaud, M. Ashdown, F. Atrio-Barandela, J. Aumont, C. Baccigalupi, and A. J. Banday et al. Planck 2013 results. XXIV. Constraints on primordial non-Gaussianity. *Astronomy and Astrophysics*, 571:A24, November 2014, 1303.5084.

[180] Planck Collaboration, P. A. R. Ade, N. Aghanim, M. Arnaud, F. Arroja, M. Ashdown, J. Aumont, C. Baccigalupi, M. Ballardini, and A. J. Banday et al. Planck 2015 results. XVII. Constraints on primordial non-Gaussianity. *ArXiv e-prints*, February 2015, 1502.01592.

[181] Planck Collaboration, P. A. R. Ade, N. Aghanim, M. Arnaud, F. Arroja, M. Ashdown, J. Aumont, C. Baccigalupi, M. Ballardini, and A. J. Banday et al. Planck 2015 results. XVII. Constraints on primordial non-Gaussianity. *Astronomy and Astrophysics*, 594:A17, September 2016, 1502.01592.

[182] Planck Collaboration, P. A. R. Ade, N. Aghanim, M. Arnaud, M. Ashdown, J. Aumont, C. Baccigalupi, A. J. Banday, R. B. Barreiro, and J. G. Bartlett et al. Planck 2015 results. XIII. Cosmological parameters. *ArXiv e-prints*, February 2015, 1502.01589.

[183] Planck Collaboration, P. A. R. Ade, N. Aghanim, M. Arnaud, M. Ashdown, J. Aumont, C. Baccigalupi, A. J. Banday, R. B. Barreiro, and J. G. Bartlett et al. Planck 2015 results. XV. Gravitational lensing. *ArXiv e-prints*, February 2015, 1502.01591.

[184] Planck Collaboration, N. Aghanim, M. Arnaud, M. Ashdown, J. Aumont, C. Baccigalupi, A. J. Banday, R. B. Barreiro, J. G. Bartlett, and N. Bartolo et al. Planck 2015 results. XI. CMB power spectra, likelihoods, and robustness of parameters. *Astronomy and Astrophysics*, 594:A11, September 2016, 1507.02704.

[185] N. Porqueres, T. A. Enßlin, M. Greiner, V. Böhm, S. Dorn, P. Ruiz-Lapuente, and A. Manrique. Cosmic expansion history from SNe Ia data via information field theory: the charm code. *Astronomy and Astrophysics*, 599:A92, March 2017, 1608.04007.

[186] G. Pratten and A. Lewis. Impact of post-Born lensing on the CMB. *Journal of Cosmology and Astroparticle Physics*, 8:047, August 2016, 1605.05662.

[187] M. J. Rees. Polarization and Spectrum of the Primeval Radiation in an Anisotropic Universe. *The Astrophysical Journall*, 153:L1, July 1968.

[188] A. Refregier. Weak Gravitational Lensing by Large-Scale Structure. *Annual Review of Astron. and Astrophys.*, 41:645–668, 2003, astro-ph/0307212.

[189] D. M. Regan, E. P. S. Shellard, and J. R. Fergusson. General CMB and primordial trispectrum estimation. *Physical Review D*, 82(2):023520, July 2010, 1004.2915.

[190] M. Reinecke and D. S. Seljebotn. Libsharp - spherical harmonic transforms revisited. *Astronomy and Astrophysics*, 554:A112, June 2013, 1303.4945.

[191] R. Sachs. Gravitational Waves in General Relativity. VI. The Outgoing Radiation Condition. *Proceedings of the Royal Society of London Series A*, 264:309–338, November 1961.

[192] M. Schmittfull, Z. Vlah, and P. McDonald. Fast Large Scale Structure Perturbation Theory using 1D FFTs. *ArXiv e-prints*, March 2016, 1603.04405.

[193] M. M. Schmittfull, A. Challinor, D. Hanson, and A. Lewis. Joint analysis of CMB temperature and lensing-reconstruction power spectra. *Physical Review D*, 88(6):063012, September 2013, 1308.0286.

[194] M. D. Schneider, D. W. Hogg, P. J. Marshall, W. A. Dawson, J. Meyers, D. J. Bard, and D. Lang. Hierarchical Probabilistic Inference of Cosmic Shear. *The Astrophysical Journal*, 807:87, July 2015, 1411.2608.

[195] P. Schneider, J. Ehlers, and E. E. Falco. *Gravitational Lenses*. 1992.

[196] T. Schrabback, J. Hartlap, B. Joachimi, M. Kilbinger, P. Simon, K. Benabed, M. Bradač, T. Eifler, T. Erben, C. D. Fassnacht, F. W. High, S. Hilbert, H. Hildebrandt, H. Hoekstra, K. Kuijken, P. J. Marshall, Y. Mellier, E. Morganson, P. Schneider, E. Semboloni, L. van Waerbeke, and M. Velander. Evidence of the accelerated expansion of the Universe from weak lensing tomography with COSMOS. *Astronomy and Astrophysics*, 516:A63, June 2010, 0911.0053.

[197] R. Scoccimarro and H. M. P. Couchman. A fitting formula for the non-linear evolution of the bispectrum. *Monthly Notices of the Royal Astronomical Society*, 325:1312–1316, August 2001, astro-ph/0009427.

[198] N. Scoville, R. G. Abraham, H. Aussel, J. E. Barnes, A. Benson, A. W. Blain, D. Calzetti, A. Comastri, P. Capak, C. Carilli, J. E. Carlstrom, C. M. Carollo, J. Colbert, E. Daddi, R. S. Ellis, M. Elvis, S. P. Ewald, M. Fall, A. Franceschini, M. Giavalisco, W. Green, R. E. Griffiths, L. Guzzo, G. Hasinger, C. Impey, J.-P. Kneib, J. Koda, A. Koekemoer, O. Lefevre, S. Lilly, C. T. Liu, H. J. McCracken, R. Massey, Y. Mellier, S. Miyazaki, B. Mobasher, J. Mould, C. Norman, A. Refregier, A. Renzini, J. Rhodes, M. Rich, D. B. Sanders, D. Schiminovich, E. Schinnerer, M. Scodeggio, K. Sheth, P. L. Shopbell, Y. Taniguchi, N. D. Tyson, C. M. Urry, L. Van Waerbeke, P. Vettolani, S. D. M. White, and L. Yan. COSMOS: Hubble Space Telescope Observations. *The Astrophysical Journals*, 172:38–45, September 2007, astro-ph/0612306.

[199] C. Seitz and P. Schneider. Steps towards nonlinear cluster inversion through gravitational distortions. III. Including a redshift distribution of the sources. *Astronomy and Astrophysics*, 318:687–699, February 1997, astro-ph/9601079.

[200] S. Seitz, P. Schneider, and J. Ehlers. Light propagation in arbitrary spacetimes and the gravitational lens approximation. *Classical and Quantum Gravity*, 11:2345–2373, September 1994, astro-ph/9403056.

[201] M. Selig, M. R. Bell, H. Junklewitz, N. Oppermann, M. Reinecke, M. Greiner, C. Pachajoa, and T. A. Enßlin. NIFTY - Numerical Information Field Theory. A versatile PYTHON library for signal inference. *Astronomy and Astrophysics*, 554:A26, June 2013, 1301.4499.

[202] M. Selig, V. Vacca, N. Oppermann, and T. A. Enßlin. The denoised, deconvolved, and decomposed Fermi γ-ray sky. An application of the D^3PO algorithm. *Astronomy and Astrophysics*, 581:A126, September 2015, 1410.4562.

[203] U. Seljak. Gravitational Lensing Effect on Cosmic Microwave Background Anisotropies: A Power Spectrum Approach. *The Astrophysical Journal*, 463:1, May 1996, astro-ph/9505109.

[204] U. Seljak. Measuring Polarization in the Cosmic Microwave Background. *The Astrophysical Journal*, 482:6–16, June 1997, astro-ph/9608131.

[205] U. Seljak and M. Zaldarriaga. Signature of Gravity Waves in the Polarization of the Microwave Background. *Physical Review Letters*, 78:2054–2057, March 1997, astro-ph/9609169.

[206] U. Seljak and M. Zaldarriaga. Direct signature of an evolving gravitational potential from the cosmic microwave background. *Physical Review D*, 60(4):043504, August 1999, astro-ph/9811123.

[207] U. Seljak and M. Zaldarriaga. Measuring Dark Matter Power Spectrum from Cosmic Microwave Background. *Physical Review Letters*, 82:2636–2639, March 1999, astro-ph/9810092.

[208] Uroš Seljak. Weak lensing reconstruction and power spectrum estimation: Minimum variance methods. *The Astrophysical Journal*, 506(1):64, 1998.

[209] E. Semboloni, T. Schrabback, L. van Waerbeke, S. Vafaei, J. Hartlap, and S. Hilbert. Weak lensing from space: first cosmological constraints from three-point shear statistics. *Monthly Notices of the Royal Astronomical Society*, 410:143–160, January 2011, 1005.4941.

[210] C. Shapiro. Biased Dark Energy Constraints from Neglecting Reduced Shear in Weak-Lensing Surveys. *The Astrophysical Journal*, 696:775–784, May 2009, 0812.0769.

[211] C. Shapiro and A. Cooray. The Born and lens lens corrections to weak gravitational lensing angular power spectra. *Journal of Cosmology and Astroparticle Physics*, 3:007, March 2006, astro-ph/0601226.

[212] B. D. Sherwin, S. Das, A. Hajian, G. Addison, J. R. Bond, D. Crichton, M. J. Devlin, J. Dunkley, M. B. Gralla, M. Halpern, J. C. Hill, A. D. Hincks, J. P. Hughes, K. Huffenberger, R. Hlozek, A. Kosowsky, T. Louis, T. A. Marriage, D. Marsden, F. Menanteau, K. Moodley, M. D. Niemack, L. A. Page, E. D. Reese, N. Sehgal, J. Sievers, C. Sifón, D. N. Spergel, S. T. Staggs, E. R. Switzer, and E. Wollack. The Atacama Cosmology Telescope: Cross-correlation of cosmic microwave background lensing and quasars. *Physical Review D*, 86(8):083006, October 2012, 1207.4543.

[213] B. D. Sherwin, A. van Engelen, N. Sehgal, M. Madhavacheril, G. E. Addison, S. Aiola, R. Allison, N. Battaglia, J. A. Beall, D. T. Becker, J. R. Bond, E. Calabrese, R. Datta, M. J. Devlin, R. Dunner, J. Dunkley, A. E. Fox, P. Gallardo, M. Halpern, M. Hasselfield, S. Henderson, J. C. Hill, G. C. Hilton, J. Hubmayr, J. P. Hughes, A. D. Hincks, R. Hlozek, K. M. Huffenberger, B. Koopman, A. Kosowsky, T. Louis, L. Maurin, J. McMahon, K. Moodley, S. Naess, F. Nati, L. Newburgh, M. D. Niemack, L. A. Page, J. Sievers, D. N. Spergel, S. T. Staggs, R. J. Thornton, J. Van Lanen, E. Vavagiakis, and E. J. Wollack. The Atacama Cosmology Telescope: Two-Season ACTPol Lensing Power Spectrum. *ArXiv e-prints*, November 2016, 1611.09753.

[214] P. Simon. Improving three-dimensional mass mapping with weak gravitational lensing using galaxy clustering. *Astronomy and Astrophysics*, 560:A33, December 2013, 1203.6205.

[215] K. M. Smith, W. Hu, and M. Kaplinghat. Cosmological information from lensed CMB power spectra. *Physical Review D*, 74(12):123002, December 2006, arXiv:astro-ph/0607315.

[216] K. M. Smith, O. Zahn, and O. Doré. Detection of gravitational lensing in the cosmic microwave background. *Physical Review D*, 76(4):043510, August 2007, 0705.3980.

[217] R. E. Smith, J. A. Peacock, A. Jenkins, S. D. M. White, C. S. Frenk, F. R. Pearce, P. A. Thomas, G. Efstathiou, and H. M. P. Couchman. Stable clustering, the halo model and non-linear cosmological power spectra. *Monthly Notices of the Royal Astronomical Society*, 341:1311–1332, June 2003, astro-ph/0207664.

[218] Y.-S. Song and L. Knox. Determination of cosmological parameters from cosmic shear data. *Physical Review D*, 70(6):063510, September 2004, astro-ph/0312175.

[219] V. Springel, S. D. M. White, A. Jenkins, C. S. Frenk, N. Yoshida, L. Gao, J. Navarro, R. Thacker, D. Croton, J. Helly, J. A. Peacock, S. Cole, P. Thomas, H. Couchman, A. Evrard, J. Colberg, and F. Pearce. Simulations of the formation, evolution and clustering of galaxies and quasars. *Nature*, 435:629–636, June 2005, astro-ph/0504097.

[220] K. T. Story, D. Hanson, P. A. R. Ade, K. A. Aird, J. E. Austermann, J. A. Beall, A. N. Bender, B. A. Benson, L. E. Bleem, J. E. Carlstrom, C. L. Chang, H. C. Chiang, H.-M. Cho, R. Citron, T. M. Crawford, A. T. Crites, T. de Haan, M. A. Dobbs, W. Everett, J. Gallicchio, J. Gao, E. M. George, A. Gilbert, N. W. Halverson, N. Harrington, J. W. Henning, G. C. Hilton, G. P. Holder, W. L. Holzapfel, S. Hoover, Z. Hou, J. D. Hrubes, N. Huang, J. Hubmayr, K. D. Irwin, R. Keisler, L. Knox, A. T. Lee, E. M. Leitch, D. Li, C. Liang, D. Luong-Van, J. J. McMahon, J. Mehl, S. S. Meyer, L. Mocanu, T. E. Montroy, T. Natoli, J. P. Nibarger, V. Novosad, S. Padin, C. Pryke, C. L. Reichardt, J. E. Ruhl, B. R. Saliwanchik, J. T. Sayre, K. K. Schaffer, G. Smecher, A. A. Stark, C. Tucker, K. Vanderlinde, J. D. Vieira, G. Wang, N. Whitehorn, V. Yefremenko, and O. Zahn. A Measurement of the Cosmic Microwave Background Gravitational Lensing Potential from 100 Square Degrees of SPTpol Data. *The Astrophysical Journal*, 810:50, September 2015, 1412.4760.

[221] A. Suzuki, P. Ade, Y. Akiba, C. Aleman, K. Arnold, C. Baccigalupi, B. Barch, D. Barron, A. Bender, D. Boettger, J. Borrill, S. Chapman, Y. Chinone, A. Cukierman, M. Dobbs, A. Ducout, R. Dunner, T. Elleflot, J. Errard, G. Fabbian, S. Feeney, C. Feng, T. Fujino, G. Fuller, A. Gilbert, N. Goeckner-Wald, J. Groh, T. D. Haan, G. Hall, N. Halverson, T. Hamada, M. Hasegawa, K. Hattori, M. Hazumi, C. Hill, W. Holzapfel, Y. Hori, L. Howe, Y. Inoue, F. Irie, G. Jaehnig, A. Jaffe, O. Jeong, N. Katayama, J. Kaufman, K. Kazemzadeh, B. Keating, Z. Kermish, R. Keskitalo, T. Kisner, A. Kusaka, M. L. Jeune, A. Lee, D. Leon, E. Linder, L. Lowry, F. Matsuda, T. Matsumura, N. Miller, K. Mizukami, J. Montgomery, M. Navaroli, H. Nishino, J. Peloton, D. Poletti, G. Puglisi, G. Rebeiz, C. Raum, C. Reichardt,

P. Richards, C. Ross, K. Rotermund, Y. Segawa, B. Sherwin, I. Shirley, P. Siritanasak, N. Stebor, R. Stompor, J. Suzuki, O. Tajima, S. Takada, S. Takakura, S. Takatori, A. Tikhomirov, T. Tomaru, B. Westbrook, N. Whitehorn, T. Yamashita, A. Zahn, and O. Zahn. The Polarbear-2 and the Simons Array Experiments. *Journal of Low Temperature Physics*, 184:805–810, August 2016, 1512.07299.

[222] R. M. Szepietowski, D. J. Bacon, J. P. Dietrich, M. Busha, R. Wechsler, and P. Melchior. Density mapping with weak lensing and phase information. *Monthly Notices of the Royal Astronomical Society*, 440:2191–2200, May 2014, 1306.5324.

[223] M. Takada and B. Jain. Cosmological parameters from lensing power spectrum and bispectrum tomography. *Monthly Notices of the Royal Astronomical Society*, 348:897–915, March 2004, astro-ph/0310125.

[224] R. Takahashi, M. Sato, T. Nishimichi, A. Taruya, and M. Oguri. Revising the Halofit Model for the Nonlinear Matter Power Spectrum. *The Astrophysical Journal*, 761:152, December 2012, 1208.2701.

[225] A. Taruya, M. Takada, T. Hamana, I. Kayo, and T. Futamase. Lognormal Property of Weak-Lensing Fields. *The Astrophysical Journal*, 571:638–653, June 2002, astro-ph/0202090.

[226] A. N. Taylor. Imaging the 3-D cosmological mass distribution with weak gravitational lensing. *ArXiv Astrophysics e-prints*, November 2001, astro-ph/0111605.

[227] M. Tegmark, A. J. S. Hamilton, M. A. Strauss, M. S. Vogeley, and A. S. Szalay. Measuring the Galaxy Power Spectrum with Future Redshift Surveys. *The Astrophysical Journal*, 499:555–576, May 1998, astro-ph/9708020.

[228] The Polarbear Collaboration: P. A. R. Ade, Y. Akiba, A. E. Anthony, K. Arnold, M. Atlas, D. Barron, D. Boettger, J. Borrill, S. Chapman, Y. Chinone, M. Dobbs, T. Elleflot, J. Errard, G. Fabbian, C. Feng, D. Flanigan, A. Gilbert, W. Grainger, N. W. Halverson, M. Hasegawa, K. Hattori, M. Hazumi, W. L. Holzapfel, Y. Hori, J. Howard, P. Hyland, Y. Inoue, G. C. Jaehnig, A. H. Jaffe, B. Keating, Z. Kermish, R. Keskitalo, T. Kisner, M. Le Jeune, A. T. Lee, E. M. Leitch, E. Linder, M. Lungu, F. Matsuda, T. Matsumura, X. Meng, N. J. Miller, H. Morii, S. Moyerman, M. J. Myers, M. Navaroli, H. Nishino, A. Orlando, H. Paar, J. Peloton, D. Poletti, E. Quealy, G. Rebeiz, C. L. Reichardt, P. L. Richards, C. Ross, I. Schanning, D. E. Schenck, B. D. Sherwin, A. Shimizu, C. Shimmin, M. Shimon, P. Siritanasak, G. Smecher, H. Spieler, N. Stebor, B. Steinbach, R. Stompor, A. Suzuki, S. Takakura, T. Tomaru, B. Wilson, A. Yadav, and O. Zahn. A Measurement of the Cosmic Microwave Background B-mode Polarization Power Spectrum at Sub-degree Scales with POLARBEAR. *The Astrophysical Journal*, 794:171, October 2014, 1403.2369.

[229] J. A. Tyson, D. Wittman, I. Dell'Antonio, A. Becker, V. Margoniner, and DLS Team. The Deep Lens Survey: Overview. In *American Astronomical Society Meeting*

Abstracts, volume 33 of *Bulletin of the American Astronomical Society*, page 1464, December 2001.

[230] A. van Engelen, S. Bhattacharya, N. Sehgal, G. P. Holder, O. Zahn, and D. Nagai. CMB Lensing Power Spectrum Biases from Galaxies and Clusters Using High-angular Resolution Temperature Maps. *The Astrophysical Journal*, 786:13, May 2014, 1310.7023.

[231] A. van Engelen, R. Keisler, O. Zahn, K. A. Aird, B. A. Benson, L. E. Bleem, J. E. Carlstrom, C. L. Chang, H. M. Cho, T. M. Crawford, A. T. Crites, T. de Haan, M. A. Dobbs, J. Dudley, E. M. George, N. W. Halverson, G. P. Holder, W. L. Holzapfel, S. Hoover, Z. Hou, J. D. Hrubes, M. Joy, L. Knox, A. T. Lee, E. M. Leitch, M. Lueker, D. Luong-Van, J. J. McMahon, J. Mehl, S. S. Meyer, M. Millea, J. J. Mohr, T. E. Montroy, T. Natoli, S. Padin, T. Plagge, C. Pryke, C. L. Reichardt, J. E. Ruhl, J. T. Sayre, K. K. Schaffer, L. Shaw, E. Shirokoff, H. G. Spieler, Z. Staniszewski, A. A. Stark, K. Story, K. Vanderlinde, J. D. Vieira, and R. Williamson. A Measurement of Gravitational Lensing of the Microwave Background Using South Pole Telescope Data. *The Astrophysical Journal*, 756:142, September 2012, 1202.0546.

[232] A. van Engelen, B. D. Sherwin, N. Sehgal, G. E. Addison, R. Allison, N. Battaglia, F. de Bernardis, J. R. Bond, E. Calabrese, K. Coughlin, D. Crichton, R. Datta, M. J. Devlin, J. Dunkley, R. Dünner, P. Gallardo, E. Grace, M. Gralla, A. Hajian, M. Hasselfield, S. Henderson, J. C. Hill, M. Hilton, A. D. Hincks, R. Hlozek, K. M. Huffenberger, J. P. Hughes, B. Koopman, A. Kosowsky, T. Louis, M. Lungu, M. Madhavacheril, L. Maurin, J. McMahon, K. Moodley, C. Munson, S. Naess, F. Nati, L. Newburgh, M. D. Niemack, M. R. Nolta, L. A. Page, C. Pappas, B. Partridge, B. L. Schmitt, J. L. Sievers, S. Simon, D. N. Spergel, S. T. Staggs, E. R. Switzer, J. T. Ward, and E. J. Wollack. The Atacama Cosmology Telescope: Lensing of CMB Temperature and Polarization Derived from Cosmic Infrared Background Cross-correlation. *The Astrophysical Journal*, 808:7, July 2015, 1412.0626.

[233] L. Van Waerbeke and Y. Mellier. Gravitational Lensing by Large Scale Structures: A Review. *ArXiv Astrophysics e-prints*, May 2003, astro-ph/0305089.

[234] L. Van Waerbeke, Y. Mellier, T. Erben, J. C. Cuillandre, F. Bernardeau, R. Maoli, E. Bertin, H. J. McCracken, O. Le Fèvre, B. Fort, M. Dantel-Fort, B. Jain, and P. Schneider. Detection of correlated galaxy ellipticities from CFHT data: first evidence for gravitational lensing by large-scale structures. *Astronomy and Astrophysics*, 358:30–44, June 2000, astro-ph/0002500.

[235] Norbert Wiener. *Extrapolation, Interpolation, and Smoothing of Stationary Time Series*. The MIT Press, 1964.

[236] D. M. Wittman, J. A. Tyson, D. Kirkman, I. Dell'Antonio, and G. Bernstein. Detection of weak gravitational lensing distortions of distant galaxies by cosmic dark matter at large scales. *Nature*, 405:143–148, May 2000, astro-ph/0003014.

[237] A. P. S. Yadav, E. Komatsu, B. D. Wandelt, M. Liguori, F. K. Hansen, and S. Matarrese. Fast Estimator of Primordial Non-Gaussianity from Temperature and Polarization Anisotropies in the Cosmic Microwave Background. II. Partial Sky Coverage and Inhomogeneous Noise. *The Astrophysical Journal*, 678:578–582, May 2008, 0711.4933.

[238] M. Zaldarriaga. Lensing of the CMB: Non-Gaussian aspects. *Physical Review D*, 62(6):063510, September 2000, astro-ph/9910498.

[239] M. Zaldarriaga and U. Seljak. All-sky analysis of polarization in the microwave background. *Physical Review D*, 55:1830–1840, February 1997, astro-ph/9609170.

[240] M. Zaldarriaga and U. Seljak. Gravitational lensing effect on cosmic microwave background polarization. *Physical Review D*, 58(2):023003, July 1998, astro-ph/9803150.

[241] Y. B. Zeldovich. A hypothesis, unifying the structure and the entropy of the Universe. *Monthly Notices of the Royal Astronomical Society*, 160:1P, 1972.

[242] P. Zhang, M. Liguori, R. Bean, and S. Dodelson. Probing Gravity at Cosmological Scales by Measurements which Test the Relationship between Gravitational Lensing and Matter Overdensity. *Physical Review Letters*, 99(14):141302, October 2007, 0704.1932.

[243] J. Zuntz, T. Kacprzak, L. Voigt, M. Hirsch, B. Rowe, and S. Bridle. IM3SHAPE: a maximum likelihood galaxy shear measurement code for cosmic gravitational lensing. *Monthly Notices of the Royal Astronomical Society*, 434:1604–1618, September 2013, 1302.0183.

Danksagung

Danke Mama, danke Papa, dafür, dass ihr mich immer unterstützt und für mich da seid. Danke Nico, einfach für alles in den letzten vier Jahren, insbesondere deine Geduld und dein Verständnis, und für die vielen tausend Gleiskilometer, die du in dieser Zeit für uns zurückgelegt hast.